NASA Conference Publication 3344

Rotordynamic Instability Problems in High-Performance Turbomachinery 1996

Proceedings of a workshop cosponsored by
Texas A&M University, College Station, Texas,
and NASA Lewis Research Center, Cleveland, Ohio,
and held at Texas A&M University
College Station, Texas
May 6–8, 1996

National Aeronautics and
Space Administration

Office of Management

**Scientific and Technical
Information Program**

1997

PREFACE

All of the papers contained in this proceedings added significantly to the balance and discussions of the workshop. In this, the 8th Instability Workshop, we see active magnetic bearings (AMB's) as a new thread in the fabric of instability issues. Nordmann and his coworkers at the Technical University of Darmstadt demonstrate the utility of AMB's to identify the rotordynamic coefficents of a hydrostatic bearing. Similarly, Wagner and Steff demonstrate the utility of AMB's to measure rotordynamic coefficients of labyrinth gas seals. This paper culminates many years of development work at Mannesman Demag and is clearly worth the wait. Their apparatus is elegant in design and execution. The paper by Kwanka and Nagel demonstrates a fundamentally new approach to measure rotordynamic coefficients of gas labyrinth seals by using an AMB to control the onset speed of instability of a test rotor. Papers by Kirk and his colleagues at VPI and Tessier at Revolve Technology present new and interesting results concerning possible dry-friction whirl and its avoidance in drop tests of rotors supported by AMB's.

The paper by Kleynhans and Childs suggests that the long-noted discrepancies between theory and experiment for annular honeycomb seals may be resolved. It verified by a broad-frequency-range test effort, the prediction of rotordynamic coefficients for honeycomb seals may finally be accomplished.

These are a few of the papers which we found to be of note; however, we expect each reader will find his or her own favorite in this excellent collection.

Chairs:

Dara Childs and John Vance
Turbomachinery Laboratory
Texas A& M University

and

Robert C. Hendricks
NASA Lewis Research Center

TABLE OF CONTENTS

SESSION I

BEARINGS

THREE-WAVE GAS JOURNAL BEARING BEHAVIOR WITH SHAFT RUNOUT

Florin Dimofte
The University of Toledo
Toledo, Ohio

and

Robert C. Hendricks
NASA Lewis Research Center
Cleveland, Ohio

ABSTRACT:

Experimental orbits of a free-mounted, three-wave gas journal bearing housing where recorded and compared to transient predicted orbits. The shaft was mounted eccentric with a fixed runout. Experimental observations for both the absolute bearing housing center orbits and the relative bearing housing center to shaft center orbits are in good agreement with the predictions. The sub-synchronous whirl motion generated by the fluid film was found experimentally and predicted theoretically for certain speeds. A three-wave journal bearing can run stably under dynamic loads with orbits well inside the bearing clearance. Moreover, the orbits are almost circular free of the influence of bearing wave shape.

INTRODUCTION:

The wave bearing concept has been under development since 1992. At that time both the steady-state and dynamic performance under fixed side load were analyzed [1, 2]. Moreover, the influence of both the number of waves and the wave amplitude to radial clearance ratio were also analyzed [3, 4]. Since 1993, first the steady-state wave journal bearing characteristics and then the bearing dynamic stability have been experimentally measured; good agreement was found between the experimental data and theoretical predictions [5, 6, 7, and 8]. In addition the experimental work reveled good dynamic behavior of the wave bearing when the sub-synchronous whirl motion occurs. The wave bearing performed well keeping the orbit of the sub-synchronous motion inside the bearing clearance [7, 8]. Consequently, the wave bearing should perform well under dynamic loading conditions that often occur in most rotating machinery; any rotor can be subject to a dynamic load due to an unbalance or a runout of the shaft. Therefore in this paper both an experimental program and a transient analysis have been performed to record and respectively predict the orbits of the bearing housing center when the shaft has a known fixed runout.

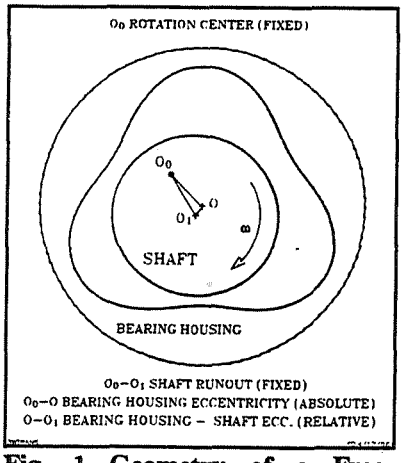

Fig. 1 Geometry of a Free-Mounted, Three-Wave Journal Bearing with Fixed Shaft Runout.

APPARATUS:

The wave bearing rig described in references [5 to 8] was used to perform the experimental work. The axis of the spindle that drives this rig was vertical and the experimental bearing housing was mounted on the rig table supported by two pressurized thrust plates. These configuration keeps the bearing housing stiff in the axial and angular directions but allows it to move freely in radial direction. The experimental shaft was an extension of the rig spindle shaft. It was mounted into the tapered end of the spindle shaft with a fixed runout (for this experiment 11 μm). A cross section by a horizontal plane of the experimental bearing is shown in Fig. 1. The fixed rotation center for the system is O_o. O_1 and O are the centers of the shaft and bearing housing, respectively. The shaft runout O_o-O_1 is fixed. The goal of this work is to record and to predict the absolute and relative orbits of the bearing housing center, O. The

motion of the center O can be observed like a absolute motion for instance with regard to the center of rotation O_o, or like a relative motion with regard to the center of the shaft O_1. Figure 2 shows the experimental bearing set up. Two sets of light beam proximity probes were used. Two probes were located at 90 degrees in the bottom side of the bearing housing and "looking" at the shaft. These probes detected the relative orbit of the bearing housing center, to the shaft center (O - O_1). The second set of two probes were located also at 90 degrees but held by supports fixed on the rig table and "looking" at the bearing housing. These latter probes detect the absolute orbit of the bearing housing center (O - O_o). A polished circumferencial strip was made on the outside bearing housing surface to avoid asperity noise from its roughness. The light beam probes were calibrated using the known, fixed, runout of the shaft. The displacement of the shaft was measured with a precision of 0.1 μm. The theoretical prediction of the orbits were made through a transient analysis of the bearing housing center motion.

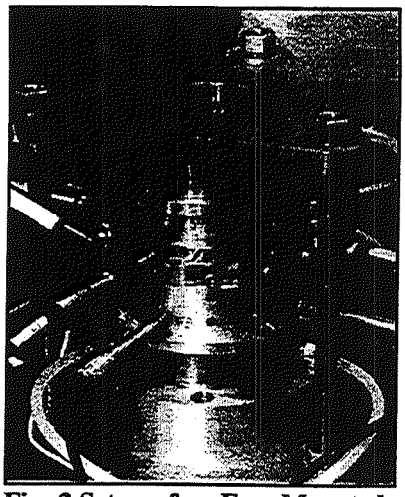

Fig. 2 Setup of an Free-Mounted, Three-Wave, Experimental Journal Bearing.

ANALYSIS:

The study of the bearing housing center movement can be done using the motion equation of this center along and perpendicular to the radial direction O_o-O (axis ζ and η in Fig.3):

$$MC\left[\frac{d^2\epsilon_o}{dt^2} - \epsilon_o\left(\frac{d\psi}{dt}\right)^2\right] + K\epsilon_o + B\frac{d\epsilon_o}{dt} = F_\zeta$$

$$MC\left(\epsilon_o\frac{d^2\psi}{dt^2} + 2\frac{d\psi}{dt}\frac{d\epsilon_o}{dt}\right) + K\epsilon_o\psi + B\epsilon_o\frac{d\psi}{dt} = F_\eta \qquad (1)$$

where: M is the bearing housing mass, C is the radial clearance (difference between shaft radius and mean wave radius of wave bearing), K is the external stiffness and B is the external damping in the bearing housing support and connection system, F_ζ and F_η are the fluid film force components acting parallel and perpendicular to the O_o-O direction, respectively. Based on the notation defined in Fig. 3, $\epsilon_o = e_o/C$ (e_o = O_o-O) is the bearing housing absolute eccentricity ratio, and ψ is the rotation angle of the O_o-O around O_o. Also, Fig. 3 shows the eccentricity e = O_1-O (O_1-O is the line joining the shaft center, O_1, and the bearing center, O), and the shaft runout ρ= O_o-O_1. Assuming that the motion starts from downward vertical where the shaft and the bearing are concentric (e = 0.), then, when the shaft rotates around O_o with the angular speed ω, ρ makes the angle Ω and drives the bearing so that e_o makes the angle ψ.

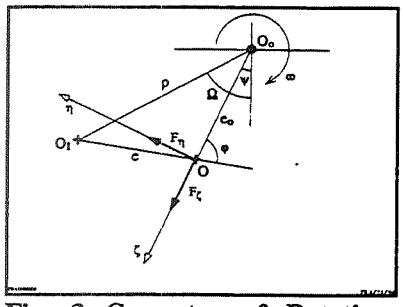

Fig. 3 Geometry of Rotation, Shaft, and Bearing Centers.

The governing equations (1) are two scalar, coupled, nonlinear ordinary differential equations. These equations are integrated simultaneously using a fourth order Runge-Kutta method for known values of M, C, F_ζ, F_η, K, and B and initial values of ϵ_o, ψ, $d\epsilon_o/dt$, and $d\psi/dt$ [9]. The fluid film forces applied to the bearing surface are:

$$F_\zeta = F_r\cos\varphi + F_t\sin\varphi$$

$$F_\eta = F_r\sin\varphi - F_t\cos\varphi \qquad (2)$$

F_r and F_t are the projections of fluid film force along and perpendicular to the line of centers O_1-O (Fig. 3):

$$F_r = F_{r_0} + K_{rr}S_r + K_{rt}S_t + B_{rr}V_r + B_{rt}V_t$$
$$F_t = F_{t_0} + K_{tr}S_r + K_{tt}S_t + B_{tr}V_r + B_{tt}V_t \qquad (3)$$

where S_i, and V_i, (i = r,t) are the space (displacement) and velocity between the shaft center, O_1, and the bearing [housing] center, O, respectively. Coordinate r is along the line of centers, O_1-O (Fig. 3), and coordinate t is perpendicular to this line. F_{i0} (i = r,t) are the bearing steady-state load projections, and K_{ij}, B_{ij} (i = r,t; j = r,t) are the bearing dynamic stiffness and damping coefficients at a given time step location. The bearing steady-state force and dynamic stiffness and damping coefficients can be computed by integrating the Reynolds pressure equation at each time step location of the shaft with respect to the bearing. This equation, assuming the gas will expand isothermal, is:

$$\frac{\partial}{R\partial\theta}\left(\frac{h^3}{\mu}p\frac{\partial p}{R\partial\theta}\right) + \frac{\partial}{\partial z}\left(\frac{h^3}{\mu}p\frac{\partial p}{\partial z}\right) =$$
$$6\left[2pV_n + 2\frac{\partial(ph)}{\partial t} + pV_\theta\frac{\partial h}{R\partial\theta} + h\frac{\partial(pV_\theta)}{R\partial\theta}\right] \qquad (4)$$

where: p, and h are the fluid film pressure and thickness, respectively; θ is the angular coordinate along the shaft circumference, starting at the line of centers (O-O^1); z is the axial coordinate parallel to the shaft axis; R is the shaft radius; t is the time; V_n is the difference between the shaft surface and bearing surface speed projected on the perpendicular direction to the shaft or bearing surface, respectively, and V_θ is the component of the shaft surface speed along its circumference.

The Reynolds equation (4) can be integrated using its complex form and a small perturbation technique. This procedure is described, for instance, in reference [10].

The solution procedure can start with input data set (bearing length, diameter, radial clearance, shaft turning speed, shaft runout, and the time step). In addition a set of starting values at time = 0 are required:

$$\epsilon_o = \rho, \qquad \frac{\partial\epsilon_o}{\partial t} = 0.$$
$$\psi = 0., \qquad \frac{\partial\psi}{\partial t} = 0. \qquad (5)$$

Then, at each time step, knowing ϵ_o, ψ, and Ω ($\Omega = \omega t$), the O_oO_1O triangle (Fig. 3) is known and all geometrical parameters as well as displacements and velocities can be calculated. Therefore, the Reynolds equation (4) can be integrated over the fluid film. Then all parameters of the motion equation (1) are known as well as the starting values for the next time step (ϵ_o, ψ, and their time derivatives, Ω) and the procedure is repeated until the orbits are completed.

RESULTS AND DISCUSSION:

The experimental bearing was 51 mm in diameter, 58 mm length, 20 μm radial clearance and 2.2 kg mass. The bearing has three waves with a 0.5 wave amplitude to radial clearance ratio. The shaft was set with a 11 μm runout. The external damping in the bearing housing support and connection system was found to be 0.05 Ns/m. The external stiffness (K in equations 1) have little influence on the bearings orbits and is approximately zero. The top

proximity probes (Fig. 2) produced 500 mV for 5.78 μm and 4.78 μm displacements in horizontal and vertical directions respectively, and the bottom probes produced 500 mV for 6.11 μm and 6.90 μm displacements in horizontal and vertical directions. (Horizontal and vertical directions refer to the directions on the oscilloscope photographs shown in the right side of the following 4 to 7 figures)

The test rig was run at four different speeds: 2156, 3288, 4588, and 5539 RPM. Up to 3100 RPM the bearing shows sensitivity to the sub-synchronous whirl. Both the absolute and relative observed orbits of the bearing housing center are shown in the oscilloscope photos shown on right side of figure 4. On the left side of figure 4 the computed orbits are presented with a time step of .00001 seconds and for 30000 steps. The experimental orbits appeared as ellipses rather than circles due to the difference in the probe sensitivity in horizontal and vertical directions mentioned above. First, Fig. 4 shows that both the experimental and theoretical orbits have the same patterns. These patterns are made by the sub-synchronous whirl motion. The transient analysis reveals these same patterns. Both the experimental and theoretical absolute orbits (top of Fig. 4) are within a region between 5 μm to 12 μm radius. Also, both the experimental and theoretical relative orbits (bottom of Fig. 4) run inside a circle of approx 5 μm radius.

The bearing stability increased as the running speed of the rig increased. Figure 5 shows the results for 3288 RPM. The experimental orbits are perfectly stable. The shaft runout makes large absolute orbits of the bearing housing (right upper corner of Fig. 5). However, the radius of the relative orbits is approx. 2.5 μm (bottom right corner of Fig. 5) despite the shaft 11 μm runout, i.e., the bearing follows the shaft very well. The predicted orbits, showed by Fig. 5, match very well with the observed orbits. In addition, the theory shows that the bearing will run stably. After a couple of rotations from the starting point the orbits are stable keeping almost the same path.

The next runs were made at 4588 RPM and 5539 RPM (Fig. 6 and 7 respectively). The conclusions found running at 3288 RPM are also valid at higher speeds. However, the relative orbits of the bearing housing increase while the absolute orbits decrease as speed increases. This effect shows the influence of both the external damping and the bearing inertia on the orbit radius magnitude. In addition the bearing runs more and more stable as speed increases and the theory shows that the number of rotations before the bearing reaches a stable orbit diminishes as speed increases.

All runs (Fig. 4 to 7) show only a small influence of the bearing waved shape on the orbit shape despite the fact that the experimental bearing has a large wave amplitude ratio, 0.5. This confirms that the wave bearing with a low number of waves, such as 3, works well under dynamic loads. The bearing behaves in such a way as to average the influence of the wave even though locally the load is changing.

CONCLUSIONS:

The experimental and theoretical work reported in this paper for a free mounted, three-wave gas journal bearing and a fix shaft runout, shows:

1. Good agreement between experimentally observed and theoretically predicted orbits at all tested speeds.

2. The sub-synchronous whirl motion influences the bearing housing orbits if the bearing speeds are in the region where the bearing itself is susceptible to the sub-synchronous whirl instability. When the bearing runs under such circumstances the orbits show a specific pattern. This was observed experimentally and was also confirmed theoretically by the transient analysis.

3. A three-wave journal bearing can run stably under dynamic rotating load, averaging its behavior when the wave exposure to the load is changing and with small orbits well within the bearing clearance. The orbits are almost circular and nearly free of the influence of wave bearing shape.

REFERENCES:

1. Dimofte, F., "Wave Journal Bearing with Compressible Lubricant; Part I: The Wave Bearing Concept and a Comparison to the Plain Circular Bearing", STLE Tribology Trans. Vol. 38, 1, pp.153-160, (1995)

2. Dimofte, F., "Wave Journal Bearing with Compressible Lubricant; Part II: A Comparison of the Wave Bearing with Wave Grooved Bearing and Lobe Bearing", STLE Tribology Trans. Vol. 38, 2, pp.364-372, (1995)

3. Dimofte, F., "A Waved Journal Bearing Concept - Evaluating Steady-State and Dynamic Performance with a Potential Active Control Alternative", Proceedings of the ASME 14th Biennial Conf. on Mechanical Vibration and Noise, September 19-22, 1993, Albuquerque, NM, DE-Vol. 60, Vibration of Rotating Systems, pp. 121-128.

4. Dimofte, F., "A Waved Journal Bearing Concept with Improved Steady-State and Dynamic Performance", presented to The 7th Workshop on Rotordynamic Instability, May 10-12, 1993, Texas A&M University, College Station, TX., published in "Rotordynamic Instability Problems in High-Performance Turbomachinery", NASA CP 1036, pp. 419-429, 1993.

5. Dimofte, F., and Addy, H. E., "Pressure Measurements of a Three Wave Journal Bearing", proceedings of the Seal Flow Code Development-93 workshop held at NASA Lewis Research Center, Cleveland, OH, Nov. 3-4, 1993, NASA CP 10136, pp. 285-294.

6. Dimofte, F., Addy, H. E., and Walker, J. F., "Preliminary Experimental Results of a Three Wave Journal Air Bearing", Proceeding of Advanced Earth-to-Orbit Propulsion Technology Conference held at NASA Marshall Space Flight Center, Huntsville, AL, May 17-19, 1994, NASA CP 3282, Vol II, pp.375-384, 1994.

7. Dimofte, F., and Hendrichs, R. C., "Fractional Whirl Motion in Wave Journal Bearings", proceedings of Forth Seal Development Workshop held at NASA Lewis Research Center in Cleveland, OH, on June 14-15, 1995, NASA CP 10181 pp. 337-340.

8. Dimofte, F., and Hendricks, R. C., "Two- and Three- Wave Journal Bearing Fractional Whirl Motion", proceedings of The Society of Engineering Science 32nd Annual Technical Meeting held in New Orleans, LA, on Oct. 29-Nov. 2, 1995, pp. 773-774.

9. Vijayaraghavan, D., and Brewe, D. E., "Frequency Effects on the Stability of a Journal Bearing for Periodic Loading", ASME Journal of Tribology, Vol. 114, No. 1, pp. 107-115, 1992.

10. Dimofte, F., "Effect of Fluid Compressibility on Journal Bearing Performance", STLE Tribology Trans. Vol. 36, 3, pp.341-350, 1993

ACKNOWLEDGMENT:

This work was performed under NASA NCC3-436 at NASA Lewis Research Center in Cleveland, Ohio. The authors would like to express their gratitude to Mr. Joseph Hemminger for continued interest and support.

Predicted

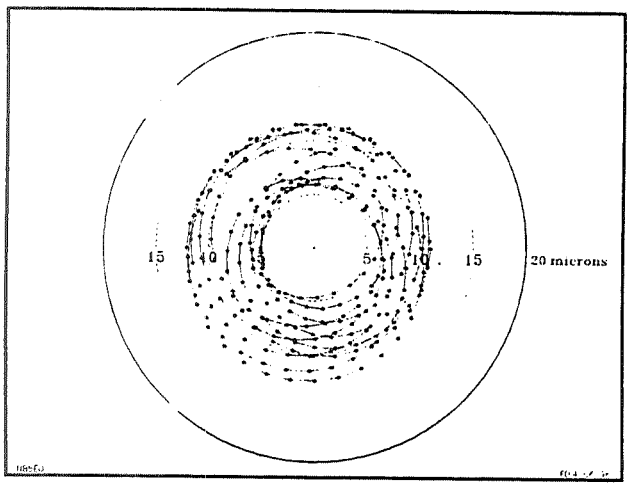

Observed

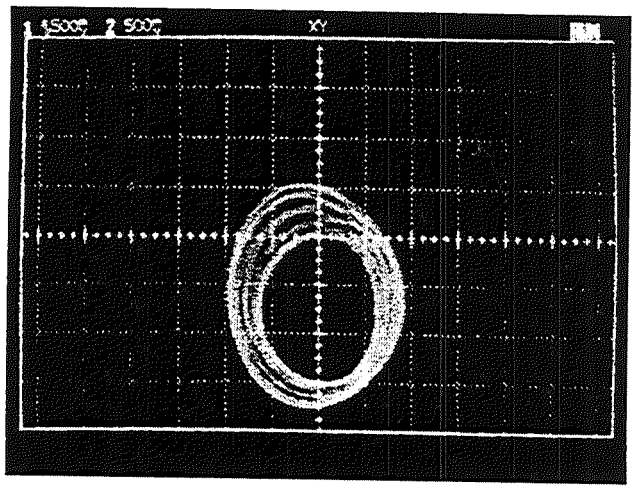

Absolute Bearing Housing Center Orbits

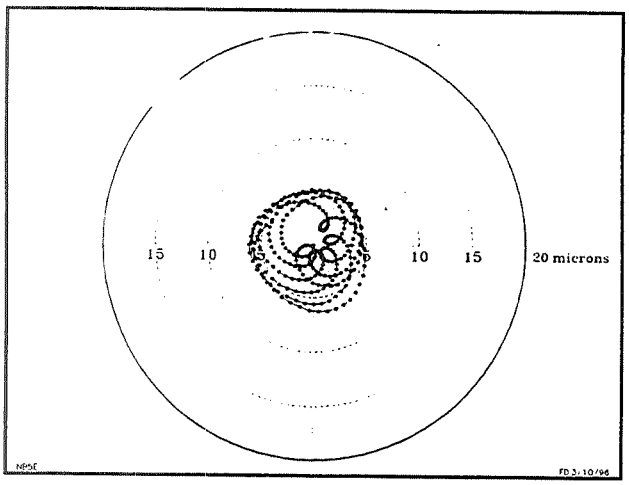

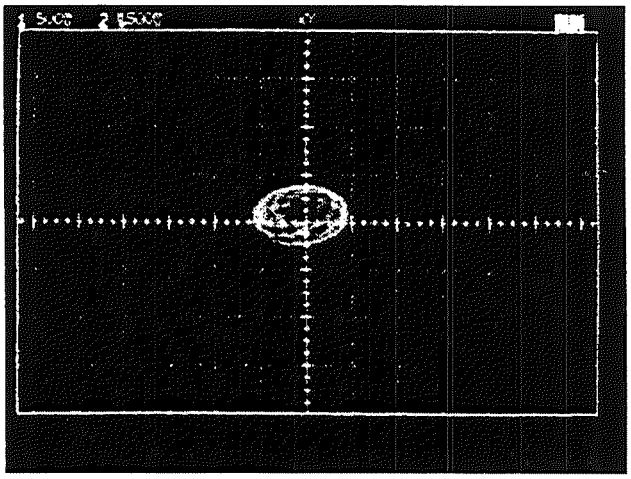

Relative Bearing Housing - Shaft Center Orbits

Fig. 4 Predicted and Experimentally Observed Orbits at 2156 RPM Shaft Rotating Speed

Predicted

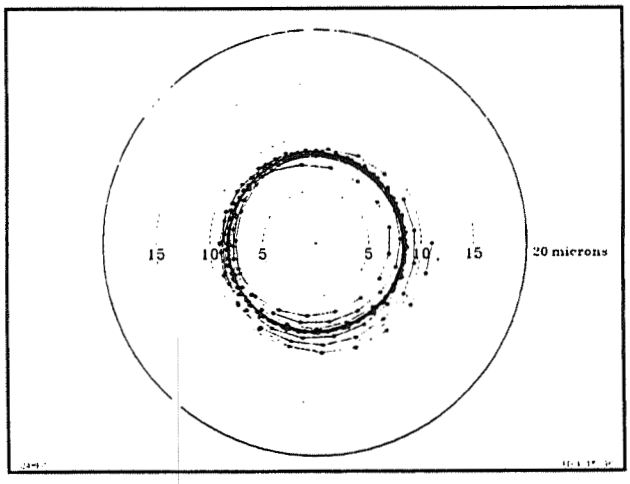

Observed

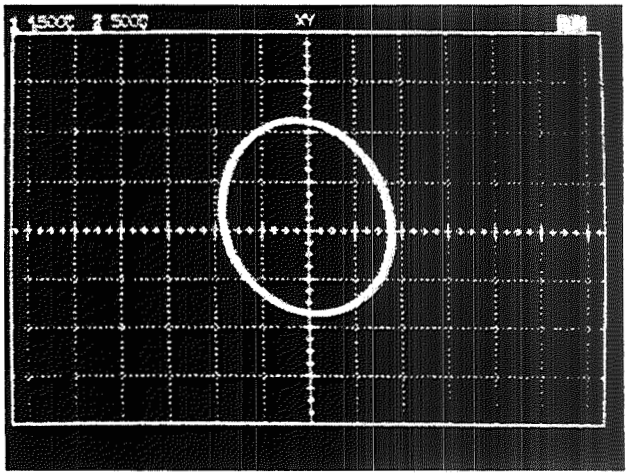

Absolute Bearing Housing Center Orbits

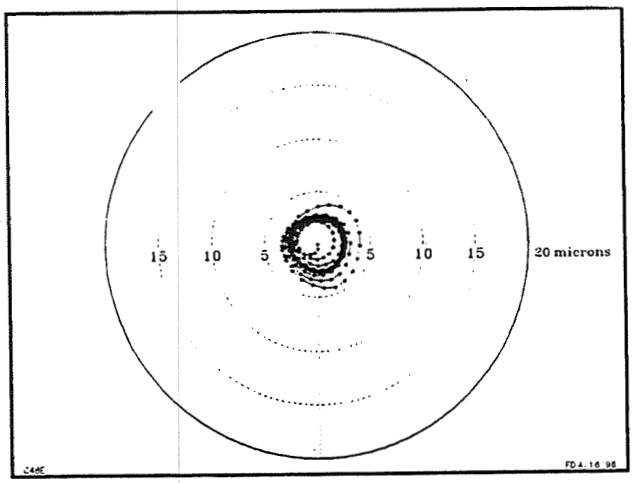

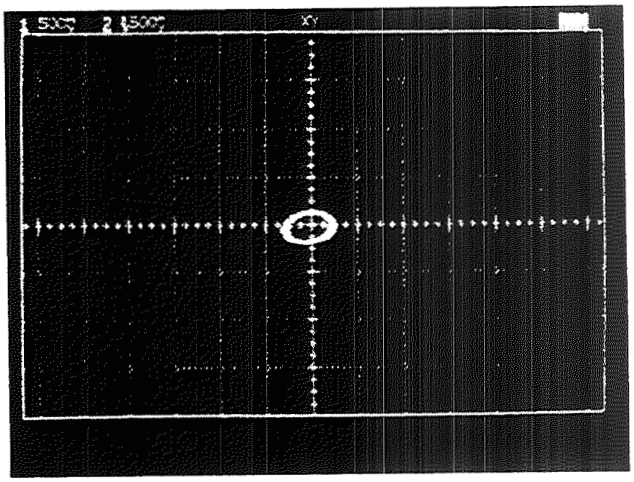

Relative Bearing Housing - Shaft Center Orbits

Fig. 5 Predicted and Experimentally Observed Orbits at 3288 RPM Shaft Rotating Speed

Predicted

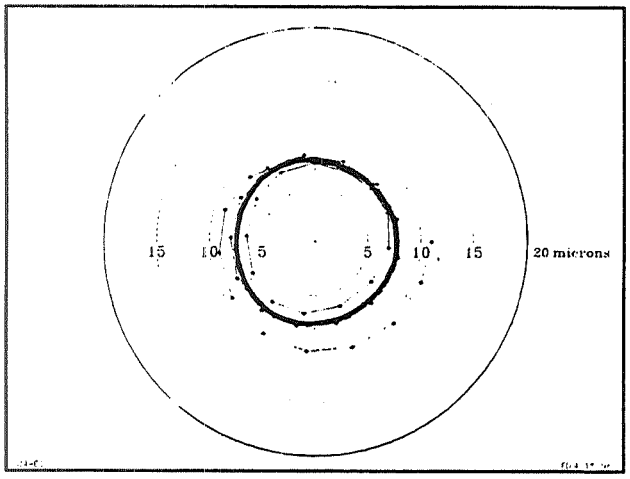

Observed

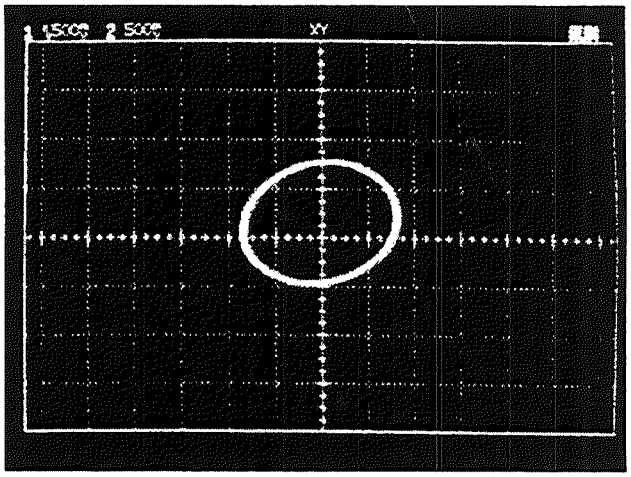

Absolute Bearing Housing Center Orbits

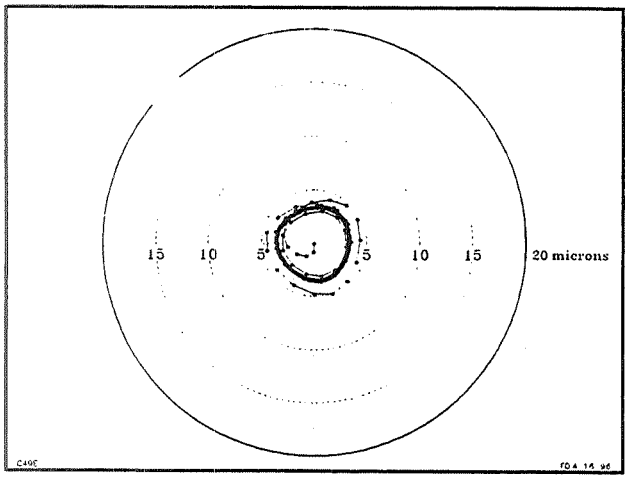

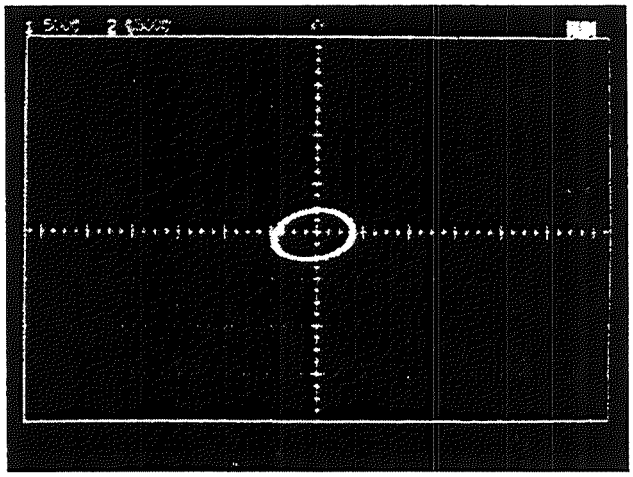

Relative Bearing Housing - Shaft Center Orbits

Fig. 6 Predicted and Experimentally Observed Orbits at 4588 RPM Shaft Rotating Speed

Predicted

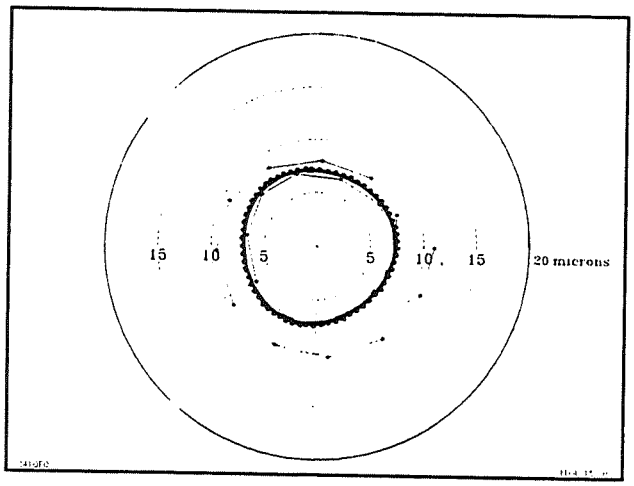

Observed

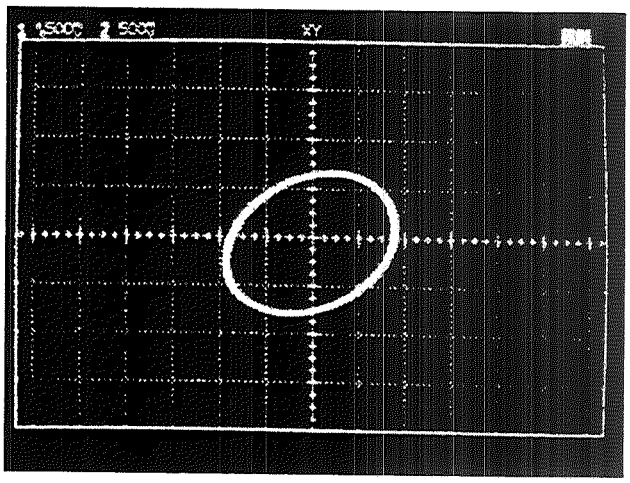

Absolute Bearing Housing Center Orbits

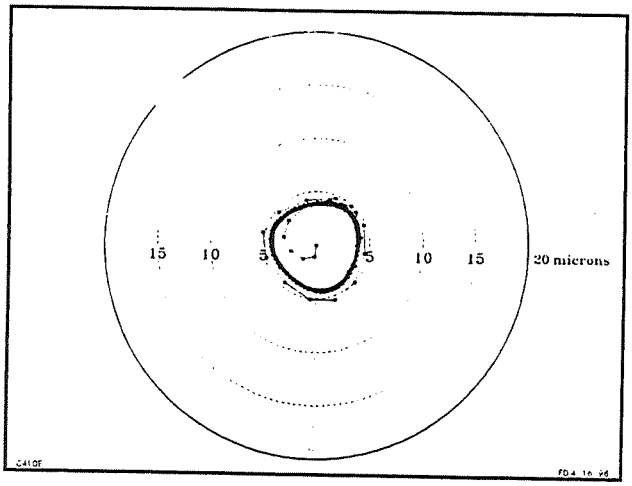

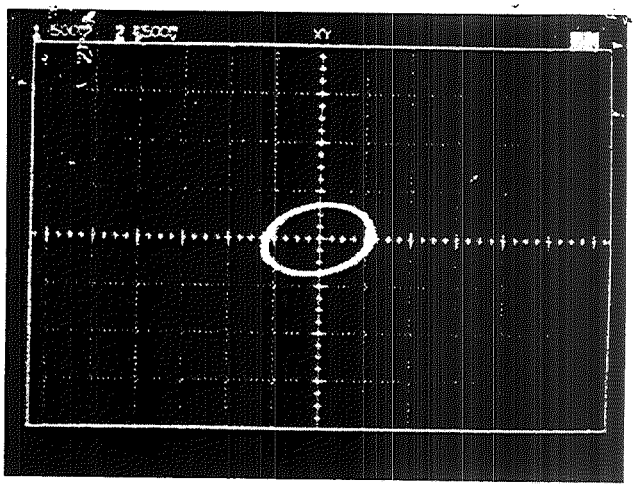

Relative Bearing Housing - Shaft Center Orbits

Fig. 7 Predicted and Experimentally Observed Orbits at 5539 RPM Shaft Rotating Speed

A TEST APPARATUS AND PRELIMINARY TEST RESULTS FOR ROTORDYNAMIC COEFFICIENTS OF A SWIRL-CONTROLLED HYBRID BEARING

Chang-Ho Kim and Yong-Bok Lee
Korea Institute of Science and Technology
Seoul, Korea

and

Dong-Hoon Choi
Hanyang University
Seoul, Korea

Abstract

A swirl-controlled hybrid(hydrostatic and hydrodynamic) bearing has been newly proposed and tested to determine stiffness, damping, and added-mass rotordynamic coefficients in addition to static operating characteristics in comparison to a conventional hybrid bearing. A new facility for testing the swirl-controlled hybrid bearing is described which has a capability of manipulating strength and direction of the swirl inside the bearing clearance. A new swirl-control mechanism is realized by pairing swirl and anti-swirl orifices to and against rotational direction of the rotor, respectively. The swirl-control mechanism is used to achieve effective control of the tangential flow inside the bearing clearance. Preliminary test results show that the swirl-control mechanism has a possibility of improving whirl-frequency ratio as well as has a capability of controlling critical speeds. However, the swirl-controlled bearing may need great deal of efforts in design modification for being considered as a serious candidate for a smart bearing, especially in the centered position and at high-speed ranges.

Nomenclature

C_{ij} Direct and cross-coupled damping coefficients, introduced in Eq. (1), (FT/L)
C_r Radial Clearance, (L)
F_x, F_y Bearing reaction-force components, introduced in Eq.(1), (F)
K_{ij} Direct and cross-coupled stiffness coefficients, introduced in Eq.(1) (F/L)
M_{ij} Added-mass coefficients, introduced in Eq.(1),(M)
X,Y Rotor to stator relative displacement, introduced in Eq.(1), (L)

Introduction

Hybrid journal bearings have been seriously investigated for a possible replacement of troublesome rolling element bearings currently used in the Space Shuttle Main Engine(SSME) high pressure turbopumps.(Kurtin, Childs, et al.(1993), Childs, and Hale(1993)). Theoretical and experimental comparisons for rotordynamic coefficients of conventional hybrid journal bearings(Francheck, Childs, and San Andres(1995)) have proven the possibility of the replacement and a successful computer code has been developed for the conventional hybrid turbulent journal bearing. In parallel, an unconventional hybrid bearing with angled-orifices has been tested to accommodate the anti-swirl concept which was originally proposed by Tondle(1967) for reduction of tangential flow inside the bearing clearance. Similar approach has been applied for turbulent annular seals with anti-swirl self-injection by Kim and Lee(1994). The angled-injection orifice bearing was tested and gave a very promising result in whirl frequency ratio improvement (Franchek and Childs(1994)), especially at low speed ranges. Numerical investigations on flow inside bearing recesses and inertia effects in hybrid bearing with the angled-injection orifice have been currently gaining more and more attentions(Hill et.al.(1995), Braun and Dzodzo(1995)).

This paper has further elaborated the anti-swirl concept for a new "swirl-controlled" hybrid bearing. A new swirl-control mechanism is achieved by pairing swirl and anti-swirl orifices to and against rotational direction of the rotor, respectively, which is illustrated in Figure 1. The swirl-control mechanism is used to achieve effective control of the tangential flow inside the bearing clearance, i.e.,

achieving more freedom in controlling strength and direction of the tangential flow inside the bearing clearance than the anti-swirl injection bearing. As a typical benefit of this bearing, unlike anti-swirl hybrid bearings, reverse rotation of the rotor can be easily accommodated.

A new test apparatus and facility described here is used to preliminarily test the feasibility of the concept to predict the steady-state hydrostatic bearing operating data(resistance torque, static load, flow rate, temperature, and pressure distributions, etc.) and rotordynamic coefficients for subsequent rotordynamic analysis. The following linearized force/displacement model for bearings has been used for comparing dynamic performances of a rotor/bearing model through the comparison of stiffness K_{ij}, damping C_{ij}, and added-mass M_{ij}.

$$-\begin{Bmatrix} F_x \\ F_y \end{Bmatrix} = \begin{bmatrix} K_{xx} & K_{xy} \\ K_{yx} & K_{yy} \end{bmatrix} \begin{Bmatrix} X \\ Y \end{Bmatrix} + \begin{bmatrix} C_{xx} & C_{xy} \\ C_{yx} & C_{yy} \end{bmatrix} \begin{Bmatrix} \dot{X} \\ \dot{Y} \end{Bmatrix} + \begin{bmatrix} M_{xx} & M_{xy} \\ M_{yx} & M_{yy} \end{bmatrix} \begin{Bmatrix} \ddot{X} \\ \ddot{Y} \end{Bmatrix} \quad \text{----- (1)}$$

where (X,Y) define the motion of the bearing rotor relative to its stator, and (F_x, F_y) are components of the fluid film reaction force acting on the rotor.

A central objective of this paper is a description of the test apparatus and a preliminary concept testing how the dynamic coefficients of the model of Eq. (1) will behave due to the combination of swirl and anti-swirl supply pressures, yielding the control of strength and direction of the tangential flow inside bearing clearance.

Test Apparatus

A new test rig was designed and built, based on the basic design reported in the reference of Massmann and Normann(1985), which was further used in the reference of Childs and Hale(1993). The principle of the test rig is simple but complicated enough to satisfy the current purpose of the test. Figure 2 illustrates the test rig. The test section consists of two stainless pedestals spaced 25 cm apart and which support a 5 cm diameter steel shaft. This shaft is driven by a 40kW variable-speed electric motor through a speed-increasing gearbox with a gear ratio of 47:1.

The movable test bearing, which is flexibly supported by four pairs of cables to the main structure of the test rig at a position midway between the support pedestals, is a eight-recess, orifice-compensated, four swirl/anti-swirl-orifices-paired hydrostatic bearing with an L/D ratio of 1(Figure1). Filtered oil at 40 ° C is the bearing lubricant and is supplied to the support ball bearing and test bearing via a vane pump with maximum pressure and flow rate capacities of 7 MPa(1,015 psi) and 72 liters/min(19.0 gpm), respectively. Flexible piping is used at the bearing housing connection to prevent any significant external restraint of the bearing. Most of system parameters such as temperature, and supply pressure were monitored and controlled remotely by a dedicated personal computer.

A static load is applied directly to the test bearing housing via a pneumatic cylinder, as is illustrated in Figure 3. The system is remotely adjustable to supply a tensile load up to 2.8 kN(630 lb). The load from the pneumatic cylinder is transmitted through a tension spring through a wire rope, through a single pulley, mounted to the test stand base. The cable is attached to the bearing housing via. an aluminum, load-sensing yoke. The line of action of the static load makes an angle of 45 degree to the horizontal and establishes the test bearing X-axis such that the tensile load exerted by the cylinder acts in the negative X-direction. Friction torque is measured by the rotational reaction force of a compression load cell which is attached to the bearing housing , as shown in Figure 3.

Instrumentation of the test bearing allows measurement of : pressure(in the supply annulus and individual recesses), flow rate, static load, frictional resistance torque, and relative motion between the shaft and bearing. Pressure measurements inside the bearing recesses and supply pressures for swirl and anti-swirl orifices are made using the Scani-valve mechanism which is connected to a strain-gage type pressure sensor.

After setting up the steady-state equilibrium condition, tests for dynamic coefficients are continued. First step for the testing is a selection of pairs of supply pressures of swirl and anti-swirl orifices. Then,

a rotational speed of the rotor and a static load are determined, and steady-state measurements such as pressures, flow rate, static load, and torque are recorded in a personal computer. Finally, dynamic testing for X and Y directions are performed.

The pressurized hydrostatic bearing generates the bearing forces which are the source of the dynamic coefficients. The movement of the bearing main body relative to the rotor was measured by four eddy-current-type proximity probes. Bearing coefficients were measured with dynamic impact tests for each test condition. Two orthogonally mounted electric impulse hammers which are remotely excited by an external pulse generator are attached to the pedestals as illustrated in Figure 3. The impulse hammers provide impulse excitation parallel and perpendicular to the static side load along the X and Y direction, respectively. Each hammer can excite the bearing with measure dynamic loads to 2224 N(500 lb) .

Test Bearing

As stated in the introduction, a new "swirl-controlled" hybrid bearing has been preliminarily tested for concept demonstration in comparison to a conventional hybrid bearing. To accommodate various orifice combinations with respect to pairing swirl and anti-swirl orifices to and against rotational direction of the rotor, respectively, eight holes with 1.6 cm diameter are machined in the bearing housing, as shown in Figure 4. Two pressurized oil supply lines which are independently connected to swirl and anti-swirl orifices, respectively, were also drilled to the holes as illustrated in Figure 4. In the eight holes, four swirl orifices and four anti-swirl orifices are loaded alternately to and against rotational direction of the rotor. Therefore, many various combinations of swirl/anti-swirl control in addition to pressure control can be tested in one test bearing housing for the future refinement of the swirl-controlled hybrid bearing. Supply pressures are remotely adjusted by two servo valves which are controlled by a personal computer, as illustrated in Figure 5. Subsequent testing of adaptive control for a possible "smart bearing" is planned.

In this paper, as a preliminary concept test, a "swirl-controlled" hybrid bearing with eight paired orifices of three different combination cases of supply pressures of (2.5 MPa, 2.5 MPa), (2.5MPa, 0.7MPa) and (2.5 MPa, 0 MPa) was tested. Both (2.5MPa, 0.7 MPa) and (2.5 MPa, 0 MPa) cases were also divided into two different cases, respectively, viz., one for stronger swirl-pressure case (2.5MPa swirl pressure , 0.7 MPa and 0 MPa anti-swirl pressures) and one for stronger anti-swirl-pressure case(2.5 MPa anti-swirl pressure , 0 and 0.7 MPa swirl-pressure). (2.5MPa, 2.5MPa) case can be considered as a conventional right-angled injection case of 2.5 MPa supply pressure. Both static equilibrium measurements and dynamic coefficients for different static loads, rotating speeds, and supply pressures were compared.

Bearing Parameter Identification

The impulse hammer technique used for dynamic testing of the parameter identification in the frequency domain(Massmann and Normann(1985), Kim and Lee(1994)) was also adopted in this paper. Detailed information will not be repeated here. The instrumental variable method is used. In conjuction with the least square method, the instrumental variable method utilizes the measured frequency function to iterate the least square algorithm for better curve-fittings. One of typical reductions for magnitudes and phases of Hxx, Hxy, Hyx, and Hyy is shown in Figure 6 for a test case defined by 0.2 eccentricity, 9,000 rpm, and (2.5 Mpa, 0.7 Mpa) supply pressure. Data points at or near the running speed were dropped in obtaining the curve-fitted lines in Figure 6. The measured transfer functions are resulted from an average of 20 separate excitations.

Steady-State Performance of Load Capacity

Before testing dynamic performances of the swirl-controlled hybrid bearing, the steady state performances of load capacity are compared. In the following figures, the first pressure in figures denotes anti-swirl orifice pressure, while the second pressure means swirl -orifice pressure. For example, 2.5-2.5 MPa means that both the swirl and anti-swirl supply pressure are the same as 2.5 MPa. 2.5-0.7

MPa means that the anti-swirl supply pressure is 2.5 MPa and the swirl supply pressure is 0.7 MPa, while 0.7-2.5 MPa means that the anti-swirl supply pressure is 7 MPa and the swirl supply pressure is 2.5 MPa.

Figures 7 and 8 show steady-state load vs. eccentricity for 6000 rpm and 12,000 rpm, respectively. Test results for load capacity show that general trend of having higher load capacity for averaged higher supply pressure is also applied in the swirl-controlled hybrid bearing. It is also interesting to see that the stronger anti-swirl supply pressure gives slightly lower load capacity for both rotating speeds. Stronger load capacity is observed for higher rotating speed which means that the hydrodynamic effect is observed.

Dynamic Coefficients

For each test case, applied load is controlled to have eccentricity ratios of 0.2, 0.3, 0.4 and 0.5. Three different rotor rotating speeds of 6,000, 9000, and 12,000 rpm are tested at 0.2 eccentricity ratio as a preliminary testing for dynamic performance of a swirl-controlled hybrid bearing.

Direct Stiffness

Figure 9 shows direct stiffness results for 9,000 rpm, as eccentricity ratio is increased. As eccentricity ratio is increased, the direct stiffness is slightly increased. Stronger swirl- supply pressure generally gives more direct stiffness. In figure 9, the direct stiffness dependency on averaged supply pressure is generally observed . This result may show a possibility of controlling critical speeds of rotor for future-planned smart bearing testing. However, at 0.2 eccentricity ratio in figure 10, direct stiffness has shown mixed results for stronger swirl vs. stronger anti-swirl supply pressure at different rotating speeds. More thorough investigations will further clarify this mixed result.

Cross-Coupled Stiffness

Figure 11 shows cross-coupled stiffness results for 9,000 rpm, as eccentricity ratio is increased. As eccentricity ratio is increased, the cross-coupled stiffness is slightly reduced, especially for different swirl/anti-swirl supply pressures. As the eccentricity ratio is increased, reduction of the cross-coupled stiffness of the stronger anti-swirl supply pressure is clearly observed which is a good sign for reduction of the whirl frequency ratio. However, at 0.2 eccentricity ratio of figure 12, cross-coupled stiffness has also shown mixed results for stronger swirl vs. stronger anti-swirl supply pressure which is generally the same case for the rest of rotordynamic coefficient results. More investigation on this matter will be followed in the near future.

Direct Damping

Figure 13 shows direct damping coefficient results for 9,000 rpm as the eccentricity ratio is increased. As the supply pressure is increased, the direct damping is increased, while direct damping for stronger swirl vs. stronger anti-swirl supply pressure shows about the same results.

Added-Mass

Figure 14 shows added-mass coefficient results for 9,000 rpm as the eccentricity ratio is increased. As generally observed in the open literature, the added-mass result is scattered and shows mixed results for stronger swirl vs. stronger anti-swirl supply pressure.

Whirl-Frequency Ratio

Fig. 15 shows whirl frequency ratio results for 9,000 rpm as the eccentricity ratio is increased. Lund's formulas(1965) for whirl frequency ratio for off-centered cases which uses all the coefficients

involved is used. Figure 15 clearly shows the reduction of whirl frequency ratio for stronger anti-swirl supply pressure. This optimistic result is getting better as the eccentricity ratio is increased. This result may be preliminarily postulated as follows: As the eccentricity ratio is increased, more recess pressure is generated which gives more anti-swirl pressure. This in turn gives more reduced tangential flow inside the bearing clearance and subsequently results in reduced whirl frequency ratio. On the other hand, for the centered-position, the above-mentioned result is barely obtained. Therefore, this may give us less reduction in whirl frequency ratio for 0.2 eccentricity ratio, as shown in figure 16. For solving this problem, a modified design of anti-swirl holes in land area may give us insensitive pressure generation due to the eccentricity ratio changes for possible better results.

Conclusions

A swirl-controlled hybrid(hydrostatic and hydrodynamic) bearing has been newly proposed and tested to determine stiffness, damping, and added-mass rotordynamic coefficients in addition to static operating characteristics in comparison to a conventional hybrid bearing. A new swirl-control mechanism is achieved by pairing swirl and anti-swirl orifices to and against rotational direction of the rotor, respectively. The swirl-control mechanism is used to achieve effective control of the tangential flow inside the bearing clearance. Preliminary test results show that the swirl-control mechanism has a possibility of improving whirl-frequency ratio as well as has a capability of controlling critical speeds. However, the swirl-controlled bearing needs great deal of efforts in design modification for being considered as a serious candidate for a smart bearing, especially in centered position and at high-speed ranges.

References

Bou-Said, B. and Chaomleffel, J., " Hybrid Journal Bearings : Theoretical and Experimental Results," ASME Trans. J. of Tribology, Vol. 111, pp. 265-269

Childs D. and Hale K.,1993, " A Test Apparatus and Facility to Identify the Rotordynamic Coefficients of High-Speed Hydrostatic Bearings," Proceeding of the 8th Rotordynamic Instability Problems Workshop, Texas A&M University, pp.403-415.

Franchek, N., Childs, D., 1994, " Experimental Test Results for Four High-Speed, High Pressure, Orifice-Compensated Hybrid Bearings," ASME Trans. J. of Tribology, Vol. 116, pp. 147-153

Franchek, N., Childs, D., and San Andres L, 1995, " Theoretical and Experimental Comparisons for Rotordynamic Coefficients of a High-Speed, High Pressure, Orifice-Compensated Hybrid Bearing," ASME Trans. J. of Tribology, Vol. 117, pp. 285-290

Hill, D., Baskharone, E., and San Andres L., " Inertia Effects in a Hybrid Bearing With a 45 Degree Entrance Region, " ASME Trans. J. of Tribology, Vol 117, pp. 498-505

Kim, C., and Lee Y., 1994, " Test Results for Rotordynamic Coefficients of Anti-Swirl Self-Injection Seals," ASME Trans. J. of Tribology, Vol. 116, pp.508-513

Kurtin, K.A., Childs D., San Andres, L, and Hale, K., 1993, " Experimental Versus Theoretical Characteristics of a High-Speed Hybrid(Combination Hydrostatic and Hydrodynamic) Bearing," ASME Trans. J. of Tribology, Vol. 115, pp160-169

Lund, J, 1965, " The Stability of an Elastic Rotor in Journal Bearings with Flexible, Damped Supports," ASME J. of Applied Mechanics, pp911-920.

Massmann, H. and Normann R., 1985,"Some New Results Concerning the Dynamic Behavior of Annular Turbulent Seals," Proceedings of Instability Problems Workshop, Texas A&M University, pp179-194

Tondle, A., 1967," Bearings with a Tangential Gas Supply," University of Southampton, Department of Mechanical Engineering, Gas Bearing Symposium, paper no.4

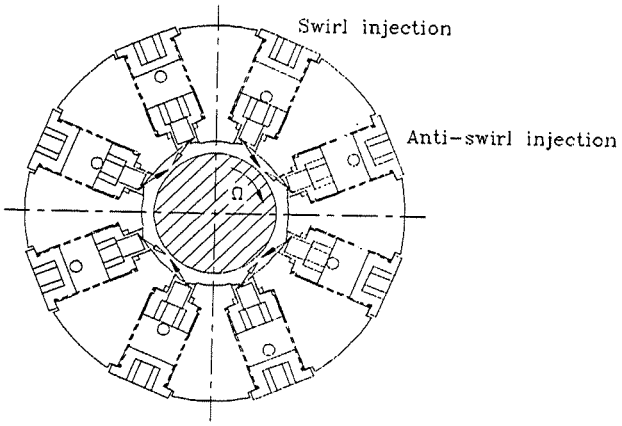

Figure 1. Configuration of swirl-controlled hybrid bearing

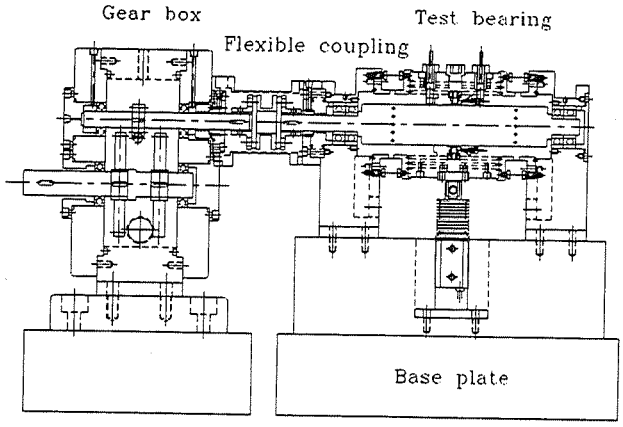

Figure 2. Hybrid bearing test rig

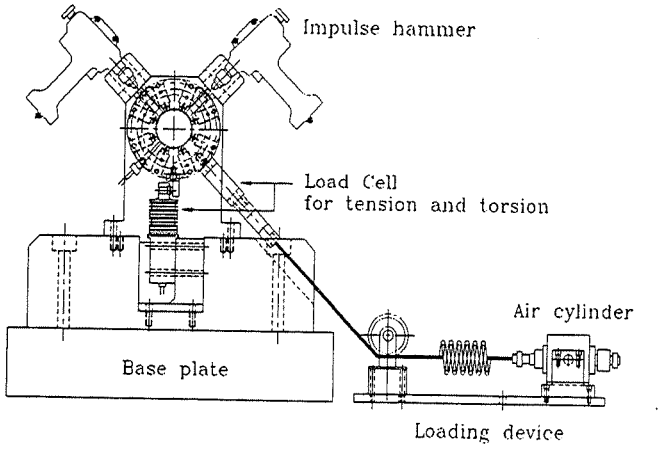

Figure 3. Static loading system layout

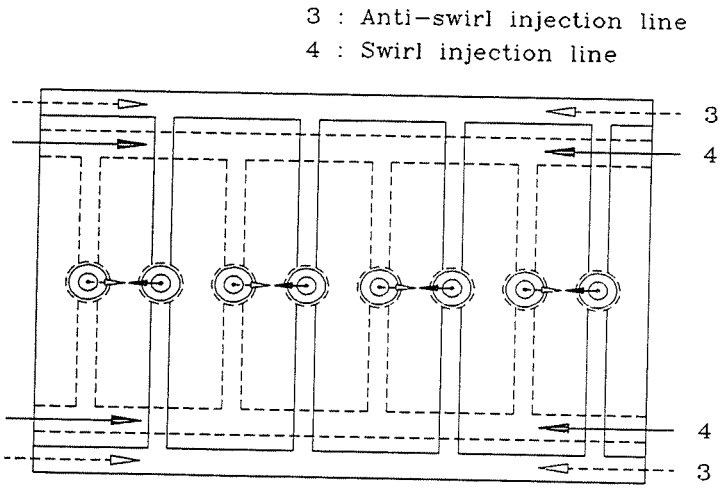

Figure 4. Swirl and anti-swirl pressure supply lines

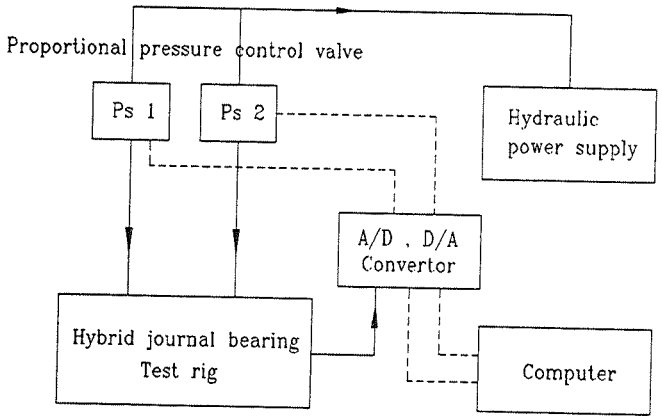

Figure 5. Control scheme of swirl/anti-swirl supply pressure

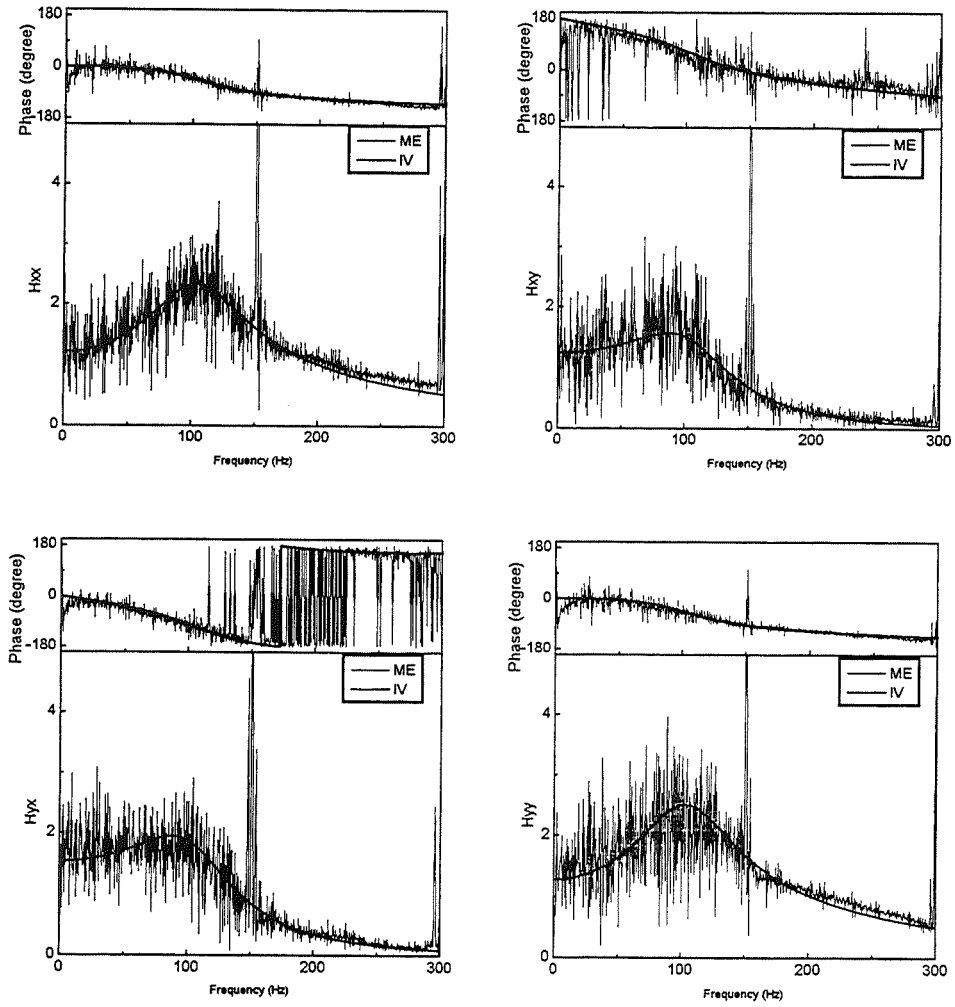

Figure 6. Typical measured vs. curve-fitted FRF

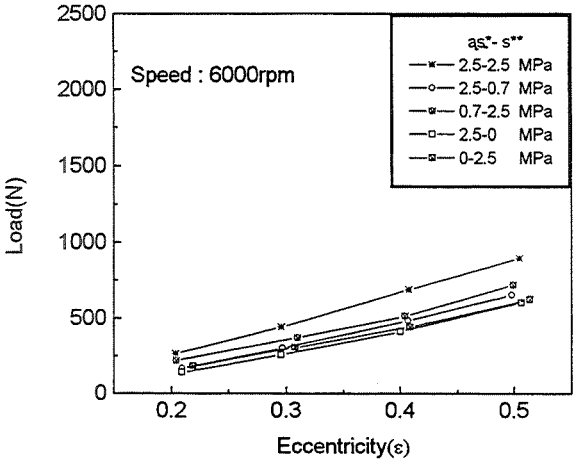

Figure 7. Load vs. eccentricity ratio for 6,000rpm

(a.s.*:anti-swirl pressure s.** : swirl pressure)

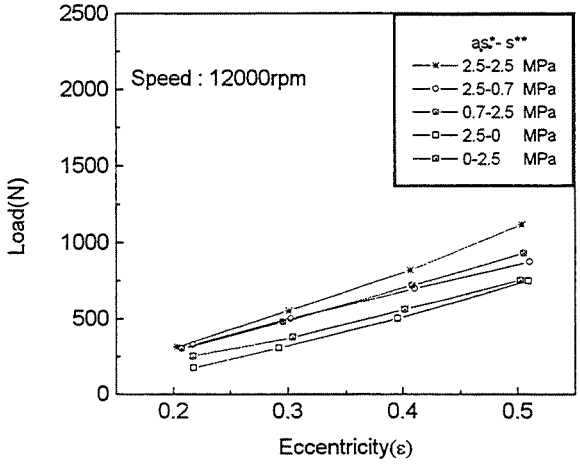

Figure 8. Load vs. eccentricity ratio for 12,000rpm

(a.s.*:anti-swirl pressure s.** : swirl pressure)

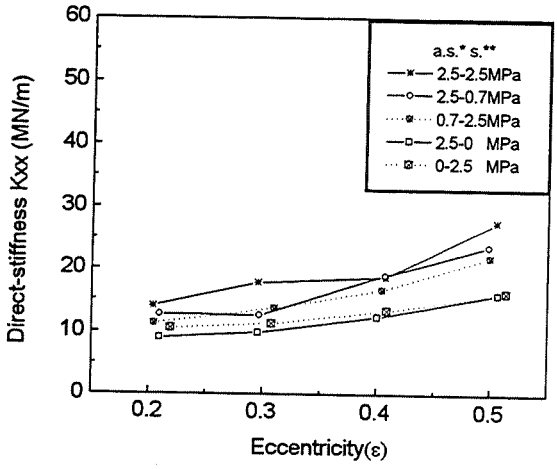

Figure 9. Direct stiffness vs. eccentricity ratio for 9,000 rpm
(a.s.*:anti-swirl pressure s.**:swirl pressure)

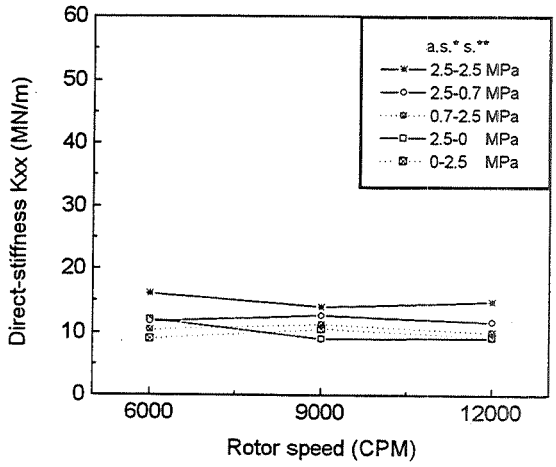

Figure 10. Direct stiffness vs. rpm at 0.2 eccentricity ratio

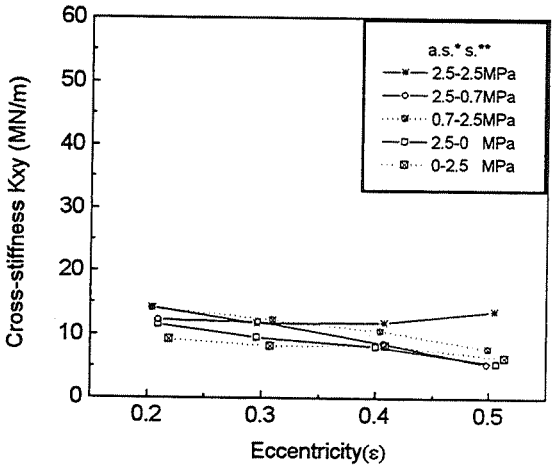

Figure 11. Cross-coupled stiffness vs. eccentricity ratio 9,000 rpm

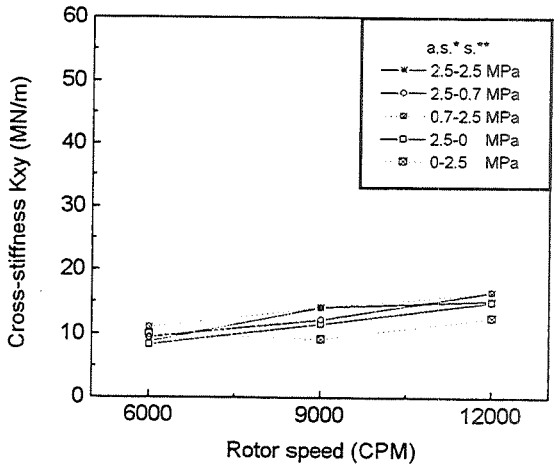

Figure 12. Cross-coupled stiffness vs. rpm at 0.2 eccentricity ratio

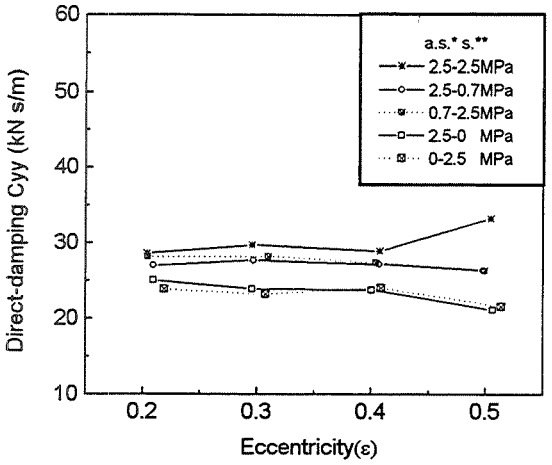

Figure 13. Direct damping vs. eccentricity ratio for 9,000 rpm

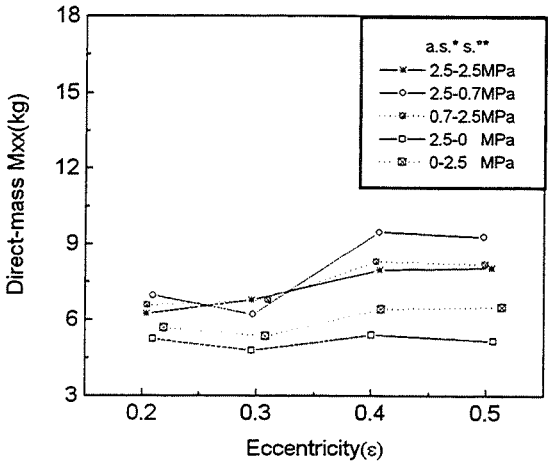

Figure 14. Added-mass vs. eccentricity ratio for 9,000 rpm

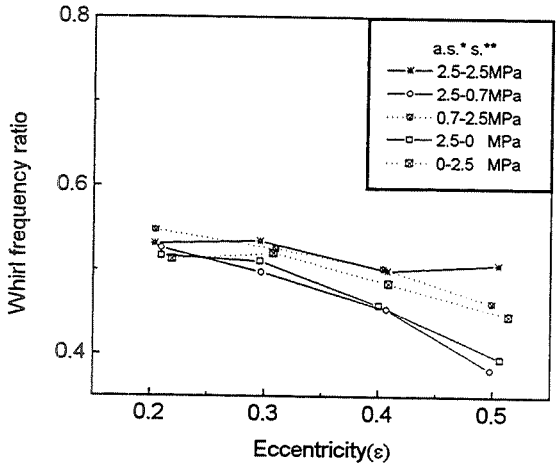

Figure 15. Whirl frequency ratio vs. eccentricity ratio for 9,000 rpm

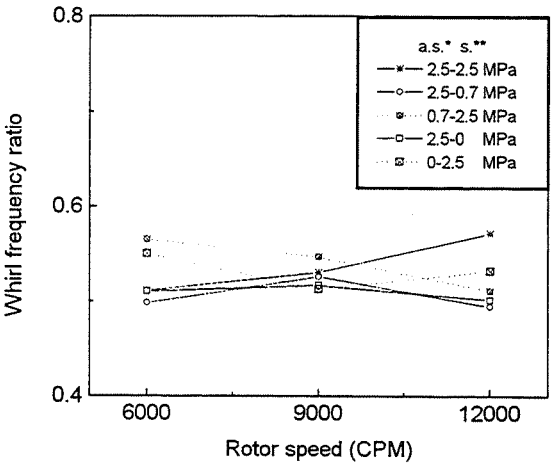

Figure 16. Whirl frequency ratio vs. rpm at 0.2 eccentricity ratio

DYNAMIC CHARACTERISTICS OF A HYDROSTATIC BEARING IDENTIFIED BY ACTIVE MAGNETIC BEARINGS

M. Matros and R. Nordmann
University of Kaiserslautern
Germany

ABSTRACT

Hydrostatic bearings are employed in rotating machinery which demand a perfect guide of the shaft, a minimum of wear and a maximum of reliability. Those types of bearings usually have a very high load capacity. The static performance can be expressed by the direct stiffness. The dynamic characteristics are described by 2x2 matrices containing stiffness, damping and inertia coefficients. These coefficients have a strong impact on the rotordynamics and on the stability of the whole shaft. In order to predict the rotordynamic properties of the machine it is necessary to take the dynamics of the bearing in consideration.

This paper presents a test-setup for a specific hydrostatic bearing used in a vertical PLR-pump. The orifice compensated bearing is externally pressurized with water and runs in the turbulent regime. The journal of the bearing is assembled to a shaft which is supported by active magnetic bearings (AMB). The AMB system is also used to apply a controlled relative motion between journal and housing. The static and dynamic forces generated by the hydrostatic bearing are measured via the coil currents of each magnet and the shaft position.

The test set-up allows the variation of different bearing variables such as speed, pocket pressure ratio and supply pressure. Initial test results in terms of rotordynamic coefficients are presented under variation of the speed and the pocket pressure ratio.

NOMENCLATURE

D	Direct Damping
d	Cross Coupled Damping
C	Radial clearance
F	External force
F_R	Radial bearing reaction force
K	Direct Stiffness
k	Cross Coupled Stiffness
L	Bearing length
M	Direct added mass
m	Cross coupled added mass
n	Rotational speed of the journal
p_S	Supply pressure
p_a	Ambient pressure
p_r	Recess pressure
p_V	Pocket pressure ratio $p_V = \frac{p_R - p_a}{p_s - p_a}$
Q	Flow rate
R	Journal radius
x, y	Journal displacements in horizontal resp. vertical direction
ω	Shaft rotational frequency
Ω	Shaft precessional frequency
Ω_W	Whirl frequency ratio

Indices

x	Horizontal coordinate
y	Vertical coordinate

INTRODUCTION

A mathematical description for the motion dependent forces generated by a hydrostatic journal bearing (HJB) is given by a linear equation of motion with two degrees of freedom (eq. (1)). It is known that the matrices are scew symmetric when the journal is in the centric position.

$$\begin{bmatrix} F_x \\ F_y \end{bmatrix} = \begin{bmatrix} K & k \\ -k & K \end{bmatrix} \cdot \begin{bmatrix} x \\ y \end{bmatrix} + \begin{bmatrix} D & d \\ -d & D \end{bmatrix} \cdot \begin{bmatrix} \dot{x} \\ \dot{y} \end{bmatrix} + \begin{bmatrix} M & m \\ -m & M \end{bmatrix} \cdot \begin{bmatrix} \ddot{x} \\ \ddot{y} \end{bmatrix} \quad \text{eq. (1)}$$

The dynamic characteristics of hydrostatic journal bearings (HJB) have been subject of many experimental and theoretical research works. Since those bearings have been used not only in applications with zero or low speed, but also in machines with higher speeds, their dynamic properties become more and more important. Especially those applications where the bearings are lubricated by the process fluid and the supply pressure is generated by the machine itself, offer the advantage of not needing an additional external pressurizing system. Not only for high journal speeds but also for liquids with low nominal viscosity the flow through the bearing becomes turbulent, even when the bearing is orifice compensated.

On the experimental side Childs et. al. [1] and Rouvas et. al. [2] reported about test results obtained from a turbulent 5-recess bearing. The results concentrate on the dependence of rotordynamic force coefficients on eccentricity ratio and on the supply pressure. Furthermore Murphy et. al. [3] published test results from a 6-pocket HJB, but especially the accuracy of the cross coupled coefficients suffer from unproved assumptions used by the identification procedures.

Concerning the numerical simulation with the subject of predicting rotordynamic coefficients of turbulent HJBs e.g. San Andres [4], [5], and [6] has published several papers. He uses a bulk flow model and solves the governing equations for the zeroth and first-order flow fields in the lands of the bearing also taking into consideration inertia effects at the recess edges.

However, there is still a lot of research work to do in order to complete the knowledge about the physical processes which determine the dynamics of HJBs.

This paper contains test results from a turbulent 8-recess HJB which is guiding the shaft of a single stage pump. Rotordynamic force coefficients are obtained under different parametrical variations. Several interesting effects are presented.

TEST RIG AND IDENTIFICATION PROCEDURE

The journal of the bearing is mounted on a shaft which is supported by active magnetic bearings (AMB). This shaft is driven by motor with variable speed up to 3000 rpm. For a more detailed description of the AMB component tester it is referred to [7] and [8]. The stator part is assembled to the housing of the AMB component tester. An external pump transports water from a tank through a valve into a distributor where the main flow is split up into 8 (fig. 2 only shows 4 of them) sub-flows. Each sub-flow pressurizes one pocket of the bearing. The pressure p_R in each recess can be set independently with help of a valve in each line. The bearing has two axial exits. The exit flow-rates Q_2 and Q_3 can also be influenced by valves in the exit pipes.

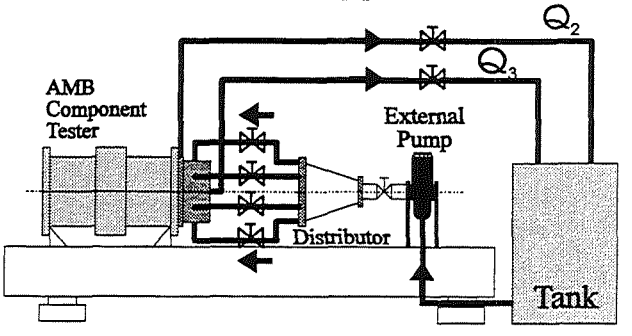

Fig. 1: Test loop

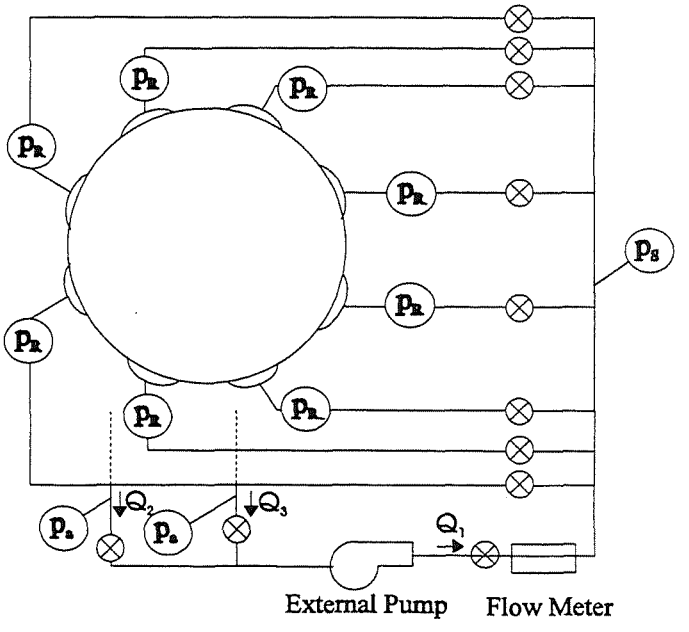

Fig. 2: Flow chart

The test setup allows the variation of operational parameters which are suspected to influence the dynamic performance of the bearing such as

- journal speed
- supply pressure p_S
- pocket pressure ratio p_V

and others more.

By the variation of the pocket pressure ratio different sizes of the orifices can be simulated.

The magnets are used to apply a well defined relative motion between the journal and the stator part. For these investigations only pure radial movements without tilting were used in order to identify the force coefficients given by eq. (1). For excitation a stepped sine procedure was used in a range from 5 to 45 Hz with steps of 2 Hz. By calculating the AMB-forces from measured coil currents and air gaps of the bearings the forces are determined. Those forces are directly correlated to the HJB-forces which are generated due to the applied relative motion. In parallel the shaft displacements are measured. From forces and displacements complex stiffness frequency response functions are calculated which are curve fitted in order to obtain the desired coefficients. A more detailed description of the identification procedure is given in [9].

HJB TESTING

In a first step it was investigated whether the direction of the applied relative motion between the journal and the bearing housing has an influence on the coefficients. Test A represents an excitation in direction of the center of a pocket, test B in direction of a land (see Fig. 4).

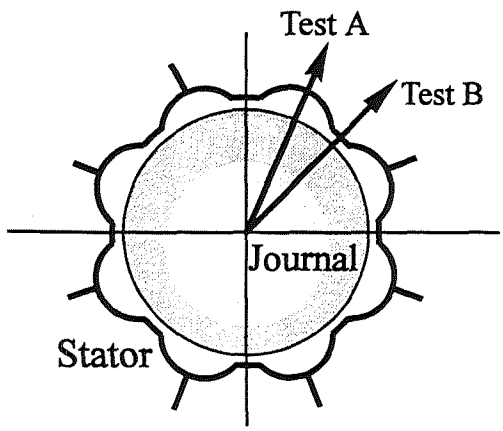

Fig. 4: Different directions of journal excitation

Table 1: Results from Tests A and B

	Test A	Test B
K [N/m]	6,02E6	6,01E6
k [N/m]	4,00E6	4,08E6
D [Ns/m]	41,1E3	42,3E3
d [Ns/m]	-2,5E3	-2,1E3
M [kg]	-16,7	-22,5
m [kg]	9,6	1,0

Both tests, A and B, where conducted at identical bearing operation conditions:

- n = 2116 rpm
- $p_V = 0.37$
- $p_S = 1.45$ bar

The results show only slight differences for all coefficients except for the mass coefficients.

Based on the results obtained form the pre-testing all further tests were performed with excitation in direction of a pocket. Table 2 includes the parameters, which were constant during all the test.

Table 2: Constant test parameters

Constant Parameters	
Bearing Pocket Area **A**	5120 mm^2
Bearing Length **L**	126 mm
Bearing Radius **R**	76 mm
Radial Clearance **C**	180 µm
Supply Pressure $\mathbf{p_S}$	1.45 bar
Fluid Temperature **T**	20 °C
Eccentricity Ratio **e**	0
Axial Flow Balance $\mathbf{Q_2/Q_3}$	1
Amplitude of excitation **u**	40 µm

This paper includes the results which show the dependence of the force coefficients on the journal speed and on the pocket pressure ratio. The flow through the bearing is turbulent due to the orifices at the entrances to the bearing pockets and because of the high Reynolds-Numbers in circumfirential direction except for the zero speed test.

Table 3: Parameter variation HJB-Testing

p_v / n [rpm]	0.26	0.31	0.37	0.44
0	✻	✻	✻	✻
1411	○	○	○	○
2116	□	□	□	□
2822	△	△	△	△

RESULTS

In figure 5 the results are summarized showing the coefficients over the pocket pressure ratio for the different rotational speeds.

Direct Stiffness K

The direct stiffness represents the static load capacity of the bearing at zero speed. It is shown that K drops when the journal starts to rotate. With further increasing speed K slightly decreases. An interesting effect can be observed for K over p_V. At a certain p_V the direct stiffness reaches a maximum, which is depending on the journal speed. The lower the speed the stronger developed is the maximum. Vice versa it can be claimed, that this effect distinguishes for higher speeds. This result contains a practical use, because it shows, that there exists an optimum of recess pressure and hence an optimum of orifice diameter for a fixed bearing geometry and supply pressure in case of low journal speeds. For high journal speeds this effect does not have a decisive influence on the load capacity any more.

Cross Coupled Stiffness k

In spite of a thin land design, where the total land area ratio to the total pocket area is about 1/3, the bearing develops significant high cross coupled stiffness k. This coefficient linearly depends on the journal speed and is nearly zero for the non-rotating case. At the highest test-speed k is nearly as high as the direct stiffness. Because of k does not react on changes of the pocket pressure ratio there is no possibility of minimizing this coefficient by changing the orifice diameter.

Direct Damping D

It is well known that k destabilizes a journal bearing whereas the direct damping D acts against this tendency. Hence, it always should be an aim to maximize the direct damping. A good indicator for stability properties is the whirl frequency ratio Ω_W which is defined as

$$\Omega_W = \frac{k}{\omega \cdot D}$$

when m is neglected. From a circular hydrodynamic bearing Ω_W is known to be about 0.5. For the tested bearing Ω_W mainly depends on p_V because D is less sensitive against changes of the journal speed while k strongly increases.

For n = 1411 rpm Ω_W decreases from 0.46 (p_V = 0.26) down to 0.38 (p_V = 0.44). Hence, concerning the stability this bearing offers only a slight improvement compared to a circular hydrodynamic bearing. However, the bearing produces a significant direct damping. This is damping can not be produced by squeeze in total because the area of lands is quite small.

Cross Coupled Damping d

The cross coupled damping d contributes to the dynamic load capacity of the bearing. This coefficient does not change with p_V but shows a significant decrease with increasing speed. For speeds higher than 1411 rpm the values even become negative. At these conditions d counteracts the direct stiffness. Due to the contribution of d the total radial bearing reaction force, which is expressed by

$$F_R = -(K - \Omega \cdot d - \Omega^2 \cdot M) \cdot u \qquad \text{(eq. 2)}$$

is reduced for about 30% at the worst case, i.e. n = 2822 rpm and p_V = 0.26, when Ω is assumed to be equal to the rotational frequency of the journal ω, which is the case for an excitation due to unbalance.

Direct Mass M

From eq. 2 it can be derived, that the dynamic load capacity can be influenced significantly by the direct added mass M at high frequencies of excitation resp. at high speeds. In the case of this bearing M has a positive impact especially when p_V or the speed increase, because the values become negative. Hence at the highest speed excitation (n = 2822 rpm) and p_V = 0.44 the inertia force due to M contributes about 50% to the total radial bearing reaction force. It is known from the analyses of San Andres, that the inertia effects are partly due to the compressibility of the fluid at the recess edges. But so far nobody reported about negative added mass values.

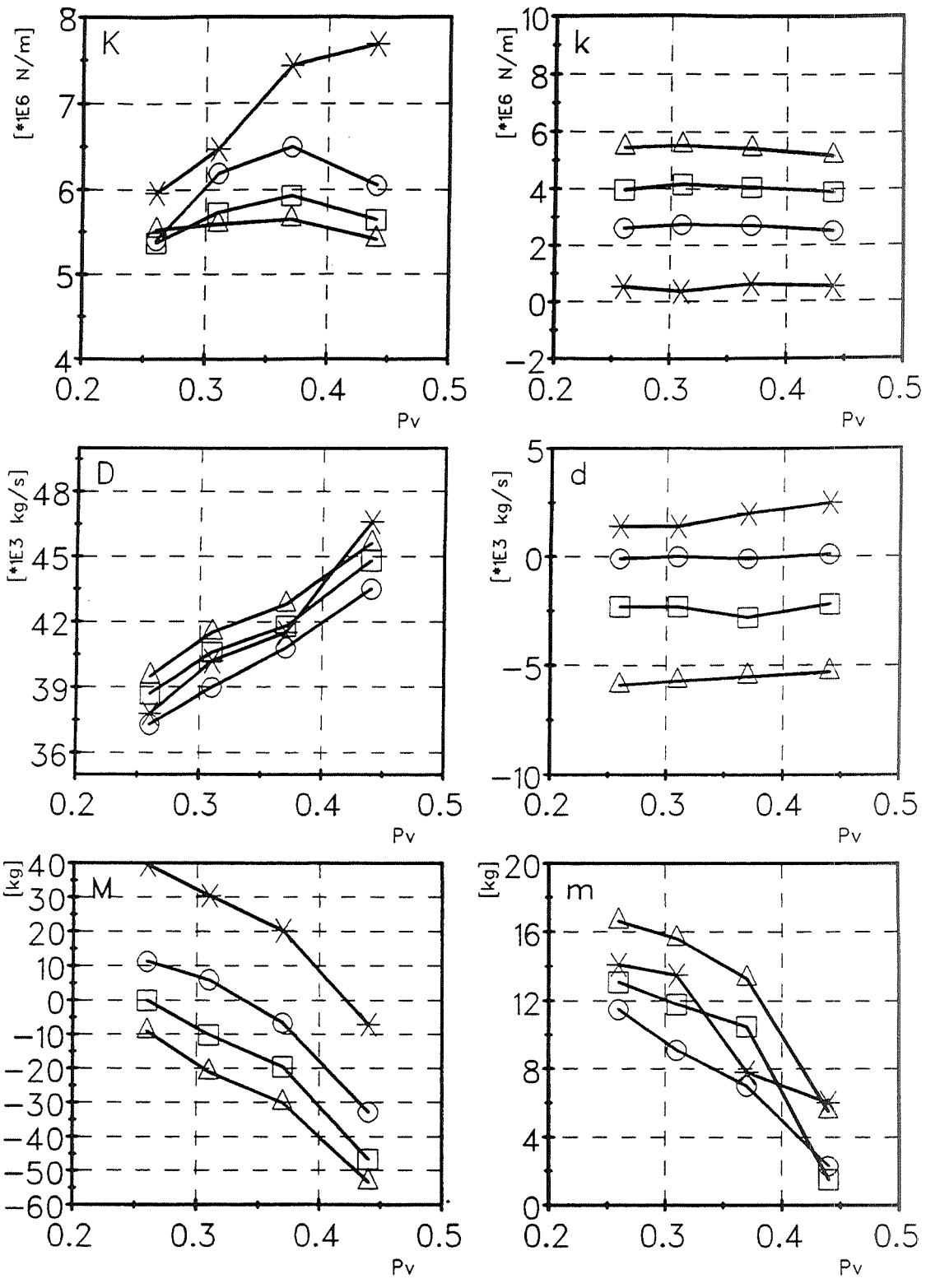

Fig. 5: Rotordynamic force coefficients for the tested HJB under variation of speed and pocket pressure ratio

✻: n = 0 rpm	○: n = 1411 rpm
□: n = 2116 rpm	Δ: n = 2822 rpm

However, the presented values have been confirmed by additional measurements of the pressure pulsations in the bearing recesses which have been taken in parallel to the force measurements via the magnets. It is assumed that there are more physical effects resulting from the jet stream and the interaction between the recess and the feeding lines which have not been taken into consideration so far. An interpretation of the negative masses can also be given by a frequency dependent direct stiffness. With an increasing frequency of excitation the bearing becomes stiffer because of an increasing resistance of the orifice.

Cross Coupled Mass m

The cross coupled Mass m also drops with p_V but much less than M. In addition to that there is only a slight dependence on the speed. This coefficient also stabilizes a bearing because it counteracts the cross coupled stiffness. In case of this bearing this effect is negligible compared to the influence of the direct damping.

CONCLUSIONS

One of the main results is, that a hydrostatic bearing with thin lands produces significant high cross coupled stiffness and direct damping values which is very important concerning the restriction of reliability due to possible instabilities. The stability can be improved by increasing the pocket pressure ratio. This may be reached either by smaller clearances under the lands or by increasing the orifice diameter. These variations also have an impact on the load capacity, which can be optimized for low speeds only by an optimized orifice diameter.

Furthermore it is shown that the dynamic stiffness of the bearing is strongly influenced by added mass terms with partly negative signs. Especially at high speeds this effect has a significant benefit to the dynamic load capacity. The investigation of the physical sources of these effects will be part of future work.

The paper also demonstrates, that for a comprehensive prediction of the dynamic characteristics of HJBs, it is necessary to include both the fluid flow through the lands and the flow field in the recess.

ACKNOWLEDGMENTS

The research reported in this paper has been supported by the European Community in the scope of the BRITE/EURAM program under contract No. BRE2-CT94-0945.

Gratitude and acknowledgment are due to the EC and to the project partners, especially to Byron Jackson Products, BW/IP Int. B.V., Etten-Leur, The Netherlands, for grant and extraordinary good cooperation. The effort of the responsible EC officer Mrs. H. Laval we would like to mention as well as the excellent project coordination by J.J. Verhoeven.

REFERENCES

[1] Childs, D. and Hale, K, "A Test Apparatus and Facility to Identify the Rotordynamic Coefficients of High-Speed Hydrostatic Bearings", *NASA Conference Publications*, **3239**, pp. 403-415, (1993).

[2] Rouvas, C. and Childs, D., "A Parameter Identification Method for the Rotordynamic Coefficients of a High Reynolds Number Hydrostatic Bearing", *ASME Journal of Vibration and Acoustics*, **Vol 155**, pp. 264-270, (1993).

[3] Murphy, B.T. and Wagner, M.N., "Measurement of Rotordynamic Coefficients for a Hydrostatic Radial Bearing", *ASME Journal of Tribology*, **Vol 113,** pp.518-525, (1991).

[4] San Andres, L., "Approximate Analysis of Turbulent Hybrid Bearings. Static and Dynamic Performance for Centered Operation", *ASME Journal of Tribology*, **Vol 112,** pp.692-698, (1990).

[5] San Andres, L., "Turbulent Hybrid Bearings With Fluid Inertia Effects", *ASME Journal of Tribology*, **Vol 112,** pp.699-707, (1990).

[6] San Andres, L., "Effects of Fluid Compressibility on the Dynamic Response of Hydrostatic Journal Bearings", *Wear*, **Vol 146,** pp.269-283, (1991).

[7] Neumer, T.U., Feng, T., Nordmann, R., Verhoeven, J., De Vis, D., "Identification of Fluid-Structure-Interactions in Centrifugal Pumps", *5th International Conference on Vibrations in Rotating Machinery*, **IMechE, C432/064**, (1992).

[8] Matros, M., Ziegler, A. and Nordmann, R. " Fluid Structure Interactions in Annular Seals of Centrifugal Pumps", *Tribology Transactions*, **Vol. 38**, pp. 353-363, (1995).

[9] Nordmann, R., Matros, M. and Neumer, T., "Parameter Identification in Rotating Machinery by means of Active Magnetic Bearings", *Proceedings of the IFToMM 4th Int. Conference on Rotordynamics*, Chicago, Illinois, (1994).

ANGLED INJECTION—TURBULENT FLOW HYBRID BEARINGS COMPARISON TO TEST RESULTS

Luis San Andres and Dara Childs
Texas A&M University
College Station, Texas

ABSTRACT

Hydrostatic/hydrodynamic (hybrid) journal bearings handling process liquids have limited dynamic stability characteristics and their application as support elements to high speed flexible rotating systems is severely restricted. Measurements on water hybrid bearings with angled orifice injection have demonstrated improved rotordynamic performance with virtual elimination of cross-coupled stiffness coefficients and null or negative whirl frequency ratios. A bulk-flow model for prediction of the static performance and force coefficients of hybrid bearings with angled orifice injection is advanced. The analysis reveals that the fluid momentum exchange at the orifice discharge produces a pressure rise in the hydrostatic recess which retards the shear flow induced by journal rotation, and thus, reduces cross-coupling forces. The predictions from the model are compared with experimental measurements for a 45° angled orifice injection, 5 recess water hybrid bearing operating at 10.2, 17.4 and 24.6 krpm and with supply pressures of 4, 5.5 and 7 MPa. The correlations include recess pressures, flow rates, and rotordynamic force coefficients at the journal centered position.

NOMENCLATURE

A_o	$C_d \pi d_o^2/4$. Effective orifice area [m^2].
b	recess circumferential length [m].
C	Radial clearance function [m].
C_p	Fluid specific heat [J/kg · °K].
$C_{XX}, C_{XY}, C_{YX}, C_{YY}$	Damping force coefficients [Ns/m].
C_d	Orifice discharge coefficient
D	2 · R . Bearing diameter [m].
d_o	Orifice diameter [m]
$f_{J,B}$	$\left[1 + \left(c_M \frac{r_{J,B}}{H} + \frac{b_M}{R_{J,B}}\right)^{e_M}\right]$; $a_M = 0.001375$, $b_M = 500{,}000$; $c_M = 10{,}0$, $e_M = 1/3.00$
	Turbulent flow friction factors at journal and bearing surfaces.

e_X, e_Y	Journal center eccentricity components [m]
F_X, F_Y	Bearing fluid film forces along {**X**,**Y**} axes [N].
h_X, h_Y	cos(Θ), sin(Θ)
H	$C + e_X(t)\cos(\Theta) + e_Y(t)\sin(\Theta)$. Film thickness [m].
H_r	Recess depth [m].
H_e	Effective film depth for rough surface bearing [m].
$K_{XX}, K_{XY}, K_{YX}, K_{YY}$	Bearing force stiffness coefficients [N/m]
L,l	Bearing axial length, recess axial length [m].
$M_{XX}, M_{XY}, M_{YX}, M_{YY}$	Bearing inertia force coefficients [kg].
P, P_r, P_s	Fluid pressure, recess pressure, supply pressure [N/m^2]
Q_o	$(\rho V_o A_o)$. Flow rate across orifice [kg/s].
Re	$(\rho\Omega CR/\mu)_*$. Nominal circumferential flow Reynolds number.
R_J, R_B	$(\rho/\mu)H\sqrt{[(U_x - \Omega R)^2 + U_y^2]}$; $(\rho/\mu)H\sqrt{[U_x^2 + U_y^2]}$ Flow Reynolds numbers relative to journal and bearing surfaces.
r_J, r_B	Roughness depths at journal and bearing surfaces [m].
t	Time [s].
T, T_s	Temperature, supply temperature [°K].
U_x, U_y	Bulk-flow velocities in circ.(x) and axial (y) directions [m/s].
V_o	fluid velocity through recess orifice [m/s]
V_r	Recess volume including supply line [m^3].
W_X, W_Y	External loads applied on journal [N].
x,y	Coordinate system on plane of bearing [m].
X,Y	Inertial coordinate system [m].
α	Fluid swirl ratio at recess edges.
β_P	$(1/\rho)(\partial\rho/\partial P)$. Liquid compressibility coefficient [m^2/N].
β_T	$-(1/\rho)(\partial\rho/\partial T)$. Liquid volumetric expansion coefficient [1/°K].
δ	angle of injection on orifice of recess [rad].
ΔP_{rv}	Hydrodynamic pressure rise within recess [N/m^2]
Δp_{rm}	Recess pressure drop due to momentum exchange [N/m2].
Θ	x/R. Circumferential or angular coordinate.
$\kappa_y = \kappa_x$	$\frac{1}{2}(\kappa_J + \kappa_B)$. Turbulence shear factors in (y,x) flow directions.
κ_J, κ_B	$f_J \cdot R_J$, $f_B \cdot R_B$. Turbulent shear parameters at journal and bearing surfaces.
ρ, μ	Fluid density [Kg/m^3], viscosity [Ns/m^2].
ξ_{xu}, ξ_{xd}	Empirical recess-edge entrance loss coefficients in circumferential (upstream, downstream) direction.
ξ_y	Empirical recess-edge entrance loss coefficients in axial direction.
Ω, ω	Rotational speed of journal, excitation or whirl frequency [1/s]

Subscripts refer to:

x,y	In direction of local circumferential and axial coordinates inplane of bearing.
o	Orifice
r,e	Bearing recesses and edges (entrance).
u,d	Upstream and downstream of recess.
B,J	Refer to bearing and journal surfaces.

INTRODUCTION

The importance of hybrid (combination hydrostatic and hydrodynamic) journal bearings as support elements in cryogenic turbomachinery has steadily grown over the past few years. Hybrid journal bearings (HJBs) enable smaller and lighter turbopumps through no bearing DN life limitation and no sub-critical rotor operation. HJBs have durability, low friction and wear, accuracy of positioning, and large direct stiffness and damping force coefficients. The growth of an "all-fluid-film-bearing" technology for advanced and less expensive (per launching cost) turbopumps demands the development of analytical models and design tools, the testing of components, and the implementation of the technology (Pelfrey, 1995).

Primary power cryogenic turbomachinery operates at high speeds and produces large fluid pressure rises (max. 30 MPa). These typical operating conditions determine the flow in the supporting fluid film bearings to be fully turbulent with dominance of fluid inertia and thermal transport effects. San Andres (1990-5) provides bulk-flow analyses and computational programs for the calculation of cryogenic bearing performance and rotordynamic force coefficients. Measurements of bearing rotordynamic force coefficients and load performance are routinely performed at a high-speed Hydrostatic Bearing Test Facility (HBTF) (Childs and Hale, 1994). Tests have been conducted with water on over 30 hybrid journal bearings and damper seals with rotational speeds ranging from 10 to 25 krpm and pressure differentials from 4 to 7 MPa (Childs and Hale, 1994). Kurtin et al. (1993), Franchek et al. (1994-5), Mosher and Childs (1995), and Yang et al. (1995) report extensive experimental data for the static performance characteristics of a 5 recess HJB for the operating conditions noted and three different bearing clearances (76 to 127 μm). These studies show bulk-flow model calculations to correlate favorably with the experimental results. Accurate predictions depend greatly on the knowledge of the bearing operating clearances, and most importantly, on the orifice discharge coefficients. The references cited along with San Andres (1995a) also discuss the sensitivity of the computed predictions to variations in the input empirical parameters.

Despite the many advantages offered by HJBs, hydrodynamic and "pneumatic hammer" stability limits and two-phase flow operation are issues of primary concern for high speed operation with large pressure differentials. Fluid vaporization is possible since the cryogenic liquid enters the bearing (or seal) at conditions close to its saturation temperature. "Pneumatic hammer" effects are avoided by appropriate selection of the flow restrictor, by designing bearing recesses with small volumes, and by restricting bearing operation to flow conditions where the pressure differential is a small fraction of the liquid bulk modules (Redecliff and Vohr, 1969).

The stability of a simple rotor-bearing system is defined by its threshold speed and the whirl frequency ratio (WFR). This instability is due to the effect of journal rotational speed on the bearing flow field. The threshold speed corresponds to the rotor speed at which a bearing is deprived from its effective damping and any small perturbation from an equilibrium position will determine unbounded rotor motions. The WFR denotes the ratio between the onset whirl frequency (typically the system first critical speed) and the threshold speed of instability. Plain journal bearings show a WFR equal to 0.50 for small to moderate operating eccentricities (light loads), and thus instability at a rotational speed equal to twice the system first critical speed is likely to occur. Measurements in hybrid bearings verify closely the theoretical WFR prediction. In some circumstances the WFR even increases above 0.50, in particular for low rotational speeds and large supply pressures (Franchek, 1992, Franchek et al. 1995).

The WFR=0.50 condition limits severely the application of HJBs to high speed, light weight turbomachinery, and thus, the research has concentrated on conceiving hybrid bearings with improved

stability and without loss in centering stiffness and damping ability. Some of the technological advances have been the natural outcome of analysis and engineering design, while others follow empirical evidence and past experience when a mathematical model is yet to be crafted. Other recommended fixes to improve the hydrodynamic stability of hybrid bearings by reducing or eliminating the WFR are the following:

- Use of machine roughened bearing surfaces to decrease the cross-coupled stiffness coefficients. Test results show a rough knurled-pattern HJB to have WFR as low as 0.30 but with a reduced load capacity and direct stiffness when compared to a smooth surface HJB (Franchek, 1992).

- Use of circumferentially asymmetric pad bearings and recesses to produce enough an isotropy on the rotordynamic force coefficients. Measurements and analysis for an engineered two pad HJB validated the concept (San Andres, 1995b). However, this bearing configuration is highly sensitive to the direction of applied static loads.

- Use of flexure-pivot, tilting pad HJBs or compliant surface (foil) journal bearings due to their inherent stability. San Andres (1995c, 1994) discusses at length these concepts and evaluates their potential for cryogenic uses. Flexure-pivot HJBs constitute a novel alternative and full-scale testing is planned for the first semester of 1996. Foil bearings have also demonstrated their performance in cryogenic turbomachinery (Genge et al., 1993). The current foil bearing technology allows only for specific loads applicable to secondary power cryogenic turbopumps. The interested reader should recall the cited references for further details.

- Use of hybrid bearings with angled liquid injection opposing journal rotation to reduce the development of the circumferential flow velocity and with virtual elimination of cross-coupled stiffness coefficients. This concept has lacked firm theoretical modeling though it has proved successful in some applications (Tondl, 1967, Brown and Hart, 1986). Experimental measurements for a 5 recess water HJB demonstrate that angled injection aids in reducing the whirl frequency ratio without decreasing the bearing centering stiffness and load capacity (Franchek, 1992, Franchek and Childs, 1995).

The thermohydrodynamic analysis of real properties, hybrid bearings with angled orifice injection is advanced. The objective is to develop a model able to predict reliably the performance of angled injection HJBs in lieu of their favorable (measured) rotordynamic performance. The motion of a fluid through the thin film lands is governed by mass, momentum and energy transport equations for the bulk-flow velocities, pressure and temperature, along with thermophysical state equations for evaluation of the cryogen material properties. The turbulent bulk-flow is modeled with simple friction coefficients and include effective film depths to accommodate for macroscopic surface roughness. A simple analysis for the angled injection - orifice flow reveals that the fluid momentum exchange produces a pressure rise in the recess which retards the shear flow induced by journal rotation. The numerical predictions from the model are correlated extensively with the experimental data of Franchek (1992).

ANALYSIS

Figure 1 shows the geometry of a hybrid (combination hydrostatic/hydrodynamic) journal bearing and the relevant nomenclature. A liquid at high pressure (P_s) and inlet temperature (T_s) is supplied (radially or angled) through orifice restrictors and impinges into the bearing recesses with a mean

pressure (P_r). The pressure field within the recesses is determined from flow continuity with the film lands, momentum exchange at the orifice plane and a viscous rise due to journal rotation. At the recess edges, an inertial pressure drop also occurs due to the sudden transition from the recess of depth (H_r) into the film lands of thickness (H). Past the recesses, the liquid then flows through the film lands and the pressure drops to the discharge value (P_a).

Equations of flow on the bearing film lands

On the thin film lands flow turbulence, fluid inertia and compressibility effects are important. The model then assumes a fully developed turbulent bulk-flow of a fluid whose material properties depend on its local thermophysical state of pressure and temperature. The equations of mass, axial and circumferential momentum, and adiabatic-flow energy transport for the bulk-flow velocities, pressure and temperature in the bearing film lands are given as (Yang et al., 1995, Kleynhans and Childs,1995):

$$\frac{\partial}{\partial t}\left(\rho H_e\right) + \frac{\partial}{\partial y}\left(\rho H U_y\right) + \frac{\partial}{\partial x}\left(\rho H U_x\right) = 0 \tag{1}$$

$$-H\frac{\partial P}{\partial y} = \frac{\mu}{H}\left\{\kappa_y U_y\right\} + \frac{\partial\left(\rho H_e U_y\right)}{\partial t} + \left\{\frac{\partial\left(\rho H U_y U_y\right)}{\partial y} + \frac{\partial\left(\rho H U_y U_x\right)}{\partial x}\right\} \tag{2}$$

$$-H\frac{\partial P}{\partial x} = \frac{\mu}{H}\left\{\kappa_x U_x - \kappa_J \frac{\Omega R}{2}\right\} + \frac{\partial\left(\rho H_e U_x\right)}{\partial t} + \left\{\frac{\partial\left(\rho H U_y U_y\right)}{\partial y} + \frac{\partial\left(\rho H U_x U_x\right)}{\partial x}\right\} \tag{3}$$

$$C_p\left\{\frac{\partial}{\partial t}\left(\rho H_e T\right) + \frac{\partial}{\partial x_\alpha}\left(\rho H U_\alpha T\right)\right\} = \beta_T H T\left\{\frac{\partial P}{\partial t} + U_\alpha\frac{\partial P}{\partial x_\alpha}\right\} + \Omega\cdot R\frac{H}{2}\frac{\partial P}{\partial x} + \frac{\mu}{H}\left\{\kappa_x\left(U_x^2 + U_y^2 + \frac{1}{2}\Omega R U_x\right) + \kappa_J \Omega R\left(\frac{1}{4}\Omega R - U_x\right)\right\}_{\alpha = x,y} \tag{4}$$

Please refer to the Nomenclature for a description of all variables. $\kappa_y = \kappa_x = (k_J + k_B)/2$ are the wall shear stress parameters determined as local functions of turbulent friction factors which depend on the bearing and journal surface conditions and the flow Reynolds numbers relative to the rotating (R_J) and stationary (R_B) surfaces, i.e $\kappa_J = f_J \cdot R_J$, $\kappa_B = f_B \cdot R_B$ (Hirs, 1973). The cryogenic liquid properties are extracted from the Benedict-Web-Rubin equation of state as given in the standard data base of McCarty (1986).

The fluid pressure at the sides of the bearing ($y = \pm L/2$) equals the discharge or ambient value (P_a). At the interface with the bearing recesses, continuity of flow and pressure must be attained as detailed below.

Angled Injection - Recess Flow and Pressure Equations

Figure 2a depicts a hydrostatic bearing recess (or pocket) with axial length (**l**) and circumferential extent (**b**). The figure shows the direction of the journal surface speed ($\Omega \cdot R$), and relative to this velocity the recess is divided into upstream (**u**) and downstream (**d**) regions. The fluid supply orifice port with injection angle (δ) is located at a distance b_u from the upstream recess edge. The orifice has an effective area A_o normal to the feed speed V_o. Radial fluid supply is indicated by $\delta=0$ while a tangential feed opposite to journal rotation is given by $\delta = \pi/2$ (90°).

Conventional analysis of hydrostatic bearings do not calculate the flow field within the recess since these are typically deep and enclose large nearly stagnant fluid volumes. Analysis then accounts only for flow continuity with the film lands and determines a (uniform) recess pressure using a simple orifice equation based on Bernoulli's principle. The complexity of the flow field in hydrostatic pockets has been discussed by Hill et al. (1995) and Braun et al. (1993, 1995) with the aid of two-dimensional computational fluid mechanics analyses. Numerical results reveal the generation of hydrodynamic pressures within the pocket and followed by sharp inertial pressure drops at the recess edges. This field of study is of utmost importance for the development of a mature technology on hybrid bearings for cryogenic applications.

The analysis of angled injection - hydrostatic pockets follows here a simplified approach which intends to be of practical use without resorting to computationally intensive three dimensional flow calculations. The flow model is evidently crude yet it grasps the fundamental mechanisms of pressure generation within the bearing pockets. The favorable correlation with hybrid bearing experimental performance characteristics given later justifies the method used.

A mass conservation equation at each bearing recess of area ($l \cdot b$) and depth H_r is defined by the global balance between the mass flow through the orifice restrictor (Q_{ro}), the mass flow into the film lands and the time rate of change of liquid mass within the recess and supply line volume (V_r), i.e.

$$Q_{ro} = \rho_r A_o V_o = \int_{\Gamma_r} [\rho H \vec{U} \cdot \vec{n}] d\Gamma_r + \frac{\partial}{\partial t}(\rho_r V_r) \qquad (5)$$

$$\text{for } r = 1, 2 \ldots, Nrecess$$

where $A_o = C_d \pi d_o^2/4$ is the effective orifice area with C_d as an empirical discharge coefficient. Γ_r denotes the closure of the recess with the film lands and has a normal **n** along the boundary line. At the orifice discharge plane, the mean recess pressure is denoted by P_r (see Figure 2b) and given from Bernoulli's equation as:

$$(P_s - P_r) = (1/2)\, \rho_r V_o^2 \qquad (6)$$

Computational fluid mechanics analysis reveals that the axial pressure within the recess is (to a first approximation) practically uniform. Hence, modeling of the flow in the pocket as a one-dimensional bulk-flow bearing determines that the pressure difference (downstream - upstream) on a recesses is given by two contributions:

a) a viscous pressure rise (ΔP_{rv}) due to shear flow induced by journal rotation (San Andres, 1992):

$$\Delta P_{rv} = \left[P_d - P_u\right] = \mu_r \kappa_{xr} \frac{b}{H_r^2}\left(\frac{\Omega \cdot R}{2} - U_{rx} \right) \qquad (7)$$

b) a pressure drop (ΔP_{rm}) at the orifice injection plane and due to the exchange of fluid momentum, and simply stated as:

$$\Delta P_{rm} = \left[P_d - P_u\right]_m = -\frac{Q_o V_o \sin(\delta)}{H_r \cdot 1} = -\frac{2A_o}{H_r \cdot 1} \cdot (P_s - P_r)\sin(\delta) \qquad (8)$$

where the orifice equation (6) has been used on the right hand side of eqn (8). Note that for radial injection ($\delta = 0$) there is no momentum pressure drop at the supply port, while the largest pressure drop occurs for large pressure differentials ($P_s - P_a$) and tangential injection ($\delta = 90°$). For simplicity the pressure field within the hydrostatic pocket is then taken as linear and combines the two pressure differences as shown pictorially in Figure 2b. Note that this simplification avoids the calculation of the complex flow field on the entire bearing recess.

Finally, the entrance pressures (P_e) to the film lands in the circumferential (upstream and downstream) and axial directions are given by (San Andres, 1992):

$$P_e\Big]_{u,d} = \left[P_r - \frac{\rho}{2}\left(+ \xi_x\right)\left\{1 - U_x^2\right\}\right]_{u,d} \qquad (9.a)$$

$$P_e = P_r - \frac{\rho}{2}\left(1 + \xi_y\right)\left\{1 - U_y^2\right\} \qquad (9.b)$$

These equations are used only when fluid flows from the recess towards the film lands. Details of energy transport at the recesses are given by Yang et al. (1995).

Perturbation Analysis

Consider the motion of the journal as the superposition of small amplitude periodic motions of frequency (ω) around a static equilibrium position. That is, the journal center displacements are given as

$$e_X(t) = e_{Xo} + \Delta e_X e^{i\omega t}, \quad e_Y(t) = e_{Yo} + \Delta e_Y e^{i\omega t}; \quad i = \sqrt{-1} \qquad (10)$$

The magnitudes of the dynamic perturbations in journal displacements are small, i.e., $|\{\Delta e_X, \Delta e_Y\}| <<< C$. The film thickness ($H$) can then be regarded as the superposition of a steady-state (H_o) and dynamic components given by the real part of the following expression:

$$H = H_o + \left\{\Delta e_X h_X + \Delta e_Y h_Y\right\} e^{i\omega t} \qquad (11)$$

where $\mathbf{H}_o = C(y) + e_{Xo}\, h_X + e_{Yo}\, h_Y$; and $h_X = \cos(\theta)$, $h_Y = \sin(\theta)$

The flow field variables (U_x , U_y , P,T), as well as the fluid properties (ρ, μ) and the shear parameters (κ_x , κ_y) are also formulated as the superposition of zeroth-order and first-order complex fields describing an equilibrium for steady-state flow, and the perturbed condition for small amplitude dynamic journal motions, respectively. In general, these fields are expressed as:

$$\Psi = \Psi_o + \left\{\Delta e_X \Psi_X + \Delta e_Y \Psi_Y\right\} e^{i\omega t} \tag{12}$$

Substitution of equations (11) and (12) into the flow equations (1-9) renders zeroth- and first-order equations for determination of the steady-state and perturbed flow-fields. These equations are not reproduced here for brevity but can be found in their full extent in the reference of San Andres (1993). The bearing static and dynamic force characteristics are evaluated once a solution to the flow equations is obtained. Fluid film forces ($\mathbf{F}_X$, $\mathbf{F}_Y$) and force coefficients (stiffness $\mathbf{K}_{\alpha\beta}$, damping $\mathbf{C}_{\alpha\beta}$ and inertia $\mathbf{M}_{\alpha\beta}$) are calculated by integration of the pressure fields over the journal surface. The appropriate formulae are:

$$F_\alpha = \int_0^L \int_0^{2\pi} P_o\, h_\alpha R \cdot d\Theta \cdot dy; \quad \alpha = X, Y \tag{13}$$

$$K_{\alpha\beta} - \omega^2 M_{\alpha\beta} + i\omega C_{\alpha\beta} = \int_0^L \int_0^{2\pi} P_\beta\, h_\alpha R \cdot d\Theta \cdot dy; \quad \alpha, \beta = X, Y \tag{14}$$

Numerical Method of Solution

The control-volume method of Launder and Leschziner (1978) is used to solve the differential equations of motion. Staggered grids containing control volumes for the primitive flow variables (circumferential and axial velocity, pressure and temperature) cover the flow domain. Algebraic difference equations are derived on each control volume for the conservation of mass, axial and circumferential momentum, and balance of energy. A pressure correction equation is derived using the SIMPLEC procedure of Van Doormaal and Raithby (1984). A Newton-Raphson scheme is also used for satisfaction of the recess mass flow constraint. Full descriptions on the accuracy and parameter sensitivity of the method as applied to hybrid bearings and annular pressure seals are given in past publications (San Andres, 1990-1995). The interested reader should consult the cited references for a detailed exposition of the numerical method used.

COMPARISONS TO TEST RESULTS FROM A WATER 5-RECESS HYBRID BEARING

Franchek (1992) presents an experimental study of five hybrid bearings with distinctive geometrical configurations. These are namely, smooth bearings with radial injection and rectangular (baseline), triangular and circular recesses, a knurled rough-surface bearing with rectangular recesses, and a smooth surface bearing with rectangular recesses and a 45° angled orifice injection. The tests consisted of the measurement of load vs. journal eccentricity, torque and flow rate, and the

identification of rotordynamic force coefficients. Childs and Hale (1994) provide a full description of the test apparatus and the experimental procedure. The nominal test conditions include:

(a) 3 rotational speeds: 10.0, 17.4 and 24.6 krpm
(b) 3 supply pressures: 4.0, 4.5 and 7.0 MPa (600, 800 and 1000 psig)
(c) 6 journal eccentricity ratios (e/c): 0.0 to 0.5 at a fluid supply temperature of 55°C (130°F).

Franchek and Childs (1994) and Franchek et al. (1995) briefly report the measurements with comparisons to predictions for the radial injection bearing (conventional design). Table 1 describes the geometry of the test bearing with angled (45°) injection. At the journal centered position the measured data for flow rate, supply and average recess pressures and operating clearance is also given. From these values, empirical orifice loss coefficients (C_d) are estimated for each test condition and used in all computations including journal off-centered operations. The values of circumferential (Re_c) and axial flow Reynolds (Re_a) numbers demonstrate the character of the flow within the test bearing. San Andres (1995e) reports detailed comparisons of predictions and test results for both radial and angled (45°) injection hybrid bearings. Selected experimental measurements (broken lines) along with predictions from the model (continuous lines) follow.

Static Performance Characteristics of Angled Injection Bearing

Figure 3 depicts the journal eccentricity versus applied load (W_X) at a nominal supply pressure of 7.0 MPa and three rotational speeds. The journal eccentricity increases linearly with the applied load as is typical in externally pressurized bearings. The predictions correlate very well with the measurements and also demonstrate that the stiffness coefficients for the bearing will not vary (greatly) with the journal center position. Figure 4 shows the predicted journal center loci as the load increases. Note the negative attitude angle at the lowest speed (10.2 krpm), an almost null angle at the medium speed (17.4 krpm), and a positive angle at the highest speed (24.6 krpm). Test results are not shown since these were not included by Franchek (1992). The predictions reveal the fundamental effect of angled injection on the bearing static load performance. Engineering design could then lead to a hybrid bearing free of cross-coupling effects with the appropriate combination of injection angle, supply pressure and operating speed.

Figure 5 depicts the recess pressure ratios $\{(P_r-P_a)/(P_s-P_a)\}$ at the journal concentric position for the three nominal supply pressures and speeds. Recess pressure ratios rise with the journal speed and decrease with supply pressures since land flow resistance and turbulence are greater. The correlations with the model predictions are good except at the largest speed and lowest supply pressure. Note that the comparisons have been made with averaged test recesses pressures. Actual measured recess pressures vary as much as 13% from the calculated (experimental) average. Figure 6 shows the predicted flow rates to agree with the measurements at the low (10.2 krpm) and medium speeds (17.4 krpm). The discrepancies at the highest test speed are attributed to the larger predicted recess pressures.

Dynamic Performance Characteristics at Journal Centered Position

The test results and numerical predictions demonstrate that the rotordynamic force coefficients are practically insensitive to the applied load for journal eccentricities to 50% of the bearing clearance. Hence, in the following, only force coefficients at the concentric position are presented.

The whirl frequency ratio (**WFR**), a stability indicator of paramount importance for the application of hybrid bearings to high speed applications, is depicted in Figure 7. Although not shown

here, the radial bearing presents a (measured) WFR ranging from 0.60 to 0.48 for most operating conditions (Franchek, 1992). On the other hand, the angled (45°) injection bearing shows a (large) negative WFR at the lowest speed and raising to the 0.5 limit as the rotational speed increases. The numerical predictions agree well with the measurements at the middle and high speeds, i.e. 17.4 and 24.6 krpm. Note that the advantages of angled injection are then lost as the journal speed increases and determines dominance of hydrodynamic effects over hydrostatic effects.

Figure 8 depicts the cross-coupled stiffness coefficients ($K_{XY} = -K_{YX}$) as the journal speed increases for the three nominal supply pressures. In the radial injection bearing, the cross-coupled stiffness are always positive and increase with the journal speed (Franchek et al., 1995). On the other hand, the angled injection bearing presents negative cross-coupled coefficient at the lowest speed. From a rotordynamics point of view this is a desirable occurrence since then these coefficients render forces opposing the development of forward whirl motions. The numerical predictions show the same trends as the measurements but do not agree well with the measurements.

Figure 9 presents the direct stiffness coefficients ($K_{XX} = K_{YY}$) versus the journal speed and nominal supply pressures. The experimental results show significant discrepancies between K_{XX} and K_{YY} and attributed to minute differences in the diameters of the feeding orifices. The numerical predictions agree well with the measurements except at the lowest speed and highest pressure where the tests show an unexpected behavior.

The direct damping coefficients ($C_{XX} = C_{YY}$) are depicted in Figure 10. The predictions and measurements show direct damping to increase with journal speed and supply pressure. Correlation test and model is best at the lowest (10.2 krpm) speed. However, direct damping is underpredicted by as much as 25% at 24.6 krpm.

Figure 11 shows the predicted cross-coupled damping coefficients ($C_{XY} = -C_{YX}$) to increase with journal speed and with little influence of the external supply pressure. On the other hand, the test results show a different behavior with cross-damping coefficients being the largest at the middle test speed (17.4 krpm). No conclusive remark can be made in regard to the correlation of prediction and identified test coefficients.

Comparisons to inertia force coefficients are given by San Andres (1995e) and not reported here for brevity. The predictions show added mass coefficients independent of external supply pressure and with a slow variation as the journal speed increases. The experimentally identified inertia coefficients are of the same order of magnitude as the predictions but present an erratic behavior. Franchek and Childs (1994) indicate the test inertia coefficients have average uncertainties of 53%.

CONCLUSIONS

The growth of an "all-fluid-film-bearing" technology for support of advanced cryogenic turbopumps demands the development of models and design tools, the testing of components, and the implementation of the technology on actual hardware. Conventional hybrid fluid film bearings have demonstrated adequate load support, direct stiffness and damping, but suffer from limited hydrodynamic stability which deters their use to high speed applications and flexible rotating structural systems. On the other hand, experiments on hybrid bearings with angled orifice injection have shown virtual elimination of cross-coupled stiffness coefficients and null or negative whirl frequency ratios. No firm analysis was available at the time of the measurements, and hence, further technological developments since then were prevented.

A bulk-flow analysis for prediction of the static load and force coefficients of hybrid bearings with angled orifice injection is advanced. A simple model reveals that the fluid momentum exchange

at the orifice discharge produces a pressure rise in the recess which retards the shear flow induced by journal rotation, and consequently, reduces cross - coupling forces. The predictions from the model are compared with measurements for a hybrid bearing with a 45° angled injection. The test bearing nominal clearance is 125 μm and operates with water from 10.2 krpm to 24.6 krpm and with supply pressures from 4 to 7 MPa. Comparison of experiments and model calculations for load, flow rate and recess pressures are good and verify the soundness of the bulk-flow model. Correlations of model and test direct stiffness and damping coefficients are also favorable. The predictions show the same trends as the test values for the whirl frequency ratio and cross-coupled stiffness coefficients but large differences are apparent. Inertia force coefficients do not agree with the experimental values perhaps due to the large uncertainty in the test coefficients. The predictions as well as the measurements demonstrate that the advantages of angled injection in hybrid bearings are lost as the journal speed increases and brings dominance of hydrodynamic over hydrostatic effects.

ACKNOWLEDGMENTS

The support of NASA Lewis Research Center under NASA Grant NAG-1434 is gratefully acknowledged. Thanks to Mr. James Walker of NASA LeRC for his interest on this work. Thanks to my daughter, Maria Jose (12), who helped on the graphical art.

REFERENCES:

Braun, M.J., Choy,F.K., and Y.M.Zhou, 1993, "The Effects of a Hydrostatic Pocket Aspect Ratio, Supply Orifice Position and Attack Angle on Steady-State Flow Patterns, Pressure and Shear Characteristics," ASME Journal of Tribology, Vol. 115, pp. 678-685.

Braun, M.J., M. Dzodzo, 1995, "Effects of the Feedline and the Hydrostatic Pocket Depth on the Flow Patterns and Pressure Distribution,"ASME Journal of Tribology, Vol. 117, pp. 224-233.

Brown, R.D., J. A. Hart, 1986, "A Novel Form of Damper for Turbomachinery," Proceedings of the Workshop on Rotordynamic Instability Problems in High Performance Turbomachinery, Texas A&M University, pp. 325,348, NASA CP 2443.

Childs, D., and K. Hale, 1994, "A Test Apparatus and Facility to Identify the Rotordynamic Coefficients of High Speed Hydrostatic Bearings", ASME Journal of Tribology, Vol. 116, pp. 337-344.

Franchek, N., 1992, "Theory Versus Experimental Results and Comparisons for Five Recessed, Orifice Compensated, Hybrid Bearing Configurations," Texas A&M University, M.S. Thesis, TAMU Turbomachinery Laboratories, August 1992.

Franchek, N., and D. Childs, 1994, "Experimental Test Results for Four High-Speed, High-Pressure, Orifice-Compensated Hybrid Bearings," ASME Journal of Tribology, Vol. 116, 2, pp. 285-290.

Franchek, N., D. Childs, and L. San Andres, 1995, "Theoretical and Experimental Comparisons for Rotordynamic Coefficients of a High-Speed, High-Pressure, Orifice-Compensated Hybrid Bearings," ASME Journal of Tribology, Vol. 117, 2, pp. 285-290.

Genge, G.G., Saville, M., and A. Gu, 1993, "Foil Bearing Performance in Liquid Nitrogen and Liquid Oxygen," AIAA/SAE/ASME/ASEE 29th Joint propulsion Conference and Exhibit, Monterrey, CA, June, Paper AIAA-93-2537.

Hill., D., E. Baskharone, and L. San Andres, 1995, "Inertia Effects in a Hybrid Bearing with a 45 degree Entrance Region," ASME Journal of Tribology, Vol. 117, 3, pp. 498-505.

Hirs, G. G., 1973, "A Bulk-Flow Theory for Turbulence in Lubricating Films," ASME Journal of Lubrication Technology, Vol.95, pp.135-146.

Kleynhans, G, and D. Childs, 1995, "The Acoustic Influence of Cell Depth on the Rotordynamic Characteristics of Smooth-Rotor/Honeycomb-Stator Annular Gas Seals," Seals Code Development Workshop, NASA Lewis Research Center, Cleveland, OH, June 15, 1995.

Kurtin, K., Childs, D., San Andres, L. and Hale, K., 1993, "Experimental versus Theoretical Characteristics of a High Speed Hybrid (combination Hydrostatic and Hydrodynamic) Bearing,"

ASME Journal of Tribology, Vol. 115, 1, pp. 160-169.

Launder, B., and M. Leschziner, 1978, "Flow in Finite Width Thrust Bearings Including Inertial Effects," ASME Journal of Lubrication Technology, Vol. 100, pp. 330-345.

McCarty, R.D., 1986, NBS Standard Reference Data Base 12, Thermophysical Properties of Fluids, MIPROPS 86, Thermophysics Division, Center for Chemical Engineering, National Bureau of Standards, Colorado.

Mosher, P., and D. Childs, 1995, "Theory Versus Experiment for the Effect of Pressure Ratio on the Performance of an Orifice-Compensated Hybrid Bearing," 1995 ASME Design Engineering Technical Conference," DE-Vol 84-2, Vol.3-Part B., pp. 1119-1129.

Pelfrey, P., 1995, "Pratt & Whitney Fluid-Film Bearing and Seal Technology Development and Implementation," Seals Code Development Workshop, NASA Lewis Research Center, Cleveland, OH, June 15, 1995.

Redecliff, J.M. and J.H. Vohr, 1969, "Hydrostatic Bearings for Cryogenic Rocket Engine Pumps," ASME Journal of Lubrication Technology, pp. 557-575.

San Andres, L.A., 1990, "Turbulent Hybrid Bearings with Fluid Inertia Effects", ASME Journal of Tribology, Vol. 112, pp. 699-707.

San Andres, L., 1992, "Analysis of Turbulent Hydrostatic Bearings with a Barotropic Fluid," ASME Journal of Tribology, Vol. 114, 4,pp. 755-765,1992.

San Andres, L., 1993, "Thermohydrodynamic Analysis of Cryogenic Liquid Turbulent Flow Film Bearings for Cryogenic Applications," Research Progress Report to NASA Lewis Research Center, NASA Grant NAG3-1434, December.

San Andres, L., 1995a, "Thermohydrodynamic Analysis of Fluid Film Bearings for Cryogenic Applications," AIAA Journal of Propulsion and Power, Vol. 11, 5, pp. 964-972.

San Andres, L., 1995b, "Two Pad Axially Grooved Hydrostatic Bearing," U.S. Patent 5,433,528, July, 18.

San Andres, L., 1995c, "Turbulent Flow, Flexure-Pivot Hybrid Bearings for Cryogenic Applications," 1995, STLE/ASME Tribology Conference, Orlando, ASME Journal of Tribology, ASME Paper 95-TRIB-14.

San Andres, L., 1995d, "Turbulent Flow Foil Bearings for Cryogenic Applications," ASME Journal of Tribology, Vol. 117, 1, pp. 185-195.

San Andres, L., 1995e, "Angled Injection - Hybrid Fluid Film Bearings for Cryogenic Applications," Annual Research Progress Report to NASA Lewis Research Center, NASA Grant NAG3-1434, December.

Tondl, A., 1967, "Bearings with a Tangential Gas Supply," Gas Bearing Symposium, University of Southampton, Dept. of Mechanical Engineering.

Van Doormaal, J.P., and D. Raithby, 1984, "Enhancements of the SIMPLE Method for Predicting Incompressible Fluid Flows," Numerical Heat Transfer, Vol. 7, pp. 147-163.

Yang, Z., L. San Andres and D. Childs, 1995, "Thermohydrodynamic Analysis of Process Liquid Hydrostatic Bearings in Turbulent Regime, Part I: The Model and Perturbation Analysis, Part II: Numerical Solution and Results," ASME Journal of Applied Mechanics, Vol. 62, 3, pp. 674-684.

Table 1. Description of water lubricated orifice compensated hybrid bearing tested by Franchek and Childs (1994).

No of recesses (Nrec)	5
Clearance nominal (C)	125.4 μm (0.005 in)
Diameter (D)	76.2 mm (3 in)
Length (L)	76.2 mm (3 in)
Land roughness (peak-peak)	0.33 μm (13 μin)

Recess dimensions: square (l) 27 mm x (b) 27 mm x 254 μm (depth) Supply volume Vs = 0.1289 dm3
Orifice at midplane of recess.diameter d = 2.49 mm, angled injection (d = p/4 [45°])
Lubricant: water at Ts = 328.3° K
Viscosity (μ) 0.4929E-3 Pa.s Density (ρ) 986.26 kg/m³
Discharge pressure Pa: 0.0 MPa (0 psig)
Empirical parameters: Entrance loss factors ξ_x , ξ_y = 0.0, Inlet swirl α = 0.5

Test Conditions and Estimated Parameters at Centered Operation

Speed Kcpm	P MPa	C μm	Q l/min	Pr_{av} MPa	C_d	Re_c (ρΩRc/μ)	Re_s (Qs/πDμ)
10.2	4.133	122.8	79.94	1.128	0.700	9,988.0	11,136.0
	5.519	124.4	92.21	1.252	0.680	10,129.1	12,845.6
	6.877	124.9	102.29	1.434	0.660	10.169.8	14,249.9
17.4	4.154	120.5	79.60	1.866	0.800	16,737.3	11,088.3
	5.521	121.5	91.67	2.148	0.763	16,876.2	11,088.9
	6.846	122.7	101.75	2.316	0.726	17,042.0	14,174.0
24.6	4.135	119.4	78.07	2.424	0.907	23,447.2	10.875.8
	5.532	120.8	92.21	2.870	0.859	23,722.0	12,942.4
	6.844	117.1	101.38	3.206	0.808	23,000.0	14,123.0

(*) Cd values estimated from measured flow rate and average recess pressures

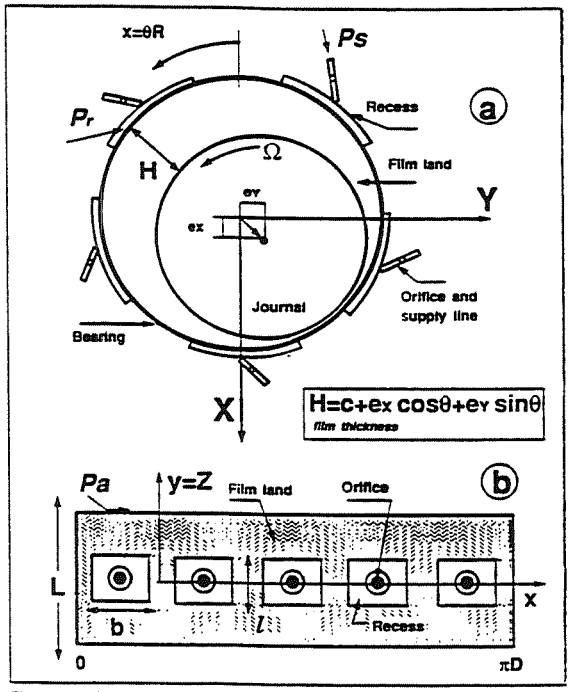

Figure 1. Geometry of an orifice compensated – angled injection hybrid bearing.
a) Axial View and Coordinate System, b) Unwrapped Bearing Surface

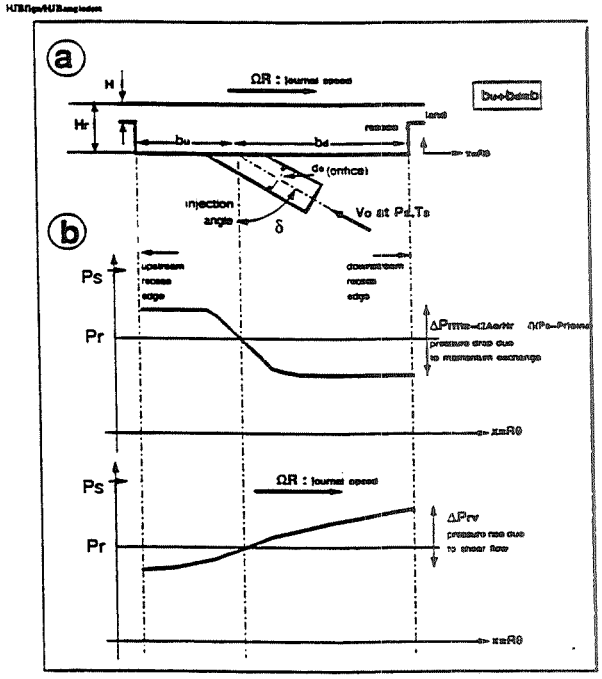

Figure 2. (a) Description of hydrostatic recess with angled injection
(b) Assumed pressure field within hydrostatic recess

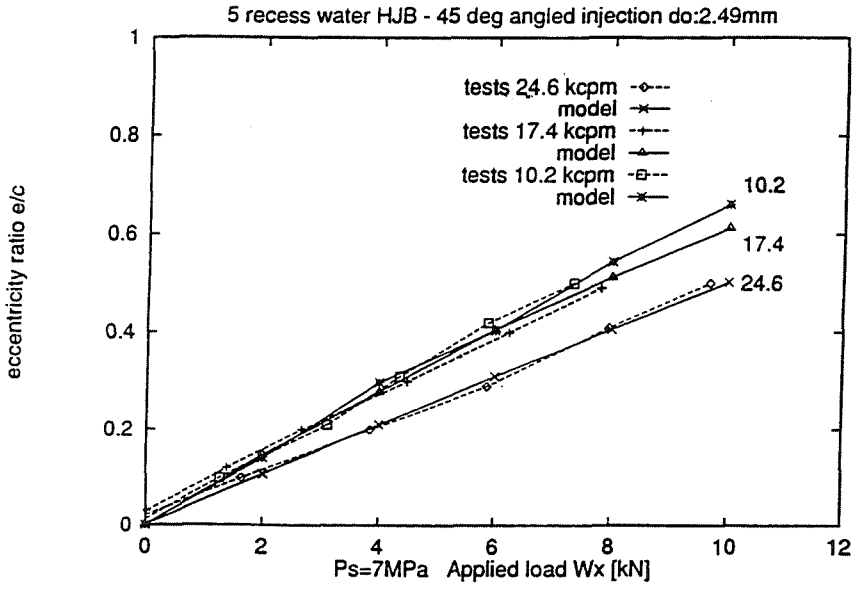

Figure 3. Journal eccentricity vs. applied load Wx for water - 5 recess hybrid bearing. Comparison to experimental results.

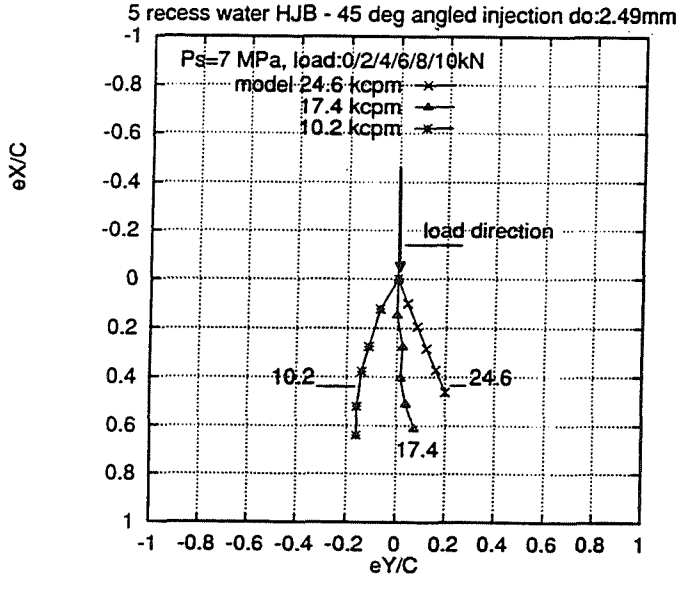

Figure 4. Journal center locus for water - 5 recess hybrid bearing. Numerical predictions for increasing loads.

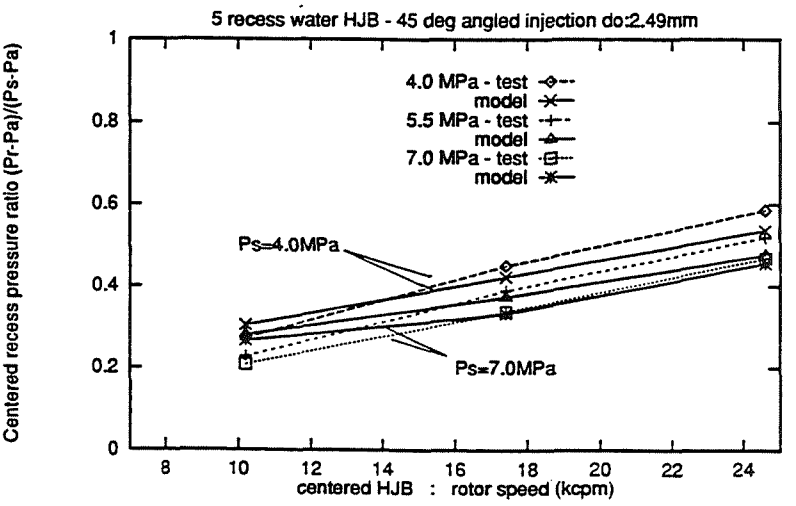

Figure 5. Centered recess pressure ratio (Pr-Ps)/(Ps-Pa) for water - 5 recess hybrid bearing. Comparison to experimental results.

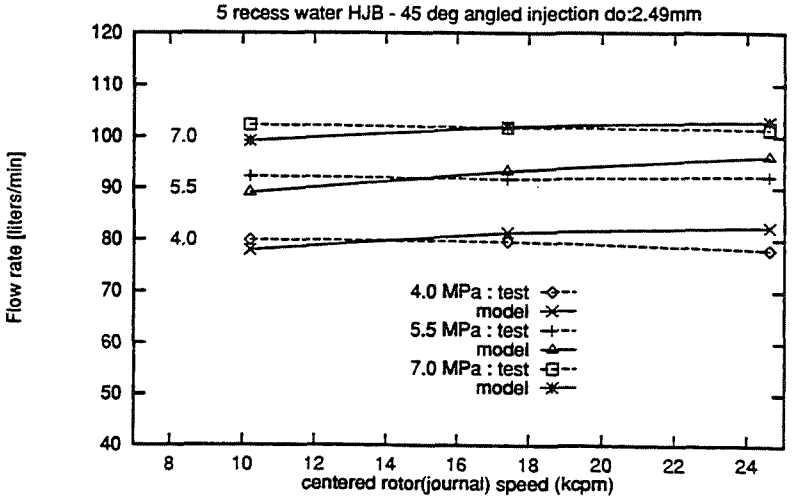

Figure 6. Bearing flow rate vs. journal speed for water - 5 recess hybrid bearing. Comparison to experimental results.

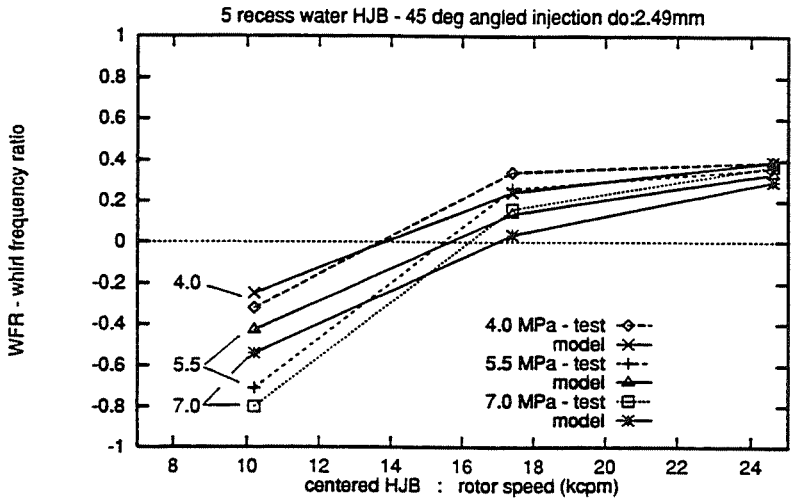

Figure 7. Whirl frequency ratio vs. journal speed for water - 5 recess hybrid bearing. Comparison to experimental results.

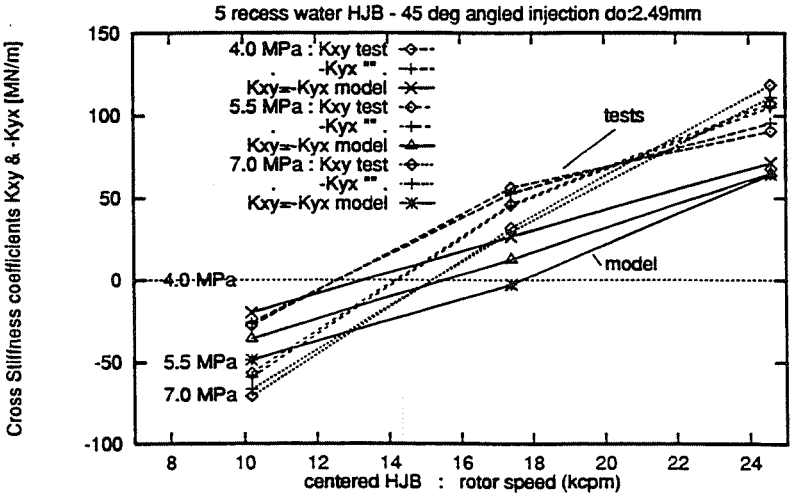

Figure 8. Cross-stiffness coefficients (KXY, -KYX) vs. journal speed for water - 5 recess hybrid bearing. Comparison to experimental results.

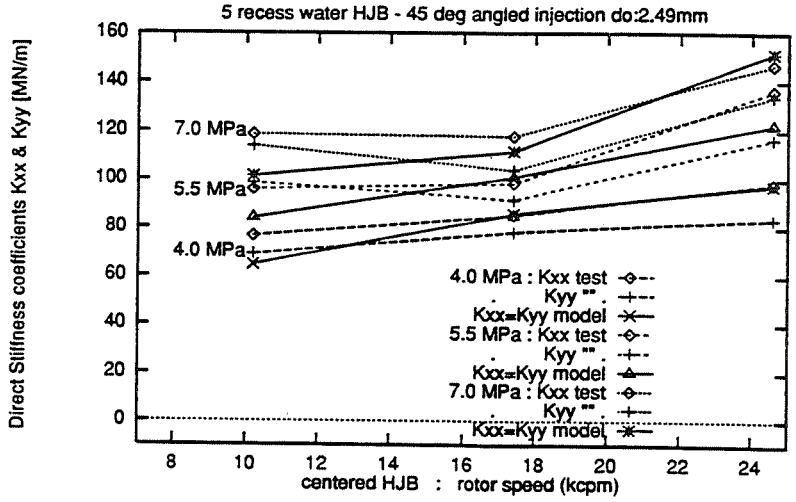

Figure 9. Direct stiffness coefficients (Kxx, Kyy) vs. journal speed for water - 5 recess hybrid bearing. Comparison to experimental results.

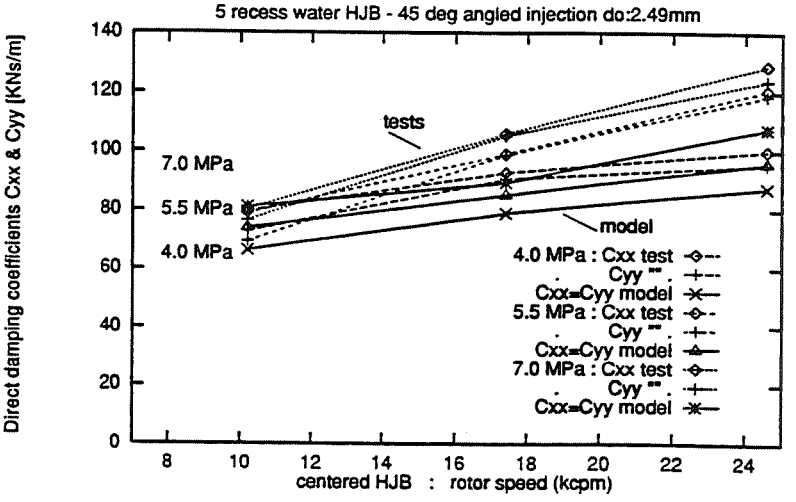

Figure 10. Direct damping coefficients (Cxx, Cyy) vs. journal speed for water - 5 recess hybrid bearing. Comparison to experimental results.

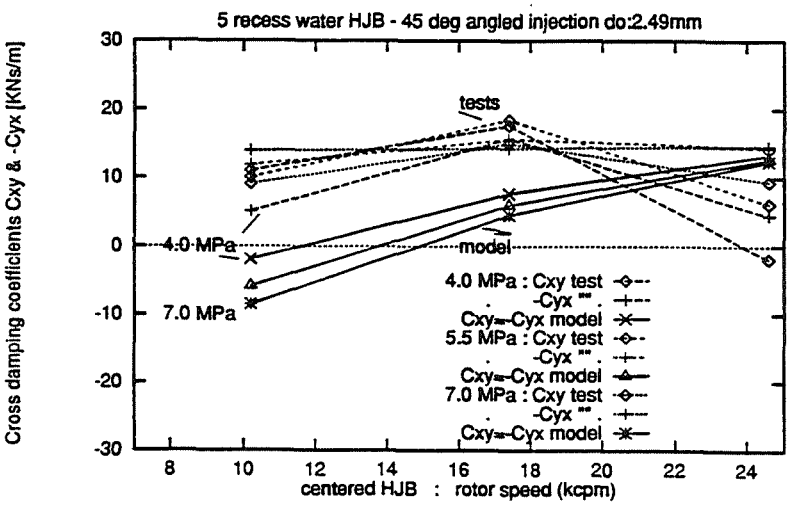

Figure 11. Cross-damping coefficients (Cxy, -Cyx) vs. journal speed for water - 5 recess hybrid bearing. Comparison to experimental results.

ONLY THIS PAGE

SESSION II

GAS SEALS

THE ACOUSTIC INFLUENCE OF CELL DEPTH ON THE ROTORDYNAMIC CHARACTERISTICS OF SMOOTH-ROTOR/HONEYCOMB-STATOR ANNULAR GAS SEALS

George Kleynhans and Dara Childs
Texas A&M University
College Station, Texas

Abstract

A two-control-volume model is employed for honeycomb-stator/smooth-rotor seals, with a conventional control-volume used for the through flow and a "capacitance-accumulator" model for the honeycomb cells. The control volume for the honeycomb cells is shown to cause a dramatic reduction in the effective acoustic velocity of the main flow, dropping the lowest acoustic frequency into the frequency range of interest for rotordynamics. In these circumstances, the impedance functions for the seals can not be modeled with conventional (frequency-independent) stiffness, damping, and mass coefficients. More general transform functions are required to account for the reaction forces, and the transfer functions calculated here are a lead-lag term for the direct force function and a lag term for the cross-coupled function. Experimental measurements verify the magnitude and phase trends of the proposed transfer functions.

These first-order functions are simple, compared to transfer functions for magnetic bearings or foundations. For synchronous response due to imbalance, they can be approximated by running-speed-dependent stiffness and damping coefficients in conventional rotordynamics codes. Correct predictions for stability and transient response will require more general algorithms, presumably using a state-space format.

Introduction

The use of honeycomb annular seals in gas compressors and turbines is an attractive retrofit or design implementation due to their favorable static and dynamic characteristics. Honeycomb seals are most often employed in the following two distinct ways: (a) A honeycomb-stator/smooth-rotor configuration for enhancing rotor stability, (b) An abradable honeycomb-stator with a labyrinth-rotor for superior leakage control. The latter configuration is typical for aircraft gas turbines, while the former is used frequently in high-pressure centrifugal compressors in the petrochemical industry and is the configuration of interest here. In the balance of this paper, "honeycomb seals" will refer to this configuration.

Honeycomb seals were initially used to eliminate a stability problem with the High Pressure Oxygen Turbopump (HPOTP) of the Space Shuttle Main Engine (SSME), Scharrer (1989). Recently, these seals have been used to eliminate rotordynamic instability problems with high-pressure compressors, Zeidan et al. (1993), Sorokes et al. (1994). The authors are aware of several other compressors plus at least one steam turbine which have been "cured" of rotordynamic instability problems via retrofits of honeycomb seals.

For small motion about a centered position, the conventional force/motion model used for annular seals is

$$-\begin{Bmatrix} F_x \\ F_y \end{Bmatrix} = \begin{bmatrix} K & k \\ -k & K \end{bmatrix} \begin{Bmatrix} x \\ y \end{Bmatrix} + \begin{bmatrix} C & c \\ -c & C \end{bmatrix} \begin{Bmatrix} \dot{x} \\ \dot{y} \end{Bmatrix} + M \begin{Bmatrix} \ddot{x} \\ \ddot{y} \end{Bmatrix} \tag{1}$$

For annular gas seals, c and M have typically been assumed to negligible. Nelson (1984,1985) developed the initial analysis for rotordynamic coefficients of annular seals. Nelson developed a bulk-flow model comprised of: (a) a compressible-flow continuity equation, (b) an axial-momentum equation, (c) a circumferential-momentum equation, (d) an energy equation, and (e) a perfect-gas equation of state. The honeycomb surface was treated as a solid wall. The only influence of the honeycomb surface was an increased friction factor in the momentum equations. This model did a notably poor job in predicting measured rotordynamic coefficients. Various improvements were attempted, starting with Elrod et al. (1989, 1990) who developed an improved model for the inlet loss. Ha and Childs (1994) implemented friction-factor data from flat-plate measurements to improve the friction-factor model for honeycomb surfaces. In a response to a discussion of their paper, Ha and Childs expanded the model to allow radial transient flow into the honeycomb surface. Their analysis uses a two-control-volume model.

An implicit requirement in all of the analyses leading to the model of Eq. (1) is that the acoustic frequencies of the gas within an annular seal be substantially above the rotordynamic frequencies of interest. This paper will use the two-control-volume model of Ha and Childs (1994) to demonstrate that this requirement is generally not met, and consequently, honeycomb seals can not be modeled adequately with frequency-independent stiffness, damping, and mass coefficients.

Two-Control-Volume Model

The prior governing equations for plain and honeycomb gas seals (Nelson, 1985, and Ha and Childs, 1994) employ a single control volume. However, the honeycomb seal geometry can clearly allow flow to radially enter and exit the honeycomb cells. In essence, the honeycomb seal land acts as a porous surface. Hence, as indicated in the authors' response of Ha and Childs (1994), the use of an additional control volume (adjacent to the main flow control volume) which allows flow to only enter and exit in the radial direction can better describe the physical nature of the flow.

Figure 1 shows the locations of the two control volumes in a honeycomb seal with the

clearance exaggerated for clarity. The nature of flow between the control volumes is shown in figure 2. Note that the cell depth H_d can be more than ten times the clearance, H. For control volume A in figure 2, the continuity equation is;

$$\frac{\partial}{\partial t}(\rho H) + \frac{1}{R}\frac{\partial}{\partial \Theta}(\rho U H) + \frac{\partial}{\partial Z}(\rho W H) + \rho V = 0, \tag{2}$$

and for control volume B,

$$\rho V = H_d \frac{\partial \rho}{\partial t} \tag{3}$$

Note that for a centered seal without a clearance perturbation, V=0. A clearance perturbation is required to generate flow between volumes A and B.

A summation of the forces in the Z and Θ directions yields the following momentum equations:

Axial Momentum Equation

$$-H\frac{\partial P}{\partial Z} = \tau_{sz} + \tau_{rz} + \rho W V + \frac{\partial}{\partial t}(\rho W H) + \frac{1}{R}\frac{\partial}{\partial \Theta}(\rho U W H) + \frac{\partial}{\partial Z}(\rho W^2 H) \tag{4}$$

Circumferential Momentum Equation

$$-\frac{H}{R}\frac{\partial P}{\partial \Theta} = \tau_{s\Theta} + \tau_{r\Theta} + \rho U V + \frac{\partial}{\partial t}(\rho U H) + \frac{1}{R}\frac{\partial}{\partial \Theta}(\rho U^2 H) + \frac{\partial}{\partial Z}(\rho U W H) \tag{5}$$

The variable V is eliminated by substituting the continuity equation for Control Volume B into the continuity equation of Control Volume A and the momentum equations. The shear-stress terms are modeled via the bulk-flow theory of Hirs (1973). The relationship between pressure P and density ρ is modeled by the equation of state for an ideal gas,

$$\rho = \frac{P}{Z_c R_g T} \tag{6}$$

For this analysis an isothermal flow is assumed; hence, the energy equation is not required. The bases for assuming isothermal flow are the following: (a) experimental measurements for honeycomb seals tested at the Turbomachinery Laboratory of Texas A&M University have shown

less than 5% temperature change through the seal, and (b) dynamic pressure measurements inside the honeycomb cells by Ha et al. (1992) indicated that the fundamental frequencies are above audible range (0 to 18 kHz); according to Potter and Foss (1982) flow with that high a frequency content is best approximated as being isothermal.

The solution of the above equations follows the procedure outlined in Childs (1993) and employs a perturbation of the variables P, H, W, and U in the following manner,

$$\begin{aligned} P &= P_0 + \epsilon P_1 \\ H &= H_0 + \epsilon H_1 \\ W &= W_0 + \epsilon W_1 \\ U &= U_0 + \epsilon U_1 \end{aligned} \tag{7}$$

The small parameter ϵ is the perturbed eccentricity ratio about a centered position. For solution, the parameters are nondimensionalized via,

$$p = \frac{P}{P_r} \qquad h = \frac{H}{C_r} \qquad w = \frac{W}{\sqrt{Z_c R_g T}} \qquad u = \frac{U}{\sqrt{Z_c R_g T}}$$
$$z = \frac{Z}{L} \qquad h_d = \frac{H_d}{C_r} \qquad \tau = t\omega \tag{8}$$

The clearance function is,

$$h = h_0 - x(t)\cos\Theta - y(t)\sin\Theta \tag{9}$$

Thus, from Eqs. (7) and (8),

$$\epsilon h_1 = -x\cos\Theta - y\sin\Theta \tag{10}$$

Given the above relation for h_1, the following separation-of-variable solution is assumed for the dependent perturbation variables,

$$\begin{aligned} w_1(z,\tau,\Theta) &= w_{1c}(z,\tau)\cos\Theta + w_{1s}(z,\tau)\sin\Theta \\ u_1(z,\tau,\Theta) &= u_{1c}(z,\tau)\cos\Theta + u_{1s}(z,\tau)\sin\Theta \\ p_1(z,\tau,\Theta) &= p_{1c}(z,\tau)\cos\Theta + p_{1s}(z,\tau)\sin\Theta \end{aligned} \tag{11}$$

This assumed solution established a sinusoidal response of the perturbed variables in the $R\Theta$ direction. The Θ dependancy is eliminated by substituting the relations of Eqs. (10) and (11) into

the first order equations. Equating coefficients of sinΘ and cosΘ terms yields six real equations. Introducing the following complex variables

$$\begin{aligned} \bar{w}_1 &= w_{1c} + jw_{1s} & \bar{u}_1 &= u_{1c} + ju_{1s} \\ \bar{p}_1 &= p_{1c} + jp_{1s} & \epsilon h_1 &= -(x + jy), \end{aligned} \tag{12}$$

reduces the problem to three complex equations in t and z. The time dependancy is eliminated by assuming a precessional seal motion of the form,

$$\epsilon h_1 = -\left(\frac{R_0}{C_r}\right) e^{j\Omega t} = -r_0 e^{jf\tau}, \tag{13}$$

where Ω is the precessional frequency for the rotor, and

$$f = \frac{\Omega}{\omega}. \tag{14}$$

Corresponding separation-of-variables solutions for the perturbed dependent variables are:

$$\bar{w}_1 = w_1 e^{jf\tau} \qquad \bar{u}_1 = u_1 e^{jf\tau} \qquad \bar{p}_1 = p_1 e^{jf\tau} \tag{15}$$

Finally, after substituting the above variables and simplifying, the governing equations are

$$[A(z)]\frac{\mathrm{d}}{\mathrm{dz}}\begin{Bmatrix} w_1 \\ p_1 \\ u_1 \end{Bmatrix} + [B(z,f)]\begin{Bmatrix} w_1 \\ p_1 \\ u_1 \end{Bmatrix} = \left(\frac{r_0}{\epsilon}\right)\{C(z,f)\} \tag{16}$$

The boundary conditions required to solve Eq. (16) can be obtained by applying the perturbations of Eq. (7) to the entrance-loss equation,

$$1 - p(0,\Theta,t) = \frac{(1+\xi)}{2} p(0,\Theta,t) w^2(0,\Theta,t), \tag{17}$$

and exit-recovery equation,

$$p(1,\Theta,t) - p_e = -\frac{(1-\xi_e)}{2} p(1,\Theta,t) w^2(1,\Theta,t), \tag{18}$$

The resultant perturbed expressions are

$$p_1(0) = -\frac{(1+\xi)}{2}[p_1(0)w_0^2(0) + 2p_0(0)w_0(0)w_1(0)], \tag{19}$$

and,

$$p_1(1) = -\frac{(1-\xi_e)}{2}[p_1(1)w_0^2(1) + 2p_0(1)w_0(1)w_1(1)] \tag{20}$$

For choked[3] flow, Eq.(20) is replaced with the requirement that the exit isothermal Mach number be constant which yields the alternative perturbed boundary condition $w_1(1)=0$. The third boundary condition is $u_1(0)=0$. Using a transition-matrix approach the missing boundary conditions at the entrance ($p_1(0)$ and $w_1(0)$) are found which satisfy Eqs. (19) and (20).

Integration of the perturbed pressure for discrete frequencies gives the following perturbation impedances,

$$\begin{aligned} I_r(f) &= -\pi \int_0^1 Re[p_1(f)]dz \\ I_\Theta(f) &= -\pi \int_0^1 Im[p_1(f)]dz \end{aligned} \tag{21}$$

If the force/motion relationship conforms to the model in Eq. (1), least-square curvefits of impedance versus frequency provide:

$$\begin{aligned} I_r(f) &= (K - Mf^2) + cf \\ I_\Theta(f) &= k - Cf \end{aligned} \tag{22}$$

With the force coefficients found, the analysis is complete. The example provided in the following section will demonstrate the inadequacy of Eq. (1) in matching calculated impedances due to an acoustic phenomenon.

Solution Example for a Long (L/D=1) Honeycomb Seal

Test conditions of a honeycomb seal which was tested at the Turbomachinery Laboratory of Texas A&M University are used in this study to define an example calculation. A description of the test facility is provided by Childs et. al. (1985) and Pelletti and Childs (1991).

---

[3]Choked flow implies that the coefficient of the dp_0/dz term is zero and thus, the pressure gradient becomes infinite.

The appropriate input data are:

TABLE 1: Input Data From Test Measurement

Absolute Inlet Pressure	18.3 bar
Absolute Back Pressure	4.4 bar
Inlet Temperature	302 K
Rotational Speed	15960 rpm
Seal Length	0.101 m
Seal Diameter	0.101 m
Seal Clearance	0.2 mm
Honeycomb Cell Width	1.59 mm
Honeycomb Cell Depth	2.29 mm
Inlet Preswirl Ratio	0.0
Entrance Loss Factor	0.5

The required gas properties conform to dry air at the above pressures and temperature.

Figures 3 and 4 show the calculated impedances in the radial and circumferential directions, respectively, with honeycomb cell depth as a parameter. Note that varying h_d will vary the shear stresses; however, here the shear stresses are held constant and h_d is allowed to vary to examine its effect on the impedances. For h_d =0, the models of Eq.(22) are adequate for precessional frequencies that range out to four or five times running speed. For deeper cell depths, the model of Eq. (22) and by inference Eq. (1) cannot describe the force/motion relationship at higher frequencies. More importantly, when the cell depth increases, figure 4 shows resonances, i.e., local minima or maxima, at frequencies that are less than running speed. Clearly, the form of Eq. (1) can not accommodate these resonances; specifically, I_r (f) can not be modeled by a quadratic function, and I_θ(f) can not be modeled by a straight line over the frequency range of interest. The resonances appear because the enclosed cell depth yields a reduction of the effective sonic speed caused by the increased effective volume. An explanation of the phenomenon is provided below.

Acoustic Model

To perform an acoustic study, the perturbed governing equations of flow are reduced in a manner described by Thompson (1988). The reduction of the general perturbation equations to an undamped wave equation entails eliminating the convection terms in the perturbed variables and the shear stress terms. For simplicity, excitation terms due to perturbations in the clearance function

are also neglected. After these simplifications, and using dimensional variables for clarity, the following equations result:

Continuity

$$\frac{\partial}{\partial t}[\rho_1(H_0 + H_d)] + \rho_0 H_0\left(\frac{1}{R}\frac{\partial U_1}{\partial \Theta} + \frac{\partial W_1}{\partial Z}\right) = 0 \tag{23}$$

Axial Momentum

$$-H_0\frac{\partial P_1}{\partial Z} = \rho_0 H_0\frac{\partial W_1}{\partial t} \tag{24}$$

Circumferential Momentum

$$-\frac{H_0}{R}\frac{\partial P_1}{\partial \Theta} = \rho_0 H_0\frac{\partial U_1}{\partial t} \tag{25}$$

Taking the divergence of the combination of Eqs. (24) and (25) and subtracting the result from the partial derivative of Eq. (23) with respect to time yields,

$$(H_0 + H_d)\frac{\partial^2 \rho_1}{\partial t^2} - H_0\nabla^2 P_1 = 0 \tag{26}$$

Simplifying Eq. (26) with the equation of state, Eq. (6), and rearranging provides,

$$\frac{\partial^2 P_1}{\partial t^2} = \left[\frac{Z_c R_g T}{\left(1 + \frac{H_d}{H_0}\right)}\right]\nabla^2 P_1 = c_0^2\nabla^2 P_1, \tag{27}$$

which is the wave equation in terms of perturbed pressure where c_o is the effective acoustic velocity. Note that setting $H_d = 0$ yields $c_0 = \sqrt{Z_c R_g T}$ the isothermal sonic speed (Potter and Foss, 1982).

A comparison of the reduction of c_0 and the resonant frequencies (f_{res}) of figure 4 versus h_d is shown in figure 5. The effective sonic speed is nondimensionalized by the isothermal sonic speed, the resonant frequencies are nondimensionalized by the resonant frequency for h_d=0, and the honeycomb cell depth is nondimensionalized by the operating clearance.

In performing the acoustic analysis, the velocity disturbances, (w_1 and u_1), are assumed to be small in comparison to the sonic speed, i.e., (Mach Number)^2 << 1. However, the flow within a seal can approach the choked condition, Mach Number = 1 at seal exit. Hence, applying the acoustic analysis may be questionable for some conditions. Nevertheless, the acoustic model explains the reduction of the resonant frequencies shown in figure 4. In figure 5, the rate of decrease of the resonant frequencies with increased cell depth is consistent with the rate of decrease of the effective sonic speed from the acoustic solution. This parallel validates the acoustic-model explanation of cell-depth influence on the effective sonic speed and, consequently, on the resonances shown in figure 4.

General-Transfer-Function Model

Because the acoustic resonant frequencies in a honeycomb seal can be less than the operating speed, causing the force/motion model in Eq. (1) to be inadequate, a new model is required for the reaction force components and the following Laplace transform model is proposed:

$$-\begin{Bmatrix} F_x(s) \\ F_y(s) \end{Bmatrix} = \begin{bmatrix} D & E \\ -E & D \end{bmatrix} \begin{Bmatrix} x(s) \\ y(s) \end{Bmatrix} \tag{28}$$

where the form of D and E is to be determined based on the solution of Eq.(16) and the boundary conditions of Eqs. (19) and (20). Following Bolleter et al. (1989), for circular precession the impedances of Eq. (21) in terms of D and E are,

$$\begin{aligned} I_r^+ &= -Re[D] - Im[E] \\ I_r^- &= -Re[D] + Im[E] \\ I_\Theta^+ &= Re[E] - Im[D] \\ I_\Theta^- &= Re[E] + Im[D], \end{aligned} \tag{29}$$

where the "+" power indicates positive excitation frequencies and the "-" power indicates negative excitation frequencies. By adding and subtracting terms in Eq. (29), D and E can be found from the solutions shown in figures 4 and 5.

To obtain analytical expressions for the transfer functions, magnitude and phase plots for D and E are required. Figures 6 and 7 show the magnitude and phase for D and E respectively. The approximate transfer functions resulting from the solutions are:

$$D(s) = \frac{K_D(s + \alpha)}{(s + \beta)}, \tag{30}$$

and,

$$E(s) = \frac{K_E}{(s + \gamma)} \tag{31}$$

For the plots depicted in figures 6 and 7, the terms in the above expressions are approximately; K_D=10.75 MN/m, K_E=2108 MNsec/m, α = -84 rad/sec, β = 600 rad/sec, and γ = 470 rad/sec. Note, that α, β, and γ are less than running speed (~1670 rad/sec). The model format for D and E shown in Eq.(30) and (31) has been found to be appropriate for a wide range of honeycomb seal configurations over a wide range of operating conditions. However, alternative formats may yet be required for some cases; e.g., second-degree denominator polynomials might result from calculated seal impedances.

Figures 8 and 9 show comparisons of measured and predicted magnitude and phase of D and E, respectively for the example case of Table 1. The predicted trends of magnitude and phase for both D and E are verified by the measurements. A large message provided by figures 8 and 9 is that data are required over a much larger frequency range to more adequately verify the predicted model format of Eqs.(30) and (31). Unfortunately, the frequency range of the investigators test rig can not be extended.

Having arrived at valid transfer functions for honeycomb seals, the next question is: How can these models be integrated into rotordynamic analyses?

General Transfer Function Models and Rotordynamic Analyses

Rotordynamic analyses generally involve solution for synchronous response due to imbalance, stability analyses, and nonlinear transient simulations. For synchronous response, the transfer functions of Eqs. (30) and (31) can be converted into running-speed-dependent stiffness and damping coefficients in the same way that people have traditionally modeled foundations, gas bearings, flexibly-supported tilting-pad bearings, etc. The effective (running-speed-dependent) stiffness and damping are found by returning to Equation (28). The bottom (y-direction) term is multiplied by j and added to the top term yielding the complex expresion,

$$-[F_x(s) + jF_y(s)] = [D(s) - jE(s)][x(s) + jy(s)] \tag{32}$$

Next, Equations (30) and (31) are substituted for D(s) and E(s) and s is replaced by $j\Omega$. Dividing the force (left-hand-side) by the motion (extreme right-hand-side) provides the following complex expression,

$$-\frac{[F_x(\Omega) + jF_y(\Omega)]}{[X(\Omega) + jY(\Omega)]} = \frac{K_D[\Omega^2 + \alpha\beta]}{\Omega^2 + \beta^2} - \frac{K_E\Omega}{\Omega^2 + \gamma^2} + j\left[\frac{K_D\Omega(\beta - \alpha)}{\Omega^2 + \beta^2} - \frac{K_E\gamma}{\Omega^2 + \gamma^2}\right] \tag{33}$$

From the above relation, the real part of the right-hand-side provides the effective stiffness and the imaginary part of the right-hand-side, divided by Ω, provides the effective damping, i.e.,

$$K_{eff} = \frac{K_D[\Omega^2 + \alpha\beta]}{\Omega^2 + \beta^2} - \frac{K_E\Omega}{\Omega^2 + \gamma^2}$$
$$C_{eff} = \frac{K_D[\beta - \alpha]}{\Omega^2 + \beta^2} - \frac{K_E\gamma}{\Omega(\Omega^2 + \gamma^2)} \tag{34}$$

Figures 10 and 11 show the predicted effective stiffness and damping, in dimensional units, for the impedances shown in figures 3 and 4, respectively. Note, that increased cell depth decreases the effective damping. At low frequencies (f<0.15) the effective damping is negative because of a relatively large cross-coupled stiffness ($K_E\gamma$) term.

An approximate and iterative stability analysis can be performed by selecting a frequency, e.g., running speed, calculating equivalent stiffness and damping coefficients for this speed from Equation (34), and then calculating damped eigenvalues. The natural frequency of the mode that is of concern with respect to stability can then be used to recalculate equivalent stiffness and damping coefficients, and the cycle is repeated until convergence is achieved between the assumed frequency and the imaginary part of the damped eigenvalue of interest. Aside from the iterative nature of this approach, an additional drawback is that the results obtained for damped eigenvalues at other than the converged natural frequency are not correct.

Beyond the weight of past practice, there is no compelling reason to continue forcing models to conform to a stiffness, damping, and inertia format. Conventional linear systems analysis (e.g., Melsa and Shultz, 1969) provides a quite adequate foundation for handling the type of reaction-force transfer function models provided by Eqs. (30) and (31). The approach can be demonstrated by a Jeffcott model formulation. Applying the reaction-force model of Eqs.(28), (30), and (31) to the mass of a Jeffcott model would yield

$$(m_r s^2 + c_r s + k_r)\,x(s) + \frac{K_D\,(s+\alpha)\,x(s)}{(s+\beta)} + \frac{K_E\,y(s)}{(s+\gamma)} = F_x(s)$$
$$(m_r s^2 + c_r s + k_r)\,y(s) - \frac{K_E\,x(s)}{(s+\gamma)} + \frac{K_D\,(s+\alpha)\,y(s)}{(s+\beta)} = F_y(s) \tag{35}$$

in the Laplace domain. By defining the new variables

$$x_1(s) = \frac{K_D\,(s+\alpha)\,x(s)}{(s+\beta)}, \quad y_2(s) = \frac{K_E\,y(s)}{(s+\gamma)}$$
$$x_2(s) = \frac{K_E\,x(s)}{(s+\gamma)}, \quad y_1(s) = \frac{K_D(s+\alpha)\,y(s)}{(s+\beta)} \qquad (36)$$

The following more useful Laplace-domain model is obtained

$$\begin{aligned}
(m_r s^2 + c_r s + k_r)\,x(s) + x_1(s) + y_2(s) &= F_x(s)\\
(s+\beta)\,x_1(s) - K_D\,(s+\alpha)\,x(s) &= 0\\
(s+\gamma)\,y_2(s) - K_E\,y(s) &= 0\\
(m_r s^2 + c_r s + k_r)\,y(s) - x_2(s) + y_1(s) &= F_y(s)\\
(s+\gamma)\,x_2(s) - K_E\,x(s) &= 0\\
(s+\beta)\,y_1(s) - K_D(s+\alpha)\,y(s) &= 0
\end{aligned} \qquad (37)$$

Note that while the original Jeffcott model has a fourth-order characteristic equation in s, Eq. (37) yields an eight-order polynomial. Modeling the seal forces with frequency-dependent stiffness, damping, and inertia terms hides the degrees of freedom which are contained in the transfer-function denominators of $\boldsymbol{D}$ and $\boldsymbol{E}$.

A time-domain, state-variable format for the model of Eq.(37) is

$$\begin{aligned}
\dot{x} - v_x &= 0\\
m_r\dot{v}_x + c_r\,v_x + k_r\,x + x_1 + y_2 &= F_x(t)\\
\dot{x}_1 + \beta\,x_1 - K_D\,v_x - \alpha\,K_D\,x &= 0\\
\dot{y}_2 + \gamma\,y_2 - K_E\,y &= 0\\
\dot{y} - v_y &= 0\\
m_r\dot{v}_y + c_r\,v_y + k_r\,y - x_2 + y_1 &= F_y(t)\\
\dot{x}_2 + \gamma\,x_2 - K_E\,x &= 0\\
\dot{y}_1 + \beta\,y_1 - K_D\,v_y - \alpha\,K_D\,y &= 0
\end{aligned} \qquad (38)$$

Again, this is an eight-order system versus the fourth-order system of the original Jeffcott model. Eq.(38) can be stated in matrix form as

$$[G_1]\,(\dot{z}) + [G_2]\,(z) = (f)$$

or

$$(\dot{z}) + [G]\,(z) = [A]^{-1}\,(f)\ ,\ [G] = [G_1]^{-1}\,[G_2]$$

The eigenvalues for $[G]$ can be calculated directly (versus iteratively), e.g., using the QR algorithm.

Due to space limitations, the following simplified eigenvalue analysis is provided as insight for the application of a transfer-function honeycomb seal force/motion model to the Jeffcott rotor. For this analysis, the Jeffcott rotor is assigned: (a) a mass of 100 kg, (b) a natural frequency of 0.75ω, (c) viscous damping corresponding to 2% of critical damping, (d) the calculated values of K_D, K_E, α, β, and γ for the input of Table 1 over a range of h_d from 0 to 5. Eigenvalue solutions indicate that the overall system critical damping, for forward precession, decreases from 10.4%, at h_d=0, to 5.1%, at h_d=5.

The Jeffcott model used in the above demonstration is obviously simpler than a general rotordynamics model involving stiffness, damping, and inertia matrices. However, the state-variable formulation demonstrated above can be readily extended to general rotor models, and has previously been employed for rotors on magnetic bearings, Palazzolo et al. (1993).

Discussion and Conclusions

The analysis presented demonstrates that the cells of honeycomb act to reduce the effective acoustic velocity of flow through the seal, which can drop seal acoustic natural frequencies into the frequency range of interest for rotordynamics. In these circumstances, the conventional (frequency-independent) rotordynamic-coefficient model is invalid, and a more general transfer-function model is required. The transfer functions calculated here are a lead-lag function for the direct term and a simple lag function for the cross-coupled term.

Given that the lowest axial acoustic mode natural frequency is approximately $\pi c_o/L$ and the lowest circumferential mode frequency is approximately c_o/R where c_o is the effective acoustic velocity, conventional, (frequency-independent) models may work for short seals with small diameters and (comparatively) low speeds. For all other cases, general transfer functions should be employed. General transfer-function models for honeycomb seals require nonconventional rotordynamics tools for stability and/or transient analysis. For synchronous response due to imbalance, running-speed-dependent stiffness and damping coefficients can be used with conventional analyses.

A reasonable question to consider at this point is: Does the new model fit test data better than the old model? Unfortunately, the answer is inconclusive with respect to the authors' test data,

because our feasible frequency range of excitation (40 to 70 Hz) is too restricted. Test data are needed from low frequencies out to frequencies in excess of running speed to verify the predictions of the present analysis. The test apparatus described by Childs and Hale (1994) for testing hydrostatic bearings has the required frequency range and has been modified to test liquid annular seals, Lindsey and Childs (1995). The test rig is currently being considered for future air-seal testing.

References

Bolleter, U., Leibundgut, E., Stürchler, R., and McCloskey, T., (1989), "Hydraulic Interaction and Excitation Forces of High Head Pump Impellers," in *Pumping Machinery-1989*, Proceedings of the Third Joint ASCE/ASME Mechanics Conference, La Jolla, CA, pp. 187-194.

Childs, D., Nelson, C., Nicks, C., Scharrer, J., Elrod, D., and Hale, K., (1986), "Theory versus Experiment for the Rotordynamic Coefficients of Annular Gas Seals: Part I-Test Facility and Apparatus," *ASME Journal of Tribology*, **108**, pp. 426-432.

Childs, D., (1993), *Turbomachinery Rotordynamics: Phenomena, Modeling, and Analysis*, John Wiley & Sons, Inc., New York, NY, pp. 243-248.

Childs, D., and Hale, K., (1994), "A Test Apparatus and Facility to Identify the Rotordynamic Coefficients of High-Speed Hydrostatic Bearings," *ASME Trans., Journal of Tribology,* April, Vol. 116, pp. 337-344.

Elrod, D., Nelson, C., and Childs, D., (1989), "An Entrance Region Friction Factor Model Applied to Annular Seals Analysis: Theory vs. Experiment for Smooth and Honeycomb Seals," *ASME Journal of Tribology*, **111**, pp. 337-343

Elrod, D., Childs, D., and Nelson, C., (1990), "An Annular Gas Seal Analysis Using Empirical Entrance and Exit Region Friction Factors," *ASME Journal of Tribology*, **112**, No. 2, pp. 254-258.

Ha, T., W., Morrison, G., L., and Childs, D., (1992), "Friction-Factor Characteristics for Narrow Channels with Honeycomb Surfaces," *ASME Trans., Journal of Tribology*, **114**, pp. 714-721

Ha, T., and Childs, D., (1994), "Annular Honeycomb-Stator Turbulent Gas Seal Analysis Using New Friction-Factor Model Based on Flat Plate Tests," *ASME Journal of Tribology*, **116**, pp. 352-360

Hirs, G., (1973), "A Bulk-Flow Theory for Turbulence in Lubricating Films," *ASME Journal of Lubrication Technology*, pp. 137-146.

Lindsey, W.T., and Childs, D.W., (1995), "The Effects of Converging and Diverging Axial Taper on the Rotordynamic Coefficients of Liquid Annular Pressure Seals: Theory Versus Experiment," accepted for presentation at the 1995 ASME Vibration Conference, Boston, Mass., September.

Melsa, J., and Shultz, D., (1969), *Linear Control Systems,* McGraw Hill Book Co., New York, NY.

Nelson, C., (1984), "Analysis for Leakage and Rotordynamic Coefficients of Surface-Roughened Tapered Annular Gas Seals," *ASME Journal of Engineering for Gas Turbines and Power*, **106**, pp. 927-934

Nelson, C., (1985), "Rotordynamic Coefficients for Compressible Flow in Tapered Annular Seals," *ASME Journal of Tribology*, **107**, pp. 318-325.

Palazzolo, A.B., Tang, P., Brown, G., DiRusso, E., and Kascak, A., (1993), "An Electromechanical Simulation Method for Active Vibration Control of a Magnetic Bearing Supported Rotor," 93-GT-382, presented at the International Gas Turbine and Aeroengine Congress and Exposition, Cincinnati, Ohio, May 24-27.

Pelletti, J, and Childs, D., (1991), "A Comparison of Experimental Results and Theoretical Predictions for the Rotordynamic Coefficients of Short (L/D=1/6) Labyrinth Seals," proceedings, *1991 ASME Design Technical Conference,* September, DE-Vol-35, pp. 69-76.

Potter, M., and Foss, J., (1982), *Fluid Mechanics*, Great Lakes Press, Inc., Okemos, MI, pp. 477-481.

Scharrer, J., (1989), discussion of the paper, "Annular Honeycomb Seals: Test Results for Leakage and Rotordynamic Coefficients; Comparisons to Labyrinth and Smooth Configurations," by Childs et al., *ASME Journal of Tribology*, **111**, pp. 293-301

Sorokes, J., Kuzdzal, M., Sandberg, M., and Colby, G., (1994), "Recent Experiences in Full Load Full Pressure Shop Testing of a High Pressure Gas Injection Centrifugal Compressor," *Proceedings of the Twenty-Third Turbomachinery Symposium*, The Turbomachinery Laboratory, Texas A&M University, College Station, Texas, pp. 3-17.

Thompson, P., (1988), *Compressible-Fluid Dynamics*, pp. 155-234.

Zeidan, F., Perez, R., and Stephenson, E., (1993), "The Use of Honeycomb Seals in Stabilizing Two Centrifugal Compressors," *Proceedings of the Twenty-Second Turbomachinery Symposium*, The Turbomachinery Laboratory, Texas A&M University System, College Station, Texas, pp. 3-15.

Nomenclature

Roman

c_0	Effective sonic speed (L/t)
c_r	Rotor damping (Ft/L)
C, c	Direct and cross-coupled damping (Ft/L)
C_r	Seal inlet clearance (L)
D	Direct impedance (F/L)
e	Precession amplitude (L)
E	Cross-coupled impedance (F/L)
f	Ω/ω Nondimensional excitation frequency
f_{res}	Nondimensional resonant frequency
F_X, F_X	Seal reaction forces (F)
H	Seal clearance (L)
H_d	Honeycomb cell depth (L)
h_d	H_d/H Nondimensional honeycomb cell depth
I_r, I_θ	Radial and tangential impedances (F/L)
j	$\sqrt{-1}$
K, k	Direct and cross-coupled stiffness (F/L)
K_D	Direct transfer function constant (F/L)
K_E	Cross-coupled transfer-function constant (FT/L)
k_r	Rotor stiffness (F/L)
L	Seal length (L)
M	Direct added mass (M)
m_r	Rotor mass (M)
p_e	P_S/P_R Ratio of absolute sump to reservoir pressures
P	Pressure (F/L^2)
P_R	Reservoir (upstream, inlet) pressure (F/L^2)
P_S	Sump (downstream, back) pressure (F/L^2)
r_0	Excitation amplitude (L)
R	Seal radius (L)
R_g	Gas constant (FL/MT)
s	Complex variable for Laplace transforms (1/t)
t	Time (t)
T	Fluid bulk temperature (T)
U	Circumferential bulk fluid velocity (L/t)
V	Radial bulk fluid velocity (L/t)
W	Axial bulk fluid velocity (L/t)
x, y	Seal/rotor relative displacement (L)
$\dot{x}$, $\dot{y}$	Seal/rotor relative velocities (L/t)
$\ddot{x}$, $\ddot{y}$	Seal/rotor relative accelerations (L/t^2)
x, y	Frequency domain seal/rotor relative displacement (L/t)
Z	Axial coordinate (L)
Z_c	Gas compressibility factor

Greek

α, β, γ	Transfer function frequencies (1/t)
ϵ	Perturbation in eccentricity ratio
Θ	Circumferential coordinate
ρ	Fluid density (M/L^3)
τ	Shear stress (F/L^2)
ξ, ξ_e	Entrance loss and exit recovery factors
ω	Rotor rotational frequency (1/t)
Ω	Rotor precession frequency (1/t)

Subscripts

0, 1	Zeroth and first order
rz, rΘ	Rotor axial and circumferential
sz, sΘ	Stator axial and circumferential
r, Θ	Radial and circumferential

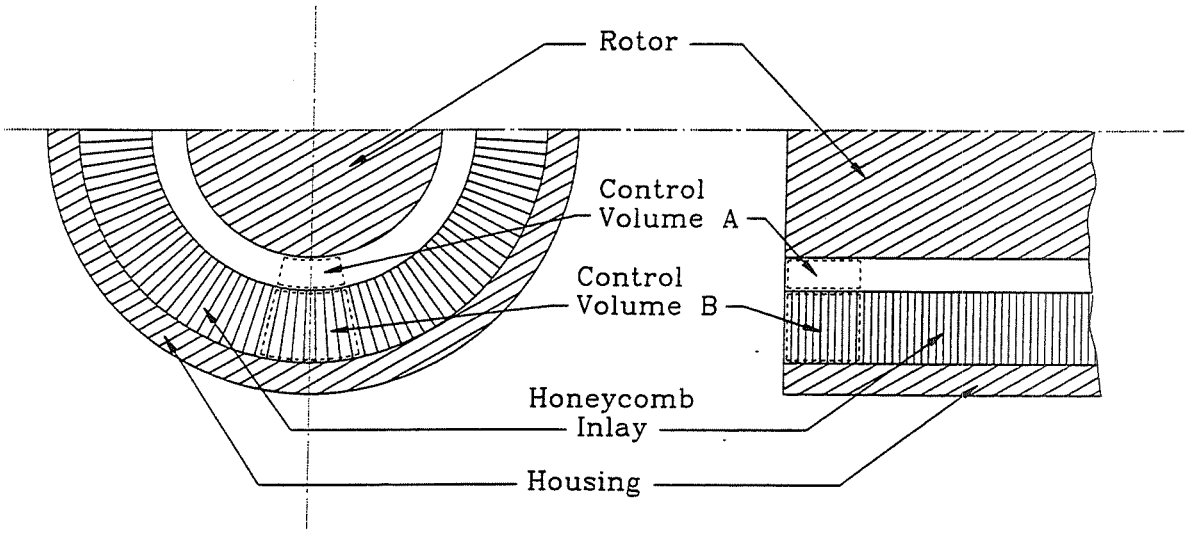

Figure 1 Control volume locations within seal.

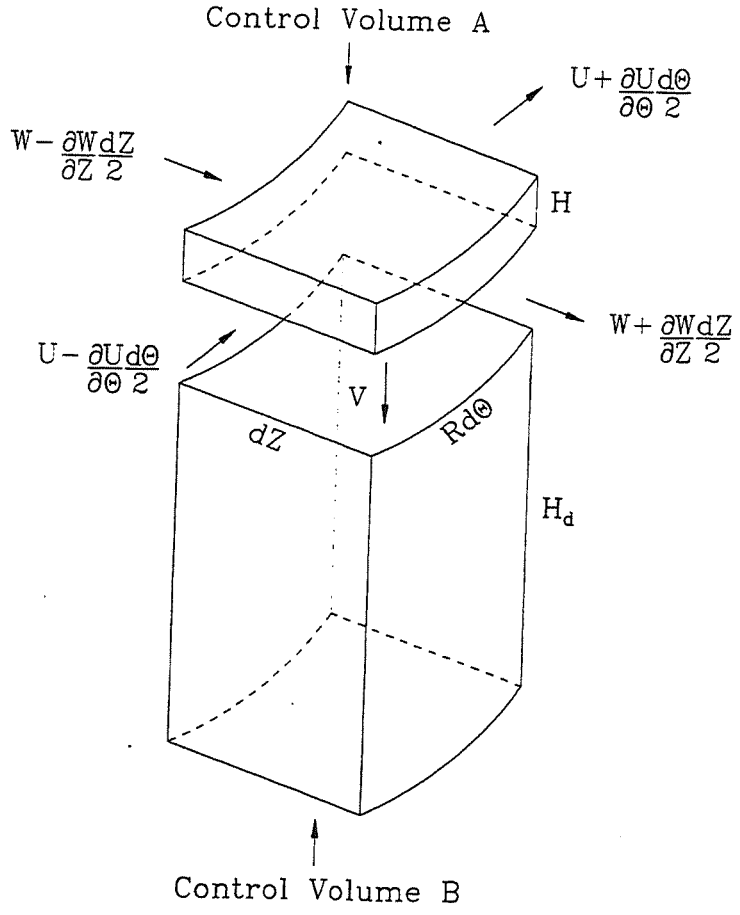

Figure 2 Flow in and out of control volumes

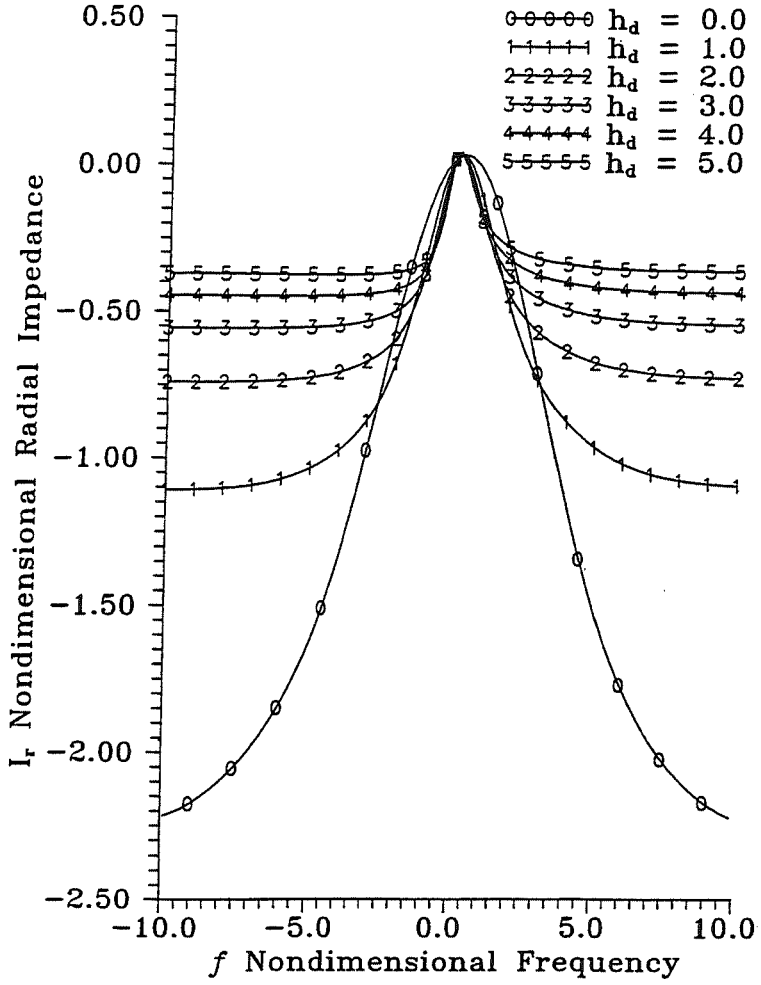

Figure 3 Radial impedance versus frequency

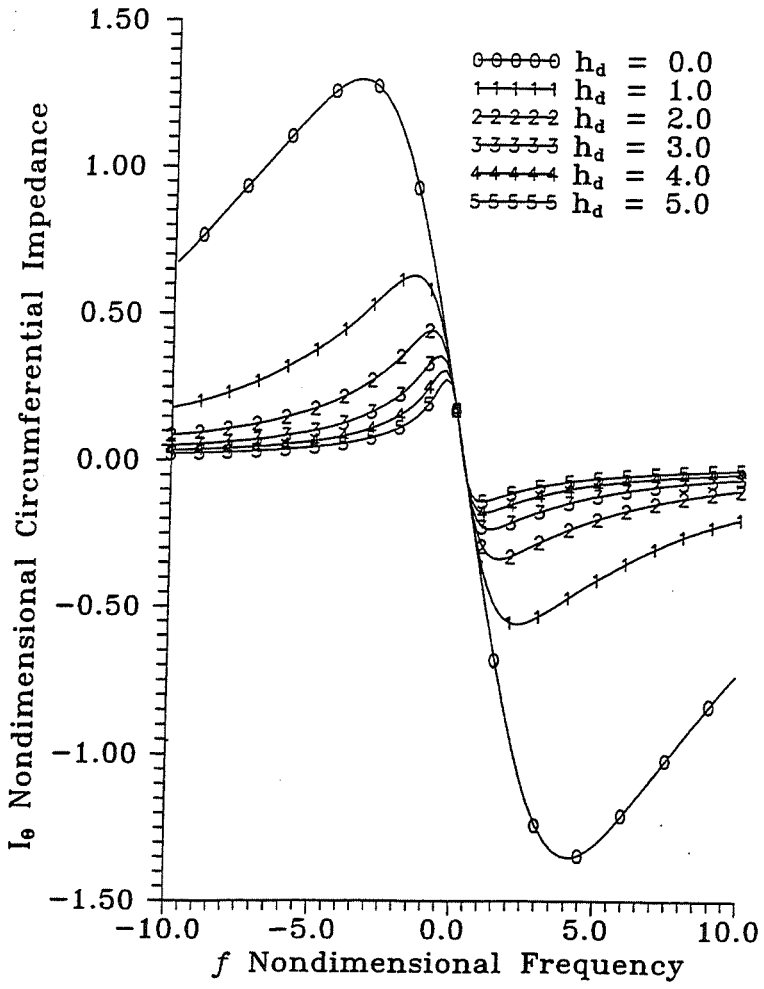

Figure 4 Tangential impedance versus frequency

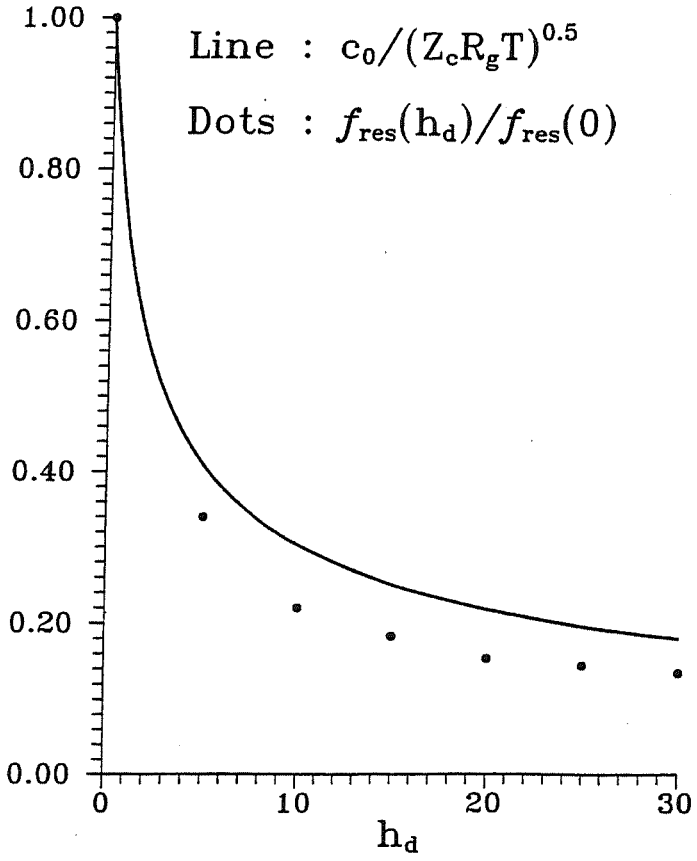

Figure 5 Effective sonic speed versus honeycomb cell depth

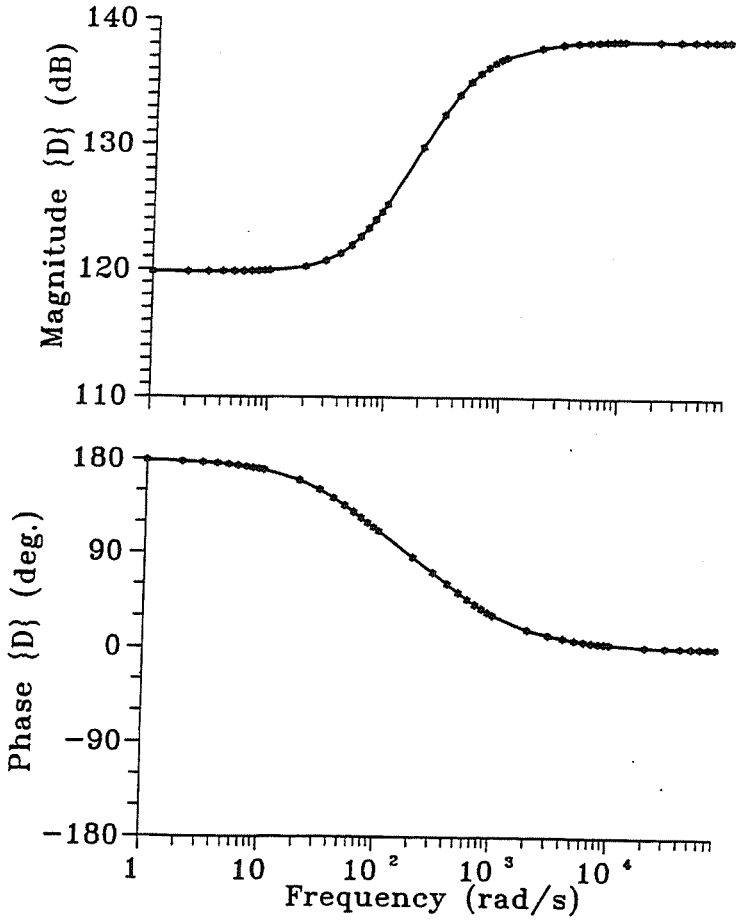

Figure 6 Magnitude and phase of calculated direct impedance versus frequency

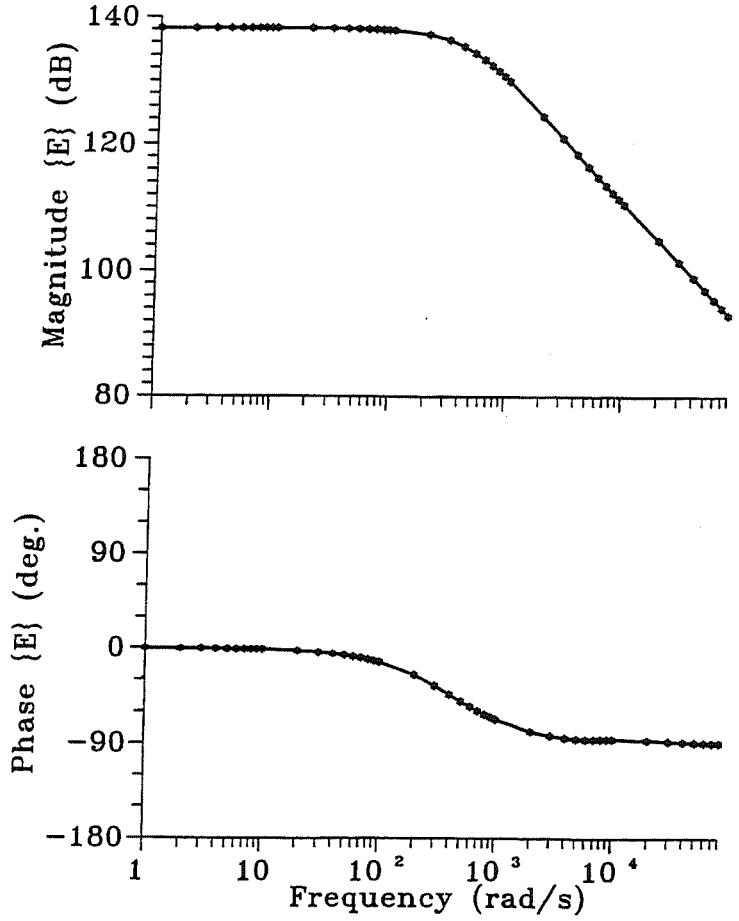

Figure 7 Magnitude and phase of calculated cross-coupled impedance versus frequency

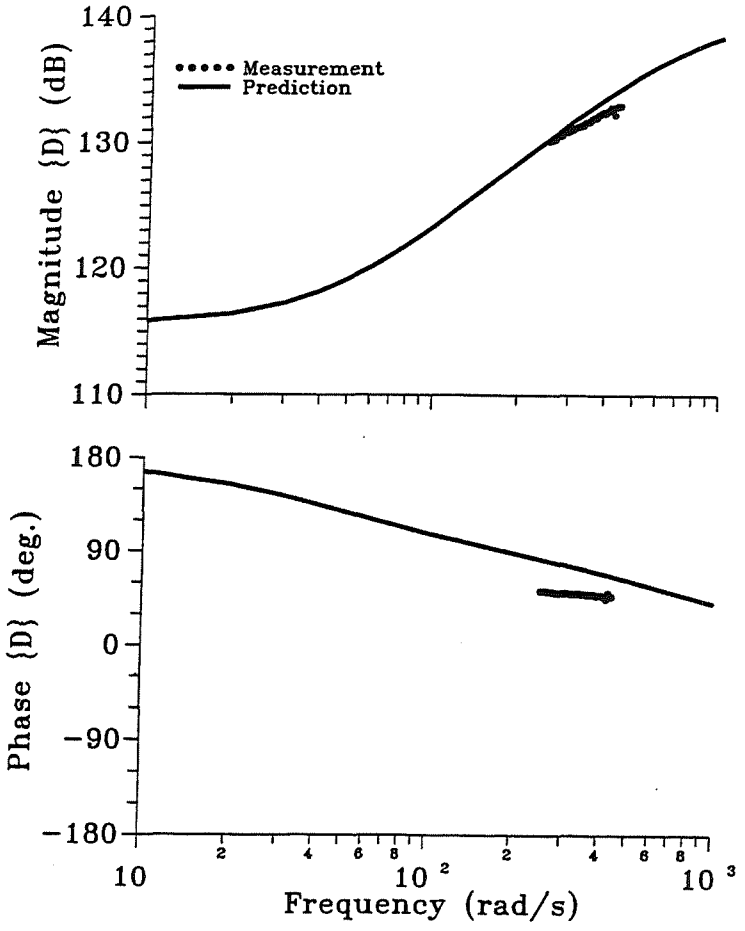

Figure 8 A comparison of measured (dots) and predicted (thin line) magnitude and phase for direct impedance **D**.

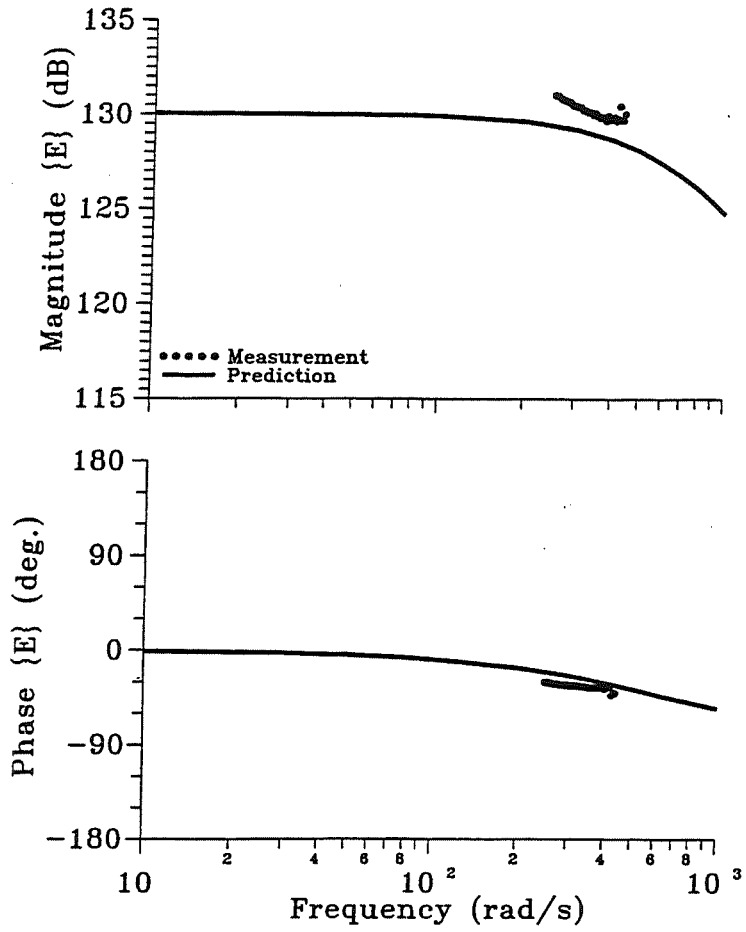

Figure 9 A comparison of measured (dots) and predicted (thin line) magnitude and phase for cross-coupled impedance **E**

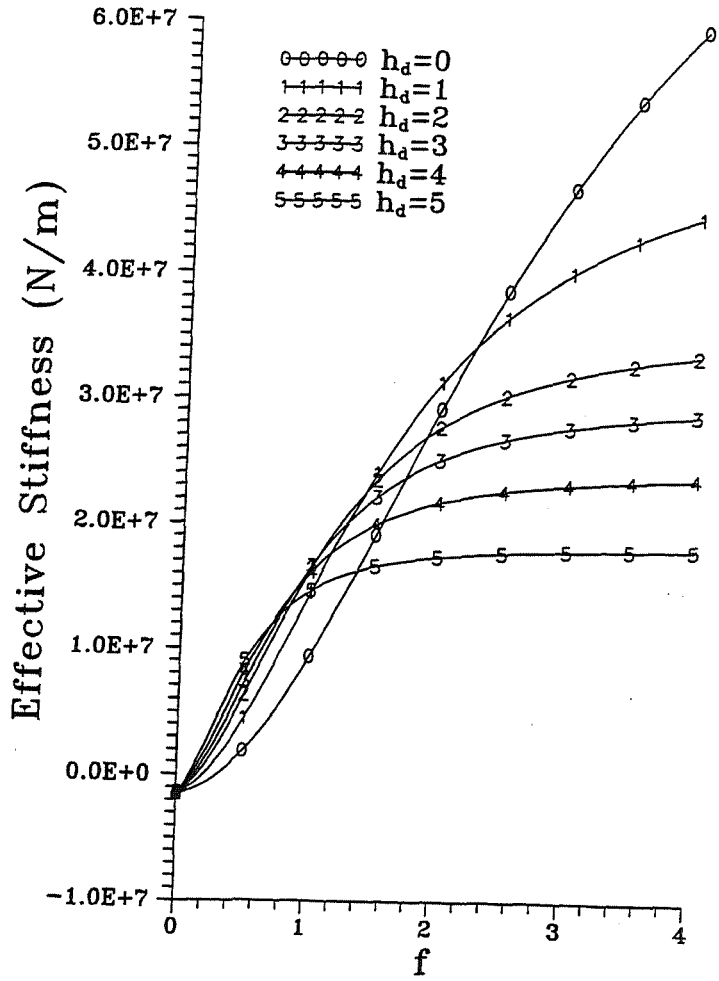

Figure 10 Effective stiffness versus frequency

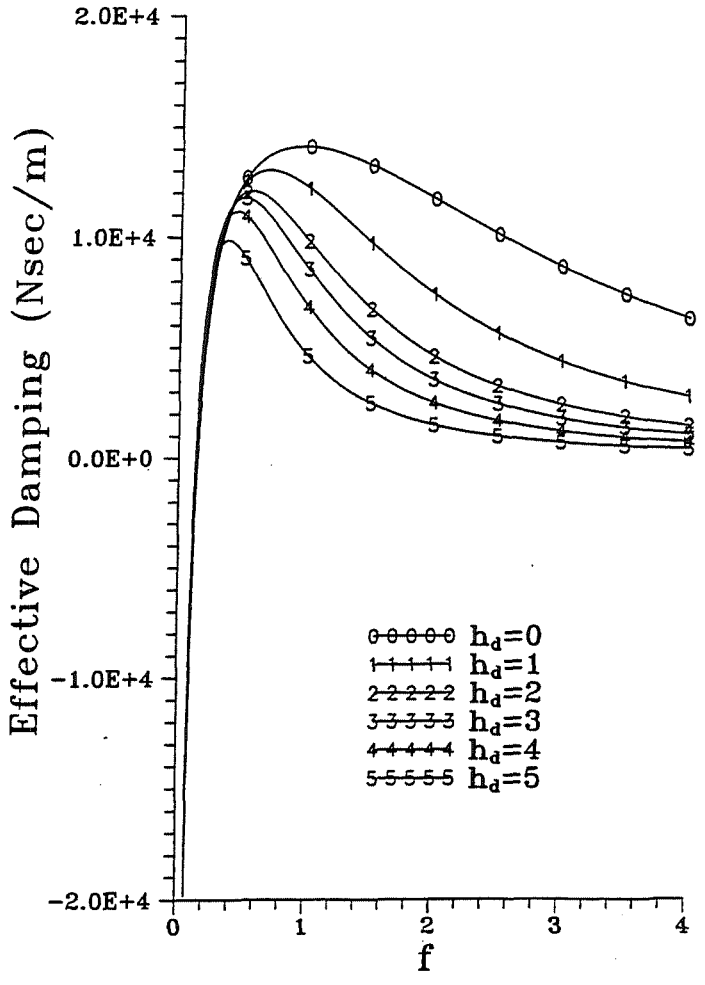

Figure 11 Effective damping versus frequency

A COMPARISON OF EXPERIMENTAL ROTORDYNAMIC COEFFICIENTS AND LEAKAGE CHARACTERISTICS BETWEEN HOLE-PATTERN GAS DAMPER SEALS AND A HONEYCOMB SEAL

Zeping Yu
Boeing
Rocketdyne Division
Canoga Park, California

and

Dara Childs
Texas A&M University
College Station, Texas

ABSTRACT

Honeycomb annular seals are an attractive design alternative due to their superior static and dynamic performance. However, their implementation in industrial practice has been delayed by the following characteristics: a) manufacturing time can be appreciable, and b) they can seriously damage the shaft if rubbing occurs. To minimize these problems, "hole-pattern" gas damper seals, which are formed by simply drilling holes into an annular smooth seal, were manufactured and tested. The hole-pattern damper seal stator can be made of high-strength plastic materials which are less likely to damage a shaft during rubbing. The experimental results presented demonstrate that, compared to a honeycomb seal, a hole-pattern damper seal with 3.18 mm hole diameters and a high percentage of hole surface has achieved: (a) an average of 12 percent reduction in leakage rate, and (b) considerably higher effective damping, especially under high speeds and low inlet pressure ratio conditions.

NOMENCLATURE

A	Whirl amplitude (mm)
A_X, A_Y	Fourier transformed absolute acceleration of stator housing (m/s^2)
C, c	Direct and cross-coupled damping coefficients (N-s/m)
C_r	Seal clearance (mm)
d	Hole-pattern damper seal hole diameter (mm)
D	Diameter of seal (mm)
D_X, D_Y	Fourier transformed motion of the stator relative to the rotor (m)
f_{SX}, f_{SY}	Measured stator housing reaction forces (N)
F_{SX}, F_{SY}	Fourier transformed components of seal reaction forces (N)
H_{XX}, H_{XY}	Direct and cross-coupled impedance functions (N/m)
K, k	Direct and cross-coupled stiffness (N/m)
M, m	Direct and cross-coupled inertia (kg)
$\dot{m}$	Mass flow rate (kg/s)

M_S	Mass of stator housing (kg)
P_b	Back pressure (bar)
P_r	Inlet (reservoir) pressure (bar)
P_{ra}	P_b/P_r, absolute pressure ratio
$\dot{Q}$	Volumetric flow rate (m^3/s)
R	Rotor radius (m)
u_0	$U_{\theta 0}/R\omega$, inlet circumferential velocity ratio
$U_{\theta 0}$	Inlet circumferential velocity (m/s)
X, Y	Displacement of the stator relative to the rotor (m)
$\ddot{X}_S$, $\ddot{Y}_S$	Absolute acceleration of stator housing (m/s^2)
γ	Area fraction factor introduced in equation (7)
ω	Rotor angular velocity (rad/s)
Ω	Rotor precession frequency (rad/s)

INTRODUCTION

Annular pressure seals with small clearance are employed in turbomachines such as pumps, compressors, or gas-turbine engines between stationary and rotating elements to limit the leakage of fluid from different pressure stages. However, high pressures and tight clearances within annular seals can produce reaction forces on the rotor which have great impact both on rotordynamic stability and response.

If seal relative motion is small and is about a centered position within an annular seal, the reaction-force model in equation (1) applies, Childs (1993).

$$-\begin{Bmatrix} F_x \\ F_y \end{Bmatrix} = \begin{bmatrix} K & k \\ -k & K \end{bmatrix} \begin{Bmatrix} X \\ Y \end{Bmatrix} + \begin{bmatrix} C & c \\ -c & C \end{bmatrix} \begin{Bmatrix} \dot{X} \\ \dot{Y} \end{Bmatrix} + M \begin{Bmatrix} \ddot{X} \\ \ddot{Y} \end{Bmatrix} \qquad (1)$$

Here, F_x and F_y are the components of reaction forces acting on the rotor, X and Y define the components of the seal-rotor displacements relative to the stator, and the rotordynamic coefficients K, k, C, c, M are the direct stiffness, cross-coupled stiffness, direct damping, cross-coupled damping, and direct added mass coefficients, respectively.

Figure 1 illustrates the rotordynamic force components acting on a rotor which is whirling in the direction of rotation at a constant angular frequency ω and amplitude A. In this figure, $(K - M\omega^2 + c\omega)A$ is the radial force component which acts toward the center of the rotor. This force component is defined by the direct stiffness K, the added mass M, and the cross-coupled damping c. A sufficient change of K can cause a shift of a critical speed. However, the radial force component has generally been considered to be small for gas seals and typically has a negligible influence on rotordynamics.

Returning to Figure 1, $(k - C\omega)A$ is the tangential force , that changes with the cross-coupled stiffness k and direct damping C. This component of force is most responsible for the impact of seals on rotordynamic response and rotordynamic stability. To take both direct damping C and cross-coupled stiffness k into consideration, effective damping $C_{eff} = C(1 - k/C\omega)$ is a useful parameter to evaluate and compare rotordynamic performance for seals.

Realizing the importance of seal forces, various types of seals have been designed to achieve better rotordynamic and leakage control performance. From a rotordynamic view point, honeycomb seals have shown very promising characteristics. They provide considerably higher effective direct damping, lower cross-coupled stiffness, and better leakage control than see-through labyrinth seals. In practice, honeycomb seals have been used to eliminate a stability problem in the High Pressure Oxygen Turbopump (HPOTP) of the Space Shuttle Main Engine (SSME), Scharrer (1989). In centrifugal compressors, honeycomb seals have been used to eliminate unwanted vibrations, Zeidan et al. (1993), and Sorokes et al. (1994). However, honeycomb seals can have the following disadvantages:

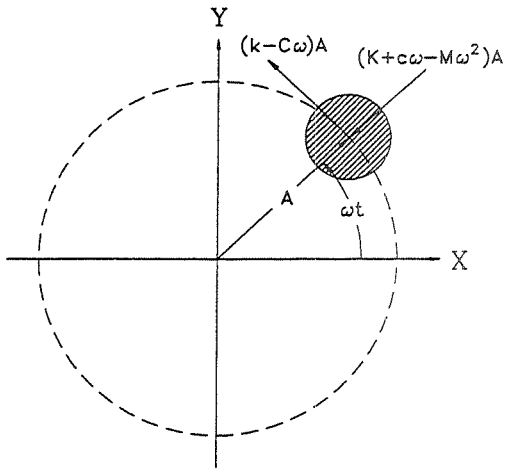

Figure 1 Forces on a whirling rotor

a) On occasions, their comparatively long manufacturing time have prevented their use in retrofits,

b) They can seriously damage the shaft if rubbing occurs.

As an alternative to honeycomb seals, hole-pattern damper seals are considered in this study. Figure 2 illustrates geometric differences between honeycomb and hole-pattern damper seals. Compared to a honeycomb seal, the hole-pattern damper seal has a much simpler surface configuration, which is formed by simply drilling holes into an annular smooth seal stator.

The "damper seal" concept for liquid seals was originated by Von Pragenau (1982) who reasoned that a rough-stator/smooth-rotor combination would yield a lower, asymptotic, circumferential velocity than a smooth rotor, thus yielding lower cross-coupled stiffness values. Childs and Kim (1986) conducted tests for nine hole-pattern damper liquid seals with various percentage of surface areas in holes. Their tests used roughened stators and a smooth rotor, and showed that an optimum configuration of hole-pattern takes up about 34 percent coverage of holes and yielded a 37 percent increase of direct damping, while reducing leakage by 46 percent as compared to a smooth seal. A subsequent series of tests were done by Childs et al. (1990) at smaller clearances, and showed approximately the same damping performance for hole-pattern damper seals and smooth seals at the same clearances, about 20 percent lower stiffness values, and one third lower leakage. However, hole-pattern damper gas seals have not been tested before.

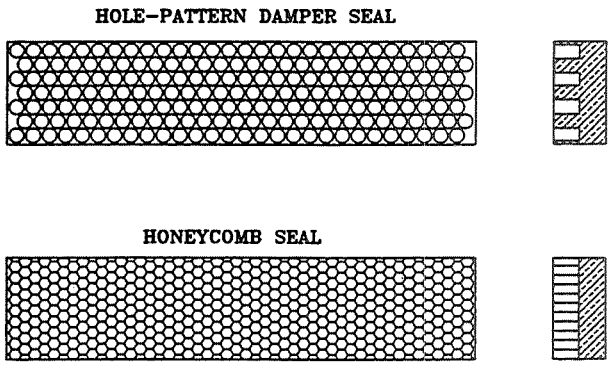

Figure 2 The surface configuration for hole-pattern damper and honeycomb seal

TEST APPARATUS AND EXPERIMENTAL SET UP

The test apparatus utilizes air as the test fluid and consists of a rotor shaft which is suspended (pendulum fashion) from an upper, rigidly-mounted, pivot shaft as illustrated in Figure 3. This configuration allows horizontal static and dynamic motion of the rotor, while an eccentric cam within the pivot shaft provides static vertical position capability for the rotor; Childs et al. (1986a), Pelletti (1990).

The rotor is excited horizontally by a hydraulic shaker head, which acts on the rotor shaft housing. The excitation frequency range is from 40 to 70 Hz. The rotor excitation produces seal reaction forces which are measured by three load cells which support the seal stator in a trihedral fashion. Two accelerometers mounted in the X and Y directions are used to subtract the forces on the stator housing due to external residual vibrations.

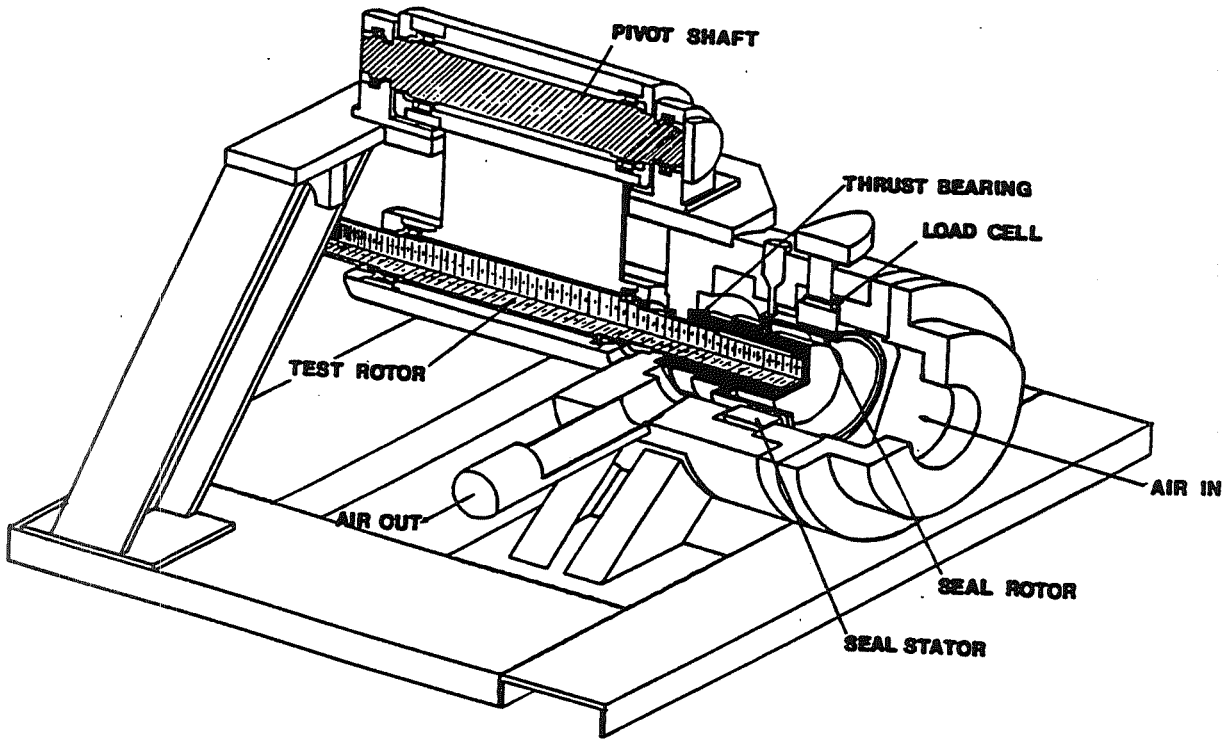

Figure 3 Test apparatus

As Figure 4 illustrates, high pressure air enters the test section from one side of the rig and passes a pre-swirl guide vane before entering the test seal. Inlet pressure is manually regulated by a control valve

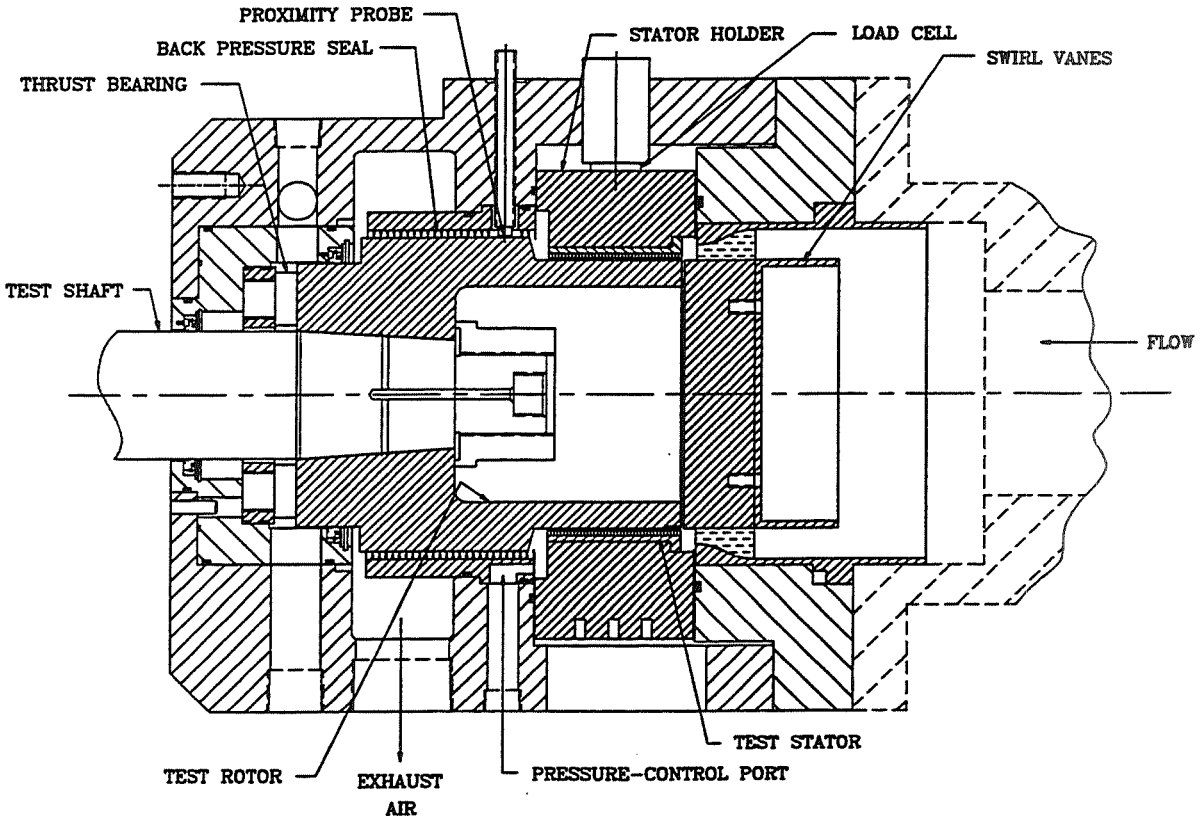

Figure 4 Cross section of test rig

located upstream of the test section. The seal pressure ratio cross the seal, defined as absolute exit pressure divided by absolute inlet pressure, is controlled by a back-pressure seal with inlet and exhaust ports. Air is injected (or withdrawn) through the ports to decrease (or increase) the pressure drop across the seal.

The test apparatus yields three inlet swirl velocities. Inlet swirl is controlled by the two swirl vanes illustrated in Figure 5 plus a set of straight vanes. The calculation of inlet circumferential velocity is initiated by dividing the volumetric flow rate $\dot{Q}$, measured with a turbine flow meter, by the sum of the area which are normal to the exit vane angles.

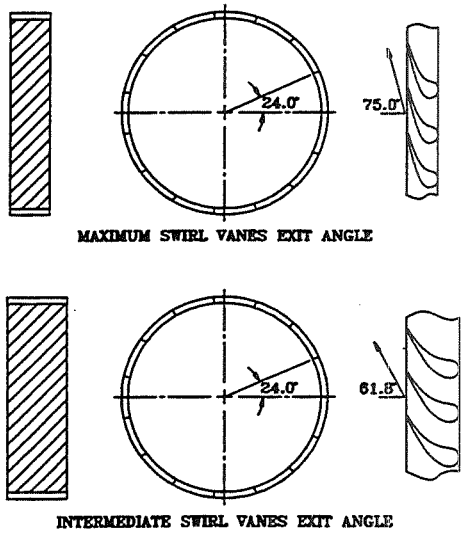

Figure 5 Swirl vanes exit angles

Rotordynamic-Coefficient Identification

The equation of motion for the seal stator housing is,

$$\begin{Bmatrix} f_{SX} - M_S\ddot{X}_S \\ f_{SY} - M_S\ddot{Y}_S \end{Bmatrix} = \begin{bmatrix} K & k \\ -k & K \end{bmatrix} \begin{Bmatrix} X \\ Y \end{Bmatrix} + \begin{bmatrix} C & c \\ -c & C \end{bmatrix} \begin{Bmatrix} \dot{X} \\ \dot{Y} \end{Bmatrix} + M \begin{Bmatrix} \ddot{X} \\ \ddot{Y} \end{Bmatrix} \tag{2}$$

where M_S is the stator housing mass, and f_{SX} and f_{SY} are the measured reaction forces on the stator housing. The acceleration components of the housing, measured by the accelerometers, are denoted by $\ddot{X}_S$ and $\ddot{Y}_S$.

An analog circuit is used to generate $f_{SX} - M_S\ddot{X}_S$ and $f_{SY} - M_S\ddot{Y}_S$ from measured reaction-forces and acceleration components. The Fourier transform of equation (2) is represented by

$$\begin{Bmatrix} F_{SX} - M_S A_X \\ F_{SY} - M_S A_Y \end{Bmatrix} = \begin{bmatrix} H_{XX} & H_{XY} \\ -H_{XY} & H_{XX} \end{bmatrix} \begin{Bmatrix} D_X \\ D_Y \end{Bmatrix}, \tag{3}$$

where,

$$\begin{aligned} H_{XX} &= (K - \omega^2 M) + j\omega C \\ H_{XY} &= k + j\omega c \end{aligned} \tag{4}$$

Rearranging equation (3) produces the following relation,

$$\begin{Bmatrix} F_{SX} - M_S A_X \\ F_{SY} - M_S A_Y \end{Bmatrix} = \begin{bmatrix} D_X & D_Y \\ D_Y & -D_X \end{bmatrix} \begin{Bmatrix} H_{XX} \\ H_{XY} \end{Bmatrix} \tag{5}$$

from which H_{XX} and H_{XY} are solved and yield the following impedance relations,

$$\begin{aligned} H_{XX} &= \frac{(F_{SX} - M_S A_X)D_X - (F_{SY} - M_S A_Y)D_Y}{D_X^2 + D_Y^2} \\ H_{XY} &= \frac{(F_{SX} - M_S A_X)D_Y - (F_{SY} - M_S A_Y)D_X}{D_X^2 + D_Y^2} \end{aligned} \tag{6}$$

Equation (4) shows that the real components of the above impedances, H_{XX} and H_{XY}, contain the stiffness coefficients, while the imaginary component contains the damping coefficients. Thus, the rotordynamic coefficients are calculated via a least-squares curve fit of the real and imaginary components of H_{XX} and H_{XY}.

Test Parameters

The test rig can be used to study the effects of the following six independent test parameters on the rotordynamic and leakage characteristics of a variety of seals:

1) Rotor speed
2) Seal inlet pressure

3) Pressure ratio across the seal
4) Inlet fluid rotation
5) Seal clearance
6) Seal geometry

Test points are measure by varying the above first 4 parameters over the values specified in Table 1. The seal clearance can be controlled by changing the rotors. In this study, each seal has been tested at two clearances 0.30mm and 0.23mm.

Table 1 Test Points

Rotor Speed ω (rpm)	Inlet Pressure P_r (bar)	Pressure Ratio P_{ra} (-)	Inlet Preswirl in the Direction of Rotor Rotation
4680	7.9	0.65	None
8640	13.1	0.45	Intermediate
16500	18.3	0.3	High

Seal Geometries

Three hole-pattern damper seals with different surface configurations and a honeycomb seal were tested. Hole-pattern damper seals were designed using liquid hole-pattern seals experience, Childs (1989) as reference. All seals have the same diameters (152mm), lengths (50.8mm), and hole (or cell) depths (2.29mm). The surface geometries of hole-pattern damper seals are shown in Figure 6, where γ is the hole-area fraction, defined as:

$$\gamma = \frac{Hole\ Surface\ Area}{Seal\ Surface\ Area} \qquad (7)$$

TEST RESULTS AND RELATIVE PERFORMANCE

Three hole-pattern damper seals and a honeycomb seal were tested under the same test condition (table 1) with two radial clearances (0.30mm and 0.23mm). Unfortunately, due to an equipment failure which damaged the seal, only one non-swirl condition at one radio clearance C_r=0.23mm tests was completed for the d=3.175mm (γ=0.69) hole-pattern damper seal. Hence, for this seal, the graphical test results are presented by single point.† Seals were evaluated based on leakage control performance, cross-coupled stiffness k, direct damping C, and effective damping C_{eff}.

As noted, comparisons can not be made between the d=3.175mm (γ=0.69) hole-pattern damper seal and the honeycomb seal at larger clearance, since the tests were not completed. For the other two hole-pattern seals, test results are generally poorer than for the honeycomb seal. Therefore, test results at this clearance will not be presented.

†*figures 7-14.

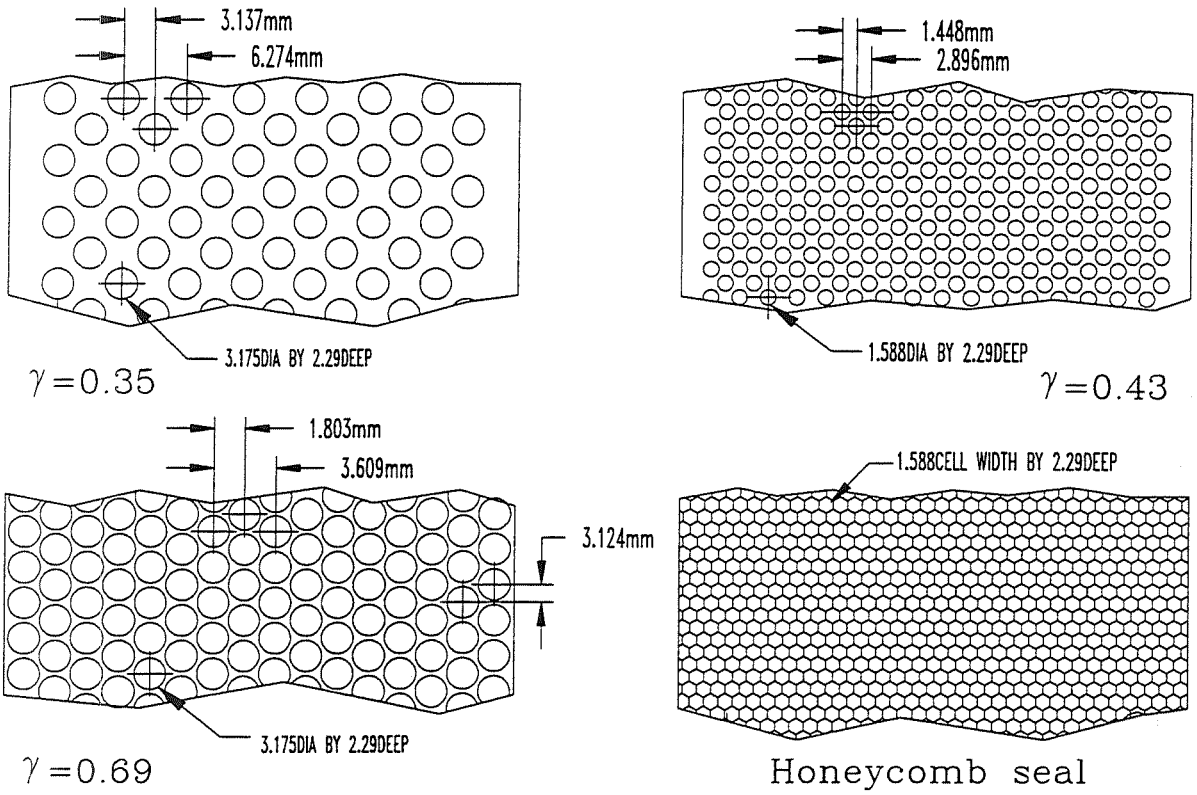

Figure 6 Surface geometry for test seals.

Figures 7 through 14 illustrate mass flow rate, K, C, and C_{eff} for three hole-pattern damper seals and a honeycomb seal, with pressure ratio P_{ra} = 0.45 and 0.3. An examination of these figures supports the following conclusion:

(1) The d=3.175mm (γ=0.69) hole-pattern damper seal has better leakage control performance. There is an average of 12 percent leakage rate reduction when compared to the honeycomb seal. However, the leakage rate for the other two hole-pattern damper seals are normally higher than the honeycomb seal.

(2) The magnitudes of cross-coupled stiffness and their sensitivities to increasing inlet circumferential velocity are higher for all hole-pattern damper seals than for the honeycomb seal under all test conditions. Cross-coupled stiffness for all hole-pattern damper seals increases with increasing running speed, absolute inlet pressure, and decreasing inlet pressure ratio.

(3) Direct damping for the d=3.175mm (γ=0.69) hole-pattern damper seal is considerably higher than the honeycomb seal under most test conditions. At P_{ra} = 0.30, all hole-pattern damper seals have higher C values than the honeycomb seal. Direct damping for hole-pattern damper seals increases with increasing inlet pressure and pressure ratio. For the honeycomb seal, interestingly enough, C decreases with increasing pressure ratio.

(4) The effective damping values for the d=3.175mm (γ=0.69) hole-pattern damper seal are generally higher than the honeycomb seal. The magnitudes of effective damping for hole-pattern damper seals increase with increasing inlet pressure and running speeds. Note that the effective damping for the d=3.175mm (γ=0.69) hole-pattern damper seal tends to increase with increasing running speed, while those for the honeycomb seal decrease.

CONCLUSION

Test results have been obtained for three hole-pattern damper seals configuration. According to these results and their comparison with honeycomb seal, the following conclusions hold:

a) Of the three hole-pattern damper seals tested, the d=3.175mm (γ=0.69) yields the highest effective damping and lowest leakage rate.

b) The d=3.175mm (γ=0.69) hole-pattern damper seal has achieved an average of 12 percent reduction in leakage rate, and a considerably higher effective damping than the honeycomb seal, especially under high inlet pressure ratio and high speed.

c) Based on test results and comparison, Hole-pattern damper seals can be a very attractive alternative to honeycomb seal.

REFERENCES

Childs, D. W., Nelson, C. C., Nicks, C., Scharrer, J., Elrod, D., and Hole, K., 1986a, "Theory Versus Experiment for the Rotordynamic Coefficients of Annular Gas Seals: Part 1-Test Facility and Apparatus," ASME *Journal of Tribology,* Vol. 108, pp. 426-432.

Childs, D. W., Kim, C. H., 1986b, "Test Results For Round-Hole-Pattern Damper Seals: Optimum Configurations and Dimensions for Maximum Net Damping," ASME *Journal of Tribology*, Vol. 108, pp 605-611.

Childs, D. W., Nolan, S. A., and Kilgore, J. J., 1990, "Additional Test Results for Round-Hole-Pattern Damper Seals: Leakage, Friction Factors, and Rotordynamic Force Coefficients," ASME *Journal of Tribology,* Vol. 112, pp 365-371.

Childs, D. W., 1993, *Turbomachinery Rotordynamics: Phenomena, Modeling, and Analysis*, John Wiley & Sons, Inc., New York, NY, p. 228.

Pelletti, J. M., 1990, "A Comparison of Experiment and Theoretical Predictions for the Rotordynamic Coefficients of Short (L/D=1/6) Labyrinth Seals," Master's Thesis, Texas A&M University.

Scharrer, J., 1989, discussion of the paper, "Annular Honeycomb Seals: Test Results for Leakage and Rotordynamic Coefficients; Comparisons to Labyrinth and Smooth Configurations, " by Childs, D. W., ASME *Journal of Engineering for Gas Turbines and Power*, Vol.106, pp. 927-934.

Sorokes, J., Kuzdzal, M., Sandberg, M., and Colby, G., 1994 "Recent Experiences in Full Load Full Pressure Shop Testing of a High Pressure Gas Injection Centrifugal Compressor," *Proceedings of the Twenty-Third Turbomachinery Symposium,* The Turbomachinery Laboratory, Texas A&M University, College Station, Texas, pp 3-17.

Von Pragenau, G. L., 1987 "Damping Seals for Turbomachinery," NASA Technical Paper 1987.

Zeidan, F., Perez, R., and Stephenson, E., 1993, "The Use of Honeycomb Seals in Stabilizing Two Centrifugal Compressors," *Proceedings of the Twenty-Second Turbomachinery Symposium*, The Turbomachinery Laboratory, Texas A&M University System, College Station, Texas, pp.3-15.

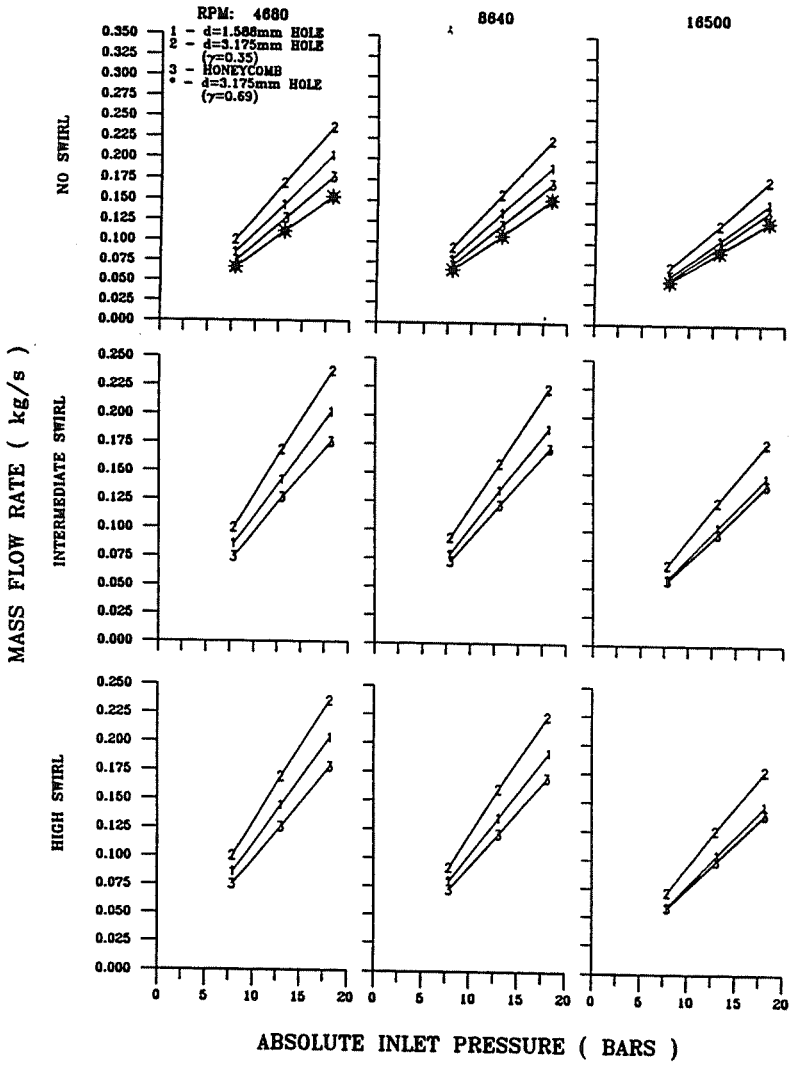

Figure 7 A comparison of mass flow rate versus inlet pressure for all seals at P_{ra}=0.45

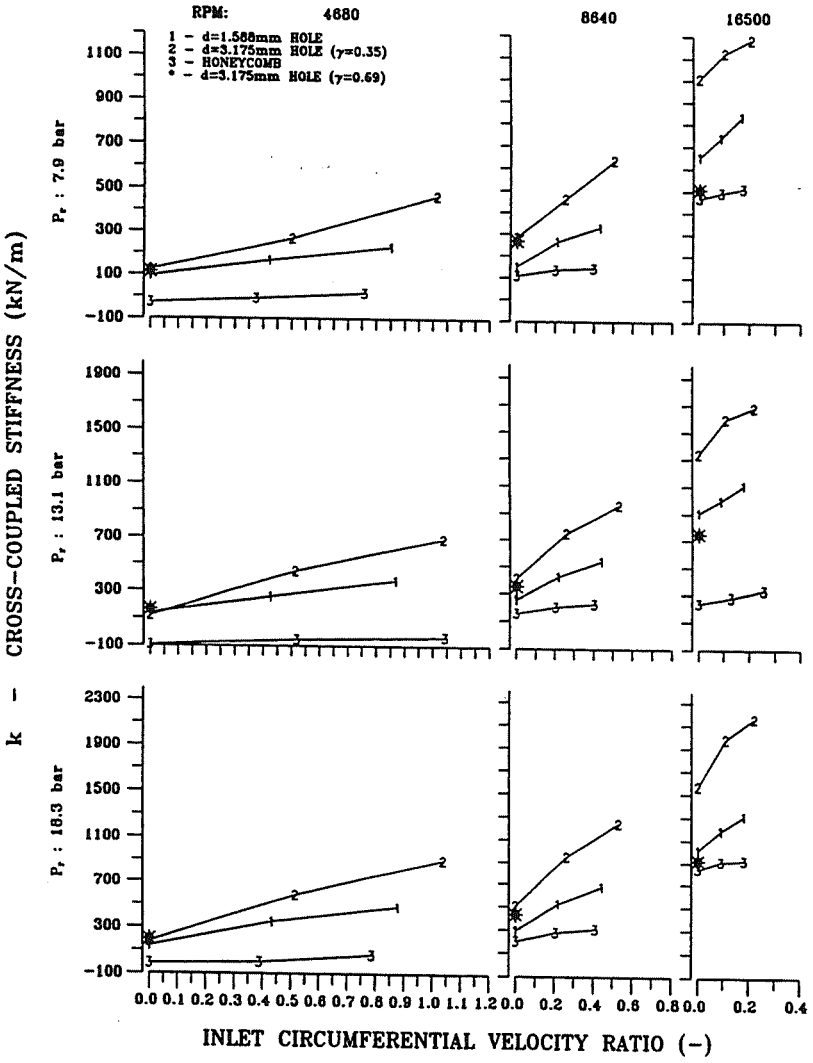

Figure 8 A comparison of cross-coupled stiffness versus inlet circumferential velocity ratio for all seals at P_{in}=0.45

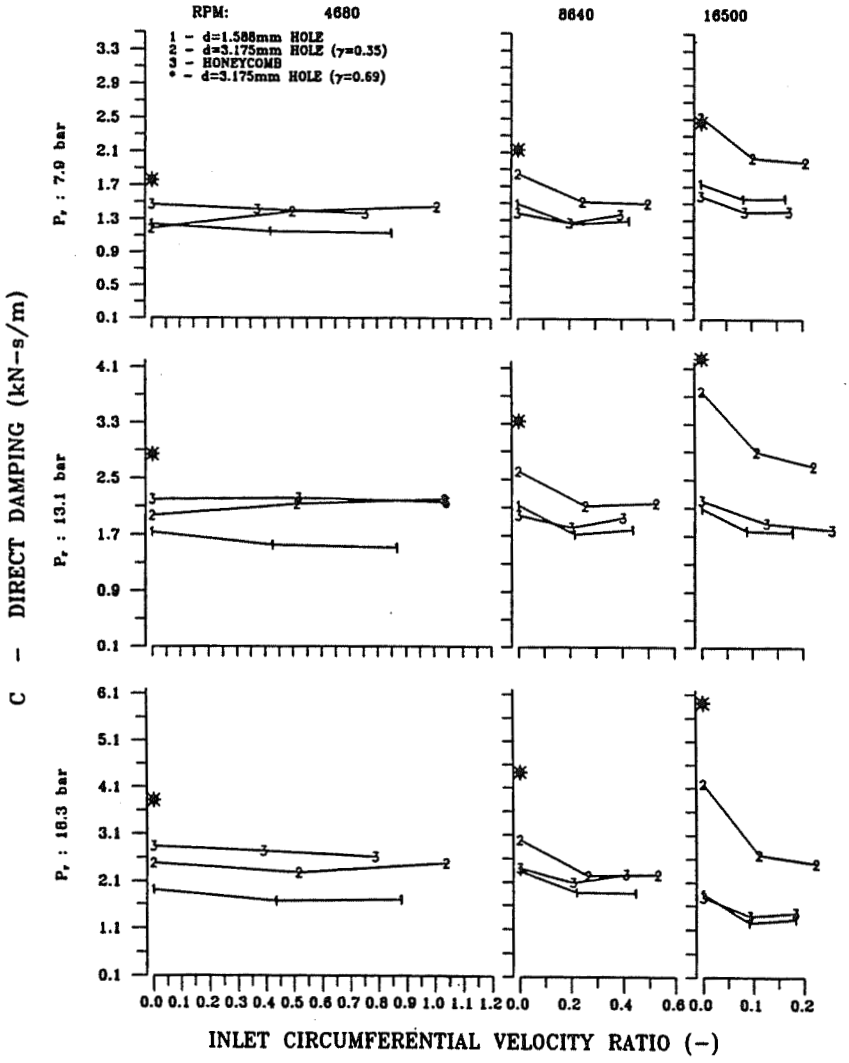

Figure 9 A comparison of direct damping versus inlet circumferential velocity ratio for all seals at P_{ra}=0.45

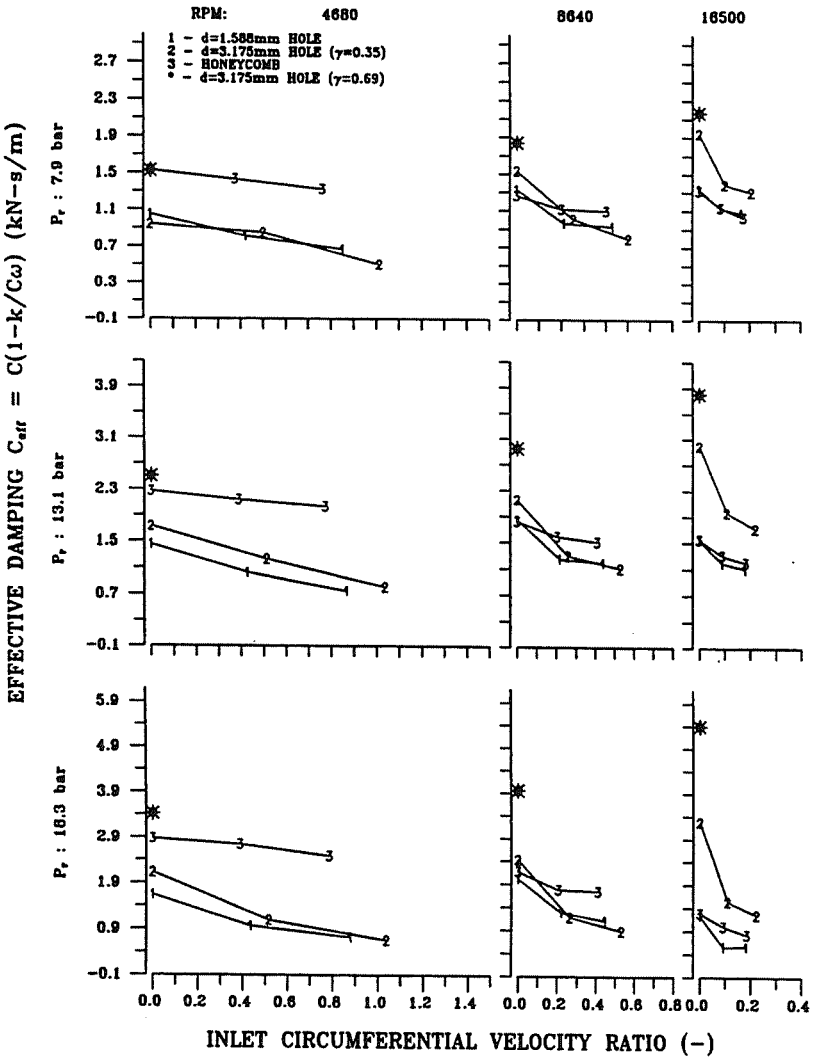

Figure 10 A comparison of effective damping versus inlet circumferential velocity ratio for all seals at P_{ra}=0.45

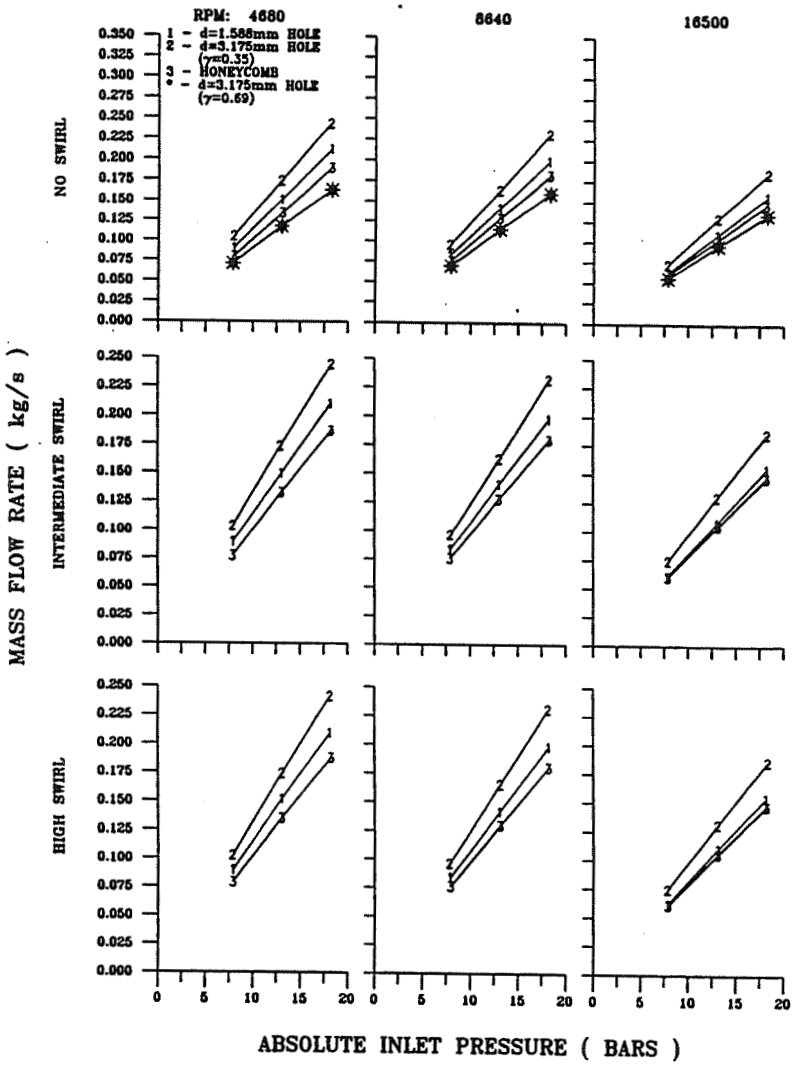

Figure 11 A comparison of mass flow rate versus inlet pressure for all seals at P_{ra}=0.30

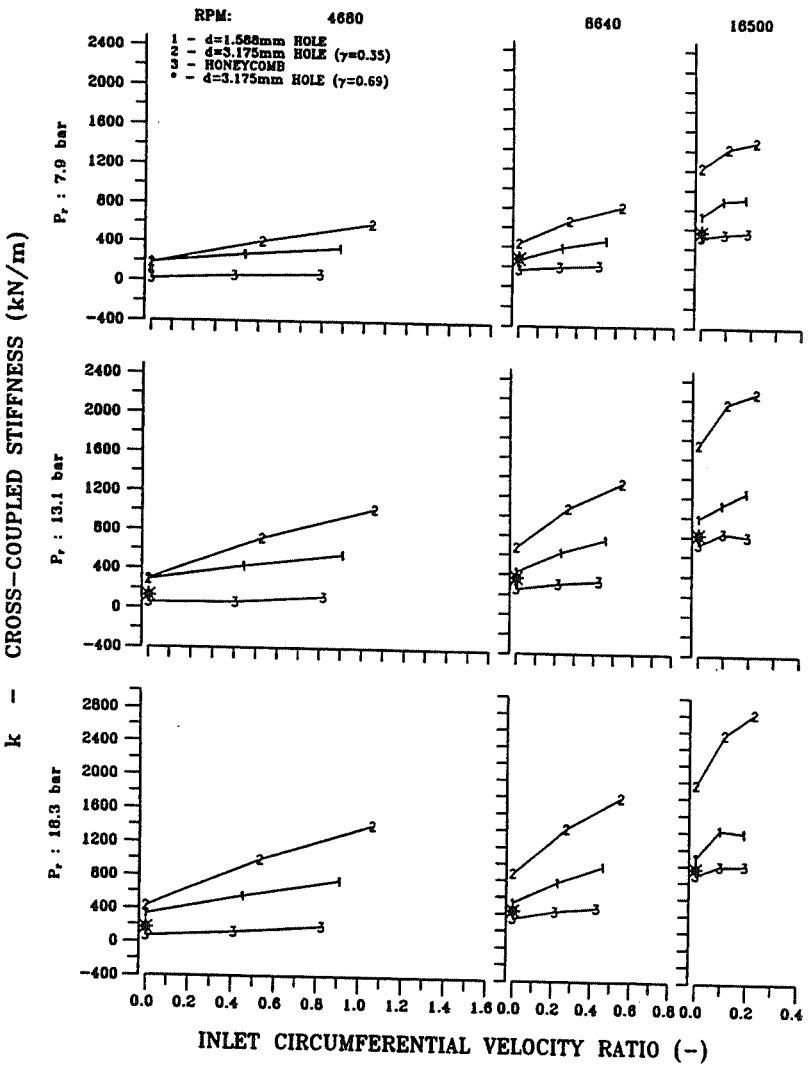

Figure 12 A comparison of cross-coupled stiffness versus inlet circumferential velocity ratio for all seals at P_{ra}=0.30

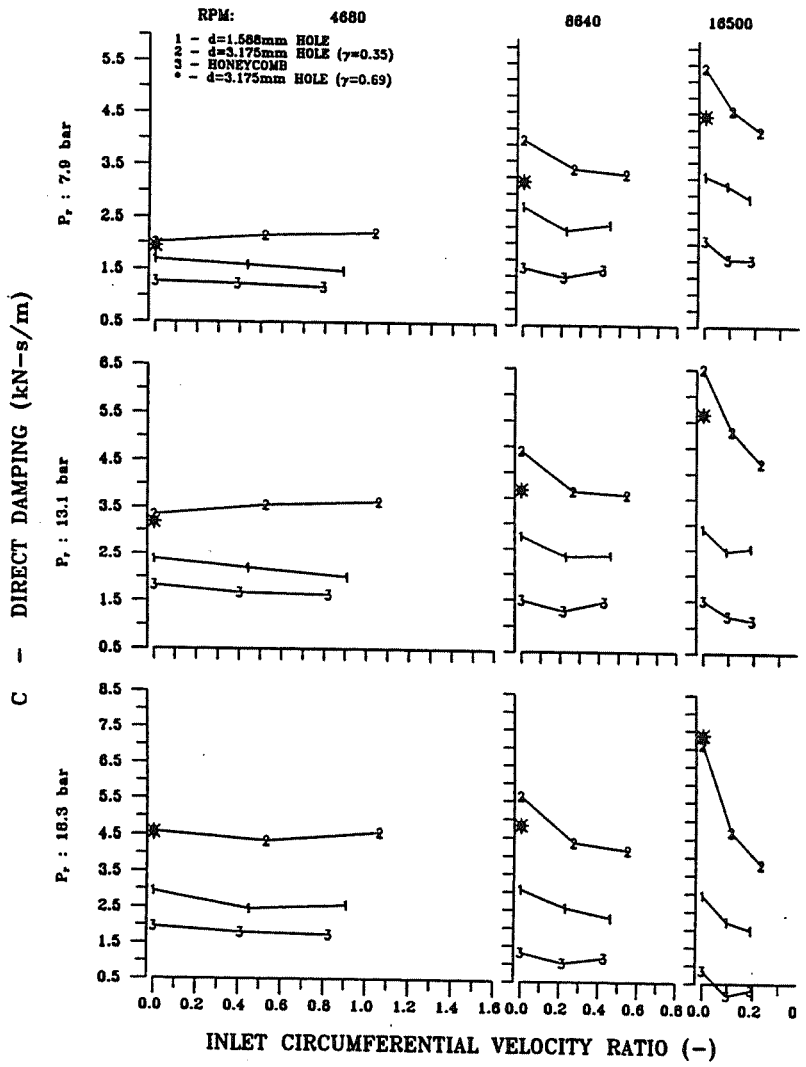

Figure 13 A comparison of direct damping versus inlet circumferential velocity for all seals at P_{ra}=0.30

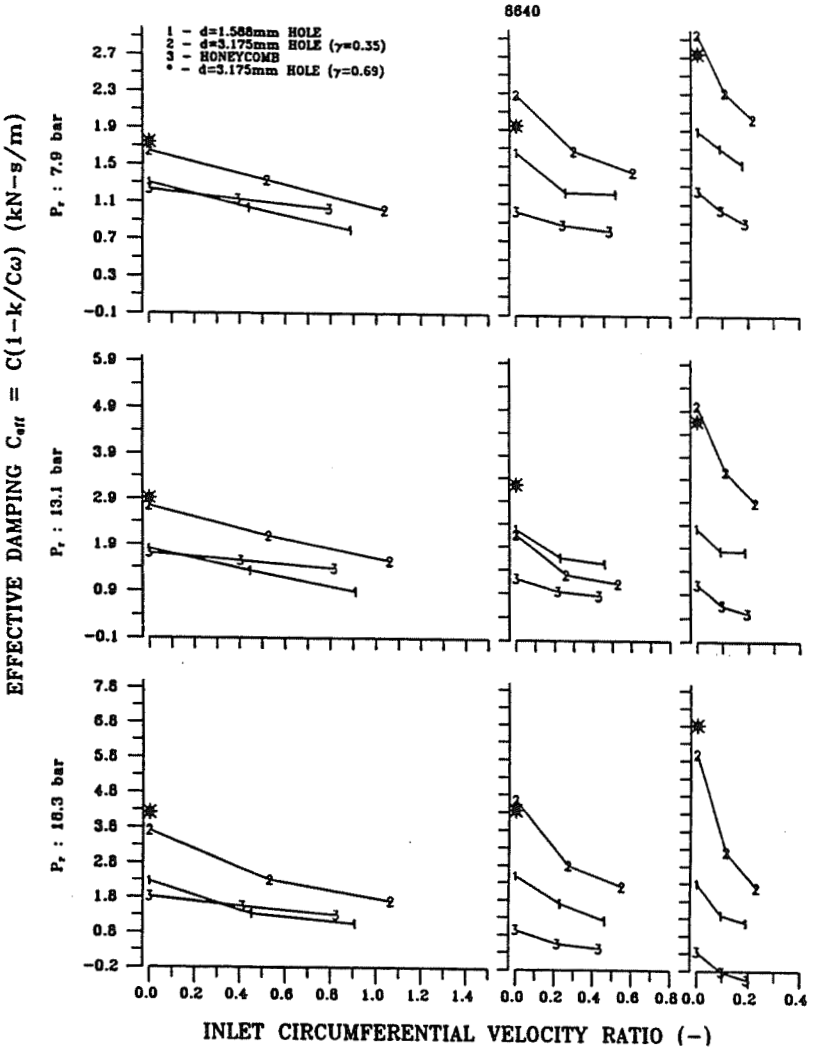

Figure 14 A comparison of effective damping versus inlet circumferential velocity for all seals at P_{ra}=0.30

DYNAMIC LABYRINTH COEFFICIENTS FROM A HIGH-PRESSURE FULL-SCALE TEST RIG USING MAGNETIC BEARINGS

Norbert G. Wagner and Klaus Steff
Demag Delaval Turbomachinery
Duisburg, Germany

Abstract

A safe rotor dynamic design for high pressure centrifugal compressors requires precise knowledge of the dynamic labyrinth coefficients. The objective of the test rig design and operation is to simulate original high-pressure compressor conditions in every aspect as well as possible. A key technology for this task is the use of active magnetic bearings. Static and dynamic calibration of the system is performed immediately before and after each test run as part of the test cycle. The input/output signals of the magnetic bearing system are fed into a data acquisition and analysis system for off-line data processing.

A new analysis method uses basic ideas from magnetic bearing control theory. The equations of motion are prepared in such a way that the identification of the spring and damper coefficients reduces to a linear curve fit in the frequency domain. A coherence-based filter algorithm improves the quality of the results, which are presented in numerical and graphical form. The method is applied to determine the four coefficients for the centered position as well as the full matrices for arbitrary rotor position.

Some typical results visualize the effect of different geometrical and operational parameters.

1 Introduction

In turbo compressors with very high power densities the fluid forces originating from the interstage seals and from the balance piston may endanger the operational reliability of the machine and, consequently, of an entire installation. Typical examples of this are small high-pressure compressors such as those used for the reinjection of natural gas. Owing to their low rotor mass, such compressors react relatively sensitively to every change in parameters. The high gas densities cause large aerodynamic excitations and, therefore, even at the design stage of such machines the gas forces arising from the seals must be taken into account for the rotor-dynamic design. An analytical calculation of these forces is desirable. In literature, the CFD-method [1],[2] is occasionally suggested for this purpose and, more frequently, the „bulk-flow"- method e.g. [3],[4],[5],[6],[7] in its various versions. The results of analytical calculation, however, are very highly dependent on the selected boundary conditions and parameters, in particular on the calculated shear stresses [1],[2],[4]. It is not sufficient to simply verify good coincidence between a calculation and measured values on the basis of a small number of test points. It was demonstrated in [8] that the calculated values may show an acceptable coincidence at low speeds and pressures. Where the parameters are high, however, they may deviate sharply from the measured values and even reproduce erroneous trends.

The authors take the view that in the long term experimental methods for determing the gas forces will remain indispensable owing to the high requirements as regards reliability.

The first experimental verification of labyrinth stiffness involving a systematic examination of various geometries was made by [9]. No damping force, however, is obtained by measuring the static pressure distribution in the individual chambers, as has been carried out in the meantime also by other authors (e.g. [4],[10]).

On the basis of the results from [9] and the recalculations made for stable-running machines, it was established at a very early stage that damping forces have to be taken into account. Otherwise, the machine will become larger in size and lower in speed and, as a result, competitive disadvantages will arise.

The series of measurements made at the Texas A&M University which provide stiffness *and* damping coefficients are of outstanding importance for practical application. These measurements are described together with other sources in summarised form in [11]. The scope of utilisation of the test stand from [12] was extended [13] in order to come yet closer to the original conditions. Further literature [3],[14] describes interesting interrelationships which, however, cannot be directly employed for practical design purposes.

Careful study of the literature leads to a coherent understanding of the main influencing variables but also uncovers a large number of contradictions, cf. [11]. The published data are not always complete, which makes it very difficult to structure any reliable correlations on these. As previously, therefore, there continues to be a need for comprehensive experimental data. For this not only the geometrical data of the test pieces but also the operating conditions relating to the test stand should correspond as far as possible to the original conditions.

These requirements can be implemented in a most favourable manner by the use of active magnetic bearings. A test stand of this type was presented for the first time in [15]. Here, attempts were made to utilise the signal processor for the digital control and for the on-line determination of the labyrinth parameters at one and the same time with the aid of a recursive parameter estimation algorithm. In this present work, on the other hand, an off-line process in the frequency domain is being implemented with a powerful computer. This enables the strict requirements relating to the parameters being sought to be fulfilled more efficiently.

2 Testing concept

The basic requirements relating to the test stand are to produce significant gas forces and to take measurements which in every respect come as close as possible to the original conditions. The first of these requirements has led to the construction of a high-pressure test stand in which the inlet pressure and the back-pressure can be set independently of one another. In particular, the greater the damping forces, the more reliably these can be measured. Active magnetic bearings are suitable for simulating original operating conditions. They make it possible, independently of the rotor speed, to set the static eccentricity as well as a superimposed circulatory movement with freely adjustable frequency, amplitude and direction of precession. The force can be measured directly via the magnetic bearings and there is therefore no need for additional force transducers as in [12],[13],[16]. The major measuring challenge when employing additional force transducers arises from the need to correct the signal provided by them by measuring precisely the acceleration at the stator. A further advantage of the method used here is that those forces which are actually acting on the *rotor* are measured. In the case of high circumferential velocities, it is conceivable that a radial distribution of pressure takes place in the labyrinth chambers and, therefore, the pressures or forces measured at the *stator* are not identical with the forces which act on the rotor.

2.1 Test stand

Fig. 1 is a sectional view of the high-pressure barrel type test stand. The drive is conventional, using a variable-speed motor via a gear unit. Since the drive is not integral to the stand, disturbing moments originating from the drive are avoided and the test rotor is simple and symmetric. The dynamic separation of the test rotor (3) from the drive (1) is through a highly bendable and torsionally elastic bar (2) introduced through the hollow rotor. This quill shaft also isolates any forces generated in the seal (10) to the atmosphere which is positioned on the drive shaft (1). The symmetric arrangement of two identical labyrinths (4) provides balanced thrust.

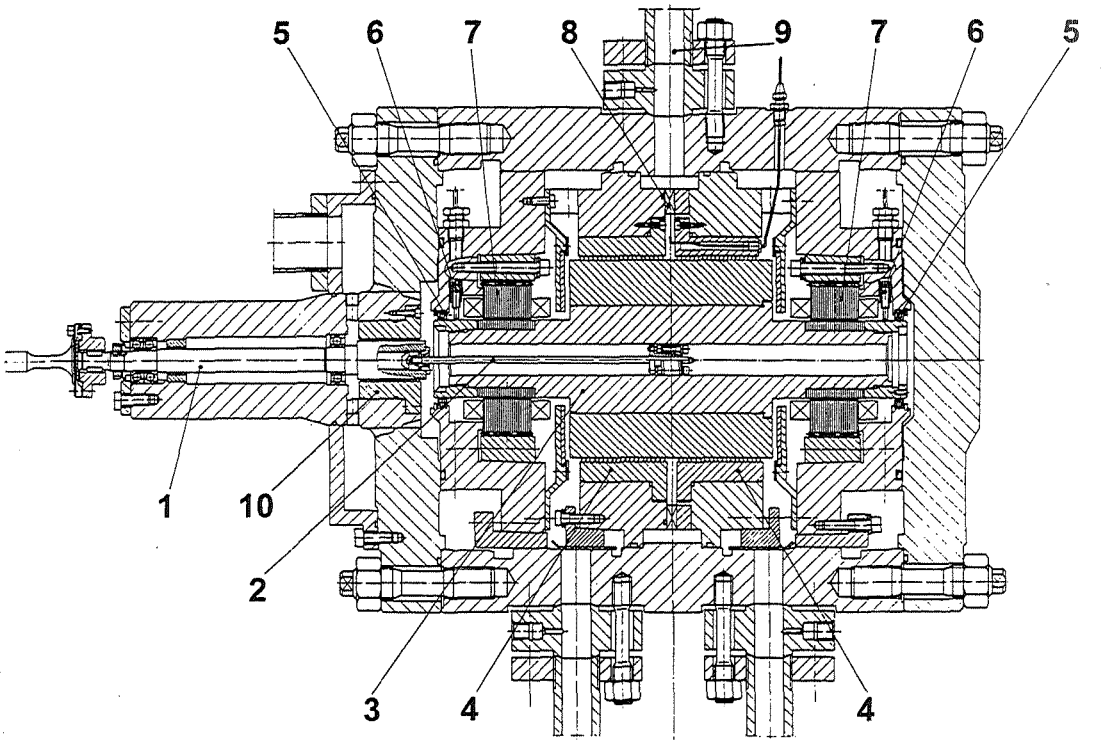

Fig. 1: Labyrinth test stand with active magnetic bearings

The test gas is admitted into the casing centre (9) and accelerated tangentially by interchangeable swirl rings (8). All inlet and outlet openings are symmetrically spaced over the circumference. The magnetic bearings (7) are jointly installed with the auxiliary bearings (5) and sensors (6) in a housing and are radially adjustable. The electrical lines to the sensors and bearings leave the housing through pre-stressed glass penetrations.

Straight-through, stepped and comb-groove labyrinth and honeycomb seals, with exactly same geometrical features as those utilised in high-pressure compressors, were manufactured for the tests. Geometry-based errors in the dynamic labyrinth coefficients are minimised by manufacturing the test pieces with the greatest possible accuracy. This includes above all checking of the tip width, of the edge sharpness and of the true-running quality on a 3D precision measuring machine.

The test stand is normally supplied with N_2 from a 250 bar accumulator station. The inlet pressure and the back-pressure are each set separately to the desired values using electronically controlled valves. The mass flow rate is measured with an orifice plate after the medium has flowed through the test stand.

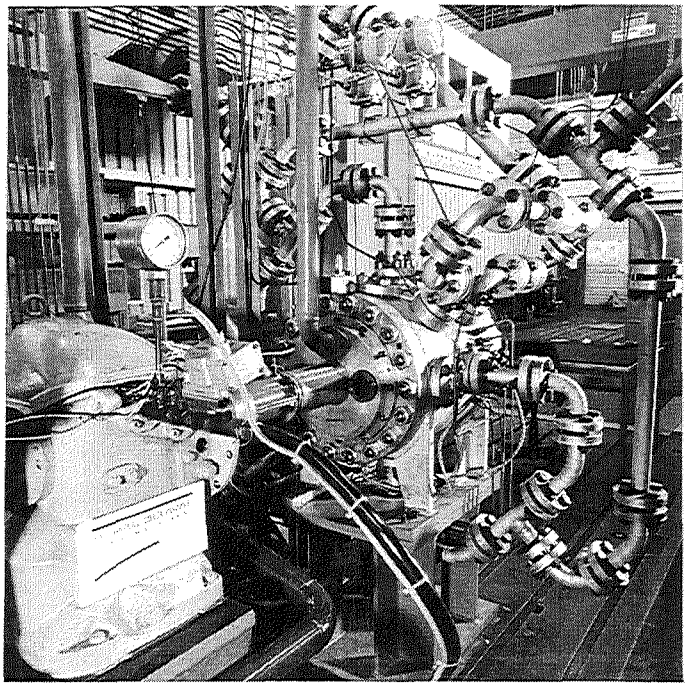

Fig. 2: Photograph of the labyrinth test stand

The temperature upstream and downstream of the labyrinth is measured with thermocouples. In addition to the pressures at the casing inlet and outlet, measurement is made of two static and two total pressures at two different diameters in the annular space between the swirl ring (8) and the labyrinth inlet. These measured values are entered as data points into a procedure for calculating the flow in the annular space and make it possible to determine precisely the swirl at the labyrinth inlet. The authors attach great importance to this procedure because the inlet swirl is a main influencing variable which is often only measured indirectly on other test rigs.

The testing times are restricted owing to the fact that gas is supplied from an accumulator. For this reason, in place of a scanivalve for all 13 pressure measuring points, use is made of Rosemount transmitters in the precision class 0.2%. This measurement technique enables all of the thermodynamic variables to be measured and stored within a few seconds. Furthermore, in order to increase the precision of measurement, all of the pressures measured in the annular space are recorded as differential pressures at a somewhat higher pressure level.

The complete test set-up is represented in fig 3.

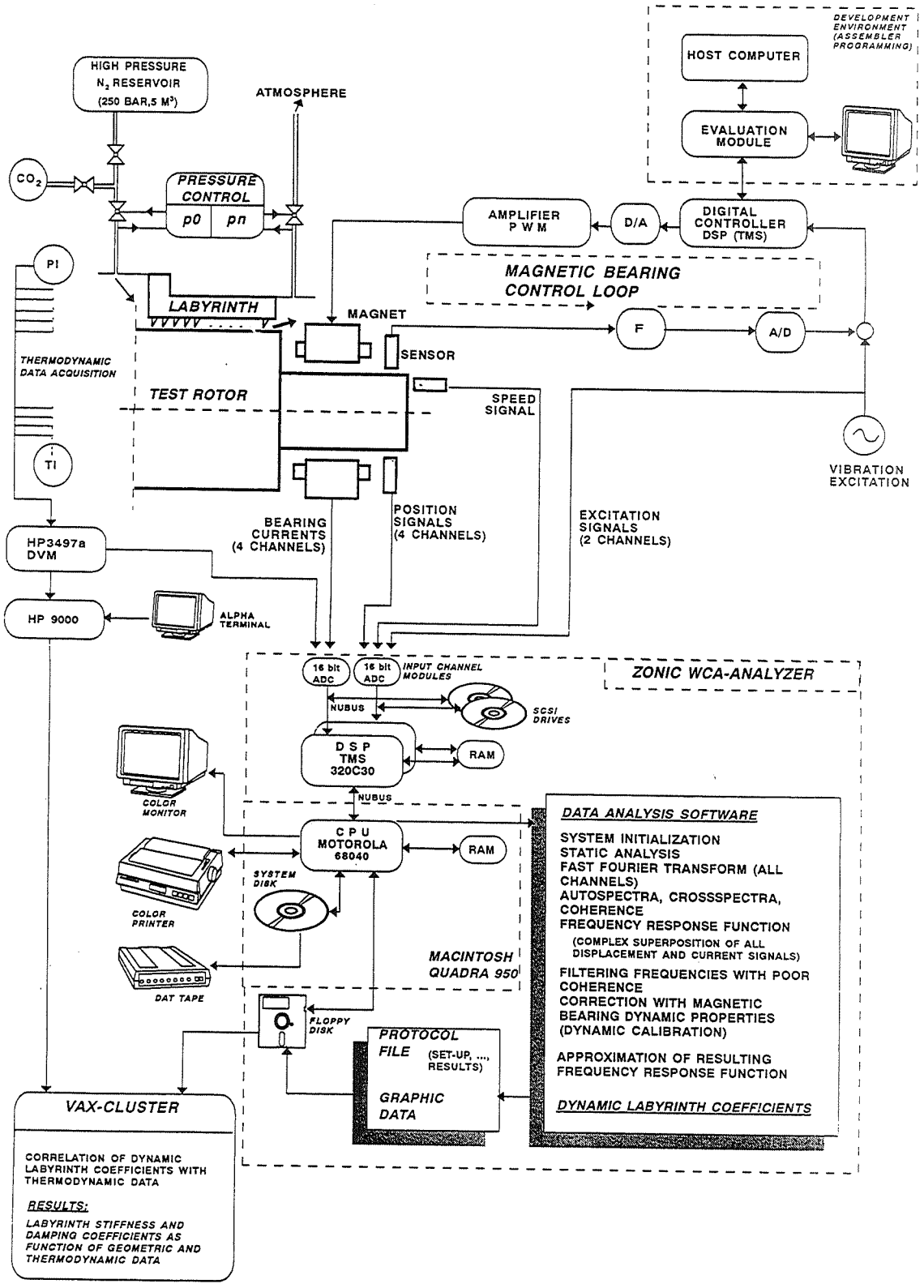

Fig. 3: Diagram of the complete test set-up

2.2 Mathematical model

It is not necessary to take account of the axial motion of the rotor since positioning is provided by the torsionally elastic bar (2). The radial motions of the rigid rotor are described by the coordinates of the centre of gravity x,y and by the cardan angles α,β . In addition to the magnetic forces in the right and left bearing planes $F_{Rx,y}$, $F_{Lx,y}$ a static unbalance e_1 and a dynamic unbalance E are applied. The labyrinth forces are applied as linear functions in displacement (F_k) and velocity (F_d):

$$-F_k = -\begin{bmatrix} F_{kx} \\ F_{ky} \end{bmatrix} = \begin{bmatrix} k_{xx} & k_{xy} \\ k_{yx} & k_{yy} \end{bmatrix} \cdot \begin{bmatrix} x \\ y \end{bmatrix} \qquad -F_d = -\begin{bmatrix} F_{dx} \\ F_{dy} \end{bmatrix} = \begin{bmatrix} d_{xx} & d_{xy} \\ d_{yx} & d_{yy} \end{bmatrix} \cdot \begin{bmatrix} \dot{x} \\ \dot{y} \end{bmatrix} \qquad (1)$$

Only in those special cases where the rotor is centric the two matrices in eq.(1) are skew-symmetrical:

$$d_R=d_{xx}=d_{yy}, \quad d_Q=d_{xy}=-d_{yx}, \quad k_R=k_{xx}=k_{yy}, \quad k_Q=k_{xy}=-k_{yx}.$$

Even though the procedure for identifying parameters for the general case as per eq. (1), as also for the case of a centric rotor, has been applied successfully, we shall limit ourselves in this report to the simpler notation for the centric rotor. The equations of motion read as follows with the rotor mass m and the mass moments of inertia A, C:

$$\begin{aligned} m\cdot\ddot{x} + k_a\cdot x - k_a\cdot s\cdot\beta &= m\cdot\Omega^2\cdot e_1\cdot\cos\Omega t + F_{Lx} + F_{Rx} + 2F_{kx} + 2F_{dx} + m\cdot g \\ m\cdot\ddot{y} + k_a\cdot y + k_a\cdot s\cdot\alpha &= m\cdot\Omega^2\cdot e_1\cdot\sin\Omega t + F_{Ly} + F_{Ry} + 2F_{ky} + 2F_{dy} \\ A\cdot\ddot{\alpha} + C\cdot\Omega\cdot\dot{\beta} + k_a\cdot s\cdot y + k_a\cdot s^2\cdot\alpha &= -\Omega^2 E\cdot\sin\Omega t - F_{Ly}\cdot h_L + F_{Ry}\cdot h_R \\ A\cdot\ddot{\beta} - C\cdot\Omega\cdot\dot{\alpha} - k_a\cdot s\cdot x + k_a\cdot s^2\cdot\beta &= +\Omega^2 E\cdot\cos\Omega t + F_{Lx}\cdot h_L - F_{Rx}\cdot h_R \end{aligned} \qquad (2)$$

k_a Coupling stiffness — $h_{R,L}$ Distance from magnetic bearing right, left to centre of gravity

Ω Rotational frequency — s Distance from coupling to centre of gravity

On introducing the complex displacements and bearing forces

$$z = x + j\cdot y \qquad \varphi = \beta - j\cdot\alpha \qquad (3)$$

$$F_{Lz} = F_{Lx} + j\cdot F_{Ly} \qquad F_{Rz} = F_{Rx} + j\cdot F_{Ry}$$

the four real differential equations from eq. (2) can be combined to form two complex differential equations. Furthermore, following applies for the symmetrical rotor: $h_R = h_L = h$

$$\begin{aligned} m\cdot\ddot{z} + \left(2d_R - j2d_Q\right)\dot{z} + \left(k_a + 2k_R - j2k_Q\right)z - k_a\cdot s\cdot\varphi &= m\Omega^2 e_1\cdot e^{j\Omega t} + F_{Lz} + F_{Rz} + mg \\ A\cdot\ddot{\varphi} - j\Omega C\dot{\varphi} - k_a\cdot s\cdot z + k_a\cdot s^2\cdot\varphi &= \Omega^2 E\cdot e^{j\Omega t} + h\cdot\left(F_{Lz} - F_{Rz}\right) \end{aligned} \qquad (4)$$

In accordance, for example, with [17] the force in a single magnet is as follows on disregarding the permeability of the iron ($\mu_r >> 1$).

$$F = \frac{\mu_o \cdot N^2 \cdot A}{4} \cdot \frac{I^2}{s^2} \tag{5}$$

wherein N= number of windings, A = pole face, $\mu_0 = 4\pi 10^{-7}$ permeability in vacuum, I = current and s = gap.

Use is made here of alternating actuation in place of the frequently used differential connection of two opposing magnets. In other words, only those magnets in the direction of which a force is to be produced carry current. The losses in the bearing are thereby kept to a minimum. Linearisation takes place in the signal processor on the basis of an inverted measured characteristic curve. We obtain the following for the resulting force of two opposing magnets:

$$F = w \cdot i_v^2 \frac{4 s_0 x_{brg}}{\left(s_0^2 - x_{brg}^2\right)^2} + w \cdot sgn(i) \frac{2 i_v |i| + |i|^2}{\left(s_0 - sgn(i) \cdot x_{brg}\right)^2} \tag{6}$$

wherein $w = \mu_0 N^2 A / 4$, $x_{brg} = x_0 + \tilde{x}$, $i = i_0 + \tilde{i}$, i_v magnetic biasing current, i_0 bias current for compensation of weight and additional static forces, $\tilde{i}$ control current. Linearisation around the static equilibrium state $x_{brg}=x_0$, $i=i_0$ yields

$$F = F_0 + k_s \tilde{x} + k_q \tilde{i} \tag{7}$$

with the coefficients

$$F_0 = w \left[i_v^2 \frac{4 s_0 x_0}{\left(s_0^2 - x_0^2\right)^2} + sgn(i_0) \frac{2 i_v |i_0| + |i_0|^2}{\left(s_0 - sgn(i_0) \cdot x_0\right)^2} \right] \tag{8}$$

$$k_s = w \left[i_v^2 \frac{4 s_0 \left(s_0^2 + 3 x_0^2\right)}{\left(s_0^2 - x_0^2\right)^3} + \frac{2\left(2 i_v |i_0| + i_0^2\right)}{\left(s_0 - sgn(i_0) \cdot x_0\right)^3} \right] \qquad k_q = w \cdot sgn(i_0) \frac{2\left(i_v + |i_0|\right)}{\left(s_0 - sgn(i_0) \cdot x_0\right)^2}$$

Eq. (8) could undergo further simplification for the special case x_0 =0. We shall, however, retain this more general form since varying equilibrium states x_0 arise as a result of unavoidable alignment errors in each bearing plane. The coefficients k_s, k_q eq. (7) may vary in the individual magnets. Furthermore, owing to the arrangement of bearing planes below 45° to the vertical, a transformation is required from the system of bearing coordinates to the modal coordinates before eq. (7) can be inserted into eq. (4).

2.3 Controller design for the magnetic bearing

The magnetic bearings are controlled in a digital manner using a signal processor (DSP) of the TMS 320 family. The advantage over using an analog system is that additional functions such as compensation of static and rotational-frequency disturbances, linearisation of the magnetic force and vibration monitoring can also be performed by the DSP without extra hardware. In [15] it is also described how system parameters can be identified on-line and, for example, used for adaptive control purposes. For the controller design it is first necessary to transfer the differential equations (4) into the discrete-time notation with the aid of the transition matrix (e.g. according to [18]).

Following introduction of the magnetic forces from eq. (7) and discarding of unbalance and static forces, the equation of motion finally reads as follows:

$$\ddot{z}_S + \frac{d_L}{m}\dot{z}_S + \frac{1}{m}\left(k_a + k_L\right)\cdot z_S = \qquad (14)$$

$$\frac{2}{m}\left\{+q_{Rx}\cdot x_{SR} + q_{Lx}\cdot x_{SL} + j\left(q_{Ry}\cdot y_{SR} + q_{Ly}\cdot y_{SL}\right) + k_{qLx}\cdot i_{Lx} + k_{qRx}\cdot i_{Rx} + j\left(k_{qLy}\cdot i_{Ly} + k_{qRy}\cdot i_{Ry}\right)\right\}$$

wherein $q_{Rx} = \frac{1}{2}\left[\left(1-\frac{h}{b}\right)\cdot k_{sLx} + \left(1+\frac{h}{b}\right)\cdot k_{sRx} - k_a\frac{s}{b}\right]$, q_{Lx}, q_{Ry}, q_{Ly} analog,

b=distance from sensor plane to centre of gravity.

This eq. (14) is now transformed into the frequency domain and divided by Z_S. After inserting eq.(13) we obtain

$$+j\omega\left(d_R - jd_Q\right) + k_R - jk_Q - \frac{m}{2}\omega^2 + \frac{1}{2}k_a = \Lambda \qquad (15)$$

wherein $$\Lambda = q_{Rx}\cdot\frac{X_{SR}}{Z_S} + q_{Lx}\cdot\frac{X_{SL}}{Z_S} + k_{qLx}\cdot\frac{I_{Lx}}{Z_S} + k_{qRx}\cdot\frac{I_{Rx}}{Z_S}$$
$$+j\cdot\left(q_{Ry}\cdot\frac{Y_{SR}}{Z_S} + q_{Ly}\cdot\frac{Y_{SL}}{Z_S} + k_{qLy}\cdot\frac{I_{Ly}}{Z_S} + k_{qRy}\cdot\frac{I_{Ry}}{Z_S}\right)$$

and $$Z_S = X_{SL} + X_{SR} + j\cdot\left(Y_{SL} + Y_{SR}\right)$$

After separating the real and imaginary components, we obtain two real equations for determing the four labyrinth coefficients which are being sought:

$$\boxed{\begin{aligned}\omega d_Q + k_R &= \frac{m}{2}\omega^2 - \frac{1}{2}k_a + Re(\Lambda)\\ \omega d_R - k_Q &= Im(\Lambda)\end{aligned}} \qquad (16)$$

The identification is thus reduced to a linear regression with ω as variable. The terms relating to damping correspond to the linear gradient and the terms relating to stiffness are obtained directly as an intersection of ordinates.

3 Performance of tests

Prior to commencement of the labyrinth tests, examinations were made to provide assurance about the operational reliability of the test stand and the quality of the measurements. In addition to a procedure for operational balancing according to [19], a controller was designed for the magnetic bearing for the purpose of counteracting the flow excitation and shifting the stability limit towards higher pressures.

Knowledge of the dependency of the static and dynamic transfer characteristics on the speed, the static eccentricity and the amplitude of the test signal is decisive as regards the precision of the gas forces measured. These dependency relationships govern both the course of testing and the evaluation.

The translation of the centre of gravity with the sampling values $z(k) = z(t=kT)$, T sampling time and the control variables $u(k)$ is described by

$$z(k) + a_1 z(k-1) + a_2 z(k-2) = b_1 u(k-1) + b_2 u(k-2) + w_G + w_0 + w_s s(k-1) \qquad (9)$$

with the disturbance variables w_i and $s(k-1)=exp(j\Omega(k-1)T)$. We obtain an analog equation for the tilting motion. The advantage of using modal coordinates is that, from the point of view of control technology, two complex single input/single output systems are involved. Thus, for the translation and the tilting motion, separate pole positions can be specified and independent algorithms can be introduced for compensation of the disturbances. This quality is important for measurement of the labyrinth forces since the rotor is supposed to perform pure transverse movements and tilting motions need to be specifically suppressed. Details of the implemented controller design and of compensation of disturbances are provided in [15] and [19].

2.4 Equations for identification purposes

For identification of the stiffness and damping coefficients from eq. (1) it is found to be practicable to represent the equation of motion eq. (4) and the equation of magnetic force eq. (7) in the sensor coordinates, marked by index 'S'. The sensor signals from each bearing plane can be combined in a complex manner. As a result of suppressing the tilting motion of the rotor through the controller design, the differential equations z_{SL} and z_{SR} continue to be summated to an average translation z_S with

$$z_S=z_{SL}+z_{SR} \qquad \text{whereby} \qquad z_{SL}=x_{SL}+j\,y_{SL} \qquad z_{SR}=x_{SR}+j\,y_{SR} \qquad (10)$$

The complex combined total magnetic force in this system of coordinates reads

$$F_z = \left(F'_{Lx} + j \cdot F'_{Ly}\right) + \left(F'_{Rx} + j \cdot F'_{Ry}\right) \qquad (11)$$

After several conversions, there thus remains a complex 2nd order differential equation:

$$\ddot{z}_S + \frac{d_L}{m} \cdot \dot{z}_S + \frac{1}{m}\left(k_a + k_L\right) \cdot z_S + \frac{k_a \cdot s}{m \cdot b}\left(z_{SR} - z_{SL}\right) = \Omega^2 \cdot (1-j)\sqrt{2} \cdot e_1 \cdot e^{j\Omega t} + \frac{2}{m} \cdot F_z + \sqrt{2} \cdot (1-j) \cdot g \qquad (12)$$

Here, the following complex labyrinth coefficients were introduced into eq. (12):

$$d_L = 2 \cdot \left(d_R - j \cdot d_Q\right) \qquad k_L = 2 \cdot (k_R - j \cdot k_Q) \qquad (13)$$

This particularly compact notation eq. (12), (13) is, nevertheless, only possible with skew-symmetrical matrices in eq (1), i.e. with a centric rotor. No further consideration is given to the unbalance component in eq. (12) since the rigid rotor is subjected to trim-balancing in the test stand and the influence of the residual unbalance is insignificant for evaluation of the spectra. The rotor weight is in a state of equilibrium with the static magnetic forces when the bearings are active. It will be explained at a later point how this fact is utilised for static calibration.

In order to measure and evaluate the overall transfer function Λ, the system has to be excited to vibrations with the aid of a test signal. Provided that genuinely linear system behaviour is present, this can be attained by means of a harmonic excitation or also a wide-band noise or a pulse excitation. The authors have their reservations, however, as to whether this linearity can also be expected from the flow processes. In accordance with the basic intention that original conditions should be simulated in all respects, we shall employ a harmonic excitation. Motion through the circular orbit can take place in the direction of shaft rotation or counter to it by performing an appropriate positive or negative phase shift between the x and y test signals. The best results were achieved with a sweep sine excitation.

3.1 Static and dynamic calibration

The coefficients k_s, k_q of the linear magnetic force equation (7) depend on the bias current i_0 which serves to compensate static forces. Since the gas forces also have a static component, owing to unavoidable eccentricities, the coefficients k_s, k_q depend on the respective operating point and are therefore not constants in the usually accepted sense. All the same, the winding constant $w = \mu_0 N^2 A / 4$ for each bearing axis is an invariable magnitude. We shall introduce here a correction coefficient k_{stat} in $w = k_{stat}\mu_0 N^2 A / 4$ for adaptation to the actual properties. This coefficient can be calculated specifically for each bearing using eq. (12), (11), (8) from the condition of static equilibrium for the case without gas forces. Using this winding constant and the time-related mean value of i_0, x_0 bearing-specific k_s, k_q-values are calculated and inserted in eq. (15) for each operating point.
At the beginning and end of each series of measurements, a dynamic calibration is made in addition to the above static calibration. When the test stand is pressureless, all labyrinth coefficients are identical to zero. The following is thus obtained from eq. (16):

$$Re(\Lambda) = \tfrac{1}{2}k_a - \tfrac{1}{2}m\omega^2 \qquad Im(\Lambda) = 0 \tag{17}$$

An analysis of the measured frequency response Λ shows that these equations (17) are fulfilled relatively well but not exactly. A cause of the deviations involved may be that in (15) no actually measured currents through the magnets are inserted but the desired currents of the controller output. Therefore, for the dynamics of the PWM amplifiers, a corrective transfer function $F_{amp}(\omega)$ is inserted in eq. (15) . This transfer function can be determined within the computer accuracy by using the conditions from eq. (17)

$$\Lambda = q_{Rx}\frac{X_{SR}}{Z_S} + q_{Lx}\frac{X_{SL}}{Z_S} + F_{amp}\left(k_{qLx}\frac{I_{Lx}}{Z_S} + k_{qRx}\frac{I_{Rx}}{Z_S}\right)$$

$$+ j\left\{q_{Ry}\frac{Y_{SR}}{Z_S} + q_{Ly}\frac{Y_{SL}}{Z_S} + F_{amp}\left(k_{qLy}\frac{I_{Ly}}{Z_S} + k_{qRy}\frac{I_{Ry}}{Z_S}\right)\right\} \tag{18}$$

This step can be expressed in an illustrative manner as a frequency-dependent evaluation of the force/current factor k_q. The basis of this dynamic calibration is the equilibrium between the rotor inertia forces and the magnetic forces. This calibration is made upon every change in speed using the actual vibration spectra of the system.

3.2 Test procedure

Various inlet and back pressures are set following recording of the reference state in the pressure-less condition for the above-described calibration. The pressure ratio is thus made to vary independently of the pressure level. In addition, by exchanging the swirl rings the circumferential velocity of inlet into the labyrinth is altered. Furthermore, for each setting of pressure the speed is increased progressively from zero up to maximum speed in order that the influence of all essential parameters can be clearly determined. The frequency of the test signal is varied from 30 to 300 Hz during the recording of all time signals. The coherence γ^2 of all four signal pairs is indicated on-line in addition to the orbit of both bearings and the spectra of all displacement signals and controller outputs, cf. fig. 4 . Since the coherence is a function representing the quality of the linear

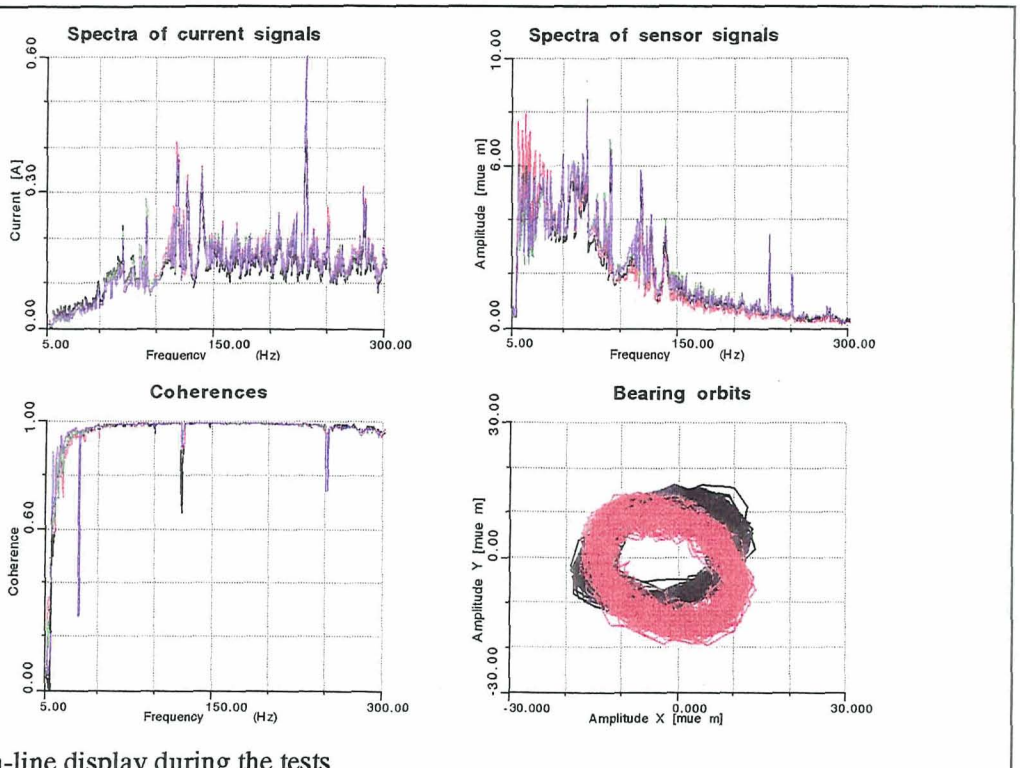

Fig. 4 On-line display during the tests

interrelationship between two signals [20], the frequency range of the sweep sine is adapted continuously during the measurement in order to enable the coherence of all signal pairs in the whole frequency range to be as close as possible to the ideal value $\gamma^2 = 1$. This means that the quality of the result can be favourably influenced during the test and the need to repeat a test owing to a poor result of the off-line evaluation can be avoided. All of the real-time data are stored on SCSI-drives (cf. fig. 3) and the determination of the labyrinth coefficients according to eq.(16) takes place off-line. After they have been processed, these real-time data are saved on a DAT recorder, and can be read into the computer at any time when required for further analyses without need for the test to be performed again.

Each test evaluation commences with the static and dynamic calibration with the aid of the reference state measurement. This is followed by calculation of the averaged cross and auto spectra from which the overall frequency response eq. (18) is finally determined.

The overall frequency response Λ is also filtered before making the linear regression according to eq.(16), which provides the labyrinth coefficients being sought. When doing this, the frequency lines with a low coherence of the signal pairs are marked in such a manner that they are not taken into consideration for the linear regression.

Fig. 5 shows an example of this coherence-based filtering of the frequency response Λ.

Upon termination of the measurements with various swirl rings, the test seals are removed from the test stand and their geometry altered. The influence of the number of tips, the gap and the chamber height is measured step-by-step. Examination is made of straight-through labyrinths and comb-groove labyrinths in two different diameters as well of stepped labyrinths and various honeycombs. In addition to the difference between rotating and stationary sealing tips, the influence of various swirl brakes and of abradable rotor coatings is examined.

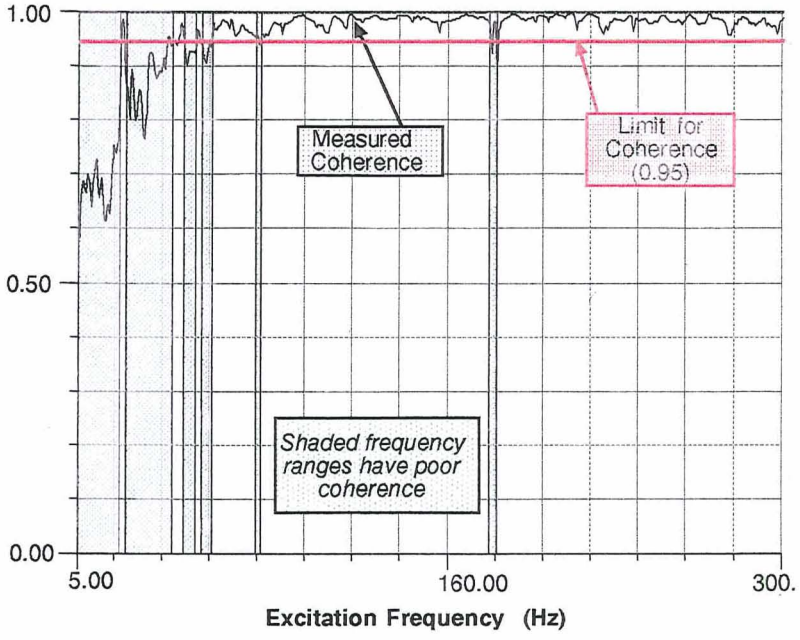

Fig. 5 Coherence-based filter function

4 Results of experiments

A test cycle in accordance with fig. 6 is performed for each test assembly. The inlet pressure, the pressure ratio and the speed are made to vary. The inlet swirl into the labyrinth depends on the inlet volume flow and therefore on the pressure ratio. The inlet swirl is made to vary independently of all of the other parameters by exchanging the swirl ring and repeating the entire test cycle.

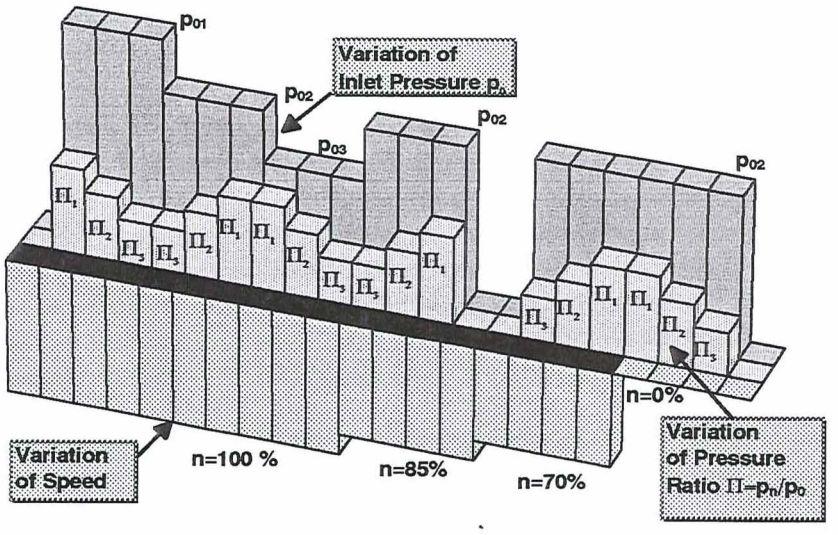

Fig. 6 Parameter changes during a test cycle

The purpose of the first part of the test cycle is to check the density-proportionality of the labyrinth coefficients.
Fig. 7 shows that this density-proportionality is actually satisfied even at high densities. Tests can be carried out up to the operating range of 70 bar set on the pressure controllers. Higher pressures result in short testing times owing to the limited gas supply available. The variation in the pressure ratio $\Pi=p_N/p_0$ in fig.6 takes place in accordance with the number of sealing tips. For long seals of balance pistons, pressure ratios of Π=0.4, 0.6, 0.8 are set. The pressure ratios are Π=0.7, 0.8, 0.9 for short shroud labyrinths.

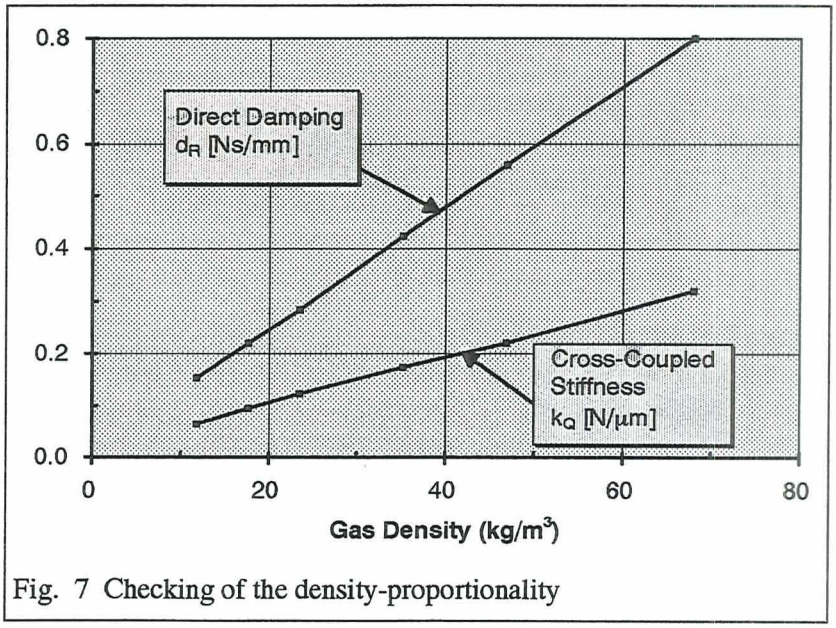

Fig. 7 Checking of the density-proportionality

Fig. 8 shows a typical result for a test point. The graphical output of the overall FRF is produced for each test point since it allows an excellent "visual" inspection of the curve-fitting and, where required, enables manual corrections to be made. It is conspicuous that the cross-coupled damping (slope of the real component of Λ) is in no way negligibly small, as is assumed in some literary references. Even though, just as the direct stiffness, it primarily influences the rotor stiffness and does not have a direct influence on the stability and is therefore of subordinate importance, it may in terms of value be even larger than the direct damping, as in the example shown below.

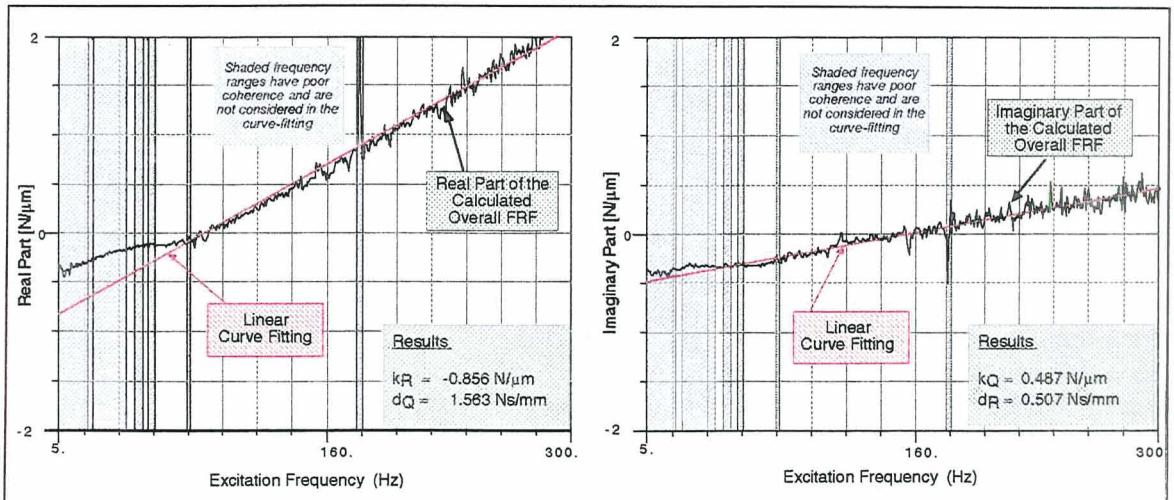

Fig. 8 Test point, representation of eq. (16) with curve-fitting

On the whole, it should be noted that good coherences cannot be attained in the low frequency range f<45.Hz and that there the frequency response deviates markedly from the linear form. In the case of the reference measurements, on the other hand, the coherence is virtually identical to "one" throughout the entire frequency range.

This range of poor coherence is made to fade out by using the above-described filter function for the curve-fitting in order that the determined labyrinth coefficients can remain unaffected by it. In view of the fact that the measured frequency response in this range is normally smaller in terms of absolute value than the value of the linear regression, the forces which arise at low frequencies are smaller than those calculated and, therefore, this fact does not represent any design risk. It becomes clear from fig. 8 that those evaluation procedures which only make use of the information relating to certain frequencies may cause one to arrive at different results than those obtained from the procedure used here which takes account of the system response over a larger frequency range.

With the intermediate gear utilised at present, running can take place at circumferential velocities of up to 102. m/s or 157. m/s, depending on the labyrinth diameter. With the comb-groove labyrinth the cross-coupled stiffness k_Q at up to approx. 50. m/s, is hardly dependent on the circumferential velocity. Where the circumferential velocities are higher, the linear dependency increases considerably, cf. fig. 9.The direct damping d_R, on the other hand, is weakly dependent on the circumferential velocity over the whole range.

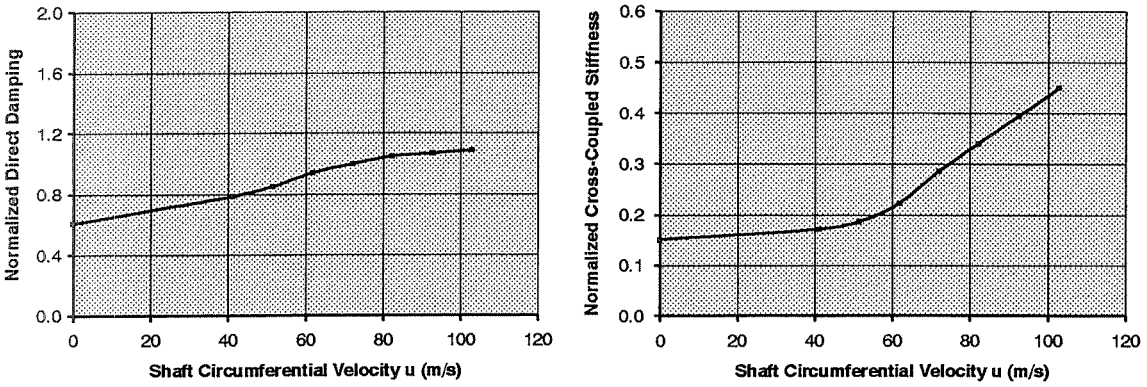

Fig. 9 Influence of circumferential velocity on cross-coupled stiffness and direct damping

The inlet swirl into the labyrinth likewise has only a small effect on the direct damping. Even so, the inlet swirl into the labyrinth, as is generally known, is a main influencing variable as regards the cross-coupled stiffness, with the parameter sensitivity being highly variable for different types of labyrinth. The obvious conclusion is to reduce this destabilising influence by using swirl brakes. The tests demonstrated that the use of a swirl brake with aerodynamically optimised channels enables the cross-coupled stiffness to be reduced more strongly than by using the familiar type with radial channels. The efficiency of the swirl brakes is highly dependent on the circumferential velocity and on the pressure ratio, cf. fig. 10.

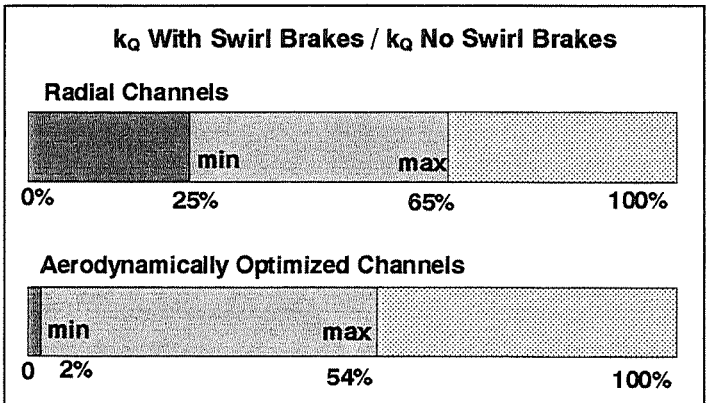

Fig. 10 Reduction of cross-coupled stiffness by swirl brakes, depending on Π, u_w

Fortunately, the direct damping is only slightly affected by the swirl brakes. Therefore, swirl brakes have a clear positive impact on rotor stability.

Even though, for the sake of simplicity, in this report only the identification equations were derived for the special case of a centric rotor position, measurements and analysis with the general equations were also conducted for an eccentric rotor. Fig. 11 indicates the stiffnessess for an eccentricity

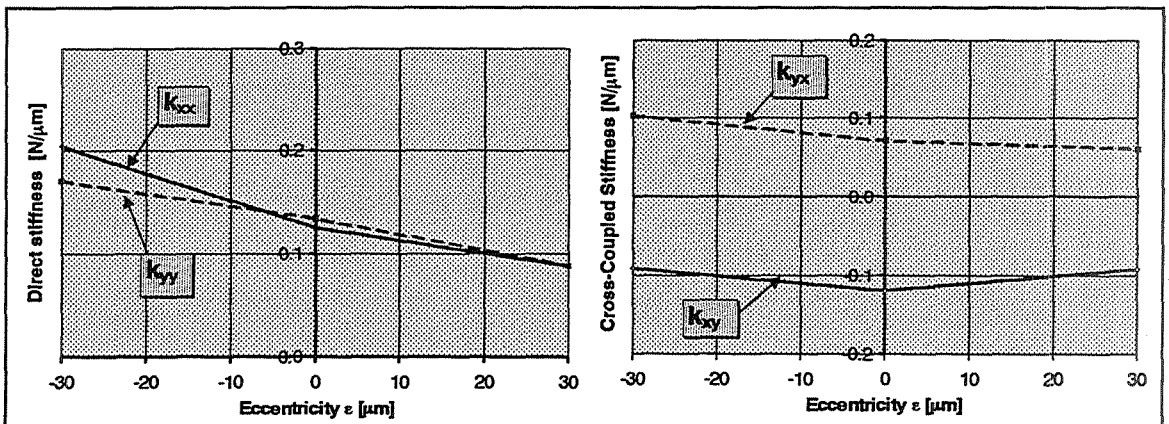

Fig. 11 Stiffnesses for an eccentric rotor

of 30 µm. Both elements of the secondary diagonals k_{xy} and k_{yx} are of more or less equal size as regards their absolute values and, as expected, have opposing signs. Contrary to the main diagonal elements, the values of k_{xy} and k_{yx} only undergo slight alteration with eccentricity. There therefore appears to be every justification for designing rotors with the labyrinth coefficients for the centric position. The influence of eccentricity can be taken into account, as an initial approximation, using correction factors from those measurements.

When evaluating the labyrinth coefficients, the so-called whirl-frequency ratio is often used in literature

$$f = \frac{k_{xy}}{\Omega \cdot d_{xx}} \tag{19}$$

with Ω as the rotational frequency. For fixed-arc journal bearings, f is an inherent stability parameter. For a comparison of labyrinth seals, on the other hand, we have had very good experience with direct plotting of the imaginary part

$$Im\{\Lambda\} = \omega \cdot d_R - k_Q$$

cf. eq. (16).
In the case of a harmonic motion, this representation corresponds directly to the destabilising tangential force, relative to the amplitude of the vibration:

$$F_{exc}/A = -\omega \cdot d_R + k_Q \tag{20}$$

Where this relative force is positive, it acts in the direction of rotor movement and destabilises this movement. If the force is negative, the damping predominates and the movement is stabilised.

Fig. 12 shows a qualitative comparison between a comb-groove labyrinth and a straight-through labyrinth. The comb-groove labyrinth has a considerably smaller cross-coupled stiffness k_Q but also a lower damping d_R. At individual test points, k_Q and d_R of the comb-groove labyrinth are smaller than those for the straight-through labyrinth by more or less the same percentages. The whirl-frequency ratio according to eq. 19 is thus of equal magnitude for both seals and it is therefore not possible to make any statement as to which seal is more favourable.

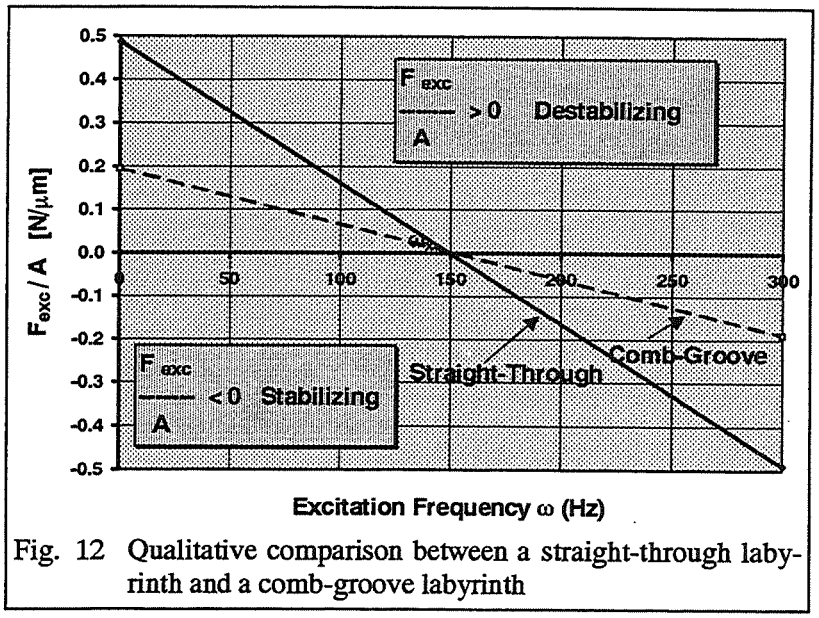

Fig. 12 Qualitative comparison between a straight-through labyrinth and a comb-groove labyrinth

Fig. 12 shows, however, that up to the frequency ω_x the comb-groove labyrinth produces a smaller degree of destabilisation than does the straight-through labyrinth. Modes of vibration with natural frequencies above ω_x become stabilised. It is therefore advantageous to design rotors to be as rigid as possible, i.e. with a high natural frequency. It can then happen, however, in the case of very stiff rotors that the rigid-body mode becomes destabilised because its natural frequency is usually lower than that of the first flexural mode.

5 Summary

The most important aim of this development project was to make available reliable data for calculating the stability behaviour of industrial turbocompressors.
This aim was achieved by means of a test stand which enables original conditions to be simulated in every respect. The magnetic bearings used make it possible to generate realistic vibration conditions and, at the same time, represent the system of measurement for the gas forces acting on the rotor. The influence of all important paramters was analysed for various types of seals. In the frequency range under consideration, i.e. up to 300 Hz, the newly developed evaluation method only takes account of those points with very good coherence. The graphic display of the numerically determined results allows a "visual check" of the curve-fitting in the frequency range to be made.
These results not only enable a precise and reliable design to be made but also allow minimisation of the destabilising forces. This forms the basis for the designing of safe and reliable turbocompressors.

Note

The authors wish to thank the management of Mannesmann Demag Compressors Division for authorising the publication of this development project.

6 Literature

[1] *Athavale, M.M., Przekwas, A.J., Hendricks, R.C.:* A 3D-CFD Code for Accurate Prediction of Fluid Flows and Fluid Forces in Seals, Rotordynamic Instability Problems in High-Performance Turbomachinery, 1993, NASA Conf. Publ. 3239, pp.137-148

[2] *Weiser, P., Nordmann, R.:* Determination of Rotordynamic Coefficients for Labyrinth Seals and Application to Rotordynamic Design Calculations, Rotordynamic Instability Problems in High-Performance Turbomachinery, 1990, NASA Conf. Publ. 3122, pp.203-222

[3] *Millsaps, K.T., Martinez-Sanchez, M.:* Rotordynamic Forces in Labyrinth Seals: Theory and Experiment, Rotordynamic Instability Problems in High-Performance Turbomachinery, 1993, NASA Conf. Publ. 3239, pp.179-208

[4] *Kwanka,K., Ortinger,W., Steckel,J.:* Calculation and Measurement of the Influence of Flow Parameters on Rotordynamic Coefficients in Labyrinth Seals, Rotordynamic Instability Problems in High-Performance Turbomachinery, 1993, NASA Conf. Publ. 3239, pp.209-218

[5] *Millsaps, K.T., Martinez-Sanchez, M.:* Static and Dynamic Pressure Distributions in a Short Labyrinth Seal, Rotordynamic Instability Problems in High-Performance Turbomachinery, 1990, NASA Conf. Publ. 3122, pp.135-146

[6] *Nordmann,R., Weiser,P.:* Evaluation of Rotordynamic Coefficients of Look-Through Labyrinths by Means of a Three Volume Bulk Flow Model, Rotordynamic Instability Problems in High-Performance Turbomachinery, 1990, NASA Conf. Publ. 3122, pp.147-164

[7] *Scharrer,J.K.:* A Comparison of Experimental and Theoretical Results for Labyrinth Gas Seals, Doctoral Dissertation, Texas A&M University, 1987

[8] *Childs, D.W., Ramsey, C.:* Seal-Rotordynamic-Coefficient Test Results for a Model SSME ATD-HPFTP Turbine Interstage Seal with and without a Swirl Brake, Rotordynamic Instability Problems in High-Performance Turbomachinery, 1990, NASA Conf. Publ. 3122, pp.179-190

[9] *Benckert,H.:* Strömungsbedingte Federkennwerte in Labyrinthdichtungen, Doctoral Dissertation, Universität Stuttgart, 1980

[10] *Thieleke, G., Stetter, H.:* Experimental Investigations of Exciting Forces caused by Flow in Labyrinth Seals, Rotordynamic Instability Problems in High-Performance Turbomachinery, 1990, NASA Conf. Publ. 3122, pp.109-134

[11] *Childs, D.W.:* Turbomachinery Rotordynamics, Phenomena, Modeling & Analysis, John Wiley & Sons, Inc., 1993

[12] *Childs, D.W., Scharrer, J.K.:* Experimental Rotordynamic Coefficient Results for Teeth-on-Rotor and Teeth-on-Stator Labyrinth Gas Seals, ASME-Paper 86-GT-12

[13] *Childs, D.W., Baskharone, E., Ramsey, C.:* Test Results for Rotordynamic Coefficients of the SSME HPOTP Turbine Interstage Seal with Two Swirl Brakes, Rotordynamic Instability Problems in High-Performance Turbomachinery, 1990, NASA Conf. Publ. 3122, pp.165-178

[14] *Wright, D.V.:* Labyrinth Seal Forces on a Whirling Rotor, Rotor Dynamical Instability, ASME, New York, 1983, pp. 19-31

[15] *Wagner, N.G., Pietruszka, W.D.:*Identification of Rotordynamic Parameters on a Test Stand with Active Magnetic Bearings, Proceedings of the First International Symposium on Magnetic Bearings, Zurich, June 1988, pp. 289-299, Springer-Verlag

[16] *Murphy, B.T., Scharrer, J.K., Sutton, R.F.:* The Rocketdyne Multifunction Tester - Part I: Test Method, Rotordynamic Instability Problems in High-Performance Turbomachinery, 1990, NASA Conf. Publ. 3122, pp.363-374

[17] *Schweitzer,G., Traxler,A., Bleuler,H.:* Magnetlager, Grundlagen, Eigenschaften und Anwendungen berührungsfreier, elektromagnetischer Lager, Springer-Verlag, 1993

[18] *Ackermann, J.:* Abtastregelung, Springer-Verlag, 1983

[19] *Pietruszka, W.D.:* Zeitdiskrete Schwingungsbeeinflussung magnetisch gelagerter Rotoren mit Mikrorechnern, VDI-Berichte Nr. 603, VDI-Verlag, 1986

[20] *Herlufsen, H.:* Dual Channel FFT Analysis (Part I), Bruel&Kjaer Technical Review No 1, 1984

A STUDY ON DYNAMIC CHARACTERISTICS OF DOUBLE SPIRAL GROOVED SEALS

H. Iwatsubo, T. Nishino, H. Ishimaru
Kobe University
Kobe, Japan

Abstract

Double Spiral Grooved Seal(DSGS) is often used for pumps because of lower leakage and removal of impurities through the groove path. Thus, it is important to investigate the dynamic characteristics of DSGS. In this study, the fluid force induced by DSGS is experimentally and theoretically investigated. In the experimental study, the fluid forces induced by DSGS with different helix angles are measured under various conditions such as the pressure difference between inlet and outlet of the seal, preswirl velocity and the ratio of whirling speed to rotating speed of the rotor. In the theoretical study, different models are considered for static and dynamic analysis. In the static analysis, a three-layer bulk flow in which the flow in DSGS is divided into two groove flows and a clearance flow is introduced. The results of the static analysis are used for the dynamic analysis. In the dynamic analysis, however, DSGS is looked upon as a circumferential grooved seal with grooves on both rotor and stator. At that time, the governing equations are derived using continuity and momentum equations. These equations are solved numerically by using the perturbation method. The results show that the calculated tangential forces are good agreement with the experimental ones but the radial forces don't agree as well.

1. Introduction

A turbomachinery such as a pump tends to be operated at high speed and high pressure. Under these conditions, the fluid forces occuring in non-contacting seals become larger, and these forces can sometimes cause an unstable vibration in the turbomachinery. Therefore, the design of seals for high speed and high pressure turbomachinery seeks not only good seal performance, but also stable dynamic characteristics.

Spiral grooved seals (with grooved rotor, grooved stator, or with grooves on both rotor and stator) are widely used in turbopumps because of lower leakage due to its pumping effect, and removal of impurities through the grooves. The pumping effect acts upstream with respect to the normal leakage flow. Several studies on the dynamic characteristics of single spiral grooved seals have been published by Iwatsubo et al. (Ref.1,2) and Childs et al. (Refs.3,4). However, knowledge about double spiral grooved seals with grooves on both rotor and stator is very scarce. Kanki et al. carried out experimental research to mesuare the static and dynamic characteristics of DSGS with different lengths.(Ref.5)

The object of this study is to investigate the dynamic characteristics of DSGS both experimentally and theoretically. In the experimental study, the leakage flow for five types

of DSGS are measured. All the seals have the same nominal clearance and groove depths but different helix angles. The fluid forces are measured under various conditions such as preswirl velocities, pressure difference between inlet and outlet of the seal, rotating speed, and whirling speed. In the static analysis, a three-layer bulk flow is introduced in which the flow in DSGS is divided into two groove flows and a clearance flow. In the dynamic analysis, for simplicity, the DSGS is looked upon as consisting of parallel grooved seals with grooves on both rotor and stator. The parallel grooved seal is divided into land parts and groove parts. The governing equations are derived using continuity and momentum equations for each part. These equations are solved numerically by using the perturbation method. The fluid forces acting on the rotor are obtained by integrating pressure distributions. Finally, the results obtained by the theory are compared with the experimental results.

2. Nomenclature

B : Groove depth (m)
C : Nominal seal radial clearance (m)
D : Diameter of rotor (m)
h : Thickness of fluid film (m)
L : Seal length (m)
L_l, L_g : Land and groove lengths (m)
m, n : Constants of friction factors
p : Fluid pressure (Pa)
Q : Leakage (m^3/s)
R : Radial of rotor (m)
r : Radial coordinate
r_0 : Whirling amplitude of rotor (m)
t : Tangential coordinate
u : Circumferential velocity (m/s)
w : Axial velocity (m/s)
z : Axial coordinate
β : Helix angle (rad)
θ : Circumferential coordinate
λ : Friction factor
ξ : Loss coefficient
ρ : Fluid density
τ : Shear stress (N/m^2)
Ω : Whirling angular velocity (rpm)
ω : Rotating angular velocity (rpm)

Subscripts

- c : Clearance flow
- d : Boundary layer between clearance flow and groove flow
- e : Equivalent
- in : Entrance
- l : Land
- r : groove flow on rotor
- s : groove flow on stator
- 0 : Zeroth perturbation
- 1 : First perturbation

3. Test Apparatus and Measurement

Figs.1,2 show the assembly of the test apparatus and the layout of the facility, respectively. The working fluid, which is water, is injected into the apparatus through three pairs of preswirl passages to yield different swirl velocities as shown in the cross section C. The water passes through the seal, then it flows from the outlets. The water is continuously added to the tank in order to keep the temperature constant.

The bearing parts, consisting of two ball bearings are used to yield the rotating and whirling motions of the rotor. An inside and an outside sleeve which are eccentric to each other are attached between the two bearings, as shown in cross section A. By rotating the two eccentric sleeves relatively, an arbitrary whirling amplitude can be adjusted in the range of 0 mm $\sim$ 0.1 mm. The sleeves of both sides are synchronously driven by a motor through timing belts to obtain a whirling motion. The whirling speeds and their directions are controlled by an electric inverter. The rotating speed and the direction of the rotor can also be changed by another motor controlled by an electric inverter.

The measuring system consists of the measurements of rotating and whirling speeds of the rotor, pressure, preswirl velocity, leakage, fluid force, and displacement of the rotor. The fluid forces acting on the stator are measured by pressure transducers and load cells, as shown in cross section B. The signals from the measuring instruments are recorded on a data recorder and analyzed by a computer.

The geometries of DSGS are shown in Figs.3 and 4. The specifications of DSGS are given in Table 1. The experimental conditions are shown in Table 2.

4.Analysis

This chapter is devoted to represent a method to calculate the seal forces. Fig.5 shows the coordinate system. The axial flow (in z direction) is considered as a pressure flow (Poiseulle flow) which is caused by the pressure difference between seal inlet and outlet, while the circumferential flow (in θ direction) is considered as a shear flow (Couette flow) which is caused by the rotor rotation. In this analysis, Hirs'turbulent lubrication theory is used as the basis for governing equations(Ref.6). In the static analysis, the flow is divided into three layers because the two groove flows and the clearance flow can be separated. In the groove flow, an equivalent clearance (C_s, C_r) is introduced. DSGS cross section is shown in Fig.6 to explain thr equivalent clearance. The equivalent clearance means a thickness in the groove flow when the rough surface is smoothed. The groove part before and after smoothing has the same order of magnitude. Fig.7 shows model of flows. In the groove

parts, the fluid flows along the groove. So the direction of the groove flow is decided by helix angle. ($w_{gr} = u_{gr}tan\beta, w_{gs} = -u_{gs}tan\beta$) In this way, DSGS are regarded as smooth seals. In the dynamic analysis, to simplify the calculation, DSGS is regarded as a parallel grooved seal with grooves on both rotor and stator. At that time, the fluid forces are obtained for a small motion of rotor with a circular orbit by integrating the pressure distributions around and along the rotor surface.

4.1. Governing Equations

For a fully developed turbulent flow regime, the assumptions for the analysis are introduced as follows:

1. The fluid is Newtonian and incompressible.
2. The temperature of the fluid in the seal clearance is constant.
3. The dimension of seal clearance is much smaller than those of the seal radius and seal length, so that the flow velocity and pressure drop in r-direction are considered to be small and can be omitted.
4. The curvature is small, so a centrifugal force is ignored.

The governing equations are obtained by considering the shear stresses acting at the wall and the surface of the flow (Fig.8). They are written as follows:

< Continuity equation >

$$\frac{h}{t} + \frac{1}{R}\frac{\partial(hu)}{\partial\theta} + \frac{\partial(hw)}{\partial z} = 0 \tag{1}$$

< Momentum equations >

Groove flow on the stator
< z-direction >

$$\rho h\left(\frac{\partial w}{\partial t} + \frac{u}{R}\frac{\partial w}{\partial\theta} + w\frac{\partial w}{\partial z}\right) = -h\frac{\partial p}{\partial z} - \frac{1}{2}\rho[\lambda_s w_s^2 + \lambda_d(w_s - w_c)^2] \tag{2}$$

<θ-direction >

$$\rho h\left(\frac{\partial u}{\partial t} + \frac{u}{R}\frac{\partial u}{\partial\theta} + w\frac{\partial u}{\partial z}\right) = -\frac{h}{R}\frac{\partial p}{\partial\theta} + \frac{1}{2}\rho[\lambda_s w_s^2/\tan\beta + \lambda_d(w_s - w_c)(w_s/\tan\beta + u_c)] \tag{3}$$

Clearance flow
< z-direction >

$$\rho h\left(\frac{\partial w}{\partial t}+\frac{u}{R}\frac{\partial w}{\partial \theta}+w\frac{\partial w}{\partial z}\right)=-h\frac{\partial p}{\partial z}-\frac{1}{2}\rho\lambda_d[(w_c-w_s)^2+(w_c-w_r)^2] \tag{4}$$

$<\theta$-direction $>$

$$\rho h\left(\frac{\partial u}{\partial t}+\frac{u}{R}\frac{\partial u}{\partial \theta}+w\frac{\partial u}{\partial z}\right)=-\frac{h}{R}\frac{\partial p}{\partial \theta}-\frac{1}{2}\rho\lambda_d[(w_c-w_s)(u_c+w_s/\tan\beta) + (w_c-w_r)(u_c-w_r/\tan\beta)] \tag{5}$$

Groove flow on the rotor
$<$ z-direction $>$

$$\rho h\left(\frac{\partial w}{\partial t}+\frac{u}{R}\frac{\partial w}{\partial \theta}+w\frac{\partial w}{\partial z}\right)=-h\frac{\partial p}{\partial z}-\frac{1}{2}\rho[\lambda_r w_r^2+\lambda_d(w_r-w_c)^2] \tag{6}$$

$<\theta$-direction $>$

$$\rho h\left(\frac{\partial u}{\partial t}+\frac{u}{R}\frac{\partial u}{\partial \theta}+w\frac{\partial u}{\partial z}\right)=-\frac{h}{R}\frac{\partial p}{\partial \theta}-\frac{1}{2}\rho[\lambda_r w_r(w_r/\tan\beta-\omega R) + \lambda_d(w_r-w_c)(w_r/\tan\beta-u_c)] \tag{7}$$

4.2. Leakage and Circumferential Velocity

For a small motion about the centered position, the clearance, pressure , and velocities are expanded in the perturbation variables as follows:

$$h=C+\varepsilon h_1, \qquad p=p_0+\varepsilon p_1$$

$$w=w_0+\varepsilon w_1, \qquad u=u_0+\varepsilon u_1 \tag{8}$$

where $\varepsilon=r_0/C$ is the small eccentricity ratio.

The axial and circumferential velocities in the steady state can be obtained by solving the zeroth-order equations.

Zeroth-Order Equations

$<$ z-direction momentum equations $>$
Groove flow on the stator

$$\frac{dp_{s0}}{dz}=-\frac{\rho}{2C_s}[\lambda_s w_{s0}^2+\lambda_d(w_{s0}-w_{c0})^2] \tag{9}$$

Clearance flow

$$\frac{dp_{c0}}{dz}=-\frac{\rho\lambda_d}{2C_c}[(w_{c0}-w_{s0})^2+(w_{c0}-w_{r0})^2] \tag{10}$$

Groove flow on the rotor

$$\frac{dp_{r0}}{dz} = -\frac{\rho}{2C_r}[\lambda_r w_{r0}^2 + \lambda_d (w_{r0} - w_{c0})^2] \tag{11}$$

$<\theta$-direction momentum equations $>$
Clearance flow

$$\frac{du_{c0}}{dz} + \frac{\lambda_d}{2C_c w_{c0}}(2w_{c0} - w_{s0} - w_{r0})u_{c0} =$$

$$\frac{\lambda_d}{2C_c w_{c0}}[(w_{c0} - w_{r0})(w_{r0}/\tan\beta + \omega R) - (w_{c0} - w_{s0})w_{s0}/\tan\beta] \tag{12}$$

The axial and circumferential velocities in the steady state can be obtained by solving the zeroth-order Eqs. (9)$\sim$(12). The following boundary conditions are considered in the analysis.

Boundary condition:

(1) The pressure loss at the seal entrance is defined by

$$\Delta p_{in} = \frac{1}{2}\rho(1 + \xi_{in}){w_0}^2 \tag{13}$$

where $\xi_{in} = 0.25$ is entrance loss factor.

(2) The pressure loss at the seal exit is defined by

$$\Delta p_{ex} = \frac{1}{2}\rho\xi_{ex}w_0^2 \tag{14}$$

where ξ_{ex} is exit loss factor.

The results have not considered the pumping effect which is a feature of spiral grooved seals. So the axial and circumferential velocities in the steady state must be re-examined by considering this effect. It is thought that the pumping effect is a variation in velocity caused by the transmission of momentum among the clearance flow, the groove flow, and wall. In the circumferential direction, the momentum of the groove flow is given by the clearance flow and is lost by the friction between the groove flow and the wall. In this way, the circumferential velocities (δu) in the groove flow caused by pumping effect are determined. The circumferential velocities considered the pumping effect are written as follows:

$<\theta$-direction $>$

Groove flow on the stator

$$u_{s0} = -w_{s0}/\tan\beta + \delta u_s \tag{15}$$

Groove flow on the rotor

$$u_{r0} = w_{r0}/\tan\beta + \delta u_r \tag{16}$$

In the groove flow, the axial velocities are determined immediately because the direction of flow is constant.

< z-direction >

Groove flow on the stator

$$w_{s0} = -u_{s0}\tan\beta = (w_{s0}/\tan\beta - \delta u_s)\tan\beta \tag{17}$$

Groove flow on the rotor

$$w_{r0} = u_{r0}\tan\beta = (w_{r0}/\tan\beta + \delta u_r)\tan\beta \tag{18}$$

The velocities in clearance flow are determined by substituting w_{r0}, w_{s0} into Eqs. (10),(12). Furthermore, the average values of axial and circumferential velocities w_{e0}, u_{e0} are given by the following equations.

$$w_{e0} = \frac{w_{s0}C_s + w_{c0}C_c + w_{r0}C_r}{C_e} \tag{19}$$

$$u_{e0} = \frac{-w_{s0}C_s/\tan\beta + u_{c0}C_c + w_{r0}C_r/\tan\beta}{C_e} \tag{20}$$

The leakage can be obtained by integrating the average values of axial velocity w_{e0}.

$$Q = \int_R^{R+C_e} 2\pi w_{e0} r dr = \pi w_{e0} C_e (2R + C_e) \tag{21}$$

4.3. Fluid forces

In the static analysis, the flow is divided into three-layer bulk flow. In the dynamic analysis, however, DSGS is considered as parallel grooved seals with grooves on both the rotor and the stator.(Fig.9) The parallel grooved seal is divided into land parts and groove parts. Each land and groove part is regarded as a smooth seal. Using the theory of smooth seal(Ref.7), the distribution of pressure perturbation can be obtained by solving the following first-order equations.

$$\frac{d\{\boldsymbol{X}\}}{dz}[\boldsymbol{A}] = \{\boldsymbol{F}\} \tag{22}$$

where,

$$\{\boldsymbol{X}\} = \{w_1\ u_1\ p_1\}^T$$

$$\{\boldsymbol{F}\} = \frac{r_0}{\varepsilon C}\begin{Bmatrix} j(\Omega - u_0/R) \\ -\lambda(u_0 - 0.5\omega R)/C \\ -\rho\lambda w_0^2/C - j\rho w_0(\Omega - u_0/R) \end{Bmatrix}$$

$$[A] = \begin{bmatrix} 0 & -j/R & 0 \\ 0 & \lambda/C \\ & +j(\Omega - u_0/R)/w_0 & -j/\rho w_0 R \\ 2\lambda\rho w_0/C \\ +j\rho(\Omega - u_0/R) & j\rho w_0/R & 0 \end{bmatrix}$$

$< Landparts >$

$$C = C_c, u_0 = u_{c0}, w_0 = w_{c0}$$

$< Grooveparts >$

$$C = C_e, u_0 = u_{e0}, w_0 = w_{e0}$$

To solve Eqs.(22), the following boundary conditions are considered by the theory of the circumferential grooved seals.(Ref.8)

(1) The boundary conditions of the pressure
The pressure variations at the first land entrance is defined by

$$p_{1l}(0) = -(1 + \xi_{in})\rho w_{c0} w_{1l(1)}(0) \tag{23}$$

at the other land entrances

$$p_{1l(i)}(0) = p_{1g_{(i-1)}}(L_g) - \xi_{inl}\rho w_{c0} w_{1l(i)}(0) \tag{24}$$

where ξ_{inl} is the inlet-loss coefficient at the land parts and is defined by following equations(Ref.9)

$$\xi_{inl} = 1 + 1.6068\left\{\frac{w_{c0}C_c}{\nu}\right\}^{-0.43} - \left(1 + 1.6068\left\{\frac{w_{c0}(C_c + 2L_g\tan\theta)}{\nu}\right\}^{-0.43}\right)\left(\frac{C_c}{C_c + 2L_g\tan\theta}\right)^2$$

at the land exit

$$p_{1g_{(i)}}(0) = p_{1l(i)}(L_l) - \xi_{exl}\rho w_{c0} w_{1g_{(i)}}(0) \tag{25}$$

where ξ_{exl} is

$$\xi_{exl} = \left(1 - \frac{C_c}{C_c + L_g\tan\theta}\right)^2$$

at the last land exit

$$p_{1(L)} = 0 \tag{26}$$

(2) The boundary conditions of the circumferential velocities

The perturbation of the circumferential velocity at the first land entrance is

$$u_{1l}(0) = 0 \tag{27}$$

at the other land entrances

$$u_{1l(i)}(0) = u_{1g_{(i-1)}}(L_g) \tag{28}$$

at the groove entrances

$$u_{1g_{(i)}}(0) = u_{1l(i)}(L_l) \tag{29}$$

(3) The boundary conditions of the axial velocities

Except for the first land entrance, perturbation of the axial velocity at the land entrance is

$$w_{1l(i)}(0) = \frac{C_c + L_g \tan\theta}{C_c} w_{1g_{(i-1)}}(L_g) \tag{30}$$

at the groove entrances

$$w_{1g_{(i)}}(0) = w_{1l(i)}(L_l) \tag{31}$$

Integrating the first-order pressure distribution in the axial and circumferential directions yields the following fluid forces.

$$\begin{aligned} F_r &= -\pi R\Big(\sum_{i=1}^{N}\int_0^{L_l} p_{1cl(i)}(z)dz + \sum_{i=1}^{N-1}\int_0^{L_g} p_{1cg_{(i)}}(z)dz\Big) \\ F_t &= -\pi R\Big(\sum_{i=1}^{N}\int_0^{L_l} p_{1sl(i)}(z)dz + \sum_{i=1}^{N-1}\int_0^{L_g} p_{1sg_{(i)}}(z)dz\Big) \end{aligned} \tag{32}$$

DSGS shows a different tendency from other seals (smooth seal,parallel grooved seal,single spiral grooved seal) according to measured tangential forces(F_t).(Fig.13) This figure shows the tangential force of DSGS draws a curve for changing whirling speed. So it is considered that in DSGS the change of circumferential velocity δu_Ω is caused by the whirling motion of the rotor. It seems that the change of velocity is influenced by helix angle, whirling speed, and whirling amplitude.(Figs.14,15,16) In the dynamic analysis, therefore, the effect is written as follows:

$$\delta u_\Omega = k_1 \frac{r_0}{C_e} \beta^{k_2} \Omega R \tag{33}$$

where k_1 and k_2 are constants which are determined by experiment. ($k_1 = 9.0, k_2 = 0.7$)

4.4. Friction Factors

It is difficult to obtain the friction factors theoretically because the flow in DSGS is complex. However, assuming that there is an equivalent clearance to the static analysis, the equivalent friction factors can be obtained from the measured leakage. Here, the friction factors between the groove flow and wall (λ_s, λ_r) are determined by using Hirs'formulation (Ref.6).

$$\lambda_s = n_s \left(\frac{w_s C_s}{\nu} \right)^{m_s} \left[1 + \left(\frac{u_s}{w_s} \right)^2 \right]^{\frac{m_s+1}{2}}$$

$$\lambda_r = n_r \left(\frac{w_r C_r}{\nu} \right)^{m_r} \left[1 + \left(\frac{u_r}{w_r} \right)^2 \right]^{\frac{m_r+1}{2}} \tag{34}$$

Where $(m_s, n_s) and (m_r, n_r)$ are constants depending on the stator and rotor surface roughnesses. These constants $(m_s, n_s) and (m_r, n_r)$ and the friction factor (λ_d) between the groove flow and clearance flow are determined according to the measured leakage. It is considered that the friction factor (λ_d) between groove flow and clearance flow of DSGS is same as one of the single spiral grooved seal (with grooved stator or grooved rotor).(Fig.10) So the friction factors is obtained from the measured leakage of double and single spiral grooved seals. And Table 3 shows the constants of the friction factors.

5. Results

5.1. Leakage

Fig.11 shows the experimental leakages for various seals. DSGS with small helix angle(β=0.83°) has lower leakage flow than smooth seal and the same as single spiral grooved seal with equal helix angle and parallel grooved seal. The reason seems to be that pressure losses due to groove geometry have an influence on leakage. A feature of spiral grooved seal is the pumping effect that drags the fluid upstream by rotating shaft and spiral groove. For small helix angles, however, rotating speed influences leakage only slightly.

Both double and single spiral grooved seals with large helix angle (β=10.0°) leak more than smooth seal at comparatively low rotating speed. And the leakage of DSGS decreases quickly with increasing rotating speed compared to single spiral grooved seal. The fluid flows through the spiral groove path more than seal clearance at low rotating speed. With increasing rotating speed, the pumping effect due to spiral groove is stronger (especially DSGS with large helix angle).

Fig.12 shows measured and calculated leakage. The analysis predicts leakage flows well.

5.2. Fluid Forces

This section obtains dynamic characteristics for various parameters. In this paper, radial and tangential components are used as shown Fig.5 to represent fluid forces. Positive radial force (F_r) tends to unstabilize the rotor system because it acts in the same direction as displacement (r_0). And positive tangential force (F_t) also has destabilizing effect because of producing a force in the direction of positive rotor whirl. Radial force has a lesser influence than tangential force because the rotor is supported by bearings in the turbomachinery. And negative whirling motion rarely occurs. So it is important to consider tangential force for positive whirling motion ($\Omega > 0$).

Comparision to other seals Fig.13 shows fluid force coefficients versus whirling/ro tating ratio for various seals. Radial force coefficients of each seals are negative and one of the smooth seal is larger than others. In this figure, the region which is enclosed by horizontal,vertical axes and curve F_t/r_0 indicates an unstable region. Unstable region of DSGS with large helix angle is larger than ones of other seals. Tangential force coefficient of DSGS draws a curve for whirling/ rotating ratio by an effect of the helix angle and preswirl velocity.

Effect of Whirling Amplitude Fig.14 shows an effect of whirling amplitude on the force coefficients changing whriling/ rotating ratio. The absolute values of the fluid forces linearly increased with the increse of whirling amplitude in other seals.(Ref.2,10) This means the force coefficient (F/r_0) is constant for change of whriling amplitude. However, in this figure, these results show that tangential force coefficients (F_t/r_0) of DSGS obviously vary. It is considered that circumferencial velocity is affected by whirling motion of the rotor.

Effect of Helix Angle To compare the effect of helix angle, the force coefficients of the five seals are illustrated in Fig.15. The increase of helix angle shifts F_r/r_0 toward the negative direction. F_t/r_0 changes from straight lines with negative slope to curve line with positive one as the helix angle increases. This means the unstable region is larger as the helix angle increases. In the tangential force coefficients (F_t/r_0), the theoretical values agree approximately with the experimental results.

Effect of Preswirl Velocity Fig.16(a)$\sim$(c) shows the effect of preswirl velocity on the measured force coefficients of three seals. The effect of preswirl velocities on the radial force coefficient is not obvious, but the effect on tangential force coefficient is very obvious. The positive preswirl velocity (in the rotating direction of rotor) shifts F_t/r_0 towards the positive direction; while the negative preswirl velocity (opposite to the rotating direction of rotor) shifts F_t/r_0 towards the negative direction. With increasing helix angle, F_t/r_0 is influenced considerably by preswirl velocity and the characteristic of F_t/r_0 is a curve.

6. Conclusions

In this paper, the static and dynamic characteristics of DSGS are investigated experimentally and theoretically. The conclusions are as follows:

(1) DSGS with small helix angle leaks less than smooth seal and similar to single spiral grooved seal with same helix angle and parallel grooved seal.

(2) The leakages of DSGS with large helix angle seals quickly decreases as the rotating speed increases.

(3) The analysis can predict the leakage very well.

(4) Unstable region of DSGS with large helix angle is larger than ones of other seals.

(5) The increase of helix angle shifts the radial force F_r toward the negative direction.

(6) F_t/r_0 draws a curve for whirling/ rotating ratio by the effect of large helix angle and preswirl velocity.

(7) The calculated results show a good qualitative and quantitative agreement with the measured results in tangential forces.

7. References

1. Iwatsubo,T., *et al.*, 'Theoritical Approach to Obtain Dynamic Characteristics of Noncontacting Spiral Grooved Seals', NASA CP2443(1986), pp.155

2. Iwatsubo,T., Sheng, B.C., and Ono,M., 'Experiment oF Static and Dynamic Characteristics of Spiral Grooved seals' NASA. CP-3122, (1990), pp.216

3. Childs, D., *et al.*, 'Test Results for Turbulent Annular Seals Using Smooth Rotors and Helically Glooved Stators',ASME J.,(1989), pp.313

4. Childs, D., *et al.*, 'Analysis for Rotordynamic Coefficients of Helically Glooved Turbulent Annular Seals', ASME J. of Teib. Vol. 109, pp.136

5. Kanki, H., and Kwakami, T., 'Experimental Study on the Static and Dynamic Characteristics of Screw Grooved Seals', ASME Design Tech. Conf. Pub. DE-Vol.2, 1987, pp.263

6. Hirs, G. G., 'A Systematic Study of Turbulent Film Flow', ASME. J. Lubr. Technol., (1974), pp.118

7. Sheng B.,'Static and Dynamic Characteristics of Noncoctacting Seals and their effect on the stability of Rotating Fluid Machineries', The graduate school of Science and Technology, Kobe Univ. (1991)

8. Iwatsubo,T., Ibaragi, R., 'Static and Dynamic Characteristics of Parallel-Grooved Seals', NASA. CP-2443, (1986), pp.99

9. Constantinescu, V. N., and Galetuse, S., 'Pressure Drop Due to Inertia Forces in Step Bearings', Trans. ASME. J. Lubr. Technol., January 1976, pp.167

10. Iwatsubo, T., Sheng, B.C., 'An Experimental Study on the static and Dynamic Characteristics of Damper seals', 3rd Proc. IFToMM Conf., (1990), pp.307

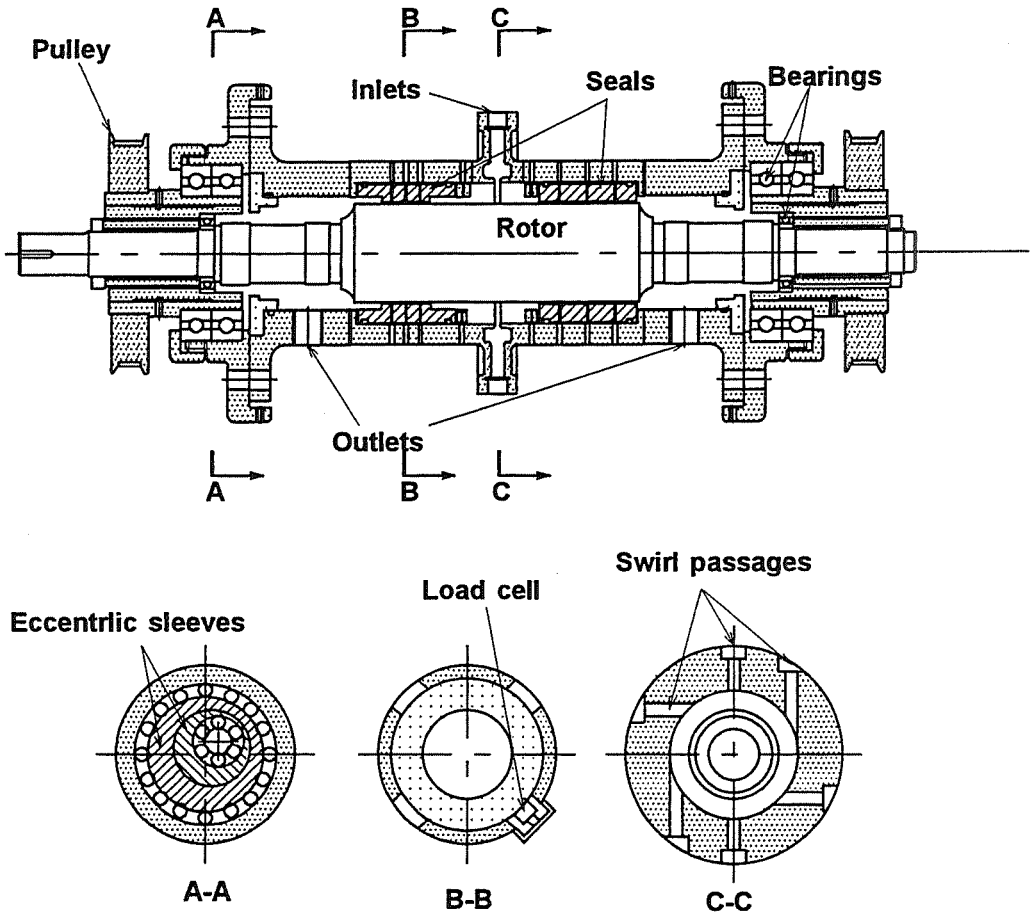

Fig.1 Test apparatus assembly

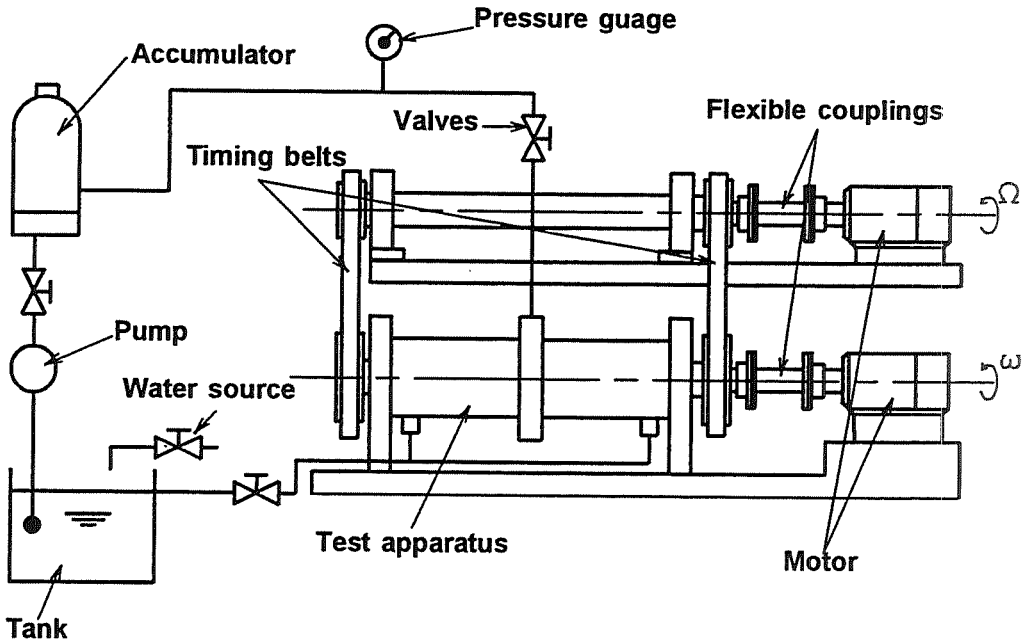

Fig.2 Test facility layout

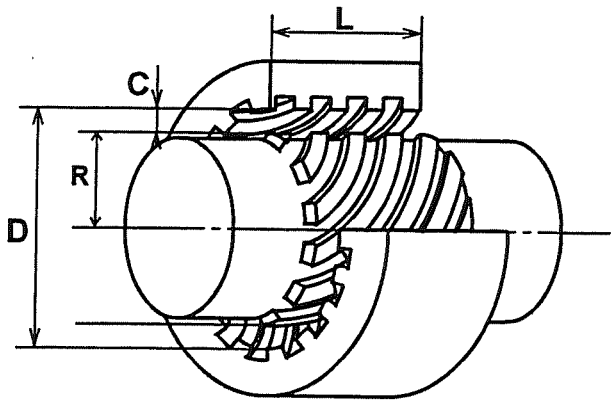

Fig.3 DSG seal

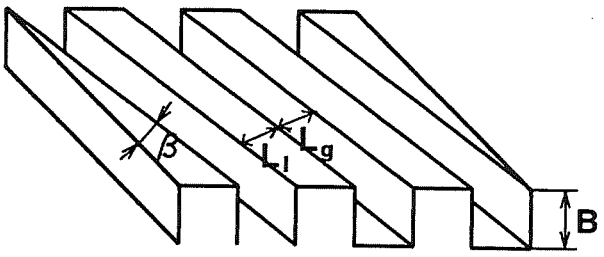

Fig.4 Configration of DSG seal

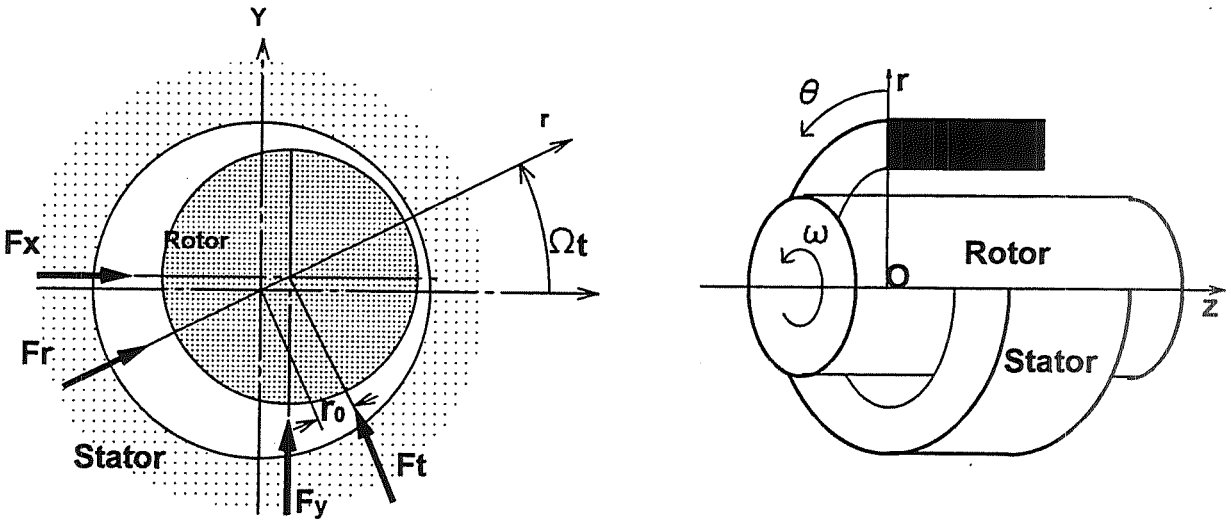

Fig.5 Seal and coordinates

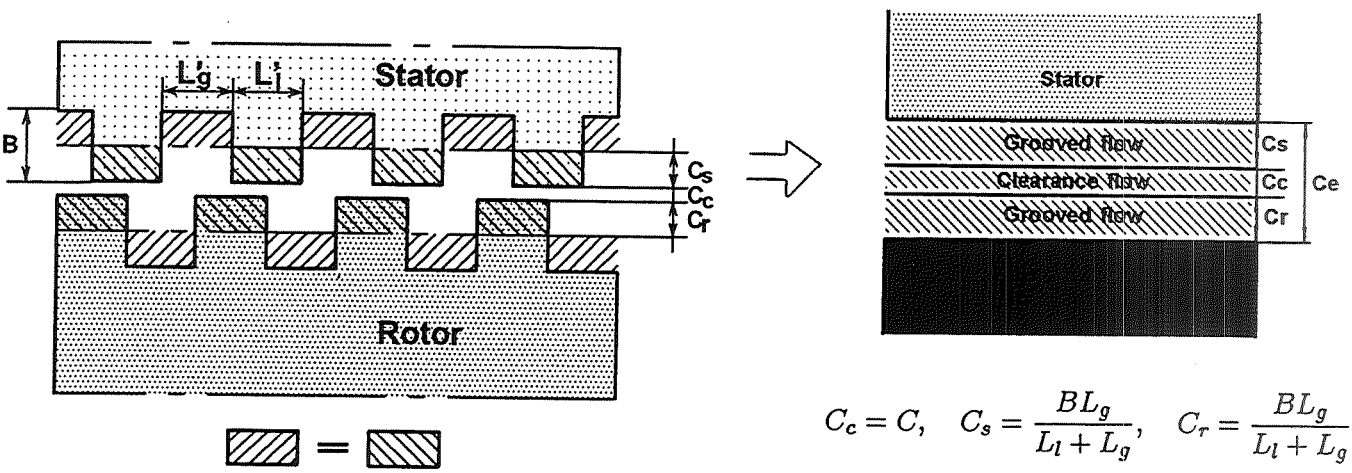

$$C_c = C, \quad C_s = \frac{BL_g}{L_l + L_g}, \quad C_r = \frac{BL_g}{L_l + L_g}$$

$$C_e = C_c + C_s + C_r$$

$$(L_l = L'_l \cos\beta, \quad L_g = L'_g \cos\beta)$$

Fig.6 Equivalent clearance

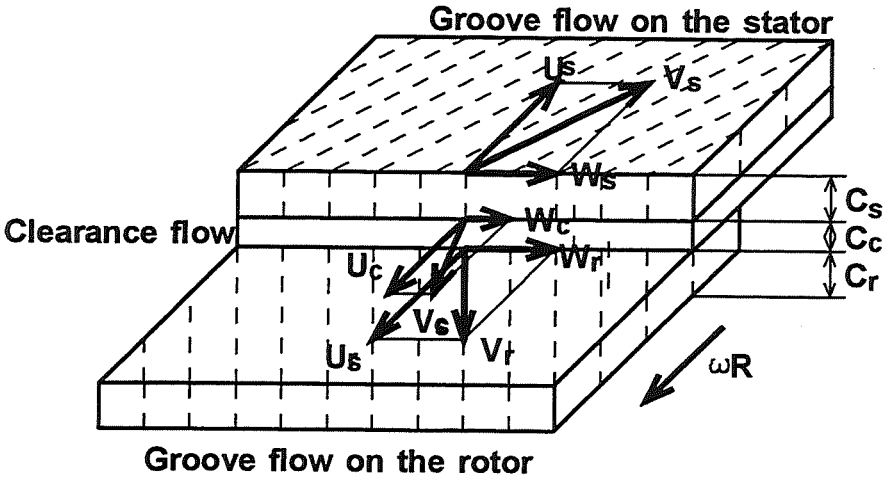

Fig.7 Model of flows for static analysis

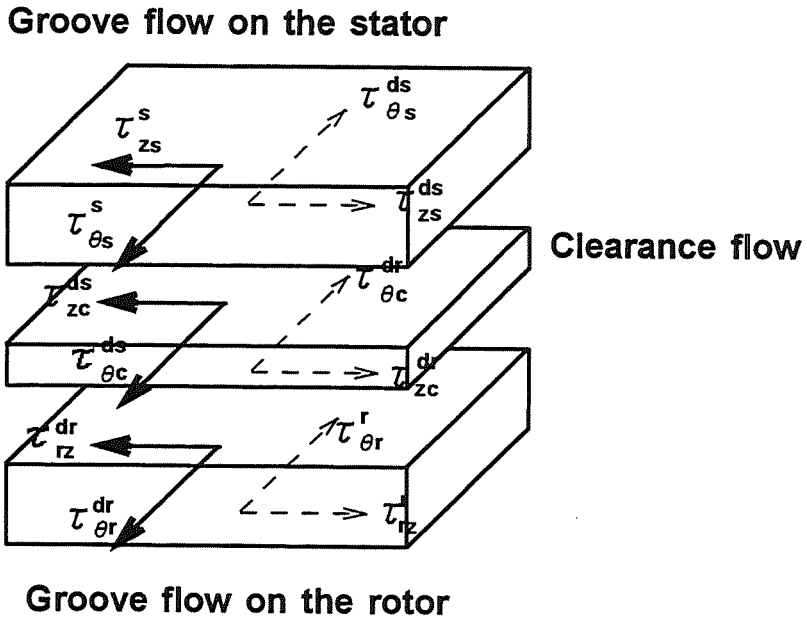

Fig.8 Shearing force on control volumes

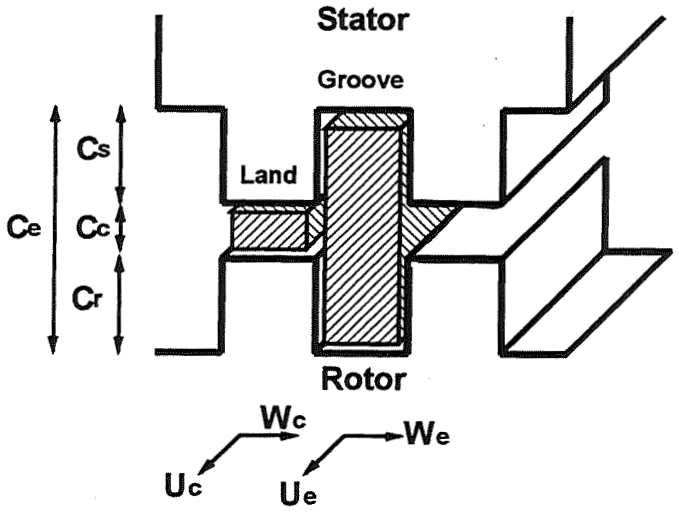

Fig.9 Model of flows for dynamic analysis

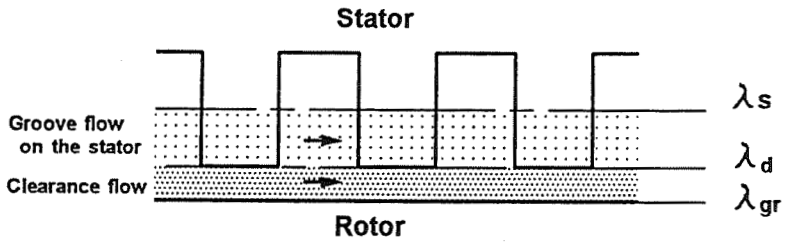

(a) Spiral grooved stator/Smooth rotor seal

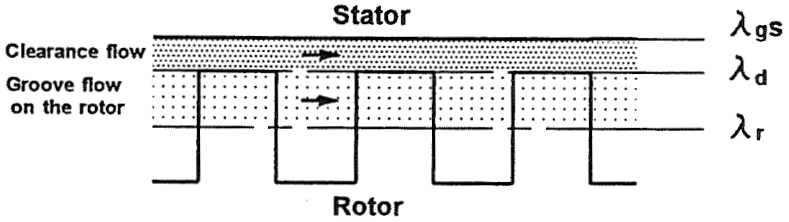

(b) Smooth stator/Spiral Grooved rotor seal

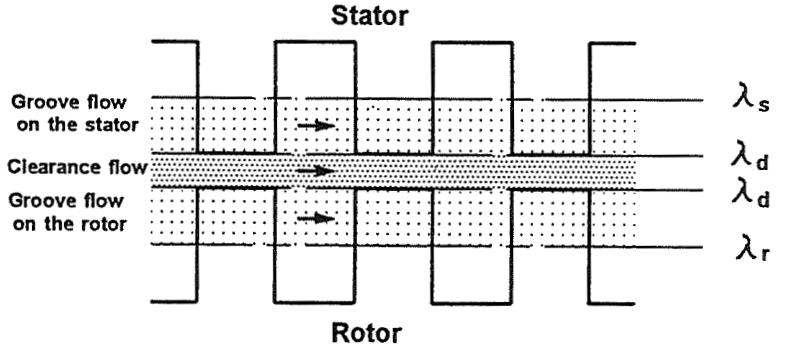

(c) Double Spiral Grooved rotor seal

Fig.10 Friction factors of spiral grooved seal

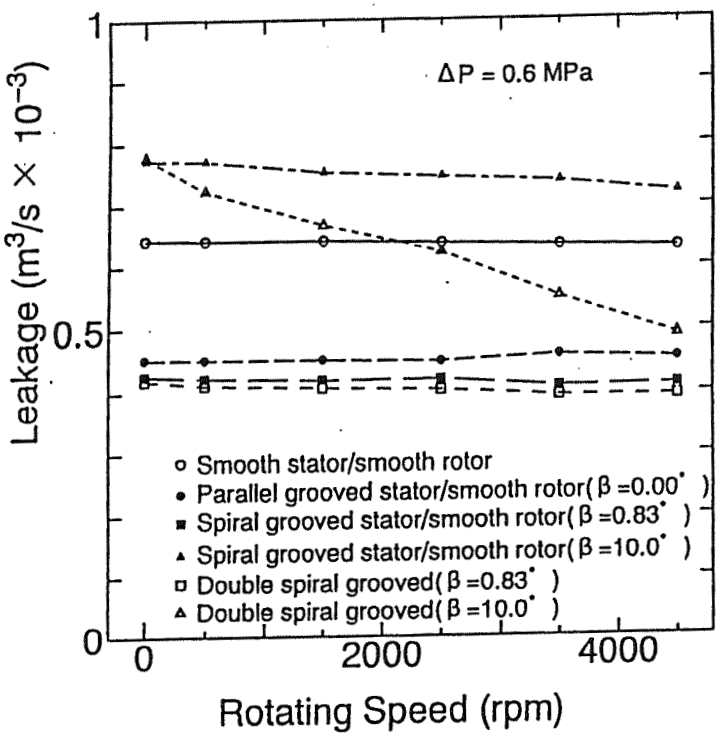

Fig.11 Measured leakages versus rotating speed

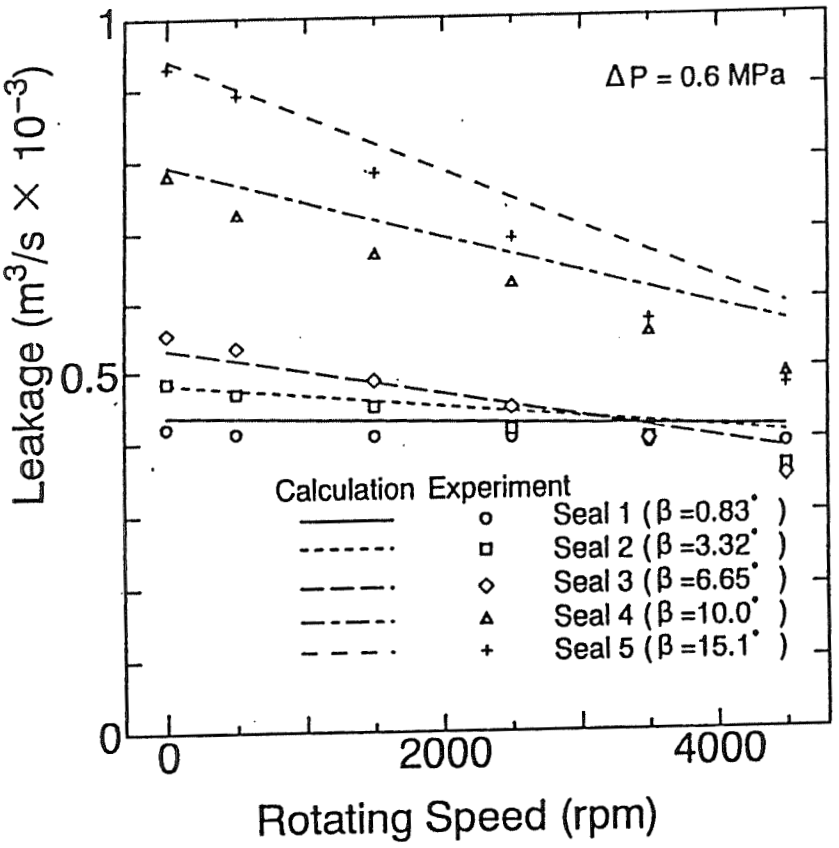

Fig.12 Measured and theoretical results for leakages

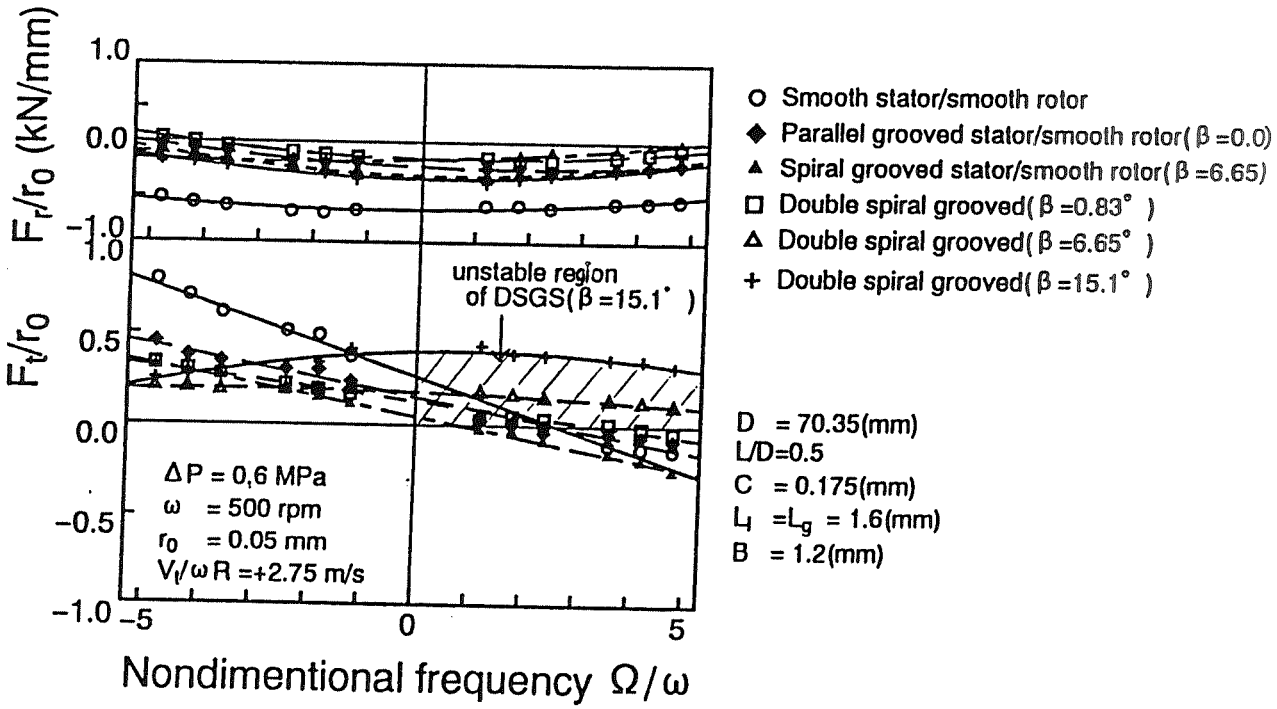

Fig.13 Fluid forces versus whirling/rotating ratio for various seals

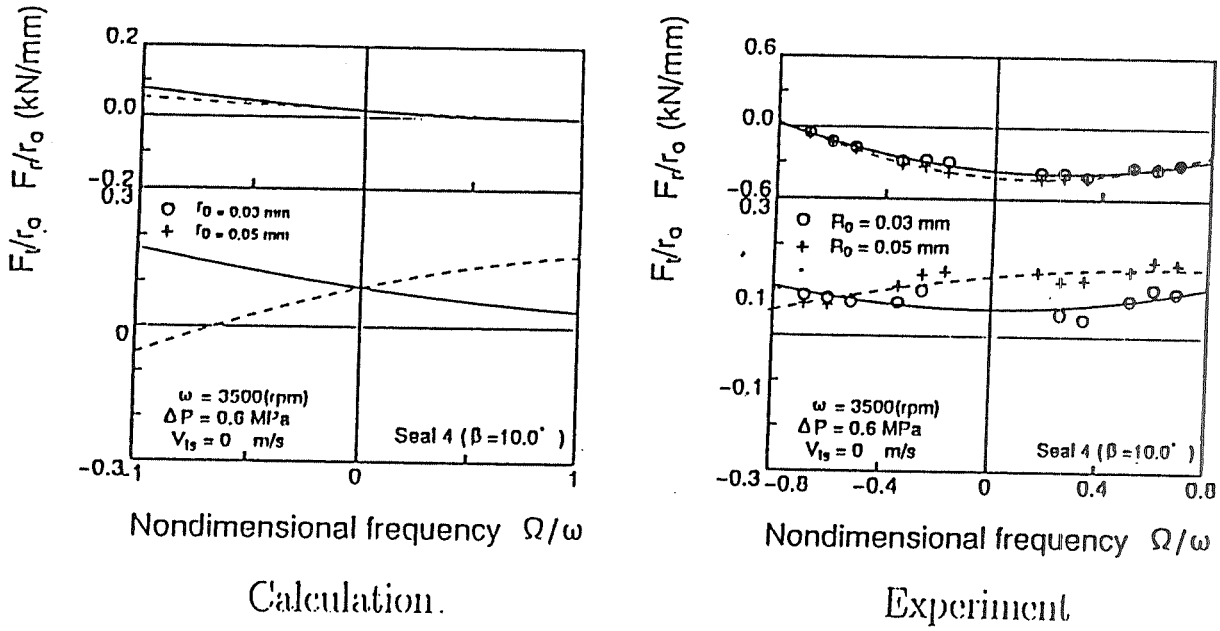

Calculation. Experiment

Fig.14 Fluid forces versus whirling/rotating ratio

(Parameter: Whirling amplitude of rotor)

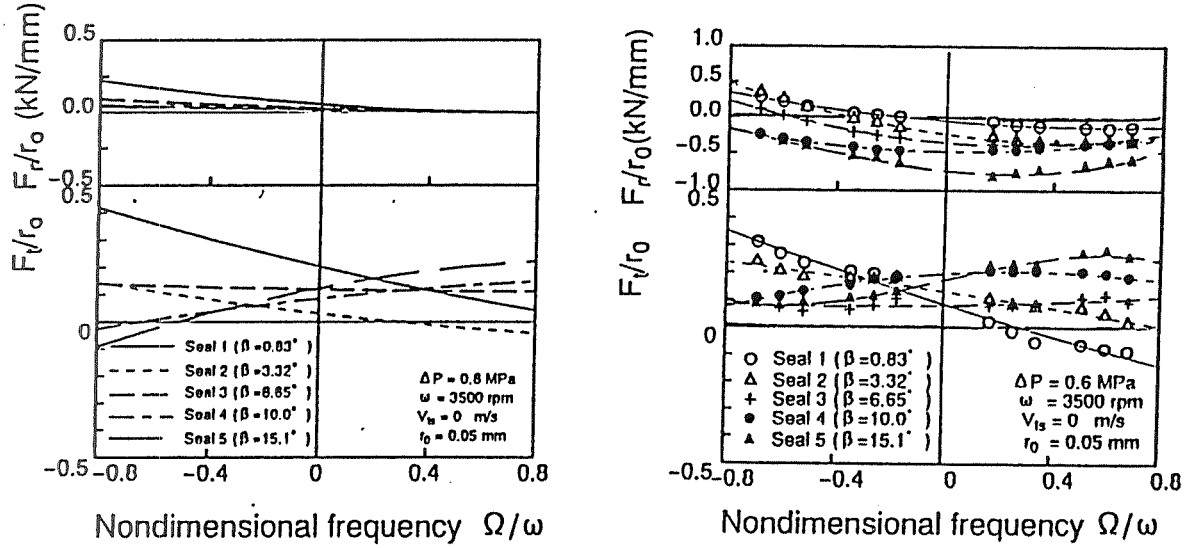

Fig.15 Fluid forces versus whirling/rotating ratio
(Parameter: Spiral angle)

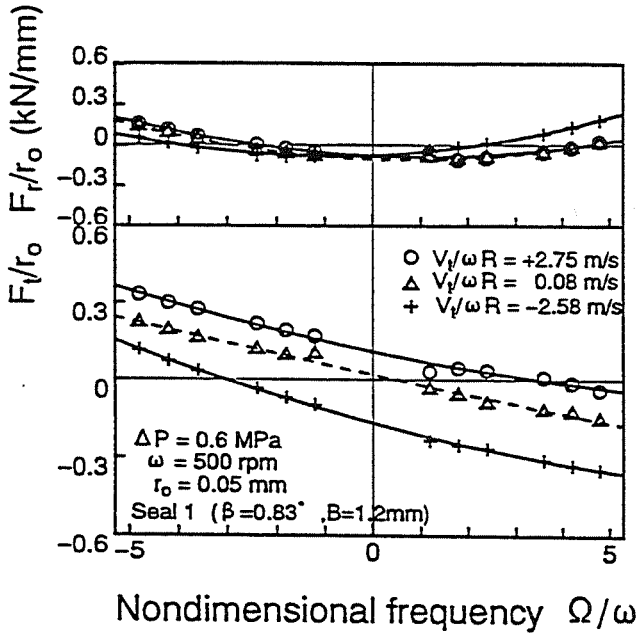

(a) Seal 1 (β=0.83°)

Fig.16 Fluid forces versus whirling/rotating ratio
(Parameter: Preswirl velocity)

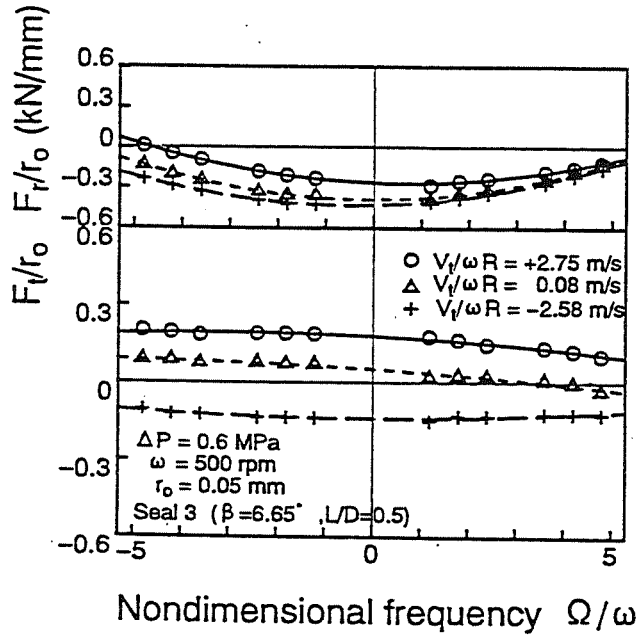

(b) Seal 3 (β=6.65°)

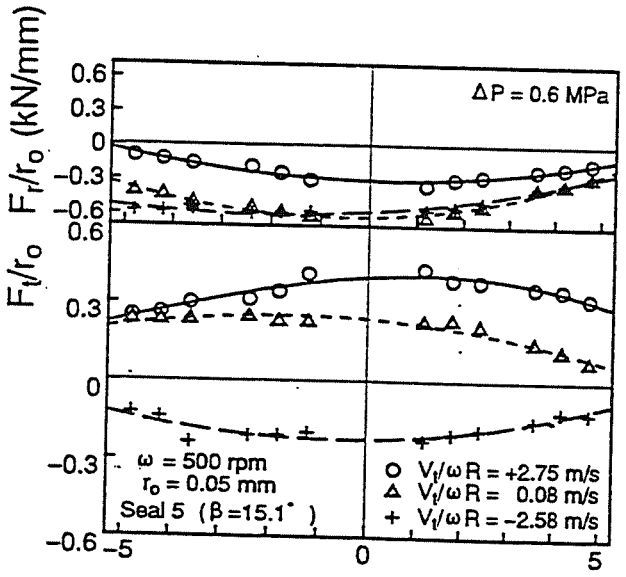

(c) Seal 5 (β=15.1°)

Fig.16 Fluid forces versus whirling/rotating ratio (Parameter: Preswirl velocity)

Table 1 Seal dimensions

Seal	$\beta(^o)$	D(mm)	L/D	C(mm)	B(mm)	L_l(mm)	L_g(mm)
Seal 1	0.83	70.35	0.5	0.175	1.2	1.6	1.6
Seal 2	3.32	70.35	0.5	0.175	1.2	1.6	1.6
Seal 3	6,65	70.35	0.5	0.175	1.2	1.6	1.6
Seal 4	10.0	70.35	0.5	0.175	1.2	1.6	1.6
Seal 5	15.1	70.35	0.5	0.175	1.2	1.6	1.6

Table 2 Experimental conditions

Pressure difference	ΔP(MPa)	0.3,0.6,0.9
Rotating speed	ω(rpm)	500 $\sim$ 3500
Whirling speed	Ω(rpm)	$\pm$600$\sim\pm$2400
Whirling Amplitude	$r_0(\mu$m)	30, 50
Temperature of Water	$T(^o$C)	19

Table 3 Constants of friction factors

Seal	$\beta(^o)$	n_s	m_s	n_r	m_r	λ_d
Seal 1	0.83	7460	-0.837	3306.07	-0.782	0.04
Seal 2	3.32	89.4	-0.406	15926.0	-0.925	0.04
Seal 3	6.65	1.34d5	-1.265	1.798d-3	0.946	0.04
Seal 4	10.0	8650	-1.074	7.369d-3	0.636	0.07
Seal 5	15.1	178	-0.669	7.793	-0.217	0.10

EXPERIMENTAL ROTORDYNAMIC COEFFICIENTS OF SHORT LABYRINTH GAS SEALS

K. Kwanka and M. Nagel
Technische Universitat Munchen
Munich, Germany

Abstract

In the design stage, the fluid-induced forces in labyrinth seals must be predicted exactly to avoid unstable vibrations of turbomachinery. For a validation of the used numerical codes, a comparison of the calculated with the measured dynamic coefficients is required. In addition, damping coefficients are necessary to realistically predict the destabilizing effects for certain seals and how this can be modified.

For short labyrinth gas seals only few measured data are available. With a new, recently presented identification procedure this lack of experimental data is reduced. The measured dynamic coefficients show the expected strong dependency on the entry swirl and the pressure ratio. For all seal geometries and test parameters presented in the paper the cross-coupled stiffness increases almost linearly along with the entry swirl. On the other hand the direct damping tends to be irregular. The influence of the seal on the stability is clearly different when the damping is considered, too.

Nomenclature

a	Amplitude of the vibrational mode
c_{U0}	Entry swirl
F_R, F_T	Radial, tangential force
i	Seal geometry
j	Number of cavities
$KNij$	Staggered labyrinth
K, C, M	Direct stiffness, damping, inertia coefficients
k, c, m	Cross-coupled stiffness, damping, inertia coefficients
n	Rotating speed
Δr	Change in direct stiffness of the magnetic bearing
R	Radius
q_0	Magnetic excitation at the stability limit without flow through the seal
q	Magnetic excitation with flow through the seal
$\Delta q = q_0 - q$	Change of magnetic excitation due to the flow through the seal
$TORij$; $TOSij$	Teeth on rotor, teeth on stator labyrinth
$u_0 = c_{U0}/R\omega$	Inlet circumferential velocity ratio
x, y	Coordinates of displacement
Ω	Whirl frequency
Ω_W	Whirl frequency ratio
$\omega = 2\pi n/60$	Rotating frequency

Introduction

Non-contacting labyrinth seals are used in turbomachinery to minimize the leakage flow between stationary and rotating parts. Long seals, for example, are placed in the balance piston or casing-ends section whereas short seals are usually interstage seals. As the power density of turbomachinery and, accordingly, the exciting forces increase, the possibility of unstable rotor vibrations must be avioded. The forces are generated by the flow through the seal and are usually described in a wellknown linearized formulation for small deflections out of the centered position.

$$\bar{F} = -\begin{pmatrix} K & k \\ -k & K \end{pmatrix}\begin{pmatrix} x \\ y \end{pmatrix} - \begin{pmatrix} C & c \\ -c & C \end{pmatrix}\begin{pmatrix} \dot{x} \\ \dot{y} \end{pmatrix} - \begin{pmatrix} E & e \\ -e & E \end{pmatrix}\begin{pmatrix} \ddot{x} \\ \ddot{y} \end{pmatrix} \qquad (1)$$

The formulation uses stiffness, damping and mass coefficients.The mass coefficients are usually neglected in gas seals. Many investigations focus on calculating or measuring these coefficients. Compared to liquid seals the experimental identification of the coefficients for gas seals is more difficult because of the low magnitude of the generated forces. The identification procedure requires a motion of the rotating rotor relative to the casing.

In his book on rotordynamics of turbomachinery Childs [1993] summarizes the few experimental approaches performed with gas seals. Wright [1993] uses a stiff shaft which is forced via actively controlled pushrods to perform a neutral conical whirling motion. The applied damping and stiffness forces include the force coefficients. The investigated seal geometry is of the teeth-on-stator type (TOS) with one cavity. The time-variant circular pressure distribution is measured by Millsaps and Martinez-Sanches [1993] to determine the dynamic stiffness and damping for a given amplitude. Due to a shaft-in-shaft arrangement the one cavity teeth-on-rotor seal (TOR) is whirling and rotating independently.

All the other papers on this issue (Childs et. al. [1986], Pelletti and Childs [1991]...) investigate more or less long labyrinth seals with cavity-numbers from 7 up to 16. The test-rigs employ very stiff and heavy rotors operated far below the stability limit. The motion of the rotating shaft relative to the casing is realized with eccentric inserts in shaft-in-shaft arrangements or external shakers. New setups (Matros, Neumer and Nordmann [1994], Wagner and Pietruszka [1988]) use stiff rotors carried in active magnetic bearings. The flow in the seals influences the dynamic system behavior which can be measured via the magnetic bearing control system. Until now, no measured coefficients with gas seals have been published. The asynchronous perturbation of a flexible rotor with an independently rotating unbalance was proposed by Bently and Muszynska [1982] with the purpose to identify rotordynamic coefficients of bearings or seals.

Procedure and Experimental Setup

A recently presented procedure (Kwanka and Mair [1995], Kwanka [1995a]) uses the change in the dynamic behavior of a flexible rotor caused by the flow through a seal to identify the rotordynamic coefficients. Starting point is a rotor of the Jeffcot type carried in fluid film bearings (fig. 1).

In the midspan position of the rotor a test-seal and a magnetic bearing is placed. The seal is the specimen for which the dynamic coefficients should be measured. With the magnetic bearing, fluid-like displacement-dependent direct and cross forces are generated and applied contactless to the rotor. The stiffness and the stability behavior of the rotor system can be altered magnetically.

The basic idea of the identification procedure consists in finding the change in the whirling frequency and in the stability limit caused by the fluid-induced forces in the test-seal. This change contains the dynamic coefficients. In a first step the whirl frequency and the stability limit of the Jeffcott without flow through the seal is measured. The stability limit is reached by increasing the cross-coupled stiffness of the magnetic bearing. At the stability limit the magnetic excitation is equal to the system damping minus the hydrodynamic bearing excitation.

In a next step, when fluid flows through the seal, the whirl frequency and the stability limit change due to the forces generated in the seal. The forces acting on the Jeffcot rotor whirling with the frequency Ω at the stability limit are displayed in fig.2. The exciting force generates the forward whirling modes and is counterbalanced by the damping force. With an excitation directed opposite to the rotation, the backward whirling modes are destabilized. The whirling frequency is approximately the natural frequency of the rotor and is given by the identity of the deflecting and the restoring force.

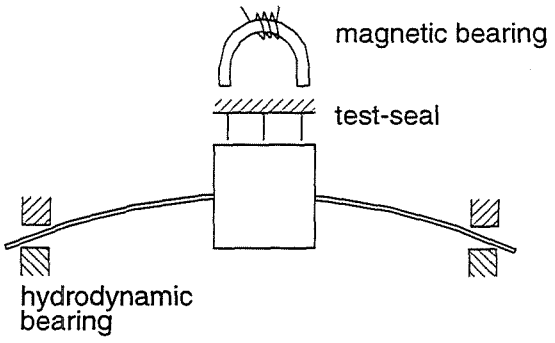

Fig. 1 Jeffcot rotor with the test-seal and the magnetic bearing

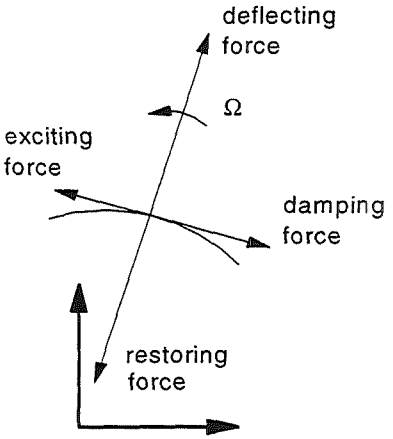

Fig. 2 Forces on a Jeffcot rotor at the stability limit

The change in the whirling frequency is compensated magnetically. When a circular whirling orbit is assumed, then the magnetic direct stiffness Δr, necessary for the compensation, is equal to the conservative dynamic coefficients.

$$\Delta r = \frac{F_R}{a} = -K - C\Omega + E\Omega^2 \tag{2a}$$

When the whirl frequency is held constant the modal amplitude a remains unchanged, too. In consequence, the only influence on the stability limit is due to the non-conservative dynamic coefficients. The change in magnetic excitation at the stability limit Δq can be expressed with dynamic coefficients.

$$\Delta q = \frac{F_T}{a} = k - C\Omega - e\Omega^2 \tag{2b}$$

The influence of the seal forces on the stability limit is shown in fig 3. A stiffer shaft leads to a higher whirl frequency and smaller modal deflection, which again causes an increase of the stability limit and the measured magnetic excitation q_0 at this point. With positive whirling frequencies, a forward excitation of the seal reduces the measured magnetic excitation by the value of Δq. When the seal excitation increases beyond the initial system damping, the rotor must be stabilized by changing the direction of magnetic excitation. On the other hand, the backward mode is stabilized by the seal excitation and the stability limit increases.

By repeating the measurement of Δr and Δq for three whirling frequencies, all the unknown six dynamic coefficients can be calculated. As mentioned above, with gas seals the mass coefficients are usually neglected. For the identification of the stiffness and the damping a

minimum of two measurements must be performed. The measured values come to lie on a straight line (fig. 4). The intersection with the abscissa indicates the stiffness and the slope of the line represents the damping.

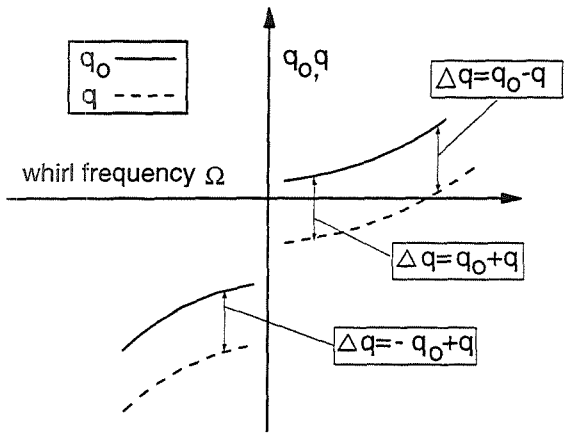

Fig. 3 The influence of the seal forces on the stability of the forward and the backward mode

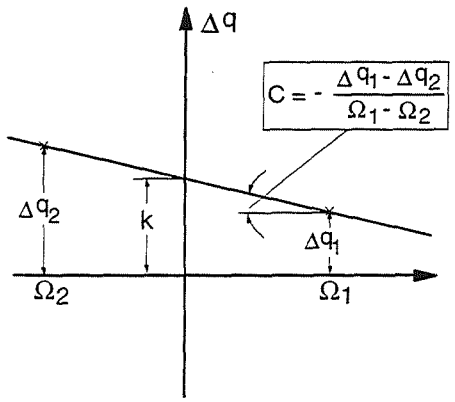

Fig. 4 The cross-coupled stiffness and the direct dampingof a gas seal

A new test rig was designed to check the identification procedure outlined above and to continue with systematic investigations of different types of seal-geometries and flow conditions (fig. 5). The test seal is placed in the central position of a slender shaft (∅ 23 mm). Two identical and easily removable seals are located symmetrically to the inflow region. Pressurized and metered air is fed through a replaceable guide vane ring into the seal and discharged to ambient.

The magnetic bearing is positioned as close as possible to the seal casing. The whirling frequency is varied by altering the length of the rotor from minimum 770 mm to maximum 890 mm. The rotor is carried in fluid film bearings and is driven by a bi-directional variable speed d.c. motor. High amplitudes of the unstable rotor, which may destroy the seal, are avoided via auxiliary bearings.

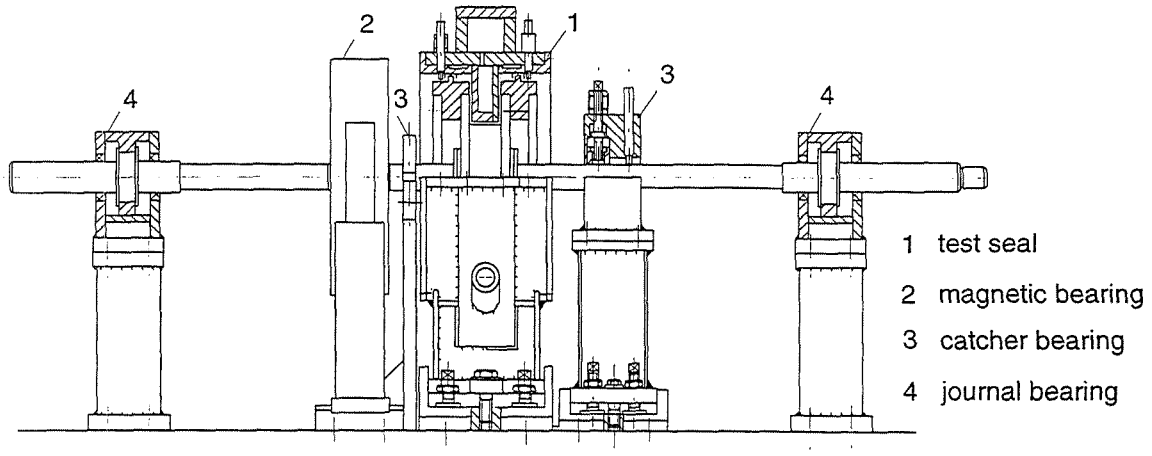

Fig. 5 Test rig with main components

Until now it was assumed that the seal and the magnetic bearing are placed at the same axial position. In reality, the position differs and conversion procedures must be applied. The

procedures consider the modal deflection of the flexible rotor and were previously derived and validated experimentally (Kwanka [1995b]).

$$\frac{\Delta q_{SEAL}}{\Delta q_{BEARING}} = \frac{\Delta r_{SEAL}}{\Delta r_{BEARING}} = \left(\frac{a_{BEARING}}{a_{SEAL}} \right)^2 \tag{3}$$

As shown above, the seal geometry can easily be varied by replacing the stator inserts or the rotor. Table 1 lists the seal geometries investigated in this paper with their main dimensions. It is assumed, that the entry swirl of the flow into the seals is the same as the tangential velocity component at the guide vane exit. For a constant pressure difference on and leakage flow through the seal, the entry swirl is altered by replacing the guide vane ring and changing the vane angle. The distance between the vane exit and the first knife of the seal is held constant at 12.0 mm for all geometries.

Table 1 Seal geometry data (j - number of cavities)

	Geometry	Pitch [mm]	Height (Cavity) [mm]	Tooth Width [mm]	Radius (Rotor) [mm]	Clearance [mm]
TOR1j	teeth on rotor	9.2	7.5	0.8	97.5	0.5
TOS2j	teeth on stator	9.2	7.5	0.8	90.0	0.5
KN1j	staggered[2)]	9.2	7.5/4.5	0.6	90.0/93.0	0.5

[2)] teeth on stator, stepped rotor

The procedure requires a clear identification of the stability limit and whirling frequency. With very few exceptions, the stability limit can be fixed within ±1-2 N/mm. The influence of the seal forces on the whirling frequency is small. The accuracy of the measured Δr values is restricted by the resolving limit of the signal analyzer. The straight lines needed for the determination of the stiffness and the damping coefficients (see fig. 4) are approximated with the least squares method using five mean values for the forward and the backward whirling direction in each case. The absolute deviation of the mean values from the straight lines depends on the seal forces. With high forces and consequently a rougher vibrational behavior, the deviations are high, too. Nevertheless, the mean relative deviations are below 1.5% except for low pressure differences (table 2a; seal KN12). There is a good reproducibility of the cross-coupled stiffness and the direct damping after a total disassembly and reassembly of the test rig (table 2b, seal TOR14).

Table 2a Maximum and mean absolute and relative deviation between the measured Δq values and the least square fit

Dp	10 kPa		100 kPa		200 kPa	
Deviation	Absolute [N/mm]	Relative [%]	Absolute [N/mm]	Relative [%]	Absolute [N/mm]	Relative [%]
Forward Mode	0.31	9.6	1.01	3.0	1.26	2.03
Backward Mode	0.35	7.25	1.06	2.47	4.14	5.22
Mean Deviation[1)]	0.17	3.62	0.52	1.32	1.03	1.31

[1)] ten whirling frequencies

Table 2b Reproducibility of identified dynamic coefficients

Measurement	k [N/mm]	C [Ns/mm]	K [N/mm]	c [Ns/mm]
1	93.3	.0592	32.8	.0151
2	91.6	.0574	33.9	.0180

Experimental Results

The dynamic coefficients are measured depending on the inlet circumferential velocity, the pressure ratio and the rotating speed. Fig. 6 displays all four dynamic coefficients of a TOR14-labyrinth with four cavities in relation to the inlet swirl. The cross-coupled stiffness shows the expected strong dependency on the inlet swirl which is almost linear for all seal geometries investigated in this paper.

The measured symbols are approximated with least square fitted lines. The direct stiffness stabilizes the rotor and increases with inlet swirl. Even with axial directed flow at the entrance the direct damping differs from zero and shows a maximum at medium swirl values. With zero inlet swirl the cross-coupled damping displays only low values in the negative to zero range.

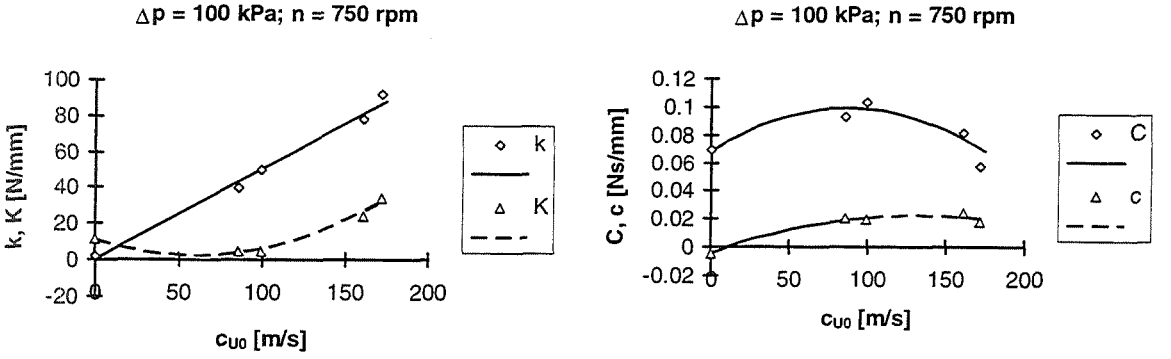

Fig. 6 Measured dynamic stiffness and damping of a TOR14 labyrinth

The linear behavior of the cross-coupled stiffness, now negative, can be stated even with negative swirl values. This means that a negative inlet swirl would generate an excitation of the backward modes and therefore stabilizes the forward modes. Changing the entrance flow conditions by swirl brakes, for example, would not only minimize the exciting mechanism but even enhance the stability behavior of the rotor which is still excited in forward direction by hydrodynamic bearings. This change in sign of the cross-coupled stiffness was observed for all seal geometries investigated in this paper. The direct stiffness and damping show the same behavior as for the co-rotating swirl. The cross-coupled damping is negative in the whole swirl range.

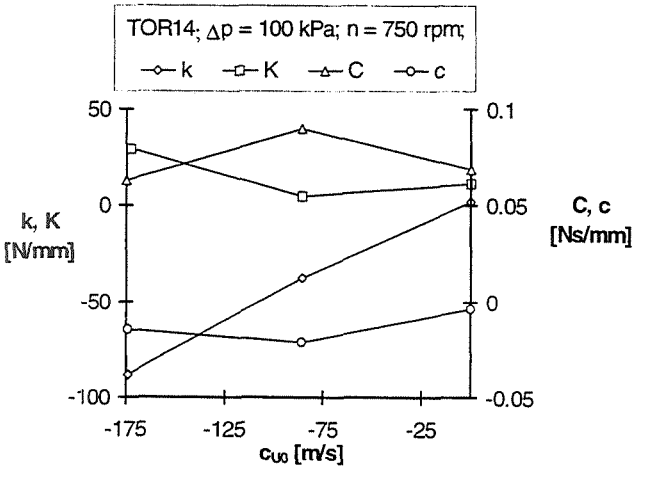

Fig. 7 Dynamic coefficients with counter entry swirl

In a next step, the measured non-conservative coefficients of a one-, two- and a three-cavity seals are compared to calculated results obtained with the one-volume bulk-flow theory (Baumgartner [1987]). The calculations are performed using the friction factors proposed by Ortinger (Kwanka, Ortinger, Steckel [1993]). The tangential velocity component at the guide vane exit is used as entry swirl input data in the calculations. The calculated results are displayed in fig. 8 as broken lines, the measured values are marked with symbols. The experimental data shows that under the given conditions the stiffness related force is generated mainly in the first two cavities. There is only a very small difference between the cross-coupled stiffness of the TOR12 and the TOR14 seal. The direct damping of the two and the four-cavity seal has approximately the same value, too, but the damping of the longer seal seems to decrease slightly with high entry swirl.

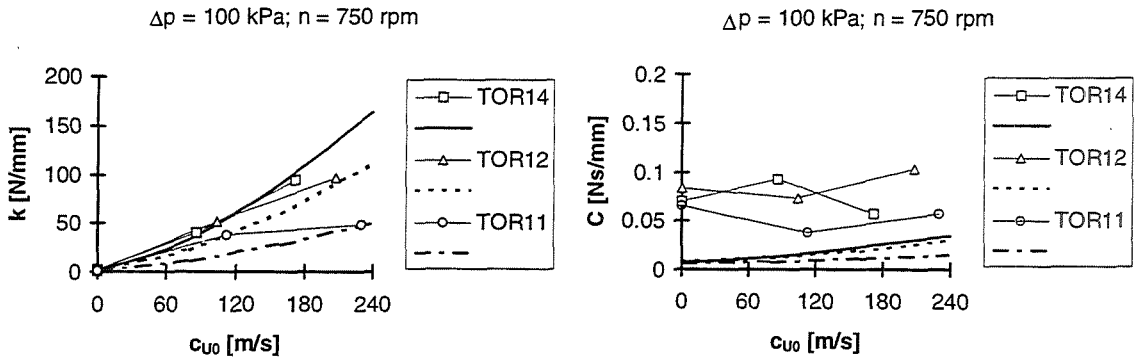

Fig. 8 Comparison of measured and calculated cross-coupled damping and direct stiffness for three different numbers of cavities

The magnitude and the trend of the cross-coupled stiffness is predicted satisfactory by the theory, although obviously the calculated distribution of the force over the seal length is not entirely accurate. The measured direct damping is distinctly higher than the calculated one which is perhaps one of the reasons for underpredicted stability limits. At this point it should be mentioned that the calculations do not include effects which showed up ahead and behind the last seal.

Only few experimental results exist for dynamic coefficients with short gas seals. Millsaps [1993] measured the transient circumferential pressure distribution and, therefore, forces on the stator of one-cavity TOR seals. By multiplying the amplitude of the whirling seal a and the change of magnetic excitation at the stability limit Δq tangential forces F_T can be calculated from the present investigations, too. The comparison of the calculated tangential forces for three pressure drops with the findings of Millsaps [1993] in fig. 9a is only in terms of quality, due to the differences in the inflow region and the seal stator surface. The value of the forces measured by Millsaps is lower because of smaller entry swirl, whereas the slope of the forces with the whirling frequency is higher due to the damping effect of the honeycomb stator.

In the cited paper Millsaps [1993] gives additional explanations of the mechanisms generating the excitation force and suggests a decomposition of these forces into an inviscid and a viscous part. The direct damping generation is attributed solely to effects in the ideal flow and is therefore independent of frictional influences and rotating speed respectively. Since the direct damping increases with rotating speed its independence of the spin rate is not confirmed by the measurements (fig. 9b). The slight decrease of the cross-coupled stiffness with spin rate complies with the findings of Millsaps.

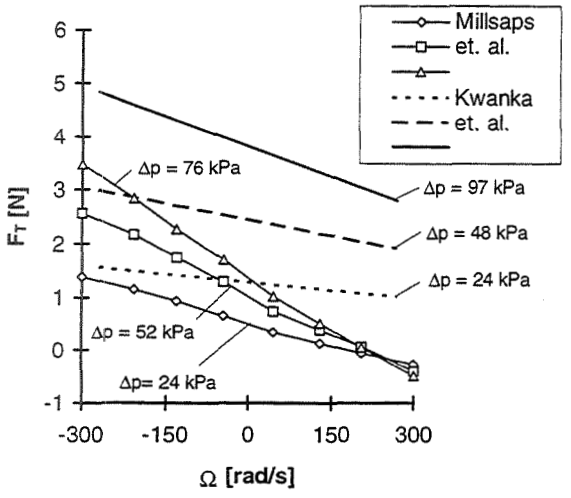

Fig. 9a Comparison of measured tangential forces for a TOR11 labyrinth with findings of Millsaps [1993]

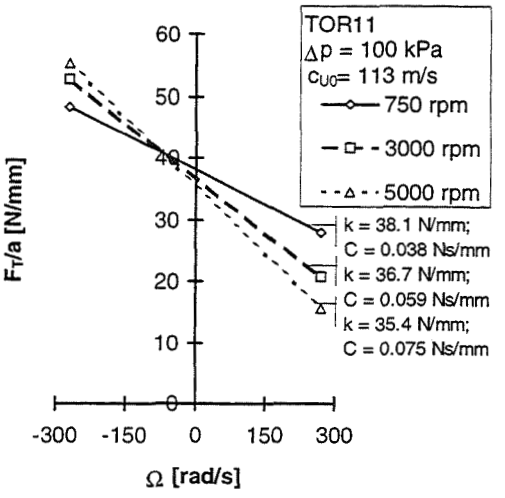

Fig. 9b Direct damping in dependence of the rotating speed

As expected, the influence of the rotating speed is relatively small with short labyrinth seals. The circumferencial velocity of the spinning rotor is varied from 7.1 m/s (750 rpm) to 47. m/s (5000 rpm). Measurements with zero rotation are impossible due to the oil-film of the used hydrodynamic bearings. For a reproduceable stability behavior, first the oil-film should be generated. On the other hand, the rotating speed is limited due to the bearing excitation which must be counterbalanced magnetically. With increasing speed the dependency on the entry swirl is still linear and the rotating speed is now slightly elevating the cross-coupled stiffness (fig. 10). In this case the influence of the rotation on the direct damping values is small.

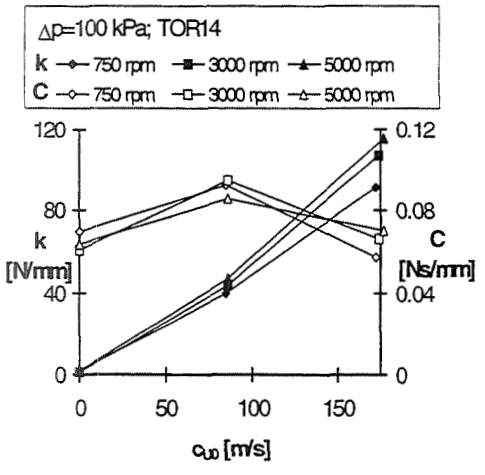

Fig. 10 Dynamic coefficients in dependence of the rotating speed

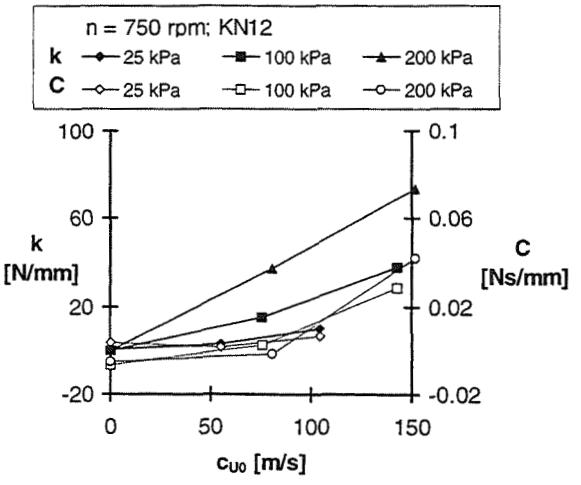

Fig. 11 The influence of the pressure difference on the dynamic coefficients

Beside the entry swirl, also the pressure difference has a strong influence on the generated forces. In fig. 11 the non-conservative coefficients for the staggered KN12 seal are displayed for three pressure differences Δp. The cross-coupled stiffness increases as expected along with the pressure difference. It is remarkable that the cross-coupled stiffness values are only half the

comparable values of the TOR14-seal. The direct damping with low and medium swirl values is almost zero and begins to increase only with high swirl values.

One main target of the investigation is to indicate which seal is the most suited from the rotordynamic point of view. Childs [1993] proposes the whirl frequency ratio Ω_W to characterize the relevant rotordynamic numbers of a seal. The whirl frequency ratio relates the exciting cross-coupled stiffness to the direct damping. The ratio is normalized with the running speed ω.

$$\Omega_W = \frac{k}{C\omega} \tag{4}$$

When the whirl frequency ratio is applied in relation to the inlet circumferential velocity ratio u_0 than the direct comparison of different seals is possible, without taking into account the rotordynamic system. The lower the whirl frequency ratio, the better the stability behavior of the seal. It should be, however, pointed out that the damping force is proportional to the whirl frequency Ω and therefore only a stiffening of the rotor would increase the damping force of a given seal.

The leakage flow of three of the seals investigated in this paper is almost the same (Δp = 100 kPa; $\dot{m} \approx 0.079$ kg/s). What would be interesting in a next step is a comparison of the three seals' stability behavior. As expected, the whirl frequency ratio of the TOS24 and TOR14 seals is approximately the same (fig. 12). At first sight, the value for the KN12 labyrinth is amazingly high despite the lower cross-coupled stiffness. The maximum of the whirl frequency ratio is caused by the negligible small direct damping with medium entry swirl values. It would therefore be better to choose a TOR14 or TOS24 seal instead of the KN12 seal when the axial length of the seal is not limited. The last figure demonstrates how important it is to include the direct damping of seals into rotordynamic stability considerations.

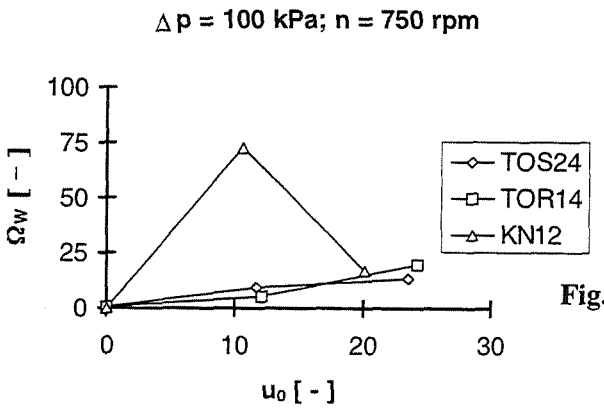

Fig. 12 Whirl frequency ratio versus inlet circumferential velocity ratio for three different seals

Conclusions

The easy-to-handle identification procedure presented in the paper allows systematic measurements of rotordynamic coefficients. Even with small forces the method shows high sensitivity and good reproducibility. The dynamic coefficients found display the same behavior as other measurements. The measured values agree satisfactory with calculated values for the cross-coupled stiffness. However, the discrepancies for the direct damping are evident.

For all seal geometries investigated, the cross-coupled stiffness increases linearly with the entry swirl. The behavior of the direct damping depends in particular on the seal geometry. Even without entry swirl teeth-on-rotor seals generate a considerable amount of damping whereas the staggered seals have no damping for low and medium entry swirl. The rotating speed has a minor

influence on the coefficients. The influence of the seal pressure difference on the cross-coupled stiffness is as strong as the influence of the entry swirl. The comparison of seals on the basis of the frequency whirl ratio demonstrates how important it is to consider the direct damping, too. Despite their high cross-coupled stiffness values, seals can be advantageous due to their high direct damping.

Further measurements are in progress with the main emphasis on finding out ways to minimize the excitation forces. Beside extensive investigations in the influence of the cavity geometry, the principal interest is directed to the use of swirl brakes, gas injection or rougher stator surfaces.

References

Baumgartner M., 1987. "Evaluation of Exciting Forces in Turbomachinery Induced by Flow in Labyrinth Seals", 11th ASME Conf. on Mech. Vib. and Noise, Boston 1987, Vol. 2, pp. 337-346.

Childs D. W., 1993. "Turbomachinery Rotordynamics", John Wiley & Sons, Inc.

Childs D. W., Nelson C. E., Nicks C., Scharrer J., Elrod D., Hale K., 1986. "Theory Versus Experiment for the Rotordynamic Coefficients of Annular Gas Seals: Part 1 - Test Facility and Apparatus", Trans. ASME, J. of Tribology, Vol. 108, pp 426- 432.

Bently D. E., Muszynska A., 1982. "Stability Evaluation of Rotor/Bearing System by Perturbation Tests", NASA Conference Publication 2250, Proceedings of a workshop held at Texas A&M University, pp. 307-322.

Kwanka K., Ortinger W., Steckel J., 1993. "Calculation and Measurement of the Influence of Flow Parameters on Rotordynamic Coefficients in Labyrinth Seals", NASA Conference Publication 2338, Proceedings of a workshop held at Texas A&M University, pp. 209-218.

Kwanka K., Mair R., 1995. "Identification of Gas Seal Dynamic Coefficients Based on the Stability Behavior of a Rotor", Proceedings of the 1st. European Conference of Turbomachinery - Fluid Dynamic and Thermodynamic Aspects, March 1-3, Erlangen-Nürnberg, Germany, VDI-Berichte 1186, VDI Verlag, Düsseldorf 1995, pp. 297-311.

Kwanka K., 1995a. "Ein neues Identifikationsverfahren für dynamische Koeffizienten von Labyrinthdichtungen", Proceedings of a conference held at the University of Kaiserslautern, SIRM '95, Irretier H., Nordmann R., Springer H. (Editors), Vieweg Verlag, pp. 216-224.

Kwanka K., 1995b. "Variation of Fluid Flow Forces in Seals with Rotor Bending", DE-Vol. 84-2, 1995 Design Engineering Technical Conferences, Volume 3 - Part B, ASME 1995, pp. 1277-1282.

Matros M., Neumer T., Nordmann R., 1994. "Identification of Rotordynamic Coefficients of Centrifugal Pump Components Using Magnetic Bearings", Preprints of the Fifth International Symposium on Transport Phenomena and Dynamics of Rotating Machinery (ISROMAC-5), May 8-11, 1994, Kaanapali, Hawaii, USA, pp. 55-72.

Millsaps K. T., Martinez-Sanches M., 1993. "Rotordynamic Forces in Labyrinth Seals: Theory and Experiment", NASA Conference Publication 3239, Proceedings of a workshop held at Texas A&M University, pp. 179-207.

Peletti J., Childs D. W., 1991. "A Comparison of Theoretical Predictions for the Rotordynamic Coefficients of Short (l/D = 1/6) Labyrinth Seals", Rotating Machinery and Vehicle Dynamics, Proceedings of the 13th Vibration Conference, Miami, FL, ASME, New York, DE-Vol. 35, pp 69-76.

Wright D. V., 1983. "Labyrinth Seal Forces on a Whirling Rotor", ASME Applied Mechanics Division, Proceedings of a Symposium on Rotor Dynamical Instability, Adams M. L. Jr. (Editor), ASME Book-Vol. 55, pp 19-31.

UPSTREAM SWIRL EFFECTS ON THE FLOW INSIDE A LABYRINTH SEAL

Gerald L. Morrison and Mark C. Johnson
Texas A&M University
College Station, Texas

Abstract

The flow field inside a seven cavity tooth on rotor labyrinth seal was measured using a 3D laser Doppler anemometer system. The seal was operated at a Reynolds number of 24,000 and a Taylor number of 6,600 using water as the working fluid. Swirl vanes were placed upstream of the seal to produce positive, negative, and no preswirl. It was found that the axial and radial velocities were minimally effected. The tangential velocity, both in the clearance region and the seal cavities on the rotor, were greatly altered by the preswirl. By applying negative preswirl, the tangential velocity was suppressed, even in the seventh cavity. The turbulence levels decreased as the preswirl varied from negative to positive.

Introduction

In turbomachinery annular and labyrinth seals are used to decrease secondary flow between high and low pressure regions. This secondary flow leakage is unwanted because it reduces the efficiency of the machine. In the compressor of a gas turbine, for example, seals are used to decrease the flow along the shaft under the stators. Simply stated seals are the very small clearance between the rotating element and the stator through which fluid would like to pass. These clearances cannot be completely eliminated because of machining tolerances, eccentricities, and wear inherent in rotating machinery. If a rotor shaft was designed to fit too snugly in its housing, rubbing between the shaft and the housing would occur which might cause the machine to fail. One solution is to design the housing of the rotor shaft with material that is meant to be rubbed and worn. This, however, causes problems because it is not possible to predict exactly the final shape, and because the efficiency will decrease with use. Another approach is to design the gap to the necessary clearance and design the geometry to maximize those features desired.

The geometry of a seal has several effects on the performance of rotating machinery. The most apparent is the slowing of leakage flow from the high to low pressure regions and the separation of flows that should not mix. Two other parameters that are affected by seal geometry are vibration and wear. Vibration can be caused when forces generated by the leakage are not uniform inside the seal and by the nonaxisymmetric blade loadings that can be caused by tip leakage. The geometry also affects how the seal itself wears. If the flow through the seal causes stress at particular points on the seal, cracks and breaks can occur which will influence the performance of the seal. The stabilizing/destabilizing effect of the seal upon the entire turbomachine is of great importance. By decreasing the tangential velocity (swirl) within the seal, a stabilining effect is generally obtained. All these factors ultimately affect the performance of the turbomachine.

Objectives

The objective of this study was to determine how varying the preswirl upstream of a labyrinth seal effected the flow field development within the seal. Specifically, measurements of the mean velocity vector and Reynolds stress tensor were performed, and how these quanties

varied with preswirl and location within the seal were observed.

Facility

The test facility used water at 30.5 ± 4°C. The water was supplied by a 15 m^3 storage tank via a centrifugal pump, water filters, and a turbine meter. The flowrate through the test section was set at a constant value of 4.86 l/s and the test section pressure was maintained at 138 kPa to prevent cavitation. The measurements were made using the seal test rig shown in Figure 1. This unit consisted of a 50.8mm diameter overhung shaft which was driven by a 0 to 5,300 rpm variable speed electric motor. For the present study, the shaft rotation rate was 3,600 rpm. The rotor, Figure 2, was mounted contentricly directly upon the shaft. The rotor had a smooth surface with an outer diameter of 164.1 mm and a length of 33.5 mm. It was manufactured of acrylic, had a polished smooth surface, and was coated with an antireflectant material. There were eight straight teeth with a thickness of 1.524 mm and a height of 3.048 mm. The tooth pitch was 4.572 mm. This resulted in a seven cavity tooth on rotor labyrinth seal. The stator was made of stainless steel and was mounted inside the main housing such that its position could be varied to set static eccentricities. The rotor/stator combination were concentric for this study. The water first entered into a plenum. It then passed through a 12.7 mm thick perforated plate with 3.2 mm diameter holes which eliminated any swirl generated by the piping system, and evenly distributed the flow around the circumference of an annular plenum. The section of the annular plenum along the centerline of the test rig was necessary to provide the inner half of the contraction leading up to the seal entrance and to support the swirl generation device. Figure 3 shows the details of how the flow approached the seal rotor. The contraction from the plenum results in an annular flow path with a clearance of 0.782 mm where 120 turning vanes were equally spaced around the circumference. Figure 4 shows the design of these blades. Three sections were manufactures, one with vanes producing positive preswirl (swirl in the direction of the seal rotation), another produced negative preswirl, and one with no vanes which is called the no preswirl case. Downstream of the turning vanes, the clearance increased to 1.524 mm. This increase in clearance decreased the axial velocity while the tangential velocity remained essentially constant. This increased the ratio of tangential velocity to axial velocity. There was a 0.508 mm gap between the swirl generating assembly and the rotor. The velocity distribution was measured across the clearance at this gap. It was determined that the ratio of tangential velocity to axial velocity just upstream of the seal entrance was -0.215, 0.122, and 0.263. The viscous effects of the rotor motion effected the magnitude of the inlet tangential velocity, as shown by these ratios being biased to a more positive value, especially the "no preswirl" case. The clearance between the rotor and stator was 1.27 mm. The larger supply nozzle clearance, 1.524 mm, was made to accommodate eccentric seals without their inlet clearance being larger than the supply nozzle.

The flow inside the seal was measured using a 3D Laser Doppler Anemometer (LDA) system. Figure 5 shows the optical access port in the stator. The trapezoidal region was fit with a quartz window. The LDA system used is shown in Figure 6. This system utilizes three colors of light, each one measuring an individual fluid velocity component. By using Bragg cells, 8.5X beam expanders, and off access back scatter light collection it was possible to measure the flow field in the small clearance and within the labyrinth seal cavity where flow reversals were present. The measurement volume was 25x25x100 μm (0.001x0.001x0.004 inches). The entire LDA system was mounted upon a 3D traversing system with a repeatable positioning accuracy of 0.01 mm. The LDA system actually measured the velocity of small seed particles suspended in the flow. Unexpanded polystyrene spheres, 6 micron in diameter with a specific gravity of 1.3, were used in this study. These particles have a frequency response of 45 kHz in water which is more than adequate for the present study. This system is more fully described in Morrison, et al. (1991).

Results

Contours of the mean axial velocity in the first, third, fifth, and seventh cavities of the labyrinth seal for negative, zero, and positive preswirl are presented in Figure 7. The top row represents the negative preswirl data, the center row represents the no preswirl data, and the bottom row represents the positive preswirl data. Also present on the figure are the axial-radial velocity vectors. Each vector shows where data were recorded. In the regions over the teeth, data were recorded at five radial positions. Inside the cavity, six axial positions were measured (except for near the base of the upstream tooth where optical access was not possible) with a total of nineteen radial positions spanning from the stator to the bottom of the cavity. There were approximately 130 measurement locations for each cavity. The first cavity has more data since ten radial positions were measured just upstream of the seal entrance. The volumetric flowrate through the seal was maintained constant with an average axial velocity through the clearance of 7.4 m/s for all preswirls. This value was used to nondimensionalize the data presented in Figure 7. All of the cavities show a maximum axial velocity of 1.1 in the central region of the clearance and a maximum negative velocity of -0.5 at the bottom of the cavity. The vectors show the fluid in the clearance region turning down into the cavity once the flow has passed the center of the cavity. This results in the flow impacting on the upstream face of the downstream tooth just slightly below its top. The fluid diverted into the cavity by this action helps to drive the large recirculation zone present in the cavity. The free shear layer between the fluid in the clearance and in the top of the cavity also helps drive the recirculation zone. From the third to seventh cavities there is very little variation in the axial velocity with preswirl and cavity number. The first cavity shows variation from the remaining cavities with varying velocity profiles over the first tooth due to the preswirl value. For negative preswirl, there is a region near the inlet tooth top where the axial velocity is below 0.9. This is the same region where the tangential velocity quickly varies from negative to positive at the tooth surface. This large radial gradient of the tangential velocity displaces the axial velocity to the top of the clearance area. As the amount of preswirl changed to zero and positive values, this region of low axial velocity over the first tooth decreased in magnitude with its presence almost absent for the positive preswirl case. This further indicates that it is the radial gradient of tangential velocity causing the effect. By the time the fluid exits the first cavity, there is almost no variation in axial velocity profiles over the downstream tooth for varying amounts of inlet swirl. The distributions at this location are very similar to the other downstream cavities.

The radial velocity contours nondimensionalized by the average axial velocity in the clearance area, 7.4 m/s, are shown in Figure 8. The values in the clearance area are typically zero, but there is a region of negative values downstream of the cavity centerline which increases in size as the flow progresses to further downstream cavities. This represents the through flow diverging into the cavity, impacting on the downstream tooth surface resulting in a stagnation point below the top of the downstream tooth. This region is decreased in size as the preswirl varies from negative to positive as shown in the fifth and seventh cavities. In fact, the positive preswirl case shows almost no variation in this negative velocity over the entire length of the seal. Inside the cavity, the maximum radial velocity is 0.4 near the upstream tooth's vertical surface and the minimum is -0.4 near the surface of the downstream tooth. This is consistent with the large recirculation zone present inside the cavity. Within the cavity there is very little variation of the radial velocity with cavity number or preswirl.

Figure 9 presents the tangential velocity contours. These have been nondimensionalized with the surface velocity of the rotor, 30.9 m/s, compared to the previously used bulk axial velocity of 7.4 m/s. The tangential velocity entering the first cavity for the negative preswirl case has an average value of -0.172. This increases to 0.107 and 0.242 for the no preswirl and positive preswirl cases. The values are relatively uniform over the inlet region. The preswirl effects the magnitude of the tangential velocity in the first cavity with the values increasing with increasing preswirl. The tangential velocity also increases with increasing downstream distance within the

seal. The tangential velocity inside the seal cavity is always larger than the value in the clearance. This is due to the larger residence time of the fluid as it is trapped in the cavity allowing the shear from the three cavity sides, rotating at 30.9 m/s, to tangentially accelerate the fluid. In the clearance region, the stator wall is stationary causing the velocity near the stator to approach zero while the tooth tops and the fluid within the cavity are producing shear causing the tangential velocity in the clearance to increase. These opposing forces act upon the value of the tangential velocity in the clearance causing the velocity profiles to vary with axial location and amount of preswirl. There is an overall trend for all cavities at all preswirls for the tangential velocity in the upstream half of the cavity to be noticeably larger than the downstream half. This is represented by the low velocity contour finger protruding from the clearance region into the cavity along the downstream tooth face. Since fluid entered the cavity in the downstream half, the fluid must flow along the back wall and bottom of the seal before moving up the front wall where its tangential velocity is slightly larger. While following this path, the rotor wall is continually applying a tangential shear stress to the fluid causing its tangential velocity to continually increase.

In order to better investigate the development of the tangential velocity, radial profiles of the tangential velocity at the axial location just upstream of the cavity centerline are presented in Figures 10 to 12 for negative, no, and positive preswirl respectively. The value at the rotor surface (Y/c=-2.5, W/Ws=1.0) was not plotted so that the velocity axis could be expanded for better visualization. Figure 13 presents the average tangential velocity over the entire clearance area and the entire cavity region. The data at the radial location of the tooth top was not used in the averaging nor were the data on the rotor and stator surfaces. For the negative preswirl case (Figure 10) the tangential velocity was relatively constant across the cavity with the average increasing from 0.14 to 0.33 as the flow progressed from the first to the seventh cavity. The tangential velocity profile varied greatly in the first cavity clearance with a minimum value of -0.2 at Y/c=0.6, increasing to zero at Y/c=1, and 0.08 at Y/c=-0.2. The minimum value remained at Y/c=0.6, but changed to -0.12 in the third cavity and the maximum increased to 0.21 at Y/c=-0.3. By the fifth cavity the minimum location shifted towards the stator wall and increased to -0.02, and the maximum remained at Y/c=-0.3 while increasing to 0.3. No negative tangential velocities were present by the seventh cavity with the tangential velocity steadily increasing from 0 at the stator wall, Y/c=1, to 0.38 at Y/c=-0.3. The average values of the tangential velocity over the entire clearance and cavity regions (Figure 13) increased from -0.15 and 0.08, to 0.05 and 0.33 respectively from the first to seventh cavity. These values differ from the values stated for the radial profile since they are averages over the entire data set obtained within each region. These data show how both the stationary stator wall and moving rotor apply shear to the flow. In the first cavity where the inlet tangential velocity is negative, both the rotor and stator are working to stop the negative swirl. This has been somewhat accomplished by the third cavity with essentially the same amount of work being done by the rotor and stator since the location of minimum velocity remained unchanged. This balance shifts by the fifth cavity, with the location of minimum tangential velocity moving towards the stator as its retarding effect becomes smaller compared to the ever larger positive tangential velocity in the seal cavity. By the end of the seal, the rotor has produced a positive tangential velocity everywhere in the seal and the stator is now retarding the positive tangential velocities. Hence, the surface shear stress on the stator changed from negative to positive in the tangential direction as the flow progressed from the inlet to the exit. On the rotor, the difference between the tangential velocity of the fluid and the rotor decreased as the flow progressed downstream. Thus, the negative tangential shear stress on the rotor decreased from the inlet to the exit.

The no preswirl case, Figures 11 and 13, exhibit much less variation with cavity than the negative preswirl. The tangential velocity in the clearance is always positive with the magnitude of variation from stator wall to seal cavity steadily increasing with downstream location. This is also reflected with the average velocity within the cavity increasing with downstream location.

Results

Contours of the mean axial velocity in the first, third, fifth, and seventh cavities of the labyrinth seal for negative, zero, and positive preswirl are presented in Figure 7. The top row represents the negative preswirl data, the center row represents the no preswirl data, and the bottom row represents the positive preswirl data. Also present on the figure are the axial-radial velocity vectors. Each vector shows where data were recorded. In the regions over the teeth, data were recorded at five radial positions. Inside the cavity, six axial positions were measured (except for near the base of the upstream tooth where optical access was not possible) with a total of nineteen radial positions spanning from the stator to the bottom of the cavity. There were approximately 130 measurement locations for each cavity. The first cavity has more data since ten radial positions were measured just upstream of the seal entrance. The volumetric flowrate through the seal was maintained constant with an average axial velocity through the clearance of 7.4 m/s for all preswirls. This value was used to nondimensionalize the data presented in Figure 7. All of the cavities show a maximum axial velocity of 1.1 in the central region of the clearance and a maximum negative velocity of -0.5 at the bottom of the cavity. The vectors show the fluid in the clearance region turning down into the cavity once the flow has passed the center of the cavity. This results in the flow impacting on the upstream face of the downstream tooth just slightly below its top. The fluid diverted into the cavity by this action helps to drive the large recirculation zone present in the cavity. The free shear layer between the fluid in the clearance and in the top of the cavity also helps drive the recirculation zone. From the third to seventh cavities there is very little variation in the axial velocity with preswirl and cavity number. The first cavity shows variation from the remaining cavities with varying velocity profiles over the first tooth due to the preswirl value. For negative preswirl, there is a region near the inlet tooth top where the axial velocity is below 0.9. This is the same region where the tangential velocity quickly varies from negative to positive at the tooth surface. This large radial gradient of the tangential velocity displaces the axial velocity to the top of the clearance area. As the amount of preswirl changed to zero and positive values, this region of low axial velocity over the first tooth decreased in magnitude with its presence almost absent for the positive preswirl case. This further indicates that it is the radial gradient of tangential velocity causing the effect. By the time the fluid exits the first cavity, there is almost no variation in axial velocity profiles over the downstream tooth for varying amounts of inlet swirl. The distributions at this location are very similar to the other downstream cavities.

The radial velocity contours nondimensionalized by the average axial velocity in the clearance area, 7.4 m/s, are shown in Figure 8. The values in the clearance area are typically zero, but there is a region of negative values downstream of the cavity centerline which increases in size as the flow progresses to further downstream cavities. This represents the through flow diverging into the cavity, impacting on the downstream tooth surface resulting in a stagnation point below the top of the downstream tooth. This region is decreased in size as the preswirl varies from negative to positive as shown in the fifth and seventh cavities. In fact, the positive preswirl case shows almost no variation in this negative velocity over the entire length of the seal. Inside the cavity, the maximum radial velocity is 0.4 near the upstream tooth's vertical surface and the minimum is -0.4 near the surface of the downstream tooth. This is consistent with the large recirculation zone present inside the cavity. Within the cavity there is very little variation of the radial velocity with cavity number or preswirl.

Figure 9 presents the tangential velocity contours. These have been nondimensionalized with the surface velocity of the rotor, 30.9 m/s, compared to the previously used bulk axial velocity of 7.4 m/s. The tangential velocity entering the first cavity for the negative preswirl case has an average value of -0.172. This increases to 0.107 and 0.242 for the no preswirl and positive preswirl cases. The values are relatively uniform over the inlet region. The preswirl effects the magnitude of the tangential velocity in the first cavity with the values increasing with increasing preswirl. The tangential velocity also increases with increasing downstream distance within the

seal. The tangential velocity inside the seal cavity is always larger than the value in the clearance. This is due to the larger residence time of the fluid as it is trapped in the cavity allowing the shear from the three cavity sides, rotating at 30.9 m/s, to tangentially accelerate the fluid. In the clearance region, the stator wall is stationary causing the velocity near the stator to approach zero while the tooth tops and the fluid within the cavity are producing shear causing the tangential velocity in the clearance to increase. These opposing forces act upon the value of the tangential velocity in the clearance causing the velocity profiles to vary with axial location and amount of preswirl. There is an overall trend for all cavities at all preswirls for the tangential velocity in the upstream half of the cavity to be noticeably larger than the downstream half. This is represented by the low velocity contour finger protruding from the clearance region into the cavity along the downstream tooth face. Since fluid entered the cavity in the downstream half, the fluid must flow along the back wall and bottom of the seal before moving up the front wall where its tangential velocity is slightly larger. While following this path, the rotor wall is continually applying a tangential shear stress to the fluid causing its tangential velocity to continually increase.

In order to better investigate the development of the tangential velocity, radial profiles of the tangential velocity at the axial location just upstream of the cavity centerline are presented in Figures 10 to 12 for negative, no, and positive preswirl respectively. The value at the rotor surface (Y/c=-2.5, W/Ws=1.0) was not plotted so that the velocity axis could be expanded for better visualization. Figure 13 presents the average tangential velocity over the entire clearance area and the entire cavity region. The data at the radial location of the tooth top was not used in the averaging nor were the data on the rotor and stator surfaces. For the negative preswirl case (Figure 10) the tangential velocity was relatively constant across the cavity with the average increasing from 0.14 to 0.33 as the flow progressed from the first to the seventh cavity. The tangential velocity profile varied greatly in the first cavity clearance with a minimum value of -0.2 at Y/c=0.6, increasing to zero at Y/c=1, and 0.08 at Y/c=-0.2. The minimum value remained at Y/c=0.6, but changed to -0.12 in the third cavity and the maximum increased to 0.21 at Y/c=-0.3. By the fifth cavity the minimum location shifted towards the stator wall and increased to -0.02, and the maximum remained at Y/c=-0.3 while increasing to 0.3. No negative tangential velocities were present by the seventh cavity with the tangential velocity steadily increasing from 0 at the stator wall, Y/c=1, to 0.38 at Y/c=-0.3. The average values of the tangential velocity over the entire clearance and cavity regions (Figure 13) increased from -0.15 and 0.08, to 0.05 and 0.33 respectively from the first to seventh cavity. These values differ from the values stated for the radial profile since they are averages over the entire data set obtained within each region. These data show how both the stationary stator wall and moving rotor apply shear to the flow. In the first cavity where the inlet tangential velocity is negative, both the rotor and stator are working to stop the negative swirl. This has been somewhat accomplished by the third cavity with essentially the same amount of work being done by the rotor and stator since the location of minimum velocity remained unchanged. This balance shifts by the fifth cavity, with the location of minimum tangential velocity moving towards the stator as its retarding effect becomes smaller compared to the ever larger positive tangential velocity in the seal cavity. By the end of the seal, the rotor has produced a positive tangential velocity everywhere in the seal and the stator is now retarding the positive tangential velocities. Hence, the surface shear stress on the stator changed from negative to positive in the tangential direction as the flow progressed from the inlet to the exit. On the rotor, the difference between the tangential velocity of the fluid and the rotor decreased as the flow progressed downstream. Thus, the negative tangential shear stress on the rotor decreased from the inlet to the exit.

The no preswirl case, Figures 11 and 13, exhibit much less variation with cavity than the negative preswirl. The tangential velocity in the clearance is always positive with the magnitude of variation from stator wall to seal cavity steadily increasing with downstream location. This is also reflected with the average velocity within the cavity increasing with downstream location.

Again, there is very little variation in the tangential velocity within the seal cavity except within the shear layer present between the cavity and clearance areas. The average clearance and cavity velocities increased from 0.15 and 0.33 to 0.25 and 0.5 from the first cavity to the seventh cavity respectively. These variations were less than those present for negative preswirl.

The positive preswirl case exhibited the least variation in tangential velocity of the three cases studied. Again, the tangential velocity was relatively constant within the cavity and only increased from 0.48 to 0.55. The tangential velocity radial profile within the clearance of the first cavity is interesting, in that, from Y/c=0.3 to 0.8 the value was constant at 0.24, the value generated by the swirl vanes. This shows the shear generated by the cavity fluid and the stator has not reached the center of the clearance at this location. Beyond the first cavity, the tangential velocity steadily increased from the stator to the cavity velocity. The average tangential velocity in the clearance region increased from 0.25 to 0.33 from the first to the seventh cavity.

The turbulence kinetic energy, $\kappa = 0.5\left[u'u' + v'v' + w'w'\right]$, was calculated from the Reynolds stress tensor data and nondimensionalized by the bulk axial clearance velocity squared, $(7.4\ m/s)^2$. This value represents the turbulence which has been generated by the flow field by transferring energy from the mean velocity to the turbulence. In essence, the effective viscosity used in numerical simulations represents the amount of this energy that is dissipated. The usual assumption is that the production and dissipation of this value are equal. Regions where κ is present represent regions of turbulence production, and hence, energy dissipation. The larger the value of κ, the larger the production. Figure 14 presents the κ contours and figure 15 presents the average value of κ over the entire cavity neglecting the rotor and stator surfaces. The largest values of κ are present in the shear layer between the clearance and cavity regions with levels of 0.5 present in all cases. This corresponds to a turbulence intensity based upon the bulk average axial clearance velocity of 87%. This is a large value compared to, say, a turbulent pipe flow where values reach about 15%. It is this large turbulence level that makes the labyrinth seal more effective in reducing the leakage for a given pressure drop than a smooth annular seal. The negative preswirl case shows larger regions of the seal possessing high levels of turbulence. In the first cavity the turbulence spans the clearance to the stator wall. This is due to the large radial gradients of both the axial and tangential velocities. In particular, the tangential velocity gradient is the largest in this cavity and is responsible for the increased turbulence production compared to the other cavities. The turbulence also penetrates to the cavity bottom along the surface of the downstream tooth. This is a result of the larger negative radial velocity along this tooth causing the clearance flow to penetrate further into the seal and impact upon the tooth surface further into the seal than the other cases resulting in additional turbulence production. In the third cavity, the turbulence levels in the clearance have reduced some in accordance with the tangential velocity being less negative resulting in a smaller tangential velocity gradient, and hence, less turbulence production. This trend of less turbulence in the clearance area continues throughout the seal as the tangential velocity becomes more positive resulting in a smaller velocity gradient. The effects of the tangential velocity radial gradient upon κ can be observed in all of the cavities. As the tangential velocity becomes closer in value to the rotor speed, the regions of large κ decrease. Figure 15 shows how the overall average value changes. With negative preswirl, κ_{ave} in the first cavity is very large, 0.22 which corresponds to an average turbulence intensity (TI) of 57%. This decreases steadily to 0.16, 49% TI, in the last cavity. With zero preswirl, κ_{ave} remains lower throughout the seal beginning at 0.20, 55% TI, and decreasing to 0.15, 47% TI, by the last cavity. The positive preswirl case exhibits an interesting trend. As expected, κ_{ave} is very low at the inlet, 0.13 or 44% TI, but increases as the flow progresses through the seal eventually reaching a value of 0.17 or 50% TI in the last cavity. This is caused by the shear layer between the clearance flow and the stator wall, as opposed to the cavity and the clearance flow in the previous cases. This is observable in the seventh cavity where there is additional turbulence present near the stator, though not as large as at the clearance-cavity interface, but sufficiently large and over a large

enough region to add to the overall turbulence level. Since the tangential velocity in the clearance has reach a large level, the tangential velocity gradient near the stator has become larger and is generating a larger level of turbulence than the cavities upstream.

Conclusions

The axial velocities showed very little variation with cavity number and preswirl value from the third to seventh cavities. A region of large axial velocity was increasingly displaced towards the stator over the first cavity inlet tooth as the preswirl went from positive to negative. This was due to the increase of the tangential velocity radial gradient in this region. By the time the fluid exited the first cavity, there was little variation in the axial velocity distributions with preswirl, and it was similar to the other downstream cavities. The radial velocities inside the cavity showed no appreciable variation with preswirl or cavity number. However, the magnitude of the negative radial velocity into the cavity over the downstream half of the cavity increased with downstream location, and decreased as the preswirl varied from negative to positive showing almost no variation for positive preswirl. The tangential velocities were essentially constant within each seal cavity increasing from a low of 0.05 for the first cavity of the negative preswirl to a high of 0.55 in the seventh cavity for positive preswirl. The axial rate of increase in the average cavity tangential velocity decreased from the negative to positive preswirl case with overall increases of 0.28, 0.17, and 0.07 respectively. The variations of the average tangential velocity within the clearance regions showed a similar trend with values ranging from -0.15 to 0.33 with individual increases over the length of the seal of 0.20, 0.10, and 0.08 respectively for increasing preswirl. The negative preswirl case maintained an average tangential velocity less than 0.05 within the clearance and 0.33 in the seal cavity while positive preswirl resulted in values of 0.33 and 0.55 within the clearance and cavity respectively. This change in tangential velocity can have a significant effect upon the stability of the seal and the shaft upon which it is mounted. Turbulence measurements show the maximum levels present just downstream of the cavity upstream tooth in the shear layer between the through flow and the recirculating fluid in the cavity. The largest overall averaged turbulence levels occur with negative preswirl in the first cavity. Since the average axial velocity through the clearance is maintained at a constant value, it is the large tangential radial velocity gradient that is generating this turbulence as the difference in tangential velocity between the rotor and fluid is very great. As the flow progresses downstream, the tangential velocity increases in value, decreasing the velocity gradient, and the turbulence level decreases for the negative preswirl case. The no preswirl case presents a similar result but lower overall turbulence levels since the tangential velocity radial gradients are smaller. The positive preswirl case begins in the first cavity with the turbulence levels below any seen in the other two cases which would be expected with the larger tangential velocity. However, it presents a surprise with the turbulence levels increasing as the flow progresses through the seal. This is due to the tangential velocity in the clearance becoming larger and results in a large velocity gradient near the stator wall which begins to generate more turbulence. Averaging the κ_{ave} values over the four cavities measured the negative preswirl case has an overall turbulence level of 0.188, the no preswirl is 0.163, and the positive preswirl is 0.154. Thus, the overall turbulence level decreases as the preswirl ranges from negative to positive. This indicates that negative preswirl will be beneficial in generating more turbulence which will dissipate more energy, and it helps keep the tangential velocity lower which is, in general, more rotordynamically stable.

Acknowledgments

This work was supported by the NASA Lewis Research Center under the direction of Mr. Robert Hendricks.

Nomenclature

c	clearance
D	rotor diameter
Re	Reynold Number, $2cU_{ave}/\nu$
Ta	Taylor Number, $(cWs/\nu)\sqrt{2c/D}$
U	mean axial velocity
U_{ave}	bulk average leakage velocity, 7.4 m/s
V	mean radial velocity
W	mean tangential velocity
Ws	rotor surface velocity, 30.9 m/s
X	axial distance from front of seal
Y	radial distance above rotor tooth top
κ	turbulence kinetic energy
ν	kinematic viscosity

References

Morrison, G.L., Johnson, M.C., and Tatterson, G.B., "3-D Laser Anemometer Measurements in a Labyrinth Seal," ASME Journal of Gas Turbines, Vol. 113, No. 1, pp. 119-125, January 1991.

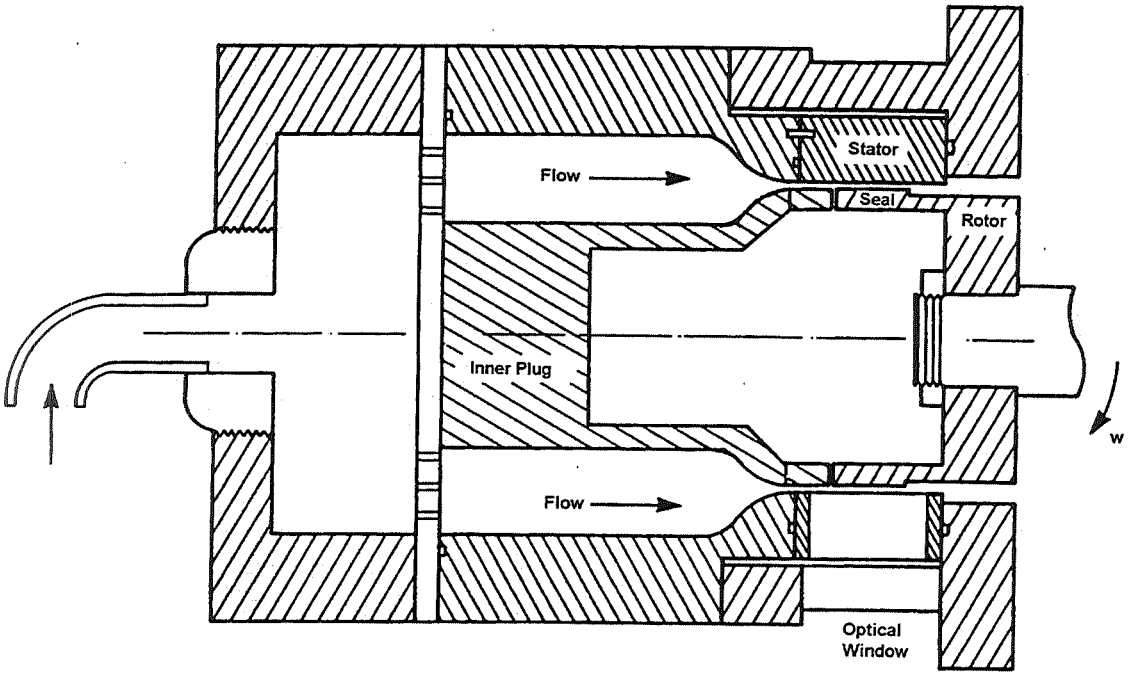

Figure 1. Seal test rig overall view.

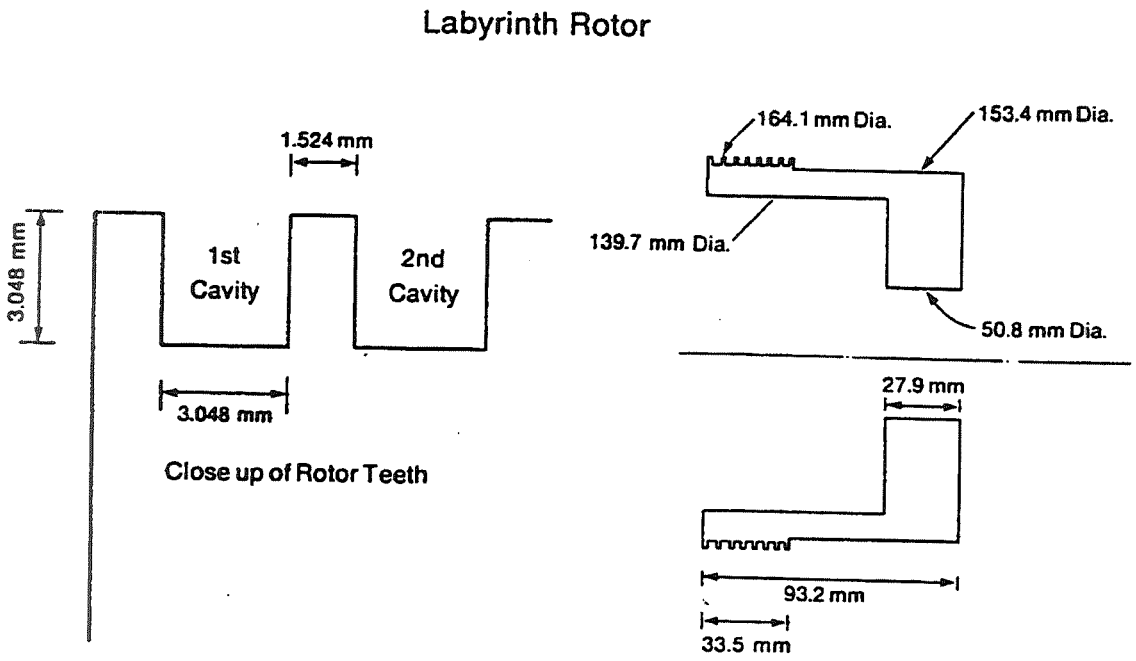

Figure 2. Labyrinth seal rotor detail.

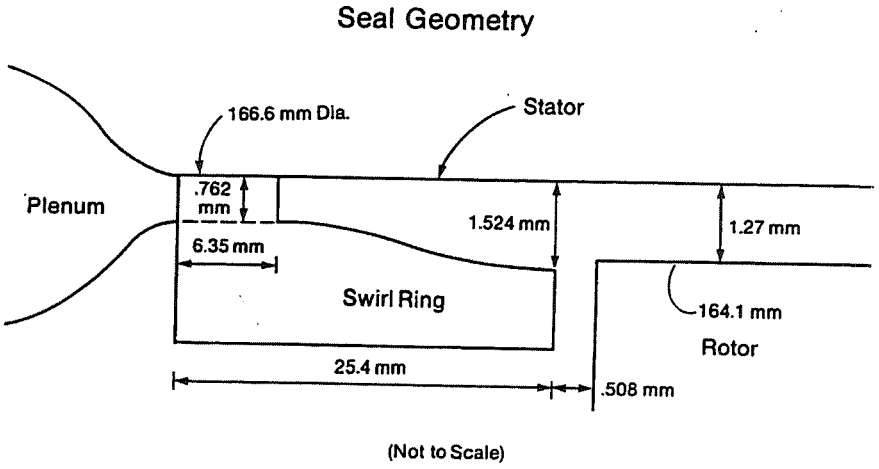

Figure 3. Seal inlet flow path detail.

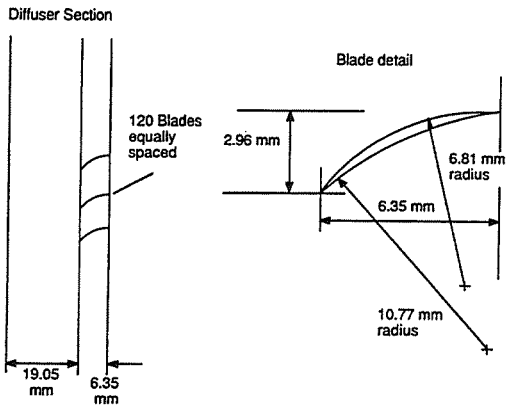

Figure 4. Detail of swirl generator.

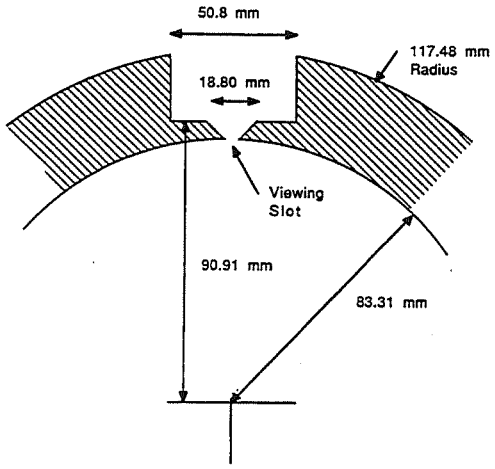

Figure 5. Laser anemometer access window

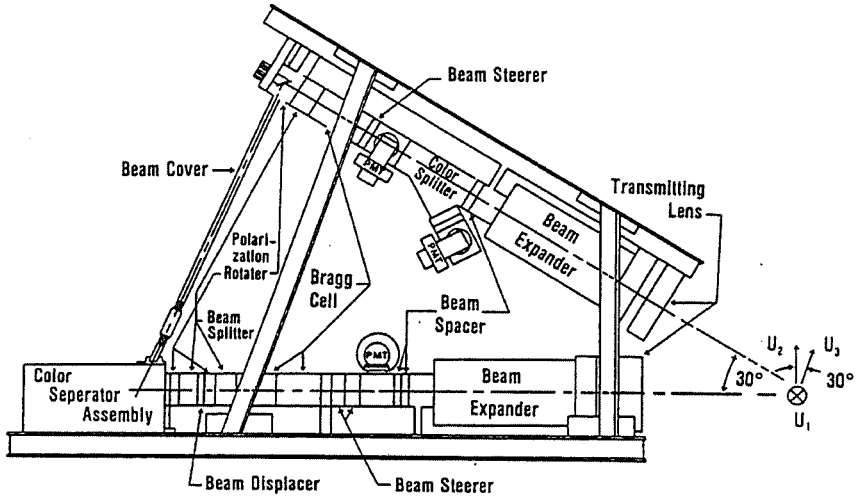

Figure 6. 3-D Laser Doppler anemometer system.

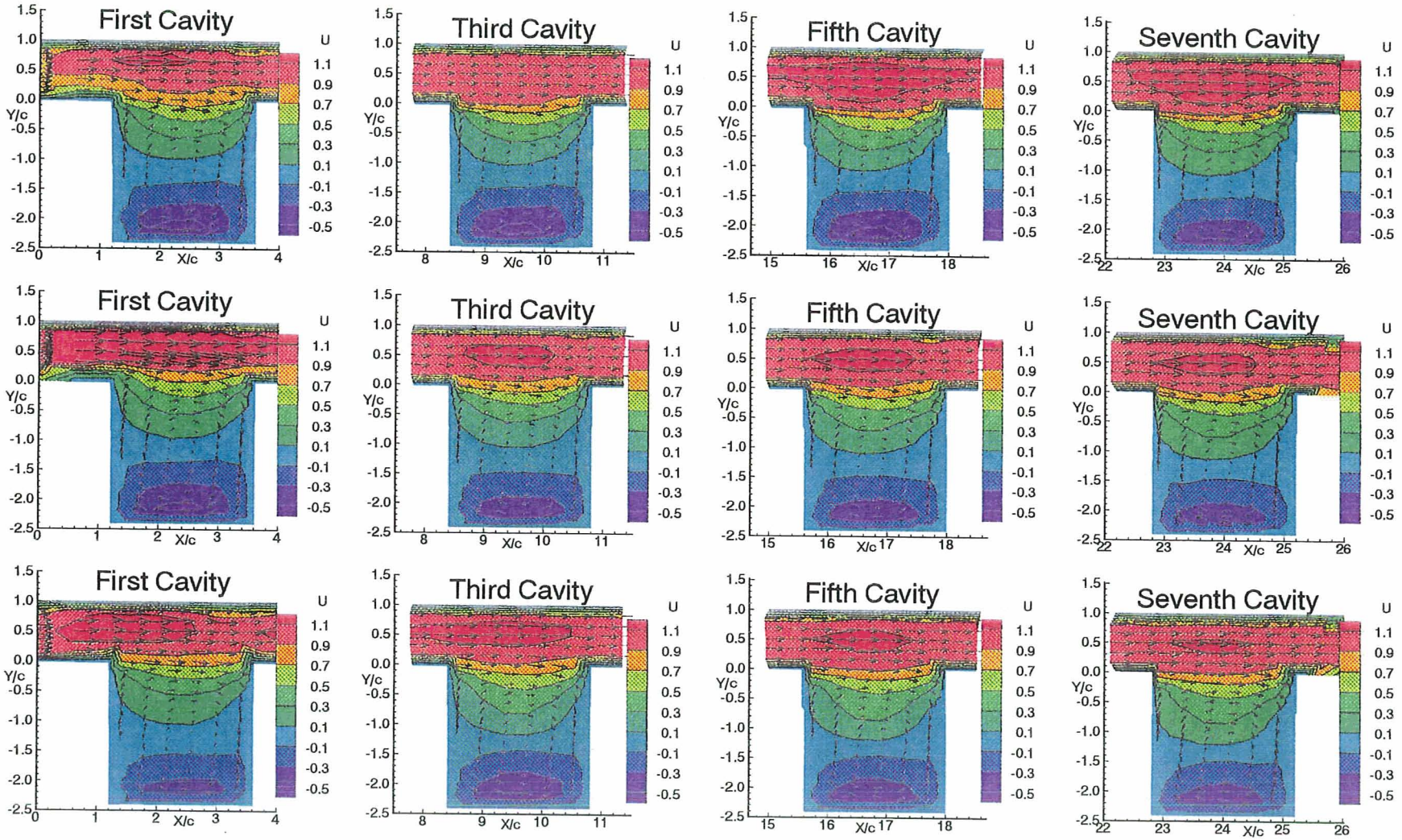

Figure 7. Axial velocity contours, first row - negative preswirl, second row - no preswirl, third row - positive preswirl.

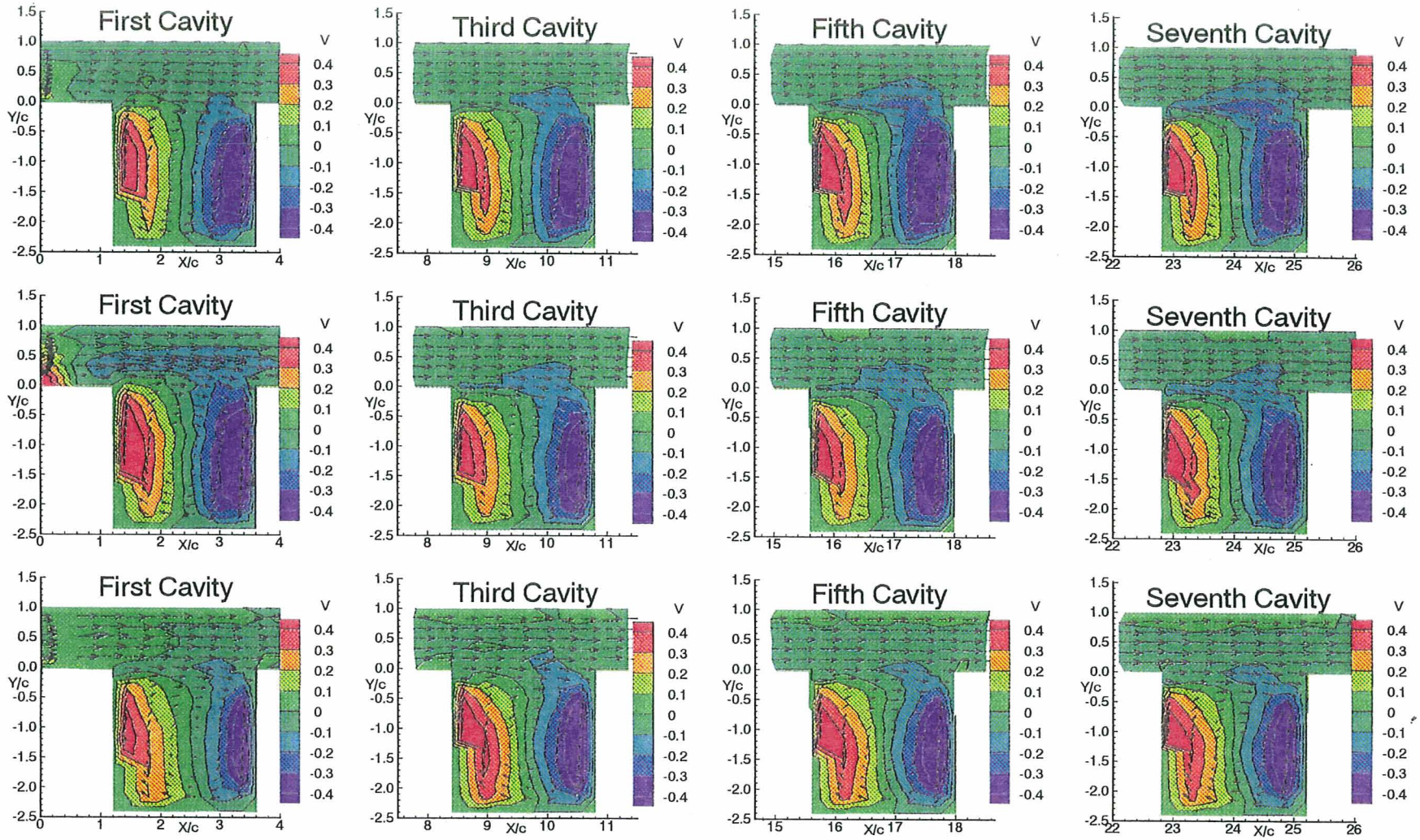

Figure 8. Radial velocity contours, first row - negative preswirl, second row - no preswirl, third row - positive preswirl.

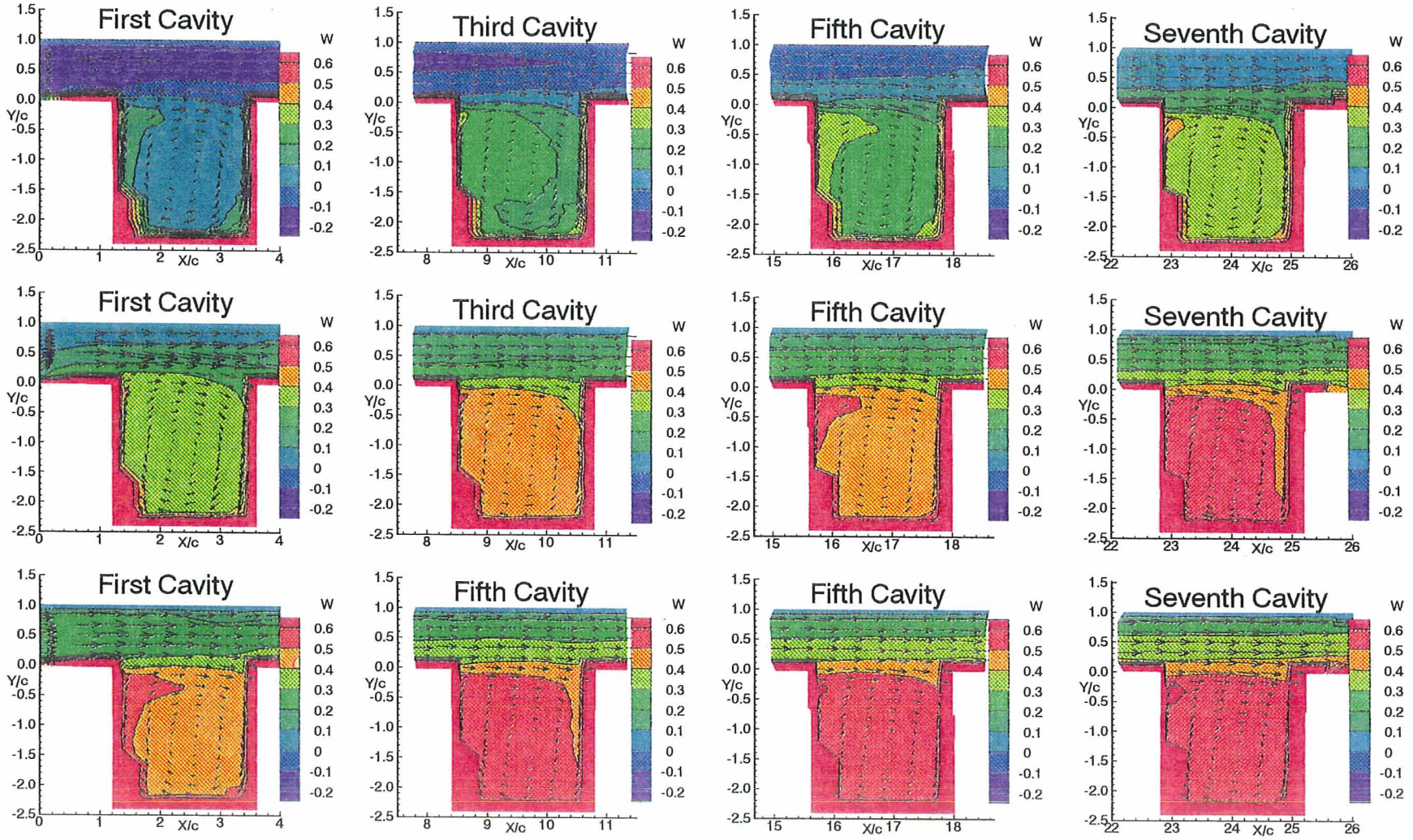

Figure 9. Tangential velocity contours, first row - negative preswirl, second row - no preswirl, third row - positive preswirl.

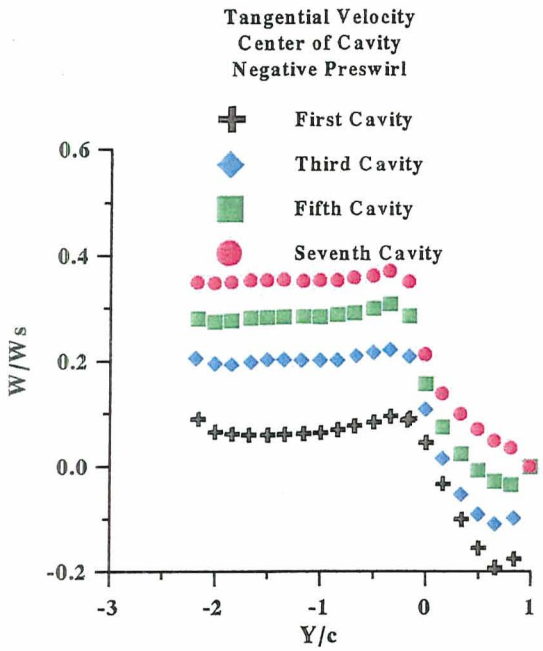

Figure 10. Tangential velocity radial profiles at X/c=2.2, 9.4, 16.5, and 23.7. Negative preswirl.

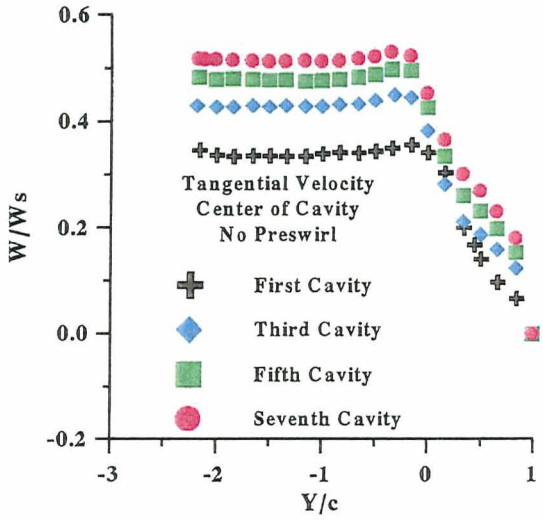

Figure 11. Tangential velocity radial profiles at X/c=2.2, 9.4, 16.5, and 23.7. No preswirl.

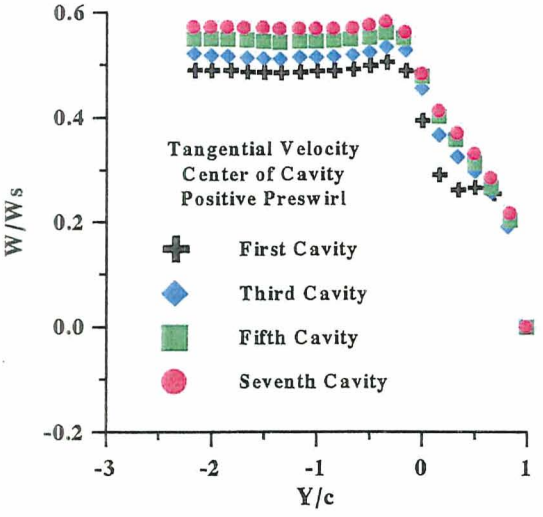

Figure 12. Tangential velocity radial profiles at X/c=2.2, 9.4, 16.5, and 23.7. Positive preswirl.

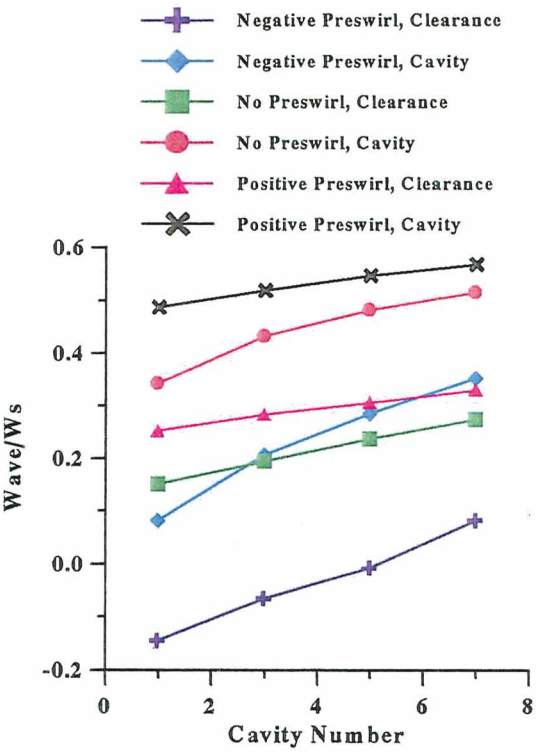

Figure 13. Tangential velocity averaged over clearance and cavity area.

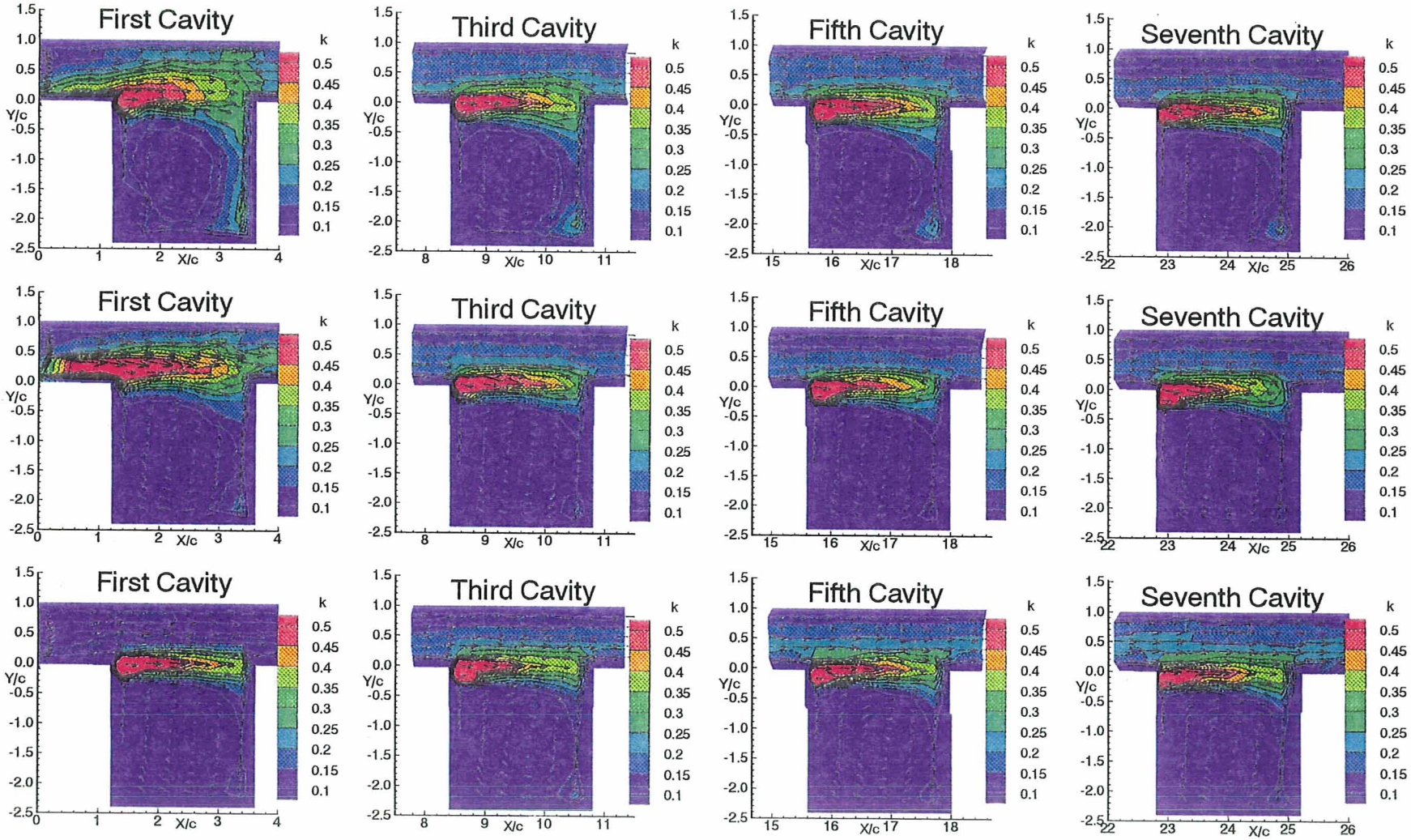

Figure 14. Turbulence kinetic energy contours, first row - negative preswirl, second row - no preswirl, third row - positive preswirl.

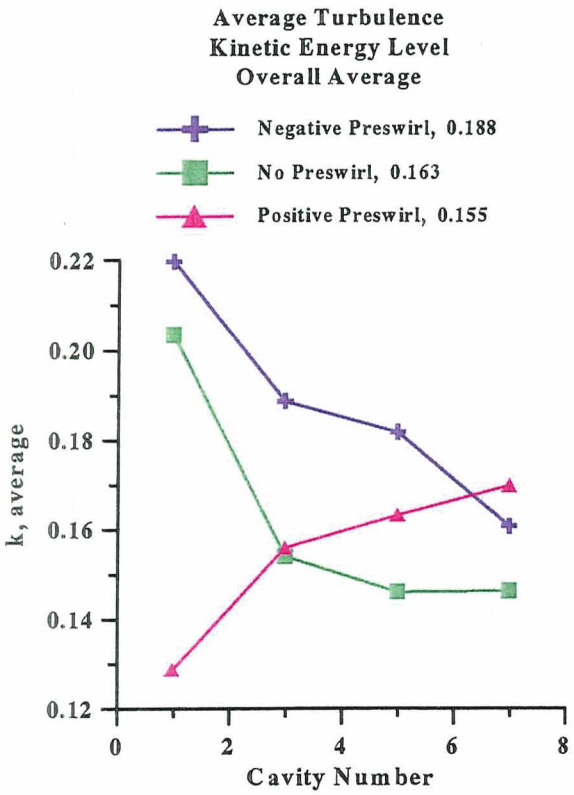

Figure 15. Average turbulence kinetic energy level contours.

Omit this Page

SESSION III

IMPELLERS

EFFECTS OF MISALIGNMENT ON THE STABILITY AND UNBALANCE RESPONSE OF STATICALLY INDETERMINATE ROTATING MACHINERY

N.S. Feng and E.J. Hahn
The University of New South Wales
Sydney, Austrailia

ABSTRACT

In statically indeterminate rotor bearings systems, where the rotor is supported by one or more hydrodynamic bearings, the reactions at each hydrodynamic bearing, and hence its stiffness and damping properties depend not only on the bearing type, the operating conditions and the bearing dimensions but also on the relative misalignment between the journal and the bearing housing. This misalignment has a significant influence on the vibration behaviour of the rotor bearing system, in particular, on its stability and unbalance response. Additional complications arise if non symmetric bearing types such as elliptic or tilting pad bearings are present. An iterative procedure is outlined which enables the bearing reactions to be determined at any speed, thereby enabling even large systems such as turbomachinery to be rapidly analysed in conjunction with existing linear rotor bearing vibration analysis software. Sample numerical examples show how misalignment and bearing type can affect the natural frequencies, the stability threshold and the unbalance response of such statically indeterminate systems.

NOMENCLATURE

$\mathbf{A}$	transformation matrix defined by Eqn. (13)
C	clearance of an imagined bearing at the mid position of the rotor = $\frac{1}{n}\sum_{i=1}^{n} C_i$
C_i	clearance of i'th bearing
$C_{yy}, C_{yz}, C_{zy}, C_{zz}$	bearing damping coefficients
e_i	eccentricity of i'th bearing of an aligned rotor
e_{iy}, e_{iz}	eccentricity components of i'th bearing in an aligned system
e^o_{iy}, e^o_{iz}	misalignment components at i'th bearing
e'_{iy}, e'_{iz}	eccentricity components of i'th bearing in a misaligned system
e_y, e_z	translational displacement components of the mid-point of the rotor
F_{iy}, F_{iz}	reaction force components at i'th bearing
F_y, F_z	total bearing reaction force components
J	objective function value
$K_{yy}, K_{yz}, K_{zy}, K_{zz}$	bearing stiffness coefficients
L_i	distance from the first bearing to the i'th bearing
M_y, M_z	resultant external moment components about Y and Z axes respectively
n	number of bearings on the rotor
T_y, T_z	resultant moment components due to bearing reactions about Y and Z axes respectively

W_y, W_z	resultant externally applied load components
Y,Z	lateral directions, horizontal and vertical respectively
$y, z; y', z'$	displacement components
$\dot{y}, \dot{z}; \dot{y}', \dot{z}'$	velocity components
α_i	angle between Y axis and eccentricity direction for i'th bearing
β_i	inclination angle between Y axis and load line at i'th bearing
$\Delta\delta_{iy}, \Delta\delta_{iz}$	components of shaft bending from the aligned rotor centreline at i'th bearing
$\Delta F_{iy}, \Delta F_{iz}$	components of reaction force variations at i'th bearing
$\varepsilon_y, \varepsilon_z$	$= e_y / C, e_z / C$
$\varepsilon_{iy}, \varepsilon_{iz}$	$= e_{iy} / C_i, e_{iz} / C_i$
$\varepsilon^o_{iy}, \varepsilon^o_{iz}$	$= e^o_{iy} / C_i, e^o_{iz} / C_i$
θ_y, θ_z	rotations of the rotor about Y and Z axes respectively
ϕ_i	attitude angle of i'th bearing
Ω	rotor speed

INTRODUCTION

Statically indeterminate rotor bearing systems, where the rotor is supported by three or more hydrodynamic bearings, occur frequently in rotating machinery. In the power generation industry it is not uncommon for a turbogenerator installation to be supported on eleven such bearings. Static indeterminacy is also present in centrifugal pump rotors with hydrodynamic bearings if the seals contribute significantly to supporting the load [1]. To determine the steady state behaviour of such systems for some given misalignment and unbalance presents significant computational difficulties. One can either linearise the system (i.e. use linearised stiffness and damping coefficients to describe the hydrodynamic bearing forces) or use a transient solution procedure [2,3]. Thus, ref. [2] investigates the problem in general, using initial value solution techniques in conjunction with truncated free-free normal modes. Owing to the difficulty of obtaining these modes in general, solutions are given only for uniform rotors, a problem overcome by using finite elements for rotor modelling [3]. Though this transient solution approach is completely general and valid even in the presence of large amplitude vibrations, computation times are necessarily lengthy and such an approach is impractical for parametric studies on the effects of clearance changes, misalignment changes, unbalance changes, etc. on the vibration behaviour of large industrial turbomachinery which requires many degrees of freedom for proper modelling. On the other hand, provided linearisation is valid, and provided convergence problems can be overcome, one can fruitfully determine the natural frequencies, the corresponding mode shapes, the stability and the small amplitude unbalance response about the equilibrium state. It thus becomes computationally feasible to determine the effects of clearance, unbalance, misalignment etc. on the vibration behaviour of even large systems such as steam turbogenerator systems. Whether the rotor is modelled via finite elements [3,4] or by transfer matrices [5,6] is not at issue and either of these rotor modelling approaches are applicable. Thus, ref. [6] uses transfer matrices to illustrate the effect of misalignment on two rotor, four bearing systems and this is the approach adopted here, since the authors have found transfer matrix modelling feasible even for large turbomachinery installations [7] yet economical in computer storage requirements.

Turbomachinery installations generally use hydrodynamic bearings. The reaction forces at each bearing are uniquely related to the eccentricity of the rotor journals in their respective bearings and hence will be dependent not only on bearing type, operating conditions and bearing dimensions but will also be influenced by any lateral misalignment in the rotor bearing installation. The static deflection of the rotor measured relative to some arbitrary datum, may also be considered to contribute to such misalignment. Since the stiffness and damping properties of the bearing supports are also dependent on these bearing reactions, to determine the vibration behaviour of such statically indeterminate systems, one must determine the location of the rotor in its respective bearing housings for some given installation at any given rotor speed making due allowance for the attendant influence of rotor bearing misalignment. There is a significant increase in analysis difficulty compared to statically determinate rotor bearing systems. Hence, the aim of this paper is to illustrate misalignment effects on the vibration behaviour of such rotor bearing systems and to highlight the difficulties associated with developing relevant transfer matrix software.

THEORY

Solution Strategy

When there are three or more bearings supporting a rotor as in Figure 1, a statically indeterminate system results. Obtaining a solution in such a case is equivalent to obtaining the correct position of the rotor in the bearings at running speed, so that the reaction forces at the bearings and the external loads on the rotor satisfy equilibrium. Once the equilibrium position is determined, the dynamic bearing coefficients which are required for the dynamic vibration analysis are readily found.

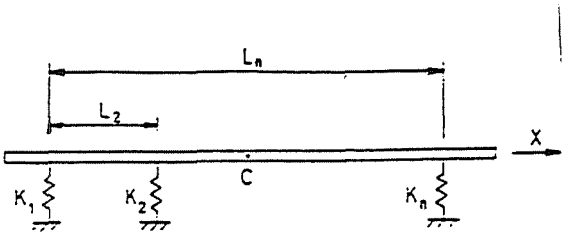

Figure 1: Statically indeterminate rotor bearing system.

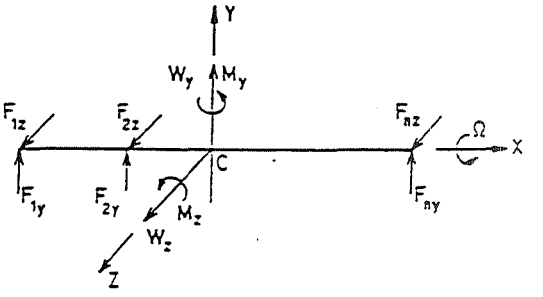

Figure 2: Free body diagram of rotor.

External Forces

A free body diagram of the rotor is shown in Figure 2. The resultant of all non-reaction external loads, e.g. gravitational loads, acting on the rotor is here represented by two moments, M_y, M_z and by two forces, W_y, W_z at the mid-point of the rotor. For equilibrium considerations, the rotor may be regarded as rigid, and since all external forces are parallel to the YZ plane, the rotor has four degrees of freedom, viz. the translations e_y, e_z and the rotations θ_y and θ_z as shown in Figure 3; i.e. there are four displacement variables, corresponding to these freedoms, determining the position of the rotor with respect to some fixed datum point in space.

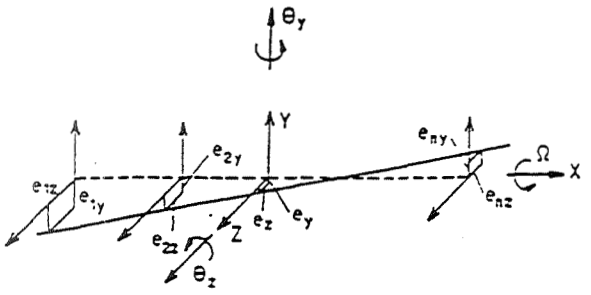

Figure 3: Translational and rotational degrees of freedom of rotor.

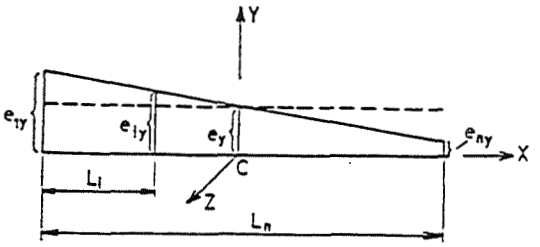

Figure 4: Geometric relationships for a rigid rotor.

Assuming the centreline of the bearings to be along the X axis, the y-component of the eccentricity of the i'th journal is then given by (see Figures 3 and 4):

$$e_{iy} = e_y + \left(e_{1y} - e_y\right)\left(1 - 2L_i / L_n\right) \quad , \tag{1}$$

or in non-dimensional form by:

$$\varepsilon_{iy} = \frac{C}{C_i}\left[\varepsilon_y + \left(\frac{C_1}{C}\varepsilon_{1y} - \varepsilon_y\right)\left(1 - 2L_i / L_n\right)\right] \quad . \tag{2}$$

Similar equations define e_{iz} and ε_{iz}. These equations are for an aligned rigid rotor.

In general the rotor bends due to gravity and support reactions. However, Eqns (1) and (2) still apply as long as the bearings are located along a bearing centreline which has the same shape as the deformed rotor centreline. Such a rotor is defined here as being an aligned rotor. Any offset of the bearing centres away from this unique (for some given speed) bearing centreline is considered as misalignment.

Once the support reactions for the aligned rotor are found, the reaction forces acting on a misaligned rotor can be found by considering the reaction force variations due to the shaft bending variation from the aligned rotor centreline. Now:

$$\Delta F_{iy} = F\left(\Delta\delta_{1y}, \Delta\delta_{2y}, \ldots, \Delta\delta_{ny}\right) \qquad (i = 1,2,\ldots,n) \tag{3}$$

where $$\Delta\delta_{iy} = e^{o}_{iy} + e_{iy} - e'_{iy} \qquad (i = 1,2,\ldots,n) \tag{4}$$

with corresponding equation for ΔF_{1z} and $\Delta\delta_{iz}$. The function F takes into account the rotor stiffness as well as the equilibrium of the reaction force variations [9].

The bearing reaction forces and the associated attitude angles are generally different from bearing to bearing. These forces need to be related to the global coordinate system. A schematic of the i'th bearing supporting a load W_i with the journal centre at (e_i, ϕ_i) is shown in Figure 5. Thus:

$$F_{iy} = -W_i \cos\beta_i \quad , \tag{5}$$

$$F_{iz} = -W_i \sin\beta_i \quad , \tag{6}$$

$$\beta_i = \alpha_i - \phi_i \quad , \tag{7}$$

and

$$\alpha_i = \tan^{-1}\left(\frac{\varepsilon_{iz}}{\varepsilon_{iy}}\right) \quad . \tag{8}$$

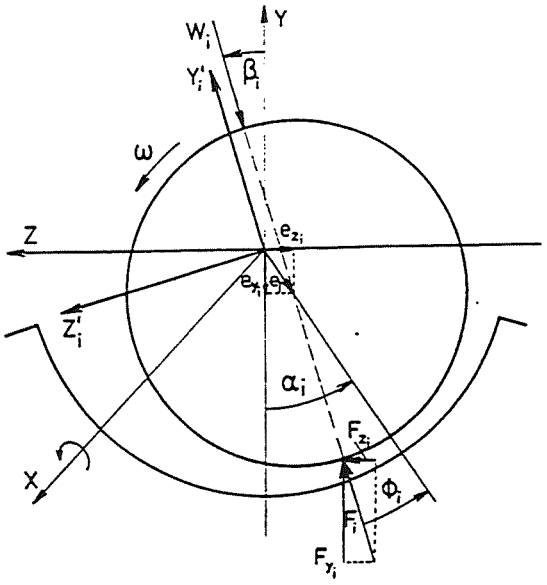

Figure 5: Bearing load inclination.

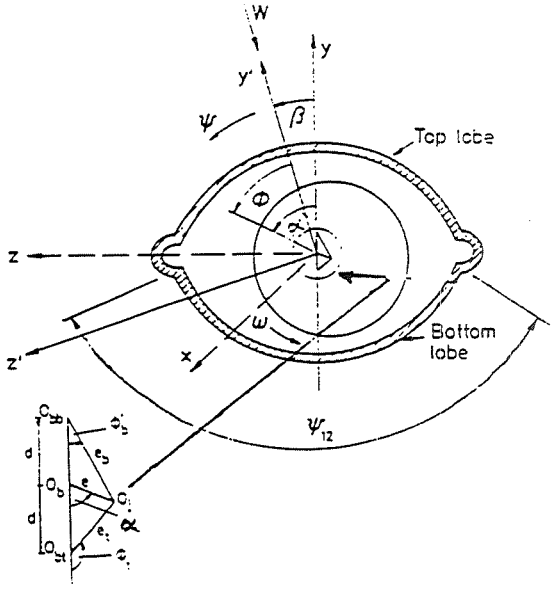

Figure 6: Schematic of elliptic bearing lobes.

Numerical solutions of the Reynolds equation are generally required to establish the pressure distribution and hence the oil film forces. Such solutions require considerable computing effort so that for a given bearing type, pre-calculated tabular data on load capacity and attitude angle as a function of ε_i are used. Such data are generally evaluated assuming the static load to be acting vertically downwards, whereas in a statically indeterminate system, the load will generally be inclined at an angle β to the vertical. This is not a problem in a plain journal bearing since the bearing configuration is not altered. However, in the case of non-circular bearings such as elliptic or tilting pad bearings, symmetry disappears once $\beta \neq 0$, resulting in different bearing configuration and behaviour. Figure 6 depicts an elliptic bearing with inclined static load. The effect of β on its static and dynamic properties at a given eccentricity $\varepsilon = 0.2$ is shown in Figure 7. It can be seen that these properties vary greatly with β. Thus, in tabulated data for such bearings, both ε and β become variables and double interpolation is needed to determine the bearing reaction forces. Since the β values are unknown, iteration for them is also usually necessary. Starting from initially assumed values for β_i (normally zero), the equilibrium position of the rotor is found. If there are any non-circular bearings present in the system, their inclination angles are evaluated using Eqns (7) and (8). If they have changed, new β values are used, until there are no significant changes in the β values between successive iterations.

The resultant of the bearing reaction forces may then be represented by two moments T_y, T_z and the two forces F_y, F_z at the mid-point of the rotor, viz:

$$T_y = \sum_{i=1}^{n} F_{iz}\left(L_n/2 - L_i\right) \quad , \tag{9}$$

and

$$F_y = \sum_{i=1}^{n} F_{iy} \quad . \tag{10}$$

Similar expressions apply to T_z and F_z.

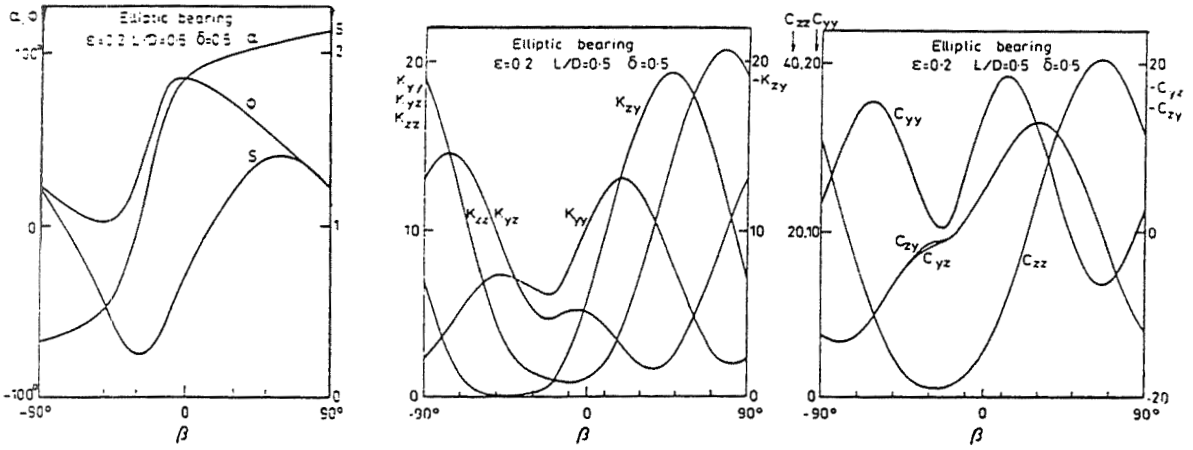

Figure 7: Effect of β on static and dynamic properties of an elliptic bearing.

The Equilibrium Position

Since the bearing load capacities are non-linearly related to the bearing displacements, for the aligned rotor one has a non-linear problem with four unknown displacement variables. Hence, an iterative approach is used to determine the equilibrium position of the rotor for some assumed rotor centreline deflection shape. Starting from some assumed initial position, the rotor position is adjusted incrementally. At each step, the corresponding reaction forces at each bearing are determined and equilibrium is checked until the desired position is found. For this purpose, the following objective function is defined:

$$J = \min\left[\left(W_y - F_y\right)^2 + \left(W_z - F_z\right)^2 + \left(\frac{M_y - T_y}{L_n}\right)^2 + \left(\frac{M_z - T_z}{L_n}\right)^2\right] \tag{11}$$

Since the stiffnesses of the journal bearings in any two perpendicular directions are cross coupled, the direction of the bearing eccentricity, or its increment, is not the same as the direction of the external load, or its increment (Figure 5). As a result, it is important to move the rotor in a stepwise manner so that at each step, the rotor is given a small translational or rotational displacement increment in the Y or Z directions. If the objective function decreases, this step is accepted and a further increment in that direction is tried; otherwise,

an increment is taken in a different direction. The iteration is continued until the value of J in Eqn (11) is smaller than some prespecified convergence criterion, indicating that the equilibrium reactions corresponding to the assumed rotor shape have been found. These loads are then used to find the new deflection shape for the rotor centreline and again a new set of equilibrium reactions are found. This procedure is repeated until successive iterations produce identical shapes for the rotor centreline.

When considering shaft flexibility, it is the variation of the rotor centreline away from the aligned one which needs to be found. This is done by another iterative approach. Thus, Eqn (4) is used to find the shaft deflection variations $\Delta\delta_{iy}$ (and $\Delta\delta_{iz}$) and Eqn (3) is used to find the reaction variations ΔF_{iy} (and ΔF_{iz}) needed to obtain the $\Delta\delta_{iy}$ (and $\Delta\delta_{iz}$). Finally, the new eccentricity components e'_{iy} and e'_{iz} under the new reaction forces F_{iy} and F_{iz} are found for each of the bearings. These steps are repeated until successive iterations produce identical shaft deflection variations. Full details are given in [9].

Transformation of the Bearing Coefficients

Once the equilibrium position of the rotor is determined, one can use tabulated data to interpolate for the dynamic bearing coefficients. All bearing coefficients are pre-determined in a coordinate system coincident with the static load line. When the loads on the individual bearings are inclined, the dynamic bearing coefficients need to be transformed into the global coordinates of the system. From the definition of those coefficients, one has:

$$\begin{Bmatrix} dF_z \\ dF_y \end{Bmatrix} = -\begin{bmatrix} K_{zz} & K_{zy} \\ K_{yz} & K_{yy} \end{bmatrix}\begin{Bmatrix} z \\ y \end{Bmatrix} - \begin{bmatrix} C_{zz} & C_{zy} \\ C_{yz} & C_{yy} \end{bmatrix}\begin{Bmatrix} \dot{z} \\ \dot{y} \end{Bmatrix} \quad . \tag{12}$$

Using the coordinate transformations:

$$\begin{Bmatrix} z \\ y \end{Bmatrix} = \begin{bmatrix} \cos\beta & \sin\beta \\ -\sin\beta & \cos\beta \end{bmatrix}\begin{Bmatrix} z' \\ y' \end{Bmatrix} = \mathbf{A}\begin{Bmatrix} z' \\ y' \end{Bmatrix} \quad , \tag{13}$$

one obtains

$$\begin{Bmatrix} z' \\ y' \end{Bmatrix} = \mathbf{A}^T\begin{Bmatrix} z \\ y \end{Bmatrix} \quad , \tag{14}$$

with the same transformations between velocities and forces. Eqn (12) may then be written as:

$$\begin{Bmatrix} dF_z \\ dF_y \end{Bmatrix} = \mathbf{A}\begin{Bmatrix} dF'_z \\ dF'_y \end{Bmatrix} = -\mathbf{A}\begin{bmatrix} K'_{zz} & K'_{zy} \\ K'_{yz} & K'_{yy} \end{bmatrix}\begin{Bmatrix} z' \\ y' \end{Bmatrix} - \mathbf{A}\begin{bmatrix} C'_{zz} & C'_{zy} \\ C'_{yz} & C'_{yy} \end{bmatrix}\begin{Bmatrix} \dot{z}' \\ \dot{y}' \end{Bmatrix} \quad , \tag{15}$$

$$= -\mathbf{A}\begin{bmatrix} K'_{zz} & K'_{zy} \\ K'_{yz} & K'_{yy} \end{bmatrix}\mathbf{A}^T\begin{Bmatrix} z \\ y \end{Bmatrix} - \mathbf{A}\begin{bmatrix} C'_{zz} & C'_{zy} \\ C'_{yz} & C'_{yy} \end{bmatrix}\mathbf{A}^T\begin{Bmatrix} \dot{z} \\ \dot{y} \end{Bmatrix} \quad , \tag{16}$$

thereby defining the global direction stiffness and damping coefficients of Eqn (12).

Program Flow Chart

Figure 8 shows the schematic program flow chart for the vibration analysis, i.e. for obtaining the natural frequency, unbalance response and stability threshold of rotor bearing systems. The flow chart part for statically indeterminate systems has a parallel structure to that for the statically determinate ones. Note that whenever the rotor speed varies, the loads at each support have to be re-evaluated. If non symmetric bearings such as elliptic or tilting pad bearings are used, triple iteration is needed to satisfy both the force equilibrium and load inclination. Moreover, coordinate transformation may be needed to bring all the bearing coefficients into the global system coordinates.

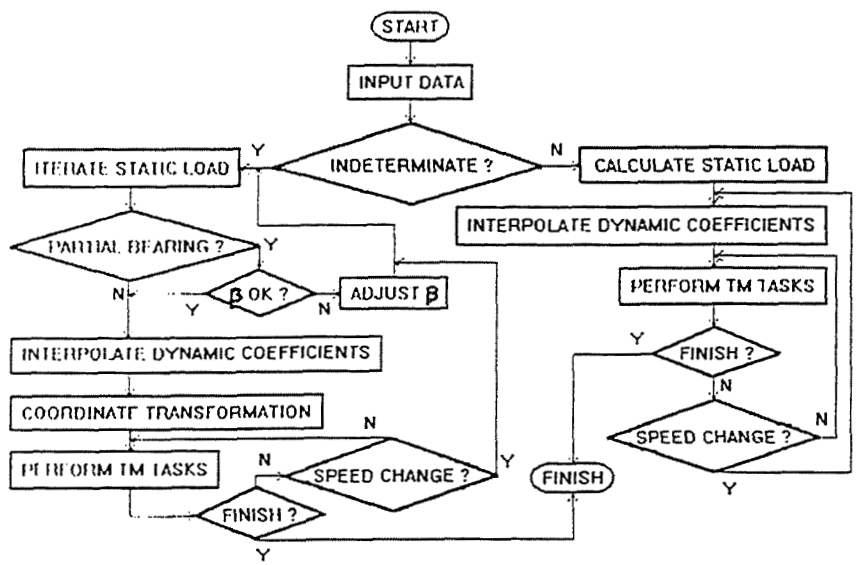

Figure 8: Program flow chart.

RESULTS

A uniform rotor supported by three identical full journal bearings as shown in Figure 9 is selected for demonstration purposes. The rotor is 2m in length and 0.1m in diameter. The bearing properties are: diameter = 0.1m, width = 0.05m, radial clearance = 0.0001m, and viscosity = 0.007Ns/m². The middle bearing is misaligned in the horizontal direction.

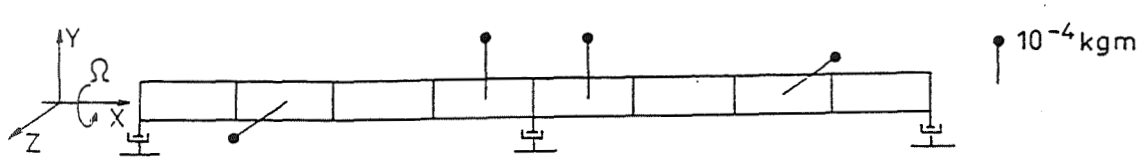

Figure 9: Uniform rotor supported by three identical hydrodynamic bearings.

Table 1 shows the first seven damped natural frequencies of the system for different alignment situations at a rotor speed Ω of 721.19 rad/s, at which speed the aligned system is critically stable.

Table 1: Sample Natural Frequency Calculation
(Rotor supported on journal bearings, $\Omega = 721.19$ rad/s)

ε^{o}_{2z}	-0.3	-0.2	-0.1	0	0.1	0.2	0.3
No.	NATURAL FREQUENCIES (Re/Im) (RAD/S)						
1	-.0684/388.6	1.016/387.8	1.030/387.8	.0015/388.4	-1.958/389.8	-4.714/391.6	-8.117/393.9
2	-78.02/412.9	-74.79/412.1	-71.92/411.3	-69.44/410.7	-67.42/410.1	-65.92/409.7	-64.95/409.5
3	-214.1/435.1	-212.3/435.0	-211.0/435.3	-210.0/436.1	-209.3/437.3	-209.0/438.9	-209.1/440.8
4	-118.8/1257.	-119.6/1257.	-120.4/1257.	-121.1/1258.	-121.7/1258.	-122.1/1258.	-122.3/1258.
5	-282.3/1281.	-282.1/1282.	-282.0/1283.	-281.9/1284.	-281.7/1285.	-281.7/1285.	-281.6/1286.
6	-990.2/2489.	-939.8/2463.	-920.4/2437.	-919.6/2422.	-933.6/2417.	-963.4/2416.	-1009./2410.
7	-872.7/2686.	-921.9/2717.	-943.2/2744.	-948.9/2753.	-942.7/2748.	-923.0/2732.	-889.5/2715.
B_i	JOURNAL POSITIONS ($\varepsilon_Y/\varepsilon_Z$) (DIM)						
1	0.010/0.179	0.019/0.174	0.028/0.169	0.037/0.163	0.046/0.158	0.056/0.153	0.065/0.147
2	0.094/0.129	0.075/0.141	0.056/0.152	0.037/0.163	0.019/0.174	0.001/0.184	-0.015/0.194
3	0.010/0.179	0.019/0.174	0.028/0.169	0.037/0.163	0.046/0.158	0.056/0.153	0.065/0.147
	MID-SHAFT BENDING FROM ALIGNED SHAPE $\left(\frac{y}{C}/\frac{z}{C}\right)$ (DIM)						
	-.0839/-.2504	-.0558/-.1672	-.0279/-.0839	0, 0	.0275/.0841	.0544/.1684	.0807/.2528

It can be seen that a negative misalignment ε^{o}_{2z} initially reduces the system stability and then increases the stability when ε^{o}_{2z} is further increased (in absolute sense). This is because the middle bearing is initially unloaded and then loaded again in the other direction. When the middle bearing is misaligned in the other direction, the stability is improved as ε^{o}_{2z} increases.

Table 2: Sample Natural Frequency Calculation
(Rotor supported on elliptic bearings, $\Omega = 721.19$ rad/s)

ε^{o}_{2z}	-0.3	-0.2	-0.1	0	0.1	0.2	0.3
No.	NATURAL FREQUENCIES (Re/Im) (RAD/S)						
1	-9.466/544.0	-77.51/559.3	-81.79/558.8	-83.42/561.8	-91.84/562.3	-98.11/560.6	-90.58/559.8
2	-419.9/565.3	-430.3/564.9	-433.2/567.9	-440.1/577.3	-439.6/575.5	-440.6/576.7	-442.1/584.9
3	-287.7/609.9	-286.3/618.4	-279.9/623.1	-272.8/637.0	-271.1/635.9	-264.6/636.9	-256.4/643.7
4	-375.3/1185.	-382.9/1183.	-401.2/1185.	-427.7/1183.	-429.0/1184.	-442.3/1189.	-462.9/1193.
5	-26.45/1255.	-26.47/1255.	-26.56/1255.	-26.56/1255.	-26.59/1255.	-26.63/1255.	-26.59/1255.
6	-203.9/1909.	-209.1/1908.	-209.6/1908.	-209.1/1908.	-208.8/1908.	-208.5/1908.	-205.8/1908.
7	-909.5/2884.	-1064./2842.	-1109./2853.	-1160./2869.	-1186./2860.	-1227./2868.	-1245./2896.
B_i	JOURNAL POSITIONS ($\varepsilon_Y/\varepsilon_Z$) (DIM)						
1	-0.006/0.086	-0.004/0.079	-0.001/0.073	0.002/0.066	0.005/0.059	0.008/0.053	0.011/0.046
2	0.015/0.026	0.013/0.039	0.008/0.053	0.002/0.066	-0.004/0.079	-0.009/0.092	-0.015/0.105
3	-0.006/0.086	-0.004/0.079	-0.001/0.073	0.002/0.066	0.005/0.059	0.008/0.053	0.011/0.046
	MID-SHAFT BENDING FROM ALIGNED SHAPE $\left(\frac{y}{C}/\frac{z}{C}\right)$ (DIM)						
	-.0217/-.2399	-.0170/-.1597	-.0086/-.0799	0, 0	.0084/.0800	.0168/.1604	.0255/.2405

When the same rotor is supported by three equivalent elliptic bearings with an ellipticity of 0.5, with all other dimensions and conditions unchanged, the system behaviour changes dramatically. Table 2 shows the first seven natural frequencies of such a system with the same misalignment arrangement as in Table 1. It can be seen that elliptic bearing supports shift the system far into the stable region. However, the stability deteriorates rapidly if the misalignment of the middle bearing in the negative horizontal direction reaches -0.3.

Sample unbalance responses at different locations along the rotor and stability thresholds are shown in Figs. 10-12 and Figs. 13-15 respectively for the same rotor bearing systems as in Tables 1 and 2. Four unbalance moments of 10^{-4} kg-m are added to the rotor, two at mid-points of segments 4 and 5 in the positive Y direction, one at mid-point of segment 2 in the positive Z direction, and one at mid-point of segment 7 in the negative Z direction, all references being at time zero. It can be seen that the effects of misalignment on unbalance responses and stability threshold speeds are sometimes significant. Such sensitivity of system stability and unbalance response to misalignment indicates that misalignment can be purposely introduced to improve system stability and to modify rotor vibrations.

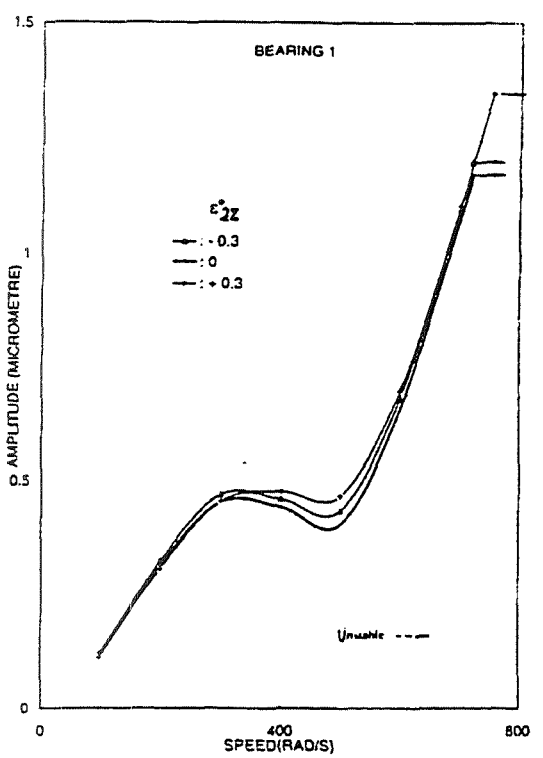

Figure 10: Unbalance response and stability threshold of sample rotor with journal bearings at bearing 1 for various misalignments.

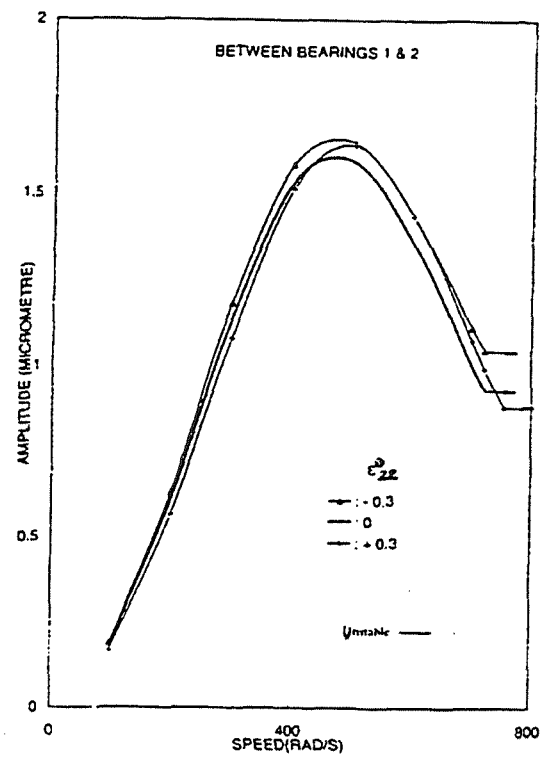

Figure 11: Unbalance response and stability threshold of sample rotor with journal bearings at a point midway between bearings 1 and 2 for various misalignments.

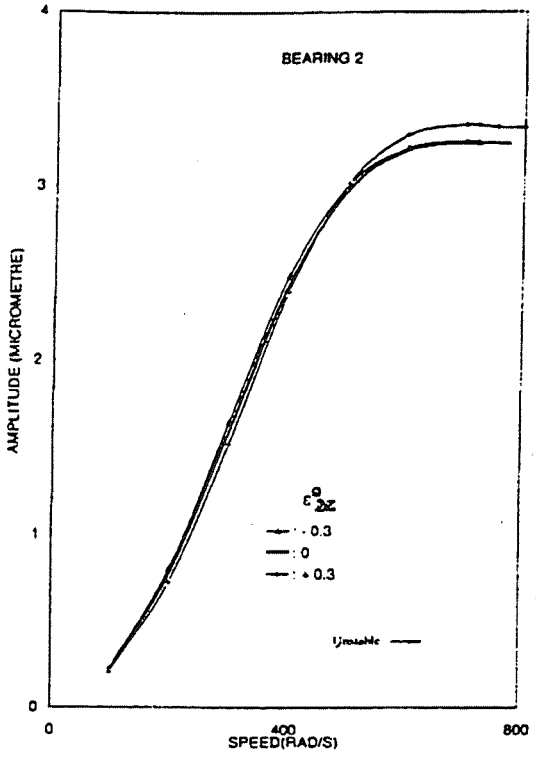

Figure 12: Unbalance response and stability threshold of sample rotor with journal bearings at bearing 2 for various misalignments.

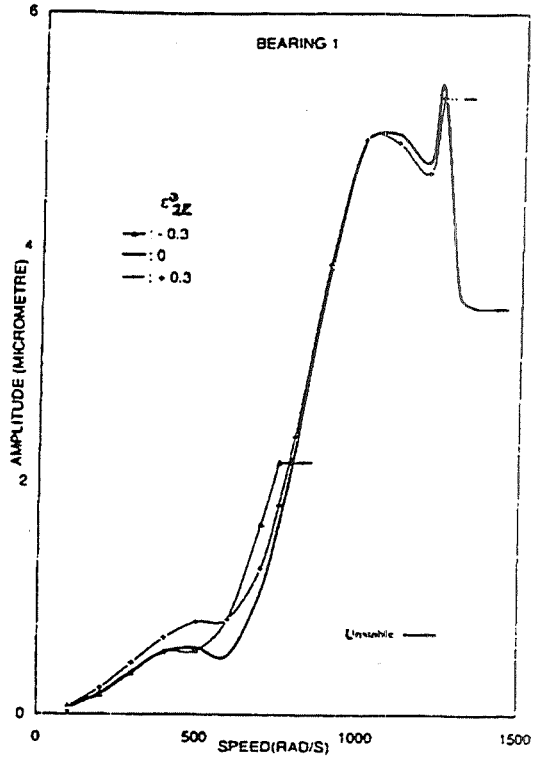

Figure 13: Unbalance response and stability threshold of sample rotor with elliptic bearings at bearing 1 for various misalignments.

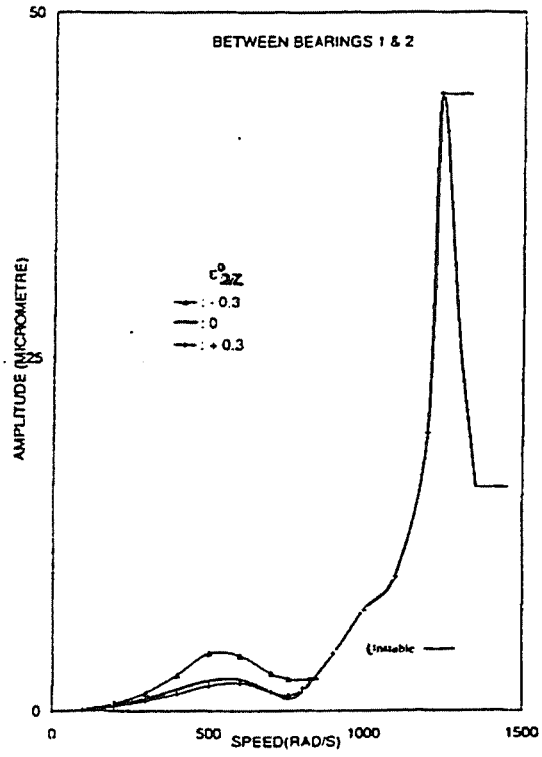

Figure 14: Unbalance response and stability threshold of sample rotor with elliptic bearings at a point midway between bearings 1 and 2 for various misalignments.

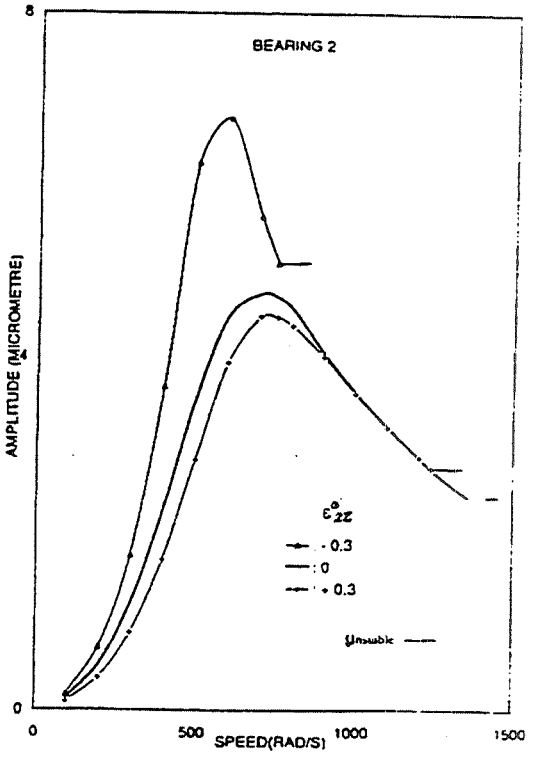

Figure 15: Unbalance response and stability threshold of sample rotor with elliptic bearings at bearing 2 for various misalignments.

COMPARISON WITH PUBLISHED RESULTS

Ref. [6] considered the effect of misalignment of support journal bearings on the stability of a two rotor, four bearing system. In order to verify the above procedures, comparison is made with some of the results in [6], where several systems comprising two rigidly coupled rotors, supported by four hydrodynamic bearings (two bearings per rotor) were considered. Unfortunately, the data in [6] is incomplete and second guessing at missing values enables only an approximate comparison. Thus, assuming $E = 210$ GN/m^2 and $\gamma = 7800$ kg/m^3 for the four sample rotors, the first pin-pin critical speeds of the individual rotors A, B, C and D, as calculated by the in-house transfer matrix (TM) software, and also according to Rayleigh's method [8] for a concentrated mass at midspan are respectively 1049, 2376, 1836 and 1060 rpm instead of the quoted 1144, 2626, 2034 and 1178 rpm in [6]. Nevertheless, in spite of this slight discrepancy between the basic input data used in [6] and the data for the in-house TM programs, the stabilities of the statically indeterminate rotor bearing systems can be compared. The rotor system A-A, as shown in Figure 16, with misalignment at bearing 3, was best suited for comparison because of the definitions of alignment used here and in [6].

Figure 17 compares the predicted stability thresholds as a function of the misalignment at bearing 3 obtained by the current approach and that of [6]. There is general agreement, especially at low misalignment values. Apart from possibly slightly different input data, the other source of the discrepancy could be due to the inclusion of the rotational stiffness and damping coefficients in [6].

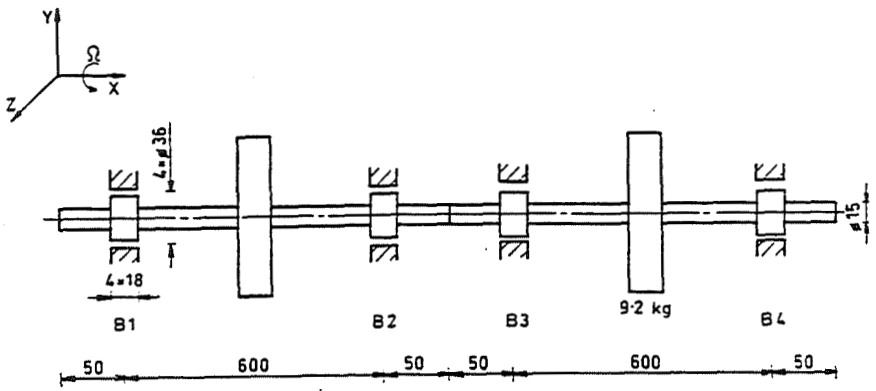

Figure 16: Flexible rotor system A-A [6].

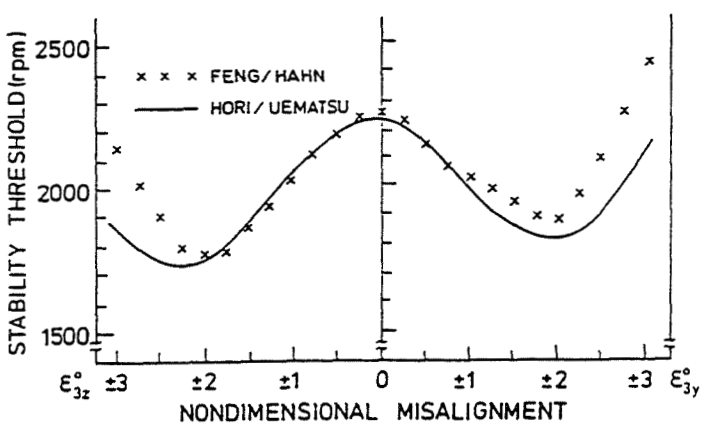

Figure 17: Effect of vertical misalignment on stability.

CONCLUSIONS

An iterative but nevertheless computationally feasible approach to evaluate the vibration behaviour of statically indeterminate rotor bearing systems using linearised bearing coefficients may be used in conjunction with the transfer matrix method to achieve computational efficiency.

To achieve computational efficiency, sufficient preparatory tabulated data is required for non symmetric bearing types to account for the dependence of static and dynamic properties on load inclination.

Misalignment in the bearing arrangement can significantly alter the natural frequencies, stability, and unbalance response of rotor bearing systems.

ACKNOWLEDGMENTS

This work was supported by the Australian Research Council and Pacific Power (Northern Region).

REFERENCES

[1] Diewald, W, and Nordmann, R, 1989, 'Dynamic Analysis of Centrifugal Pump Rotors With Fluid Mechanical Interactions', Trans. ASME, Journal of Vibration, Acoustics, and Reliability in Design, Vol. 111, pp370-378.

[2] Holmes, A G, Ettles, C M McC, and Mayes, I W, 1978, 'The Dynamics of Multi-Rotor Systems Supported On Oil Film Bearings', Trans. ASME, Journal of Mechanical Design, Vol. 100, pp156-164.

[3] Ding, J, and Krodkiewski, J M, 1993, 'Inclusion of Static Indetermination in the Mathematical Model for Nonlinear Dynamic Analysis of Multi-bearing Rotor Systems', J. of Sound and Vibration, Vol. 164, pp267-280.

[4] Nelson, H D, and McVaugh, J M, 1976, 'The Dynamics of Rotor-Bearing Systems Using Finite Elements', Trans. ASME, Journal of Engineering for Industry, Vol. 98, pp593-600.

[5] Lund, J W, 1974, 'Stability and Damped Critical Speeds of a Flexible Rotor in Fluid Film Bearings', Trans. ASME, Journal of Engineering for Industry, Vol. 96, pp509-517.

[6] Hori, Y and Uematsu, R, 1980, 'Influence of Misalignment of Support Journal Bearings on Stability of a Multi-rotor System', Tribology International, Oct 1980, pp249-252.

[7] Behzad, M, Feng, N, and Hahn, E J, 1994, 'Vibration Analysis of Rotor Bearing Systems Using the Riccati Transfer Matrix Approach', International Mechanical Engineering Congress and Exhibition, May 1994, IEAust. Conf. Publication No. 94/13, pp223-228.

[8] Thomson, W T, 1988, 'Theory of Vibration with Application', 3rd ed., Prentice Hall, N.J., 1988, p25.

[9] Feng, N, and Hahn, E J, 1996, 'Transfer Matrix Software for Statically Indeterminate Flexible Rotor Bearing Systems - PC Version 2.0', Report 1996/AM/1, UNSW, 58pp.

THEORETICAL IDENTIFICATION OF THE ROTORDYNAMIC COEFFICIENTS IN THE IMPELLER-DIFFUSER DOMAIN OF A CENTRIFUGAL PUMP

R. Fongang
Technical University of Darmstadt
Darmstadt, Federal Republic of Germany

J. Colding-Jorgensen
Colding Consult
Machine Dynamics
Horsholm, Denmark

R. Nordmann
Technical University of Darmstadt
Darmstadt, Federal Republic of Germany

ABSTRACT

A fluid model based on the unsteady potential flow theory is developed to investigate the hydrodynamic forces acting on a rotating impeller caused by the impeller-fluid-diffuser interaction in a centrifugal pump with vaneless or vaned diffuser. The impeller is assumed to have an infinite number of vanes perfectly guiding the flow and its center executes a whirling motion about the diffuser center. The flow is taken to be 2-dimensional, incompressible, inviscid and irrotational in the absolute coordinate system. The hydrodynamic forces are presented as a superposition of steady forces due to the diffuser asymmetry and unsteady forces due to the impeller center eccentricity, velocity and acceleration. The stiffness, damping and inertia coefficients are deduced from the unsteady forces decomposed into radial and tangential components relative to the orbit described by the impeller center. In comparison with most of the theoretical and experimental results found in the literature, the analysis seems to give good prediction. The study of the influence of some parameters on the results in the case of the vaned diffuser also attests to the qualitative validity of the model. It appears that, under certain operating conditions, the fluid forces on the impeller have a destabilizing effect on the pump rotor.

NOMENCLATURE

$[A]$	=	$[A_{ij}]$ (i = x, y j = x, y) hydrodynamic force matrix
b	=	impeller width
$\underline{c}$	=	(c_x, c_y) absolute velocity
$[D]$	=	$[D_{ij}]$ (i = x, y j= x, y) damping matrix
$\underline{F}$	=	(F_x, F_y) lateral force acting on the impeller
$\underline{\bar{F}}$	=	$(\bar{F}_x, \bar{F}_y)$ steady impeller force
i	=	imaginary unit ($i^2 = -1$)
$[K]$	=	$[K_{ij}]$ (i = x, y j = x, y) stiffness matrix
$[M]$	=	$[M_{ij}]$ (i = x, y j = x, y) mass matrix
ND	=	number of diffuser vanes
o, o'	=	diffuser center, impeller center
Q, Q_n	=	flow rate, design flow rate
r_1, r_2	=	inner and outer radius of the impeller

r_3, r_4	=	inlet and outlet radius of the diffuser
r_t	=	tongue radius for the spiral volute
t	=	time
$\underline{w}$	=	(w_x, w_y) velocity relative to the impeller
z	=	$re^{i\theta}$ complex position of a point in the (o, x, y) frame
z'	=	$r'e^{i\theta'} = z - \varepsilon e^{i\Omega t}$ complex position of a point in (o', x', y') frame with its axes parallel to those of (o, x, y)
α, β	=	diffuser blade angle, impeller blade angle
ε	=	eccentricity
ϕ, ϕ_n	=	flow coefficient ($= Q/2\pi b\omega r_2^2$), design flow coefficient
Γ	=	circulation of the prerotation
ω, Ω	=	angular velocity of the impeller, whirl speed of the impeller center
ρ	=	flow density

Superscript

' : refers to the frame (o', x', y')

Subscripts

r : radial relative to the whirl orbit

t : tangential relative to the whirl orbit

INTRODUCTION

It has been made clear in recent years that the rotordynamic behavior of a centrifugal pump (fig. 1) is strongly influenced by the forces acting on its shaft due to the fluid-structure interaction. These are bearing and seal forces as well as fluid forces exerted on the impeller due to the impeller-diffuser interaction. Among these, the hydrodynamic bearing and seal forces have been subject of intensive studies as attested by many papers presented in the first seven workshops on rotordynamic problems in high performance turbomachinery. Their effects and evaluation are well known. The fluid forces on the impeller contribute largely to the destabilization of the pump rotor under certain operating conditions as demonstrated theoretically (Refs. 2, 6, 7, 8) and experimentally (Refs. 1, 2, 5, 12, 13). However their predictions are still a problem.

As indicated by Nordmann (Ref. 5) and Adkins and Brennen (Ref. 2), the total hydrodynamic forces on the impeller are the sum of the seal and shroud forces and of the lateral or impeller forces. The seal and shroud forces are caused by the pressure exerted on the external surface of the impeller seals and shrouds, while the impeller forces are due to the pressure and momentum exchange in the impeller. The present work suggests a method into investigation of the impeller forces. The analysis is valid both for a centrifugal pump with vaneless and vaned diffuser, since a vaneless diffuser can be treated as a vaned diffuser only with one vane. The impeller forces are usually described in rotordynamics by the following equation,

$$\underline{F} = \overline{\underline{F}} + [A]\underline{\varepsilon} \tag{1}$$

or in more detailed form as,

$$\underline{F} = \overline{\underline{F}} - ([K]\underline{\varepsilon} + [D]\dot{\underline{\varepsilon}} + [M]\ddot{\underline{\varepsilon}}) \tag{2}$$

$\underline{\bar{F}}$ represents the mean or steady impeller forces resulting from the impeller-diffuser interaction when the impeller center coincides with the diffuser center. For a vaned diffuser , $\underline{\bar{F}}$ is quasi-null. $\underline{\varepsilon}$ is the eccentricity of the impeller or rotor center relative to the diffuser or stator center.

Many authors have investigated the hydrodynamic impeller-diffuser interaction in a centrifugal pump. Previously, the studies were focused on the steady impeller forces. Refs. 3 and 4 present two of them. The rotordynamic analysis of this interaction has begun with the work of Domm and Hergt (Ref. 9) and Hergt and Krieger (Ref. 10). They first demonstrated the dependency of the impeller forces on the rotor center eccentricity. Since then the fluid forces acting on a rotating and whirling impeller have become subject of intensive research.

Colding-Jørgensen (Ref. 8) developed a quasisteady fluid model based on the singularity theory, replacing the impeller by a single vortex-source point and the volute by a set of steady vortex segments. He then calculated the impeller forces, taking into account the impeller center eccentricity and velocity and deduced for the first time the stiffness and damping coefficients.

Shoji and Ohashi (Ref. 14) introduced an unsteady potential flow theory, substituting the diffuser vanes by a set of steady vortices and the impeller blades by a distribution of unsteady vortices. They considered the influence of free vortices shed from the trailing edge of the impeller blades in their flow calculations. They then determined the complete lateral fluid forces on the impeller resolved into tangential and radial components relative to the orbital motion of the impeller center.

Adkins and Brennen (Ref. 2) and Tsujimoto et al. (Refs. 6, 7) assumed the impeller to have a very large number of thin blades perfectly guiding the flow. They then assimulated it to an actuator disc to develop a 2-dimensional flow model. Tsujimoto et al. (Ref. 7) extended their theory to an impeller rotating and whirling in a vaned diffuser.

Apart from Shoji and Ohashi (Ref. 14), who noted the damping effect of the impeller forces on the pump rotor, all these theoretical analyses concluded that the impeller forces have a destabilizing effect on the pump rotor for forward whirling motion of the impeller center with small whirl speed ratio Ω/ω.

This conclusion was confirmed by some experimental studies of lateral fluid forces on the impeller. Chamieh et al. (Ref. 1) made measurements of quasisteady impeller forces and determined the stiffness matrix. His work was extended to the determination of the damping and mass matrices by Jery et al. (Ref. 12) who then got the first complete measurements of the impeller forces. The test facility of Refs. 1 and 12 was modified by Adkins and Brennen (Ref. 2). They isolated the impeller-volute interaction from the external influences (pressure force on the external surface of shrouds) to measure the impeller forces. The authors of these three papers observed the contribution of the impeller forces to the pump rotor destabilization under the conditions mentioned above.

Ohashi and Shoji (Ref. 13) also made measurements of lateral fluid forces on the impeller. They noted, like the others and unlike their own theory, destabilizing fluid forces at lower flow coefficients for slow forward impeller center whirl motion.

Recently, Nordmann (Ref. 5) has made measurement of the total forces on the impeller rotating and whirling in a diffuser with two guide vanes. He also noted the destabilizing forces for forward whirling motion of the impeller center with small whirl speed ratio.

To complete the work of Nordmann, a theoretical procedure should be developed for the computation of the total hydrodynamic forces acting on the impeller. The present paper contributes to this objective. It proposes a method of the impeller forces analysis. A two-dimensional fluid model is developed to study the flow in the impeller-diffuser domain of a centrifugal pump with and without guide vanes. In this model, the impeller periphery and the

diffuser vanes contour are replaced by a set of unsteady vortices. This is an improvement of the earlier quasisteady flow model of Colding-Jørgensen mentioned above. The hydrodynamic forces acting on the rotating and whirling impeller are then determined and presented in terms of rotordynamic coefficients. A comparison with most of the theoretical and experimental results found in the literature and a study of the influence of some parameters are performed.

ASSUMPTION

The analysis follows the same route as in some previous studies (Refs. 2, 6, 7). The impeller, which is supposed to have a very large number of infinitely thin blades perfectly guiding the flow, is substituted by an actuator disc. As indicated by Tsujimoto et al. (Ref. 6), the goal of this assumption is to eliminate the unsteadiness due to the rotation of the impeller blades and then, for simplification, to consider only the unsteadiness due to the whirling motion of the rotor center.

The impeller rotates at a constant angular speed ω. Its center whirls on a concentric orbit around the volute center with a constant angular speed Ω and a small eccentricity ε ($\varepsilon << r_2$). Since the unsteady or dynamic part of the impeller forces (2nd term of 2nd member of Eq. (1)) is proportional to the eccentricity, the procedure of calculation for elliptical or for any motion of the rotor center with small eccentricity consists of using the concentric whirling motion $\underline{\varepsilon} = \varepsilon e^{i\Omega t}$ to get the hydrodynamic force matrix [A]. Then [A] and the real rotor center motion are used to determine the impeller forces.

The following conditions are also assumed:

1. Incompressible, inviscid and irrotational flow in the absolute coordinate system with constant flow rate.
2. Diffuser vanes and impeller blades replaced by spirals with a constant spiral angle (α and β respectively). Constant width b.
3. Tangential flow conditions for the absolute flow on the diffuser vanes surface and for the relative flow on the impeller blades surface. This last assumption is the basis of the present theory, since the goal is to determine a flow field satisfying both conditions.

FLUID MODEL

The model is based on the unsteady potential flow theory, as mentioned above and illustrated in Fig. 2. The diffuser vanes are replaced by an unsteady vortex distribution. Since the impeller is substituted by an actuator disc, we replace its periphery by a set of unsteady vortices. This vortex distribution at the impeller outlet characterizes the change of the circulation around the impeller due to the perturbation $\underline{\varepsilon} = \varepsilon e^{i\Omega t}$ and to the variation of the flow rate. A source Q and a circulation Γ are put at the impeller center to model the flow rate and the prerotation. Γ is chosen to satisfy the tangential flow conditions at the impeller outlet for an unbound impeller.

FLOW FIELD

a) Region downstream of the impeller

According to the fluid model definition above, the absolute flow in the region downstream of the impeller can be described by the following equation:

$$c_x - ic_y = \sum_{j}^{ND} \int_{s_{1j}} \frac{i\gamma(s)ds}{2\pi(z - z_1(s))} + \int_{s_2} \frac{i\gamma(s)ds}{2\pi(z - z_2(s))} + \frac{Q - i\Gamma}{2\pi b(z - \varepsilon e^{i\Omega t})} - i\varepsilon\Omega e^{-i\Omega t} \tag{3}$$

with the prerotation given by

$$\Gamma = 2\pi r_2^2 b\omega - \frac{Q}{\tan\beta} \tag{4}$$

In Eq. (3), $\gamma(s)\,ds$ is the strength of a vortex point on the j diffuser blade s_{1j} of frame $z_1(s)$ or on the impeller periphery s_2 of frame $z_2(s)$. In this expression, γ is unknown and must be determined to satisfy the flow tangential conditions mentioned in assumption 3. In other words, the normal component of the absolute flow must vanish on the diffuser vanes,

$$\underline{c}\cdot\underline{n}_{1j}\big|_{s_{1j}} = 0 \tag{5}$$

and the velocity relative to the rotating impeller must be tangential to the blade at the impeller periphery. That means, its component normal to the blade must vanish,

$$\underline{w}\cdot\underline{n}_2\big|_{s_2} = 0 \tag{6}$$

where $\underline{w}$ is given by

$$w_x - iw_y = c_x - ic_y + ir_2\omega e^{-i\theta'} + i\varepsilon\Omega e^{-i\Omega t} \tag{7}$$

The combination of Eq. (3) with Eqs. (5) and (6) should give rise to two integral equations in which $\gamma(s)$ is unknown as mentioned above. These integral equations can be solved numerically. This consists of replacing the contours s_{1j} and s_2 by a set of discrete vortex points k of strength $\gamma_k\,ds_k$ put at frame z_k (N_1 points for each s_{1j} fixed to (o,x,y) and N_2 points for s_2 fixed to (o',x',y')). On each contour a set of control points l of frame z_l different from z_k should be chosen (N_1 points for each s_{1j} fixed to (o,x,y) and N_2 points for s_2 fixed to (o',x',y')) (see Fig. 3). This should give rise to a system of $ND*N_1+N_2$ linear equations with $ND*N_1+N_2$ unknowns.

The vector normal to s_{1j} at point l is

$$\underline{n}_{1jl} = (-\cos(\alpha-\theta_{jl}), \sin(\alpha-\theta_{jl})) \tag{8}$$

and the vector normal to the blade at point l of s_2 is

$$\underline{n}_{2l} = (\cos(\theta_l'+\beta), \sin(\theta_l'+\beta)) \tag{9}$$

The system can then be presented as follows

for $l \in s_{1j}$

$$-\cos(\alpha-\theta_{jl})c_{xjl} + \sin(\alpha-\theta_{jl})c_{yjl} = 0 \tag{10}$$

and for $l \in s_2$

$$\cos(\theta_l'+\beta)w_{xl} + \sin(\theta_l'+\beta)w_{yl} = 0 \tag{11}$$

(c_{xjl} , c_{yjl}) being the components of the absolute velocity $\underline{c}_{jl}$ at point l of the blade j and (w_{xl} , w_{yl}) the components of the relative velocity $\underline{w}_l$ at point l. $\underline{c}_{jl}$ and $\underline{w}_l$ are given by the equations (3) and (7) respectively.

As $\varepsilon << r_2$, the system can be linearized by neglecting all the terms of second or higher order of ε and by taking

$$\gamma_k = \bar{\gamma}_k + \varepsilon(\gamma_{kc}\cos\Omega t + \gamma_{ks}\sin\Omega t) \tag{12}$$

Then the system can be divided into a steady part of order ε^0 with $\bar{\gamma}_k$ as unknown and an unsteady part of order ε^1 with γ_{kc} and γ_{ks} as unknowns. First the steady system must be solved independently of the unsteady one. $\bar{\gamma}_k$ obtained must be used to solve the unsteady system. After determining γ_k and using Eq. (3), the flow in the domain under consideration can be calculated and written in the following form:

$$\underline{c} = \bar{\underline{c}} + \varepsilon\underline{c}_c\cos\Omega t + \varepsilon\underline{c}_s\sin\Omega t \tag{13}$$

b) Region between the inlet and outlet of the impeller

The flow through the impeller has been assumed to be perfectly guided by the vanes. Because of this, the continuity equation can be applied to determine the radial component of the flow at any point of the region between the inlet and outlet of the impeller. Making use of the relative flow tangential conditions on the impeller blades, the tangential components can also be found. Both of these conditions are expressed by the following equations:

$$r' c_{r'}(r',\theta') = r_2 c_{r'}(r_2,\theta_2') \tag{14}$$

$$c_{\theta'}(r',\theta') = \omega r' - \frac{c_{r'}(r',\theta')}{\tan\beta} \tag{15}$$

Equations (14) and (15) represent the continuity equation and the flow tangential condition respectively. In these equations, θ_2' is the angular position of any impeller blade tip, while $\theta' = \theta_2' + \frac{1}{\tan\beta}\ln\frac{r_2}{r'}$ is the angular position of the point of radius r' of the same blade.

IMPELLER FORCES

The hydrodynamic forces on the impeller are the sum of the momentum forces due to the momentum exchange between the impeller and the fluid, and of the pressure forces acting on the impeller:

$$\underline{F} = -\frac{\partial}{\partial t}\int_{cv}\rho\underline{c}\,dv - \oint_{cs}\rho\underline{c}(\underline{c}\cdot d\underline{A}) - \oint_{cs}p\,d\underline{A} \tag{16}$$

where cv is the control volume of length b bounded by the inlet and outlet of the impeller, cs the inlet and outlet surface of the impeller and p the pressure.

The impeller has been assimulated to an actuator disc. We can then calculate the above forces the same way as in Ref. 8. The impeller is considered to be a cylindrical body possessing a

circulation Γ in the presence of the source Q. It is assumed that the induced velocity in the impeller center has the same effect as a parallel stream $\underline{c}_\infty$ ($c_{\infty x}$, $c_{\infty y}$). Then the unsteady Bernoulli equation can be written as follows:

$$\int \frac{\partial \underline{c}}{\partial t} \cdot d\underline{s} + \frac{p}{\rho} + \frac{\underline{c}^2}{2} = \frac{p_\infty}{\rho} + \frac{\underline{c}_\infty^2}{2} \tag{17}$$

Making use of this equation and integrating Eq. (16) according to the above assumption, we obtain:

$$\frac{\underline{F}}{\rho} = \pi b \frac{\partial \underline{c}_\infty}{\partial t}(r_2^2 - r_1^2) + \underline{c}_\infty Q + \hat{\underline{c}}_\infty \Gamma + \pi b \frac{\partial \underline{c}_\infty}{\partial t}(r_2^2 - r_1^2) \tag{18}$$

where $\underline{c}_\infty$ is the velocity induced in the impeller center by the volute given as

$$c_{\infty x} - ic_{\infty y} = \sum_j^{ND} \int_{s_{1j}} \frac{i\gamma(s)ds}{2\pi(\varepsilon e^{i\Omega t} - z(s))} - \int_{s_2} \frac{i\gamma(s)ds}{2\pi(\varepsilon e^{i\Omega t} - z(s))} + i\varepsilon e^{-i\Omega t} \tag{19}$$

$$\hat{\underline{c}}_\infty = (c_{\infty y}, -c_{\infty x}) \tag{20}$$

Equation (18) is an extension of the Kutta-Jokowski theorem used by Colding-Jørgensen (Ref. 8) in the forces calculation. This expression takes into account the impeller geometry and the unsteady part of the flow, not considered in the earlier model.

RADIAL FORCE, TANGENTIAL FORCE, ROTORDYNAMIC COEFFICIENTS

Since $\varepsilon << r_2$, the impeller forces can also be linearized and expressed as follows:

$$\underline{F} = \begin{bmatrix} \bar{F}_x \\ \bar{F}_y \end{bmatrix} + \begin{bmatrix} F_{cx} & F_{sx} \\ F_{cy} & F_{sy} \end{bmatrix} \begin{bmatrix} \varepsilon \cos \Omega t \\ \varepsilon \sin \Omega t \end{bmatrix} \tag{21}$$

A comparison of this equation with Eq. (1) gives rise to the hydrodynamic force matrix [A]. The unsteady part of the impeller forces can be decomposed into radial and tangential components relative to the orbit described by the impeller center movement. The mean values of these both components have an important significance in rotordynamics as clearly explained by Shoji and Ohashi (Ref. 14). The natural frequencies in bending of the shaft are influenced by the bending moment exerted by the radial component F_r, while the tangential component F_t has either a destabilizing or a damping effect on the shaft: if F_t and the whirling motion have the same sense, F_t will promote the whirling motion, thus destabilizing the shaft. Alternatively, if they are in opposite sense, F_t will tend to reduce the kinetic energy of the whirling rotor and exert a stabilizing effect. As indicated by Jery et al. (Ref. 12), F_r and F_t are given by

$$\begin{bmatrix} F_r \\ F_t \end{bmatrix} = \frac{\varepsilon}{2} \begin{bmatrix} A_{xx} + A_{yy} \\ A_{yx} - A_{xy} \end{bmatrix} \tag{22}$$

Comparing Eq. (1) to Eq. (2), the stiffness, damping and inertia coefficients can be deduced as follows:

$$\begin{bmatrix} A_{xx} & A_{xy} \\ A_{yx} & A_{yy} \end{bmatrix} = -\begin{bmatrix} K_{xx} + \Omega D_{xy} - \Omega^2 M_{xx} & K_{xy} - \Omega D_{xx} - \Omega^2 M_{xy} \\ K_{yx} + \Omega D_{yy} - \Omega^2 M_{yx} & K_{yy} - \Omega D_{yx} - \Omega^2 M_{yy} \end{bmatrix} \tag{23}$$

The principle of the calculation of these coefficients consists of determining the impeller forces for any 3 different values of Ω and to deduce from Eqs. (21) and (23) each rotordynamic coefficient. For a centrifugal pump with vaned diffuser, we will have:

$$\begin{bmatrix} K_{xx} & K_{xy} \\ K_{yx} & K_{yy} \end{bmatrix} = \begin{bmatrix} K & k \\ -k & K \end{bmatrix}, \quad \begin{bmatrix} D_{xx} & D_{xy} \\ D_{yx} & D_{yy} \end{bmatrix} = \begin{bmatrix} D & d \\ -d & D \end{bmatrix}, \quad \begin{bmatrix} M_{xx} & M_{xy} \\ M_{yx} & M_{yy} \end{bmatrix} = \begin{bmatrix} M & m \\ -m & M \end{bmatrix} \tag{24}$$

The radial force and the tangential force will then be reduced to

$$\begin{bmatrix} F_r \\ F_t \end{bmatrix} = -\varepsilon \begin{bmatrix} K + \Omega d - \Omega^2 M \\ -k + \Omega D + \Omega^2 m \end{bmatrix} \tag{25}$$

RESULTS AND DISCUSSIONS

The calculations have been made both for a pump with vaneless diffuser and with vaned diffuser. The two cases are treated separately.

a) Pump with vaneless diffuser

In order to make a comparison with the experimental and theoretical results given in the literature (Ref. 1, 2, 6, 8, 12), the calculations in the case of a vaneless diffuser are performed for the following geometry (data of Ref. 6): $\alpha = 6.538°$, $\beta = 25°$, $r_1 / r_2 = 0.4$, $r_t / r_2 = 1.123$. The volute is modeled by $r / r_2 = 1.123 e^{\theta \tan\alpha}$ with $0 \le \theta \le 380°$. It results in a design flow coefficient of $\phi = 0.092$.

"Colding-Jorgensen" curves are calculated with the above pump data using the source-vortex representation of the impeller and replacing the spiral volute by a distribution of vortex points as introduced by Colding-Jørgensen (Ref. 8). The impeller forces are determined by making use of the unsteady forces formula given by Eq. (18). Then the unsteady hydrodynamic forces on the impeller can be expressed in terms of radial and tangential components relative to the impeller center orbit for this model.

Figures 4 and 5 present the steady flow distribution around and inside the impeller for $Q_{rel} = 0.4$ and $Q_{rel} = 1.3$ respectively, the impeller center coinciding with the volute center. As predicted by Hergt and Krieger (Ref. 11) and shown in Fig. 4, the pressure at the tongue region is so high that the flow tends to return inside the impeller for off-design flow. Then the impeller receives an energy contribution from the flow and works in that region like a turbine impeller. It results a bending moment exerted by the fluid on the impeller, hence promoting the eccentricity of the rotor center. For higher flow rates, the pressure in this region is very weak and the flow speed becomes higher.

The components in x- and y-direction of the dimensionless steady hydrodynamic forces acting on the impeller as a function of the flow coefficient are shown in Fig. 6. The results of the present calculations are compared to those of the model of Colding-Jørgensen (Ref. 8) and to the measurements of Refs. 1 and 2. The pump used in Refs. 1 and 2 is the same, with $\beta = 25°$, $\phi_n = 0.092$, and $r_t / r_2 = 1.13$. It appears that the present theory is close to that of Ref. 8 and both

agree with the measurements of Chamieh et al. (Ref. 1) and Adkins and Brennen (Ref. 2) near the design flow coefficient.

Figure 7 presents the dimensionless radial and tangential force for the design flow coefficient. The comparison of our results is made with Colding-Jørgensen's prediction calculated as indicated above, the results of Tsujimoto et al. (Ref. 6) and with the measurements of Jery et al. (Ref. 12) at 1000 rpm, with the same pump as that of Refs. 1 and 2. As explained by Adkins and Brennen and Tsujimoto et al., the forces measured by Jery et al. are a superposition of the lateral fluid forces due to the impeller-volute interaction and of the pressure forces acting on the external surface of the shrouds. This is probably the cause of the difference between the theory and the measurement of Fig. 7.

According to Fig. 7, the tangential force F_t and the whirl speed Ω are both positive for $0 \le \Omega/\omega \le 0.3$ for our model. That means, in this domain, the lateral fluid forces on the impeller have a destabilizing effect on the pump rotor. The impeller forces become stabilizing when we move away from this interval of the whirl speed ratio.

The stiffness coefficients were measured and calculated by Adkins and Brennen (Ref. 2). Their results are compared to those of our theory and that of Colding-Jørgensen (Ref. 8) in Figs. 8 and 9. It is noted that the present model better simulates the experimental measurements of Ref. 2. Figure 10 presents the damping coefficients compared to those of Ref. 8. The actual model seems to give larger damping coefficients than the calculations of Colding-Jørgensen. This is due to the impeller geometry not considered in the earlier model. The inertia coefficients have not been represented graphically because they remain constant relative to the flow rate and equal to

$$\frac{[M]}{\rho\pi b r_2^2} = \begin{bmatrix} 3.67 & -0.32 \\ 0.33 & 3.70 \end{bmatrix}$$

These inertia terms are of considerable magnitude and deserve a comment. In some pumps, they can be larger than the impeller mass and hence can be very important for the correct rotor modeling as indicated by D. Childs in his book "Turbomachinery Rotordynamics" (1993). This dynamic mass will influence particularly the first bending eigenfrequencies.

b) Pump with vaned diffuser

We have not got any experimental results in the literature to test the validity of our model in the case of a centrifugal pump with vaned diffuser. Thus the model can only be tested qualitatively by studying the influence of some parameters on the results. These results are presented in Figs. 11 to 16. The data used for the calculations are indicated on each figure.

Figure 11 shows the plots of the dimensionless radial force F_r and tangential force F_t as a function of the speed ratio Ω/ω for three different values of r_3 / r_2 at design flow coefficient. It is noted that, for $\Omega/\omega \le 0$, F_r and F_t increase with decreasing r_3 / r_2. This is essentially due to the pressure on the impeller which increases when r_3 / r_2 decreases. A destabilizing region is found for small forward whirl. This region diminishes with the increase of r_3 / r_2. A comparison of our results is also made with those of Ref. 7 for $r_3 / r_2 = 1.05$, $r_4 / r_2 = 1.3$, $r_1 / r_2 = 0.5$, $\alpha = 11°$, $\beta = 30°$ at design flow coefficient with impeller and diffuser losses. Our model seems to give forces larger than that of Tsujimoto et al. for negative whirl. However, their destabilizing interval is larger than ours. Note that this comparison is only qualitative, since the two theories are different.

Figure 12 presents the variation of the radial and tangential forces with Ω/ω and with the diffuser blade angle α. For backward whirl, when α increases, F_r decreases while F_t increases. F_t becomes dominant for $\alpha > 20°$. The destabilizing region expands with the decrease in the diffuser blade angle.

The variation of F_r and F_t with Ω/ω and with the relative flow coefficient ϕ/ϕ_n is shown in Fig. 13. The radial component of the impeller forces increases with decreasing ϕ, while the tangential component increases with the flow rate for backward whirl. This variation is in agreement with the results of Tsujimoto et al. presented in Refs. 6 and 7. The destabilizing region of the impeller center whirl velocity expands when the flow coefficient decreases.

The influence of the clearance r_3 / r_2 and of the flow coefficient on the stiffness, damping and inertial coefficients is shown in Figs. 14, 15 and 16. As indicated by the curves of Fig. 14, K and k increase in absolute value with the decrease in the clearance. The main stiffness K is negative and decrease in absolute value with the flow coefficient, while the variation of the cross coupling stiffness is small. The variation of K with the radius ratio r_3 / r_2 is greater at low flow rates. Figure 15 shows that the damping coefficients are positive and vary considerably both with the flow coefficient and with the clearance r_3 / r_2. The main damping D increases with r_3 / r_2 and with ϕ, while d decreases with r_3 / r_2 and with ϕ. At design flow coefficient ($\phi_n = 0.145$), d is two to three times larger than D. As for the case of vaneless diffuser, the present theory gives the mass coefficients quasiconstant relative to the flow rate. In Fig. 16, the variation of M and m with r_3 / r_2 and with the diffuser blade angle α is shown. The main inertia coefficient decreases when the radius ratio r_3 / r_2 increases. The absolute value of the cross coupling mass m increases with r_3 / r_2. The effect of the diffuser blade angle on M and on the absolute value of m is similar to that on F_r and F_t respectively for negative whirl velocity. Since the cross coupling inertia m is relatively small comparing to the main damping D, its effect on the tangential force F_t is also small, as indicated by Figs. 11 to 13 where the curves representing F_t are quasistraight. The main mass coefficients are of considerable magnitude and will influence the natural frequencies of the shaft in bending.

CONCLUSION

A 2-dimensional fluid model based on the unsteady potential flow theory has been developed to study the flow in the impeller-diffuser domain of a centrifugal pump with vaneless and vaned diffuser. The center of the rotating impeller has been assumed whirling on an orbit about the diffuser center. The hydrodynamic forces have been calculated and decomposed into radial and tangential components relative to the impeller center orbit, and the rotordynamic coefficients have been deduced. In the case of vaneless diffuser, a stalled angular region in the impeller due to the volute asymmetry at off-design flow has been observed. A comparison with some experimental and theoretical results found in the literature has been performed. It shows that the present model gives a good prediction of the impeller forces. It has been noted that the hydrodynamic forces on the impeller have a destabilizing effect on the pump rotor both for the vane and vaneless diffuser for small forward whirl. For the vaned diffuser, there are no experimental results available in the literature to be compared to our calculations. Only the study of the influence of some parameters on our results could attest to the quality of this model. It has been demonstrated that the destabilizing region of the impeller center whirl velocity expands when the radius ratio r_3 / r_2, the diffuser blade angle α and the flow coefficient ϕ decrease.

ACKNOWLEDGMENTS

This research was supported both by the Machine Dynamics Laboratory of the University of Kaiserslautern and the Mechatronic System in mechanical Engineering Laboratory of the Technical University of Darmstadt, Germany. One of the authors (R. Fongang) would like to thank the German Academic Exchange Service (DAAD) for the financial support of his stay in the Federal Republic of Germany for his post graduate studies. He would also like to express his gratitude to Prof. Dr.-Ing. H. Hellmann for his invaluable contribution to this work and to his colleagues of the Machine Dynamics Laboratory for their help to preparing the present paper.

REFERENCES

1. Chamieh D. S., Acosta A. J., Brennen C. E., Caughey T. K. and Franz R.: "Experimental Measurements of Hydrodynamic Radial Forces and Stiffness Matrices for a Centrifugal Pump-Impeller", NASA CP 2250, 1982, pp 382-390.
2. Adkins D. R. and Brennen C. E.: "Analyses of Hydrodynamic Radial Forces on Centrifugal Pump Impellers", 1988, ASME Journal of Fluids Engineering, Vol. 110, No. 1, pp. 20-28.
3. Csanady G. T.: "Radial Forces in a Pump Caused by Volute Casing", ASME Journal of Engineering of Power, Vol. 84, 1962, pp. 337-340.
4. Iversen H. W., Rolling R. E. and Carlson J.: "Volute Pressure Distribution, Radial Force on the Impeller and Volute Mixing Losses of a Radial Flow Centrifugal Pump", ASME Journal of Engineering for Power, Vol. 82, April 1960, pp. 136-144.
5. Nordmann R.: „Rotordynamische Kennzahlen von berührungslosen Dichtungen und Laufrädern Grundsatzreferat", VDI Berichte, 1993.
6. Tsujimoto Y., Acosta A. J., Brennen C. E.: "Theoretical Study of Fluid Forces on a Centrifugal Impeller Rotating and Whirling in a Volute", ASME Journal of Vibration, Acoustics, Stress and Reliability in Design, Vol. 110, No. 3, 1988, pp. 263-269.
7. Tsujimoto Y., Acosta A. J., Yoshida Y.: „A Theoretical Study of Fluid Forces on a Centrifugal Impeller Rotating and Whirling in a vaned Diffuser", NASA CP 3026, 1988, pp. 307-322.
8. Colding-Jørgensen J.: "Effect of Fluid Forces on Rotor Stability of Centrifugal Compressors and Pumps", NASA CP 2133, 1980, pp. 249-266.
9. Domm V. and Hergt P.: "Radial Forces on Impeller of Volute Casing Pumps", Flow Research on Blading, Elsevier Pub, 1970, Co, pp. 305-321.
10. Hergt P. and Krieger P.: "Radial Forces in Centrifugal Pumps with Guide Vanes", Proc. of Inst. of Technical Engineers 1969-1970, Vol. 184, Part. 3N, pp. 101-107.
11. Hergt P. and Krieger P.: "Theoretische und Experimentelle Bestimmung der Instationären Hydrodynamischen Kräfte auf die Laufschaufelenden", KSB Technische Berichte 18, 1984, pp. 5-9.
12. Jery B., Acosta A. J., Brennen C. E. and Caughey T. K.: "Hydrodynamic Impeller Stiffness, Damping and Inertia in the Rotordynamics of Centrifugal Flow Pumps", NASA CP 2338, 1984, pp. 137-160.
13. Ohashi H. and Shoji H.: "Lateral Fluid Forces on Whirling Centrifugal Impeller (2nd Report: Experiment in Vaneless Diffuser)", Journal of Fluids Engineering, Vol. 109, June 1987, pp. 100-106.
14. Shoji H. and Ohashi H.: "Lateral Fluid Forces on Whirling Centrifugal Impeller (1st Report: Theory)", Journal of Fluids Engineering, Vol. 109, June 1987, pp. 94-99.

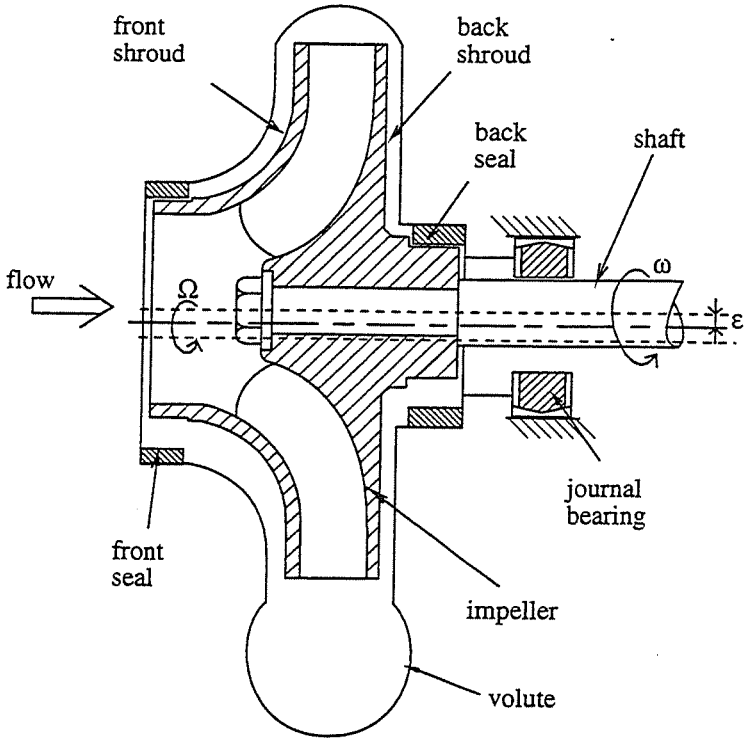

Fig. 1: Centrifugal pump with vaneless diffuser

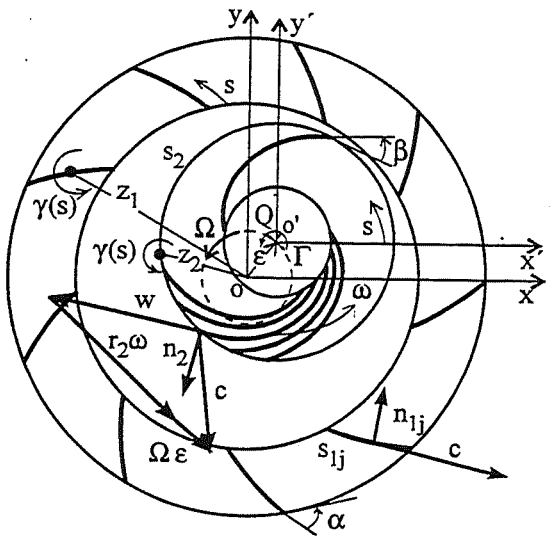

Fig. 2: 2-dimensional centrifugal pump model with vaned diffuser

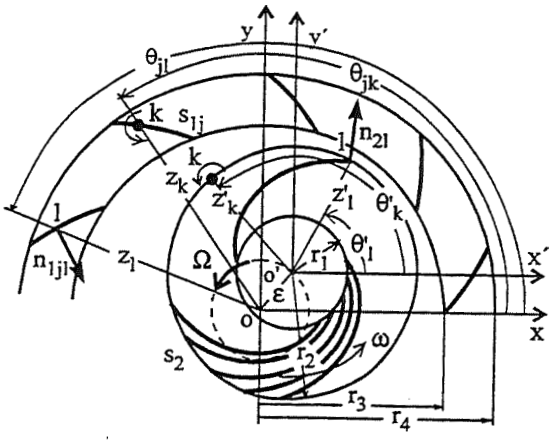

Fig. 3: Discrete vortex and control points configuration

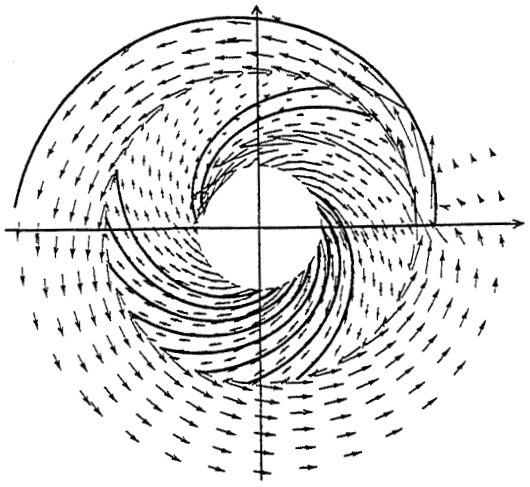

Fig. 4: Absolute flow downstream of the impeller and relative flow inside the impeller for a vaneless diffuser and for $Q_{rel} = 0.4$

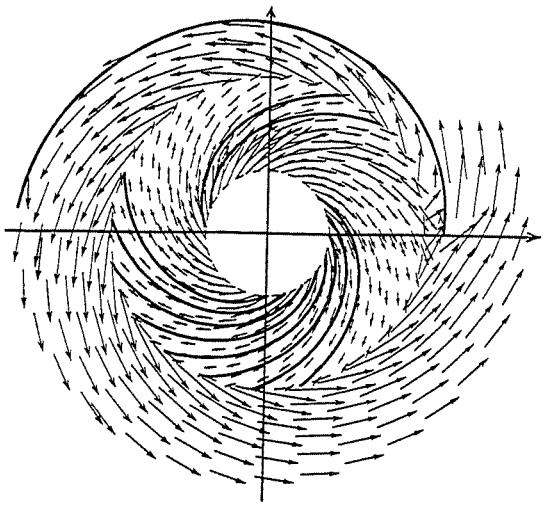

Fig. 5: Absolute flow downstream of the impeller and relative flow inside the impeller for a vaneless diffuser $Q_{rel} = 1.3$

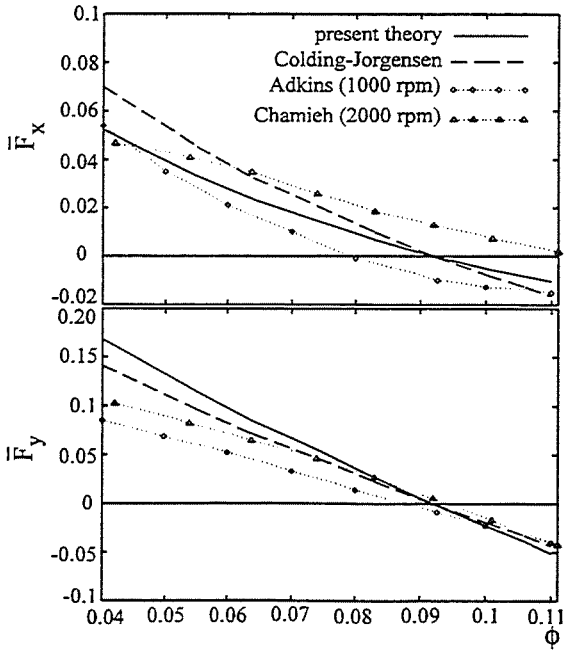

Fig. 6: Dimensionless x- and y-components of the steady impeller force (normalized by $\pi\rho b\omega^2 r_2^3$) as a function of the flow coefficient for a vaneless diffuser

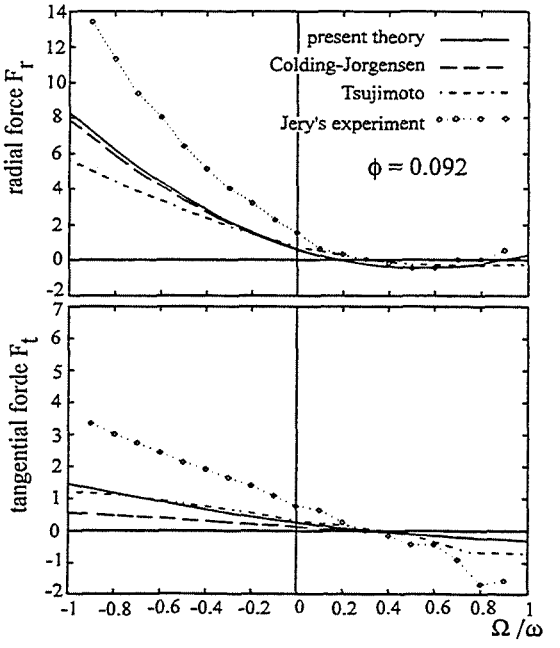

Fig. 7: Dimensionless radial and tangential force (normalized by $\pi\rho b\omega^2 r_2^2 \varepsilon$) as a function of the speed ratio at design flow coefficient for a vaneless diffuser

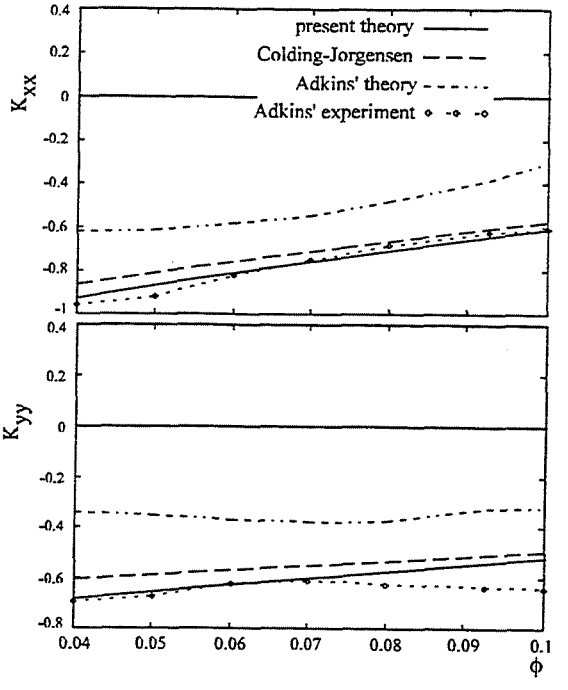

Fig. 8: Dimensionless main stiffness coefficients (normalized by $\pi\rho b\omega^2 r_2^2$) as a function of the flow coefficient for a vaneless diffuser: Comparison to the results of Colding-Jørgensen and Adkins

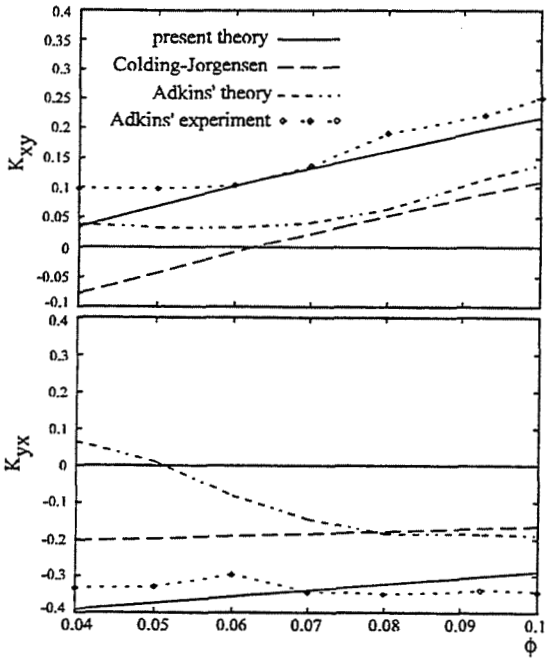

Fig. 9: Dimensionless cross-coupling stiffness coefficients (normalized by $\pi\rho b\omega^2 r_2^2$) as a function of the flow coefficient for a vaneless diffuser: Comparison to the results of Colding-Jørgensen and Adkins

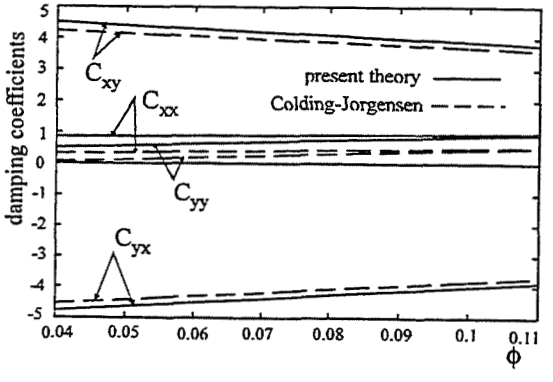

Fig. 10: Dimensionless damping coefficients (normalized by $\pi\rho b\omega r_2^2$) as a function of the flow coefficient for a vaneless diffuser: comparison to the results of Colding-Jørgensen

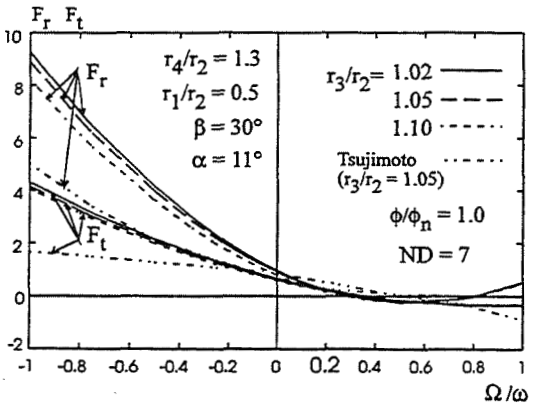

Fig. 11: Dimensionless radial and tangential force (normalized by $\pi\rho b\omega^2 r_2^2 \varepsilon$) as a function of the speed ratio at design flow coefficient: variation with r_3 / r_2 and comparison to the results of Ref. 7 (with impeller and diffuser losses)

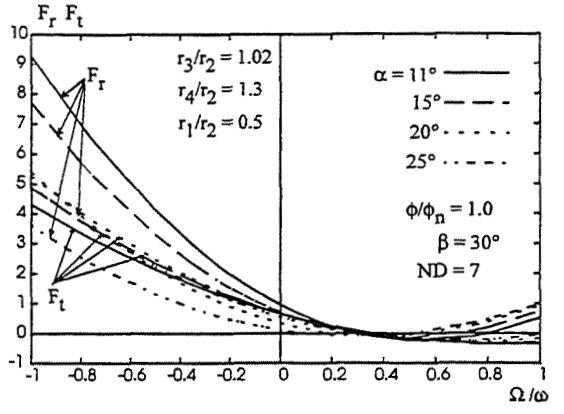

Fig. 12: Dimensionless radial and tangential force (normalized by $\pi\rho b\omega^2 r_2^2 \varepsilon$) as a function of the speed ratio at design flow coefficient for the vaned diffuser: variation with the diffuser blade angle α

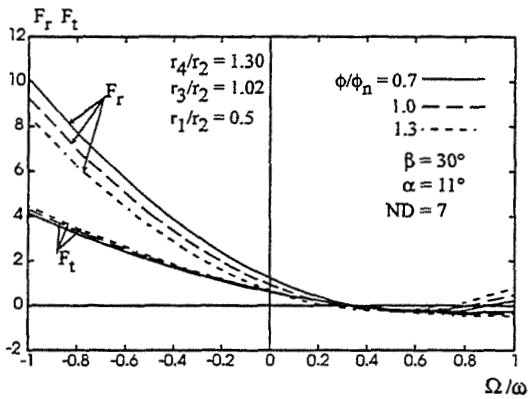

Fig. 13: Dimensionless radial and tangential force (normalized by $\pi\rho b\omega^2 r_2^2 \varepsilon$) as a function of the speed ratio at design flow coefficient for the vaned diffuser: variation with the relative flow coefficient ϕ/ϕ_n

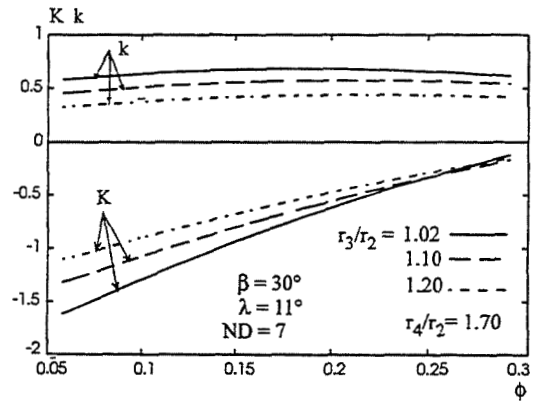

Fig. 14: Dimensionless stiffness coefficients (normalized by $\pi\rho b\omega^2 r_2^2$) as a function of the flow coefficient for the vaned diffuser: variation with r_3 / r_2

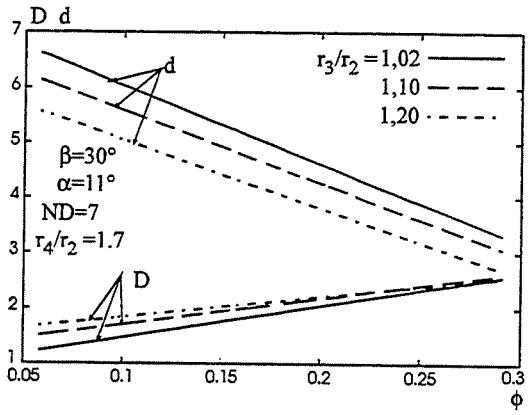

Fig. 15: Dimensionless damping coefficients (normalized by $\pi\rho b\omega r_2^2$) as a function of the flow coefficient for the vaned diffuser: variation with r_3 / r_2

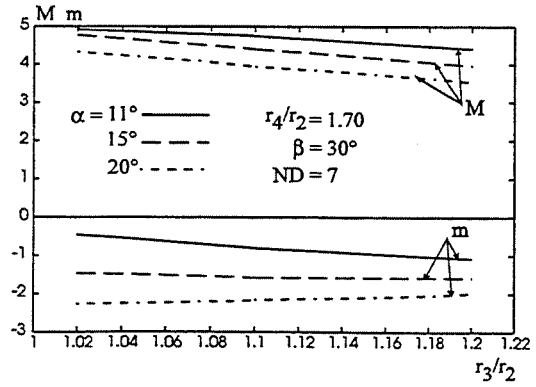

Fig. 16: Dimensionless inertia coefficients (normalized by $\pi\rho br_2^2$) as a function of r_3 / r_2 for the vaned diffuser: variation with the diffuser blade angle α

EVALUATION OF AMB ROTOR DROP STABILITY

R.G. Kirk, K.V.S. Raju, and K. Ramesh
Virginia Polytechnic Institute and State University
Blacksburg, Virginia

ABSTRACT

The use of active magnetic bearings (AMB) for turbomachinery has enjoyed substantial growth during the past decade. The advantages to many applications make this a very attractive solution for potentially low loss and efficient support for both radial and thrust loads. New machinery must be shop tested prior to shipment to the field for installation on-line. One necessary test is the operation of the emergency drop or overload touchdown bearings. A major concern treated by this paper is the calculation of the transient response and contact forces on the radial backup bearings. The calculation technique is reviewed and results of transient response evaluation of a full-size test rotor will be documented for various levels and distribution of both static and dynamic unbalance. Recommendations are also given as to how a rotor should be shop tested to improve the probability of stable operation on the test stand and in the field operating condition.

INTRODUCTION

The recent years have seen an increasingly wider application of active magnetic bearings for supporting turbomachinery due to their benefits over conventional bearings. One of the major problems associated with the use of active magnetic bearings is their dependence on safety auxiliary bearings for support in case of AMB power loss. These auxiliary bearings are meant to support the rotor and allow it to temporarily run or safely coast down to a stop for maintenance purposes. Several incidents of untimely failure of these auxiliary bearings, in both test and field conditions, have been reported by AMB technology developers and end users. This has lead researchers to study the dynamics of the rotor drop phenomena in order to help design better auxiliary bearings.

The loss of active magnetic bearing power during operation was, in analytical results, seen to produce very large amplitude vibrations and high instantaneous loads. Ishii and Kirk (1991) and Kirk and Ishii (1993) developed a transient response technique for predicting the transient response during AMB rotor drop for a simple two-mass Jeffcott rotor system for various backup bearing configurations. Fumagalli, Varadi and Schweitzer (1994) studied the dynamics of rigid rotors in retainer bearings. The vibrational behavior of a one ton compressor rotor being dropped into the auxiliary bearings after AMB failure was, through experimental and theoretical tests, reported by Schmied and Pradetto (1992). Bently (1995) expressed concerns over the reliability of backup bearings in the design of an AMB system due to the finite load capacity of AMBs. The proper design of any AMB system requires the knowledge all the dynamic loads in the system that have to be supported. Due to the difficulty in predicting these loads accurately, the AMB systems fail when subjected to overloads. The need for better understanding the dynamics of this phenomena, lead Kirk, et. al. (1994) to set up a full scale test rig to evaluate various backup bearing configurations and to develop analytical tools to simulate turbomachinery supported by AMBs. Ramesh and Kirk (1992) performed finite element based steady state analysis of AMB turbomachinery and compared the results with experimental data.

Swanson, Kirk and Wang (1995) discussed experimental data for AMB rotor drop initial transients on ball and solid backup bearings. Raju, Ramesh, Swanson and Kirk (1995) presented analytical results for finite element based rotor drop simulation and successfully compared them with experimental data. The simulation was done for cases with rigid backup bearings. The current work is an extension of that research with the goal to deduce the ideal configuration for a good AMB system design. The conditions leading to rotor dynamic instability during drop will be studied. Focus will be placed on suggesting the permissible unbalance levels as a function of the backup bearing design.

MODELING FOR TRANSIENT RESPONSE

The AMB test rotor configuration was modeled using the finite element method. The mass, stiffness and damping matrices for the system were obtained by discretizing the rotor system into smaller elements as described by Ramesh and Kirk (1992). These finite element matrices were utilized for the simulation of AMB system by applying a direct time integration technique to solve the system dynamic equilibrium equations. A direct integration scheme was considered to be ideal for performing the transient analysis to simulate rotor drop as the natural frequencies during rotor drop phenomena are not predictable and knowledge of these is important in the case of modal analysis. Of the direct integration methods, the Newmark-α method, described by Engelmann (1988), was most convenient for the current problem due to the ease with which various non-linearities in the system can be incorporated into the model.

The dynamic equilibrium equation for a rotor-bearing system in matrix form is equivalent to that of any other structural system. It can be represented as

$$[M]\{a\} + [C][v] + [K][d] = \{f\} \tag{1}$$

where [M], [K] and [C] are the mass, stiffness and damping matrices. The vectors {a}, {v} and {d} are the acceleration, velocity and displacement vectors of the system. {f} is the external force vector which propels the system. Transient analysis of this system of matrices was performed using Newmark-α method. This method has the capability of numerically dampening out the higher frequencies in the system. This feature reduces computational costs during simulation by allowing the rotor to reach its steady state in a shorter time by dampening out high frequencies. Due to the importance of high frequencies in rotor drop phenomena, numerical damping was not used during simulation after the AMB force decay. Various system non-linearities which influence the system [C] and [K] matrices were modeled as components of the forcing function vector {f}. The various forces that constitute the external force vector are as follows :

$$\{f\} = \{f_u\} + \{f_g\} + \{f_p\} + \{f_{cont}\} \tag{2}$$

where, $\{f_u\}$ is the unbalance force vector,
$\{f_g\}$ is the gravity load vector causing sag in horizontal rotors,
$\{f_p\}$ is the preload on the rotor which keeps it at the geometric center of the AMB and
$\{f_{cont}\}$ is the contact force that the rotor-AMB system experiences when the rotor hits the backup bearing after AMB power loss.

Analytical capability has been developed to simulate rotor drop phenomena for various backup bearing configurations having flexibilities and material non-linearities at various levels. The transient response of the backup bearings was calculated using the Runge-Kutta fourth order method for various support configurations as described by Ishii and Kirk (1991) and Kirk and Ishii (1993). The static and

dynamic sliding coefficients of friction between rotor and inner race of backup bearing surfaces are used while simulating ball bearings depending on whether or not there is slip between the rotor and ball-bearing inner-race.

DESCRIPTION AND STEADY- STATE ANALYSIS OF TEST ROTOR

The rotor-bearing system used in the following analysis consists of a solid 3-disk rotor representative of a typical industrial turbine or compressor, two radial magnetic bearings and an outboard thrust magnetic bearing. Backup bearings are located on the outboard side of each of the radial magnetic bearings. The influence of the thrust bearing is neglected in the analysis. This rotor was modeled using 19 elements (20 nodes) as shown in Table 1. The influence of the dry flexible coupling was taken into account by adding an external load on the inboard or coupling end of rotor, at node 20, as shown in Fig. 1. The values for magnetic bearing stiffness and damping were obtained from the frequency dependent stiffness and damping curves provided by the manufacturer. The contact stiffness between rotor and backup bearing surfaces was calculated using the Hertzian contact theory for the case of a cylinder in a cylinder. A low contact damping value was assumed during simulations. The values for coefficients of friction were selected depending on the materials coming into contact, their relative motion and on the type of lubricant used between the contact surfaces. Details of the system design parameters are given in Table 2.

Table 1: Model data for rotor used in analysis

Element #	Element Length (meters)	Element Diameter (meters)
1	0.1772	0.0540
2	0.0436	0.1494
3	0.0436	0.1494
4	0.0194	0.0896
5	0.0558	0.1888
6	0.0558	0.1888
7	0.1320	0.1018
8	0.0540	0.2508
9	0.2286	0.1142
10	0.0540	0.2508
11	0.2254	0.1080
12	0.0540	0.2508
13	0.1246	0.1018
14	0.0580	0.1888
15	0.0580	0.1888
16	0.0104	0.0896
17	0.0341	0.1494
18	0.0341	0.1494
19	0.1523	0.0456

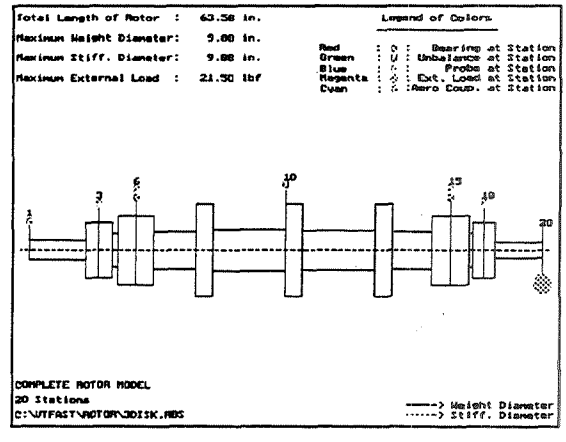

Fig. 1: Graphical model of rotor used in analysis.

Material Properties of Rotor

Density = 7832.000 kg/m^3
Poisson's Ratio = 0.2500

Other Details

Total Rotor Mass = 191.8459 kg
Total Rotor Length = 1.6149 m
Coupling Half Mass = 5.2727 kg
Unbalance Data :
1/10 g Force at 133.33Hz = 0.00028 kg-m

Table 2: Values of Parameters Used in Analysis

Inboard and Outboard AMB Properties :

Radial AMB Locations	=	Node 6 (Outboard) and Node 15 (Inboard)
Radial AMB Stiffness	=	0.7283 E +08 N/m (Manufacturer Supplied Data)
Radial AMB Damping	=	0.5076 E +05 Ns/m (Manufacturer Supplied Data)

General Backup Bearing Details :

Backup Bearing Locations	=	Node 3 (Outboard) and Node 18 (Inboard)
Rotor Radius at Backup Bearing Location (for both brgs.)	=	0.074714 m
Backup Bearing Inner Radius (for both brgs.)	=	0.074968 m
Contact Stiffness	=	5.0 E +08 N/m (Calculated)
Contact Damping	=	1000.0 N-s/m (Assumed)

Additional Solid Bronze Bushing Details :

Coefficient of dynamic sliding friction (Unlubricated)	=	0.3
Coefficient of dynamic sliding friction (Lubricated)	=	.0.1

NOTE : ♦ *All figures of rotor orbits and contact forces in the current document, unless otherwise stated, are for solid hard-mount unlubricated bronze bushings.*

♦ *The direction of rotation of the rotor is anti-clockwise.*

Damped critical speeds were calculated for the rotor model using the transfer matrix and finite element methods for different magnetic bearing support configurations. The results for possible operating conditions are presented in Table 3.

Table 3 : Damped Natural Frequencies of Rotor for Different AMB Conditions at 133.33 Hz (8000 rpm)

Mode # (First 8 Modes)	Damped Natural Frequency with Both AMBs (Hz)		Damped Natural Frequency with Only Outboard AMB (Hz)		Damped Natural Frequency with No AMBs (Free-Free) (Hz)	
	By FEM	By TMM	By FEM	By TMM	By FEM	By TMM
1	123.2837	123.8867	0.0000	0.0001	0.0000	0.0001
2	123.8817	124.3700	1.3774	1.3771	0.1451	0.1450
3	151.8159	151.7900	144.0980	144.0850	0.1547	0.1547
4	155.2939	155.2617	145.5551	145.4550	3.4260	3.4258
5	196.7796	197.7333	186.7806	188.6833	184.3246	186.4000
6	206.5416	207.7667	197.9620	200.1333	194.9057	197.1667
7	401.3689	402.1333	396.5974	396.9000	396.4844	396.8833
8	409.3597	410.0500	404.3170	404.5167	404.1722	404.4833

TMM - Transfer Matrix Method (Using ROBEST)

FEM - Finite Element Method (Using program developed by Ramesh, et. al, 1992)

The knowledge of the frequencies existing in a system helps in understanding the dynamics of the rotor and selecting an appropriate time step. The dynamic unbalance in the rotor system becomes prominent at the free-free mode. Possible rotor dynamic instability following a rotor drop may be avoided by preventing the running speed of the rotor from being close to this mode.

TRANSIENT ANALYSIS RESULTS AND DISCUSSION

Comparison of rotor orbit and contact forces when AMB power loss occurs at one and both bearings

A small unbalance of 1/10 g, computed for a design speed of 133.33 Hz, was applied at the center disk (node 10 at 0 degrees) and the inboard AMB was deactivated in case 1. For case 2, both bearings were deactivated. The rotor orbit and the contact forces were calculated for these two cases. It can be seen from Figs. 2, 4 and 6 that the depth of penetration of the rotor into the backup bearing is higher in the case when both bearings fail. The initial transient motions in both the cases are not full whirls. Although the initial contact force is almost the same in all the three cases shown in Figs. 3, 5 and 7, it is seen that the magnitude of forces in case 1 tend to become lesser with time whereas, in case 2, these forces sustain the magnitude level and even tend to increase after some time. The force plots show the results for time beyond the end of the motion shown in the drop orbit plots.

Case 1 : 1/10 g Static unbal. at 0 degrees on center disk (Node 10) with inboard AMB decay

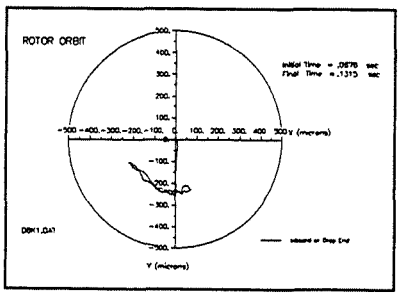

Fig. 2 : Rotor orbit at drop end for case 1.

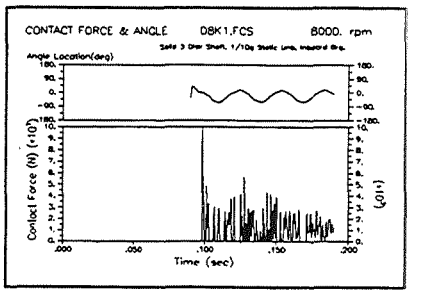

Fig. 3 : Contact force produced in case 1.

Case 2 : 1/10 g Static unbal. at 0 degrees on center disk (Node 10) with decay of both AMB's

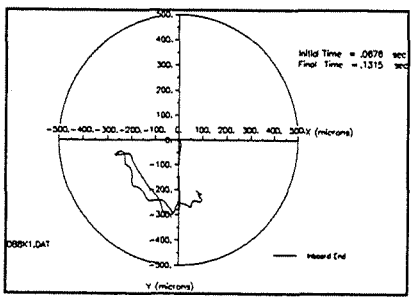

Fig. 4: Rotor orbit at inboard end for case 2.

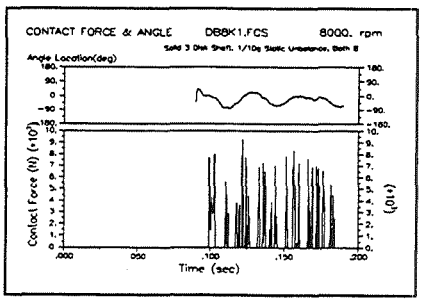

Fig.5: Contact force at inboard end for case 2.

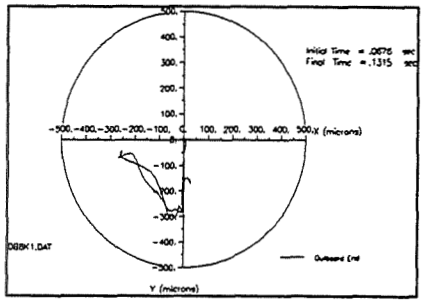

Fig. 6 : Rotor orbit at outboard end for case 2.

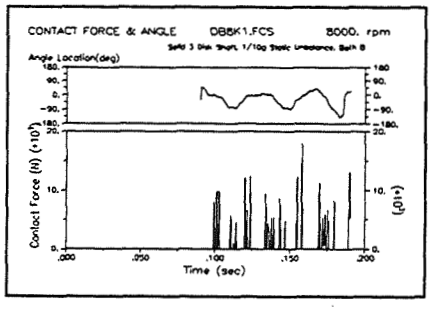

Fig. 7 : Contact forces produced in case 2 at outboard end.

Effect of static and dynamic unbalance at different locations along rotor

The effect of dynamic unbalance at different locations on the rotor, along its axis, was studied analytically by applying a 1g dynamic unbalance in the planes having the center-disk and landing sleeves (Case 3 - Nodes 2, 10 and 19) and in the planes of the three disks (Case 4 - Nodes 8, 10 and 12). It was observed that the rotor orbit at the drop end in case 3 (Fig. 8), after bearing decay, was similar to a case with high static unbalance. It became a full blown whirl after a short period. The magnitude of the contact forces (Fig. 10) also did not show any signs of decline. They even increased occasionally after some time. In case 4, the unbalance seemed to be less effective. The rotor transient motion in this case is oscillatory on the bottom surface of the backup bearing (Fig. 9). The contact forces diminish in magnitude after sometime (Fig. 11). The dynamic unbalance in a system cancels out at low speeds but they become prominent when the running speed is close to the first free-free mode.

Case 3 : 1 g Dynamic unbalance at center disk and landing sleeves with inboard AMB decay

Case 4 : 1 g Dynamic unbalance at center disk and the other two disks with inboard AMB decay

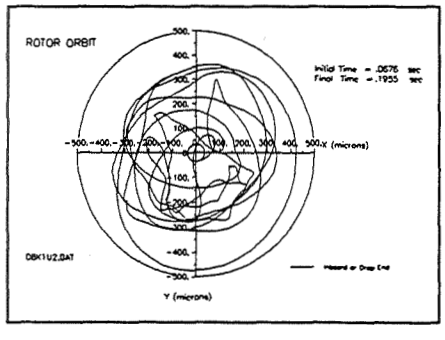

Fig. 8: Rotor orbit at inboard end for case 3.

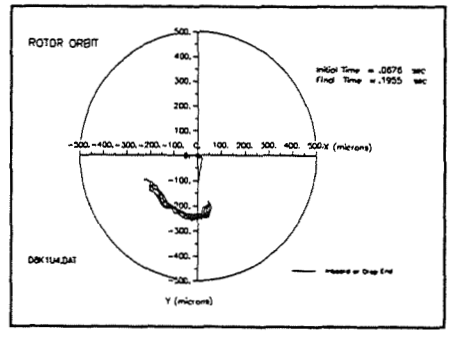

Fig. 9: Rotor orbit at inboard end for case 4.

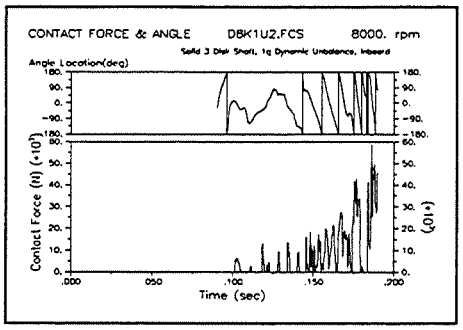

Fig. 10 : Contact force produced in case 3 at inboard or drop end.

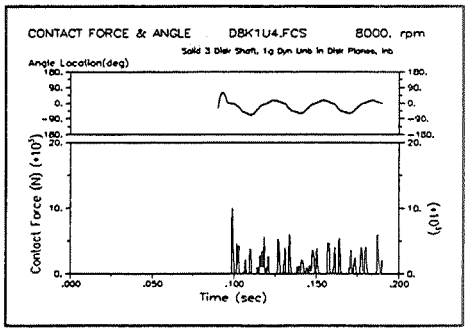

Fig. 11 : Contact force produced in case 4 at inboard or drop end.

When Both AMBs Decay :

When both the bearings decay, the case with the dynamic unbalance in planes that are further apart (Case 5) is seen to have higher activity than the case with the dynamic unbalance in planes that are closer (Case 6). The rotor transient motion in case 5 at both backup bearing locations (Figs. 12 and 14) became a full blown whirl after some time whereas during the same period, the transient motion in case 6 was less vigorous and the rotor oscillated on the bottom surface of the backup bearing. It took more time for the rotor in case 6 to go into a full backward whirl. The rotor orbits for case 6 are shown in Figs. 13 and 15. The magnitude of the steady-state rotor response, before AMB failure was also much higher in case 5 than in case 6.

Case 5 : 1 g Dynamic unbalance at center disk and landing sleeves with decay of both AMB's
Case 6 : 1 g Dynamic unbalance at center disk and the other two disks with decay of both AMB's

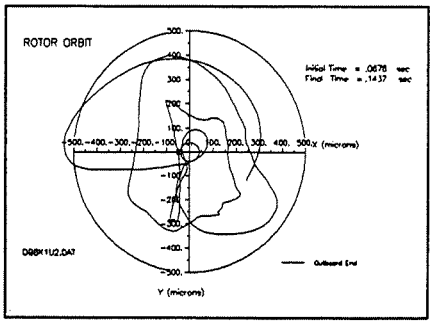

Fig. 12 : Rotor orbit at outboard end for case 5.

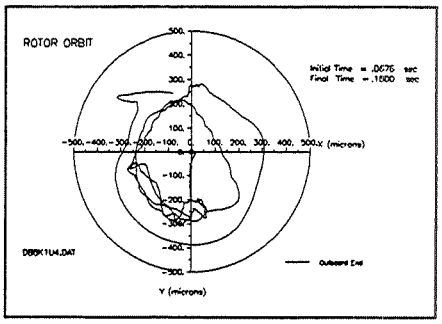

Fig. 13 : Rotor orbit at outboard end for case 6.

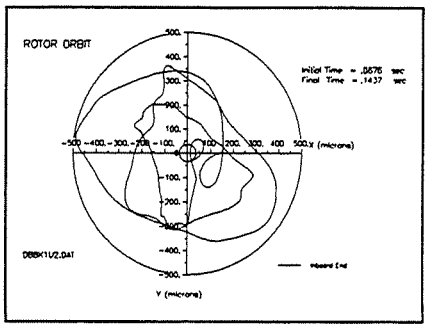

Fig. 14 : Rotor orbit at inboard end for case 5.

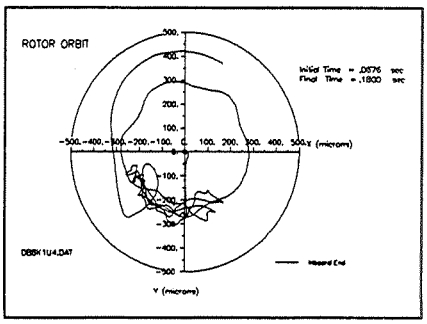

Fig. 15 : Rotor orbit at inboard end for case 6.

Different Back-up Bearing Configurations

The effect of support flexibility on the rotor drop phenomena was studied by comparing the forces and rotor orbits observed in the case of solid hard mount backup bearings (Case 1- Figs. 2 and 3) with those in the case of a soft mount bearing representing the presence of an o-ring or other means of providing a flexible damped support (Case 7 - Figs. 16 and 17). An additional non-linear stiffening effect for a 1-mil clearance space was taken into consideration in the case 7. The coefficient of contact friction was also reduced to 0.1 in order to model a lubricated surface. The depth of penetration was higher in case 7 (Fig. 16) than in case 1 (Fig. 2). The oscillations were also of lesser magnitude in case 7 due to the lower friction coefficient. The initial contact forces were seen to be much lower in case 7 than in case 1. The final range of contact forces in both cases were seen to be of similar magnitudes.

Case 7 : 1/10 g Static unbalance at center disk and decay of Inboard AMB

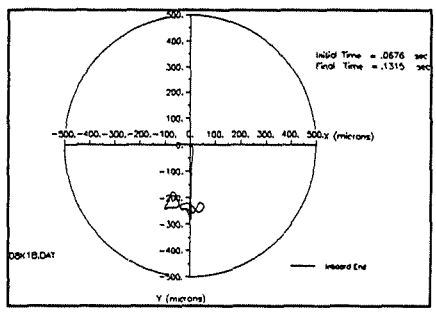

Fig. 16: Rotor orbit at inboard end for case 7.

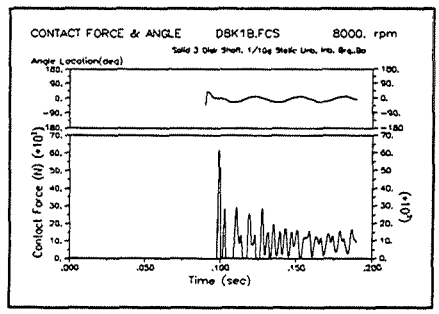

Fig. 17: Contact force at inboard end for case 7.

When the rotor is supported by AMB's, the static reaction force due to gravity at inboard AMB location is 981.2918 N and the static reaction force due to gravity at outboard AMB location is 952.3975 N. The summary of initial force and maximum force over the time of the transient is presented in Tables 4 and 5. The initial impact averages about 9 g's for the hard mount but only 6 g's for the soft mount.

It was also observed that in the low static and dynamic unbalance (0.1 g) cases of Tables 4 and 5, the average contact force at the end of transient was close to the static reaction force due to gravity at that location. When the unbalance level was higher, the magnitude of contact forces did not show a steadily decreasing trend. These forces even increased dramatically after some period of time for cases with the higher unbalance levels. The peak force is noted to be as high as 95 g's for one level of unbalance.

Lubrication of contact surfaces reduced the initial contact forces in all cases of static and dynamic unbalance levels by amounts ranging from 0.2 g to 1.3 g. Including the support flexibility in the model reduced the initial contact forces furthermore by about 3 g's. The maximum contact forces were also seen to be under better control in cases with lubricant on contact surfaces and with support flexibility.

Table 4 : Contact Force vs. Level of Static Unbalance at Center-Disk for Different Backup Bearing Configurations (During Initial 0.1 s After Inboard AMB Decay)

Static Unbalance Level	Hard Mount (Unlubricated) Backup Bearing		Hard Mount (Lubricated) Backup Bearing		Soft Mount (Lubricated) Backup Bearing	
	Initial Contact Force in N	Maximum Contact Force in N	Initial Contact Force in N	Maximum Contact Force in N	Initial Contact Force in N	Maximum Contact Force in N
0.1 g	9900	9900	9600	9600	6200	6200
0.3 g	9800	9800	9500	9500	5800	5800
0.5 g	8500	9200	8000	10000	5000	5700
0.7 g	7000	67000	6500	12000	4200	9800
1.0 g	12000	95000	11500	16000	11300	11300

Table 5 : Contact Force vs. Level of Dynamic Unbalance at Center-Disk and Landing Sleeves for Different Backup Bearing Configurations (During Initial 0.1 s After Inboard AMB Decay)

Dynamic Unbalance Level	Hard Mount (Unlubricated) Backup Bearing		Hard Mount (Lubricated) Backup Bearing		Soft Mount (Lubricated) Backup Bearing	
	Initial Contact Force in N	Maximum Contact Force in N	Initial Contact Force in N	Maximum Contact Force in N	Initial Contact Force in N	Maximum Contact Force in N
0.1 g	9800	9800	9500	9500	6200	6200
0.3 g	10000	10000	9600	9600	5800	5800
0.5 g	8800	11500	8600	9600	5200	5700
0.7 g	7000	12000	6700	10500	4000	10000
1.0 g	7000	59000	5700	17500	8000	12000

Effect of Rotor Running Speed

It was observed in this research that the transient response of the rotor after AMB failure is a function of the rotor spin speed due to its ability to excite the system natural frequencies. The contact forces for some of the cases having 0.3 g dynamic unbalance in the planes of the three disks have been tabulated in Table 6. These cases are for solid rigid unlubricated backup bearings at both the inboard and outboard ends for cases when the AMB's at both ends decay. The results in Table 6 clearly indicate a higher level of rotor response and contact forces at about 200 Hz. This is due to the presence of the first free-free mode or the first bending mode of the system in that region of rotor speed. The values given as maximum contact force in Table 6 are the maximum forces during the initial 70 milliseconds of the transient motion.

Table 6 : Contact Forces vs. Rotor Speed for 0.3 g Dynamic Unbalance in the Disk Planes and AMB Failure at Both Ends

Rotor Speed (Hz)	OUTBOARD END		INBOARD END	
	Initial Contact Force (N)	Maximum Contact Force (N)	Initial Contact Force (N)	Maximum Contact Force (N)
133.33	6000	22000	6000	22000
150.00	10000	50000	8000	50000
166.66	12000	100000	12000	100000
183.33	10000	570000	10000	550000
200.00	10000	800000	10000	700000
216.66	7000	22500	6000	24500
233.33	7500	12000	8000	13000

Table 3 gives the damped natural frequencies of the rotor for some of the possible shaft support configurations. It can be seen from the values in the table that the first bending mode of the system or the first free-free mode exists somewhere close to 190 Hz. It is adviceable for AMB designers to have the design speed of the rotor away from this mode as it may cause destructive whirls and very high forces in the event of AMB system failure even for very low system unbalances. Figures 18, 19, 20 and 21 show rotor orbits and contact forces for cases at the rotor speeds of 133.33 Hz and 200 Hz respectively.

Case 8 : 3/10 g Dynamic Unbalance at center disk and outer disks with decay of both AMB's

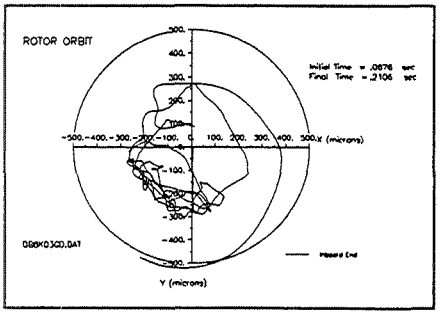

Fig. 18: Rotor orbit at inboard end for case 8 at 133.33 Hz.

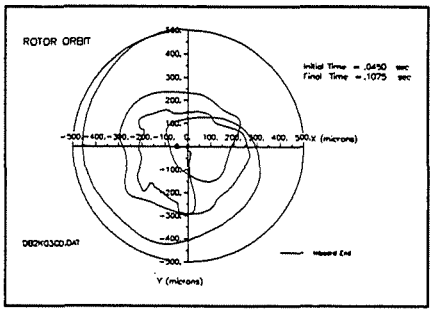

Fig. 19: Rotor orbit at inboard end for case 8 at 200.00 Hz.

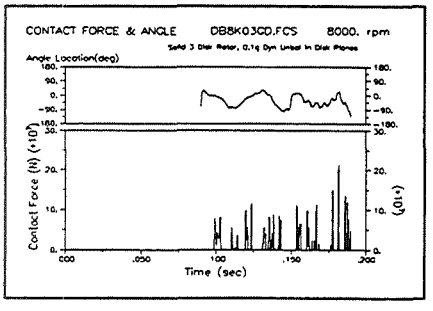

Fig. 20: Contact Force at inboard end for case 8 at 133.33 Hz.

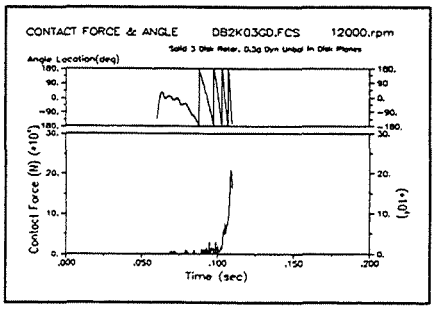

Fig. 21: Contact force at inboard end for case 8 at 200.00 Hz.

CONCLUSIONS AND RECOMMENDATIONS

Based upon the analytical results presented in this paper, the following conclusions have been reached :

1) A balanced rotor condition is necessary to have greater assurance that a drop will not initiate a violent whirl.
2) The static unbalance of 0.1 g did not cause any excessive whirling of the rotor.
3) Dynamic couples in the rotor can excite the rotor in its free-free mode upon drop. Field balancing of rotor midspan unbalance at the rotor coupling would not be desirable for AMB rotors.
4) The level of response tends to increase as the level of unbalance increases. This is true of all backup bearing designs used in current research.
5) For the hard-mount condition, it is clear that violent unstable whirling can occur for certain levels of unbalance (see Tables 4 and 5).
6) The soft mount, lubricated surface gives the best performance for both initial impact force level and the peak transient force levels.

The previous conclusions are based upon predicting results that do not include the total run down of the rotor, but rather the initial 100 msec of the transient. The recommendations from this work are as follows :

1) Step balance of rotors to reduce dynamic couples is highly desirable for AMB rotors that are expected to have safe rotor drops.
2) Field balancing at rotor couplings for midspan unbalance is not recommended.
3) Soft mounted backup bearing should be used in all designs with adequate precaution given to maximum rotor excursion in the total clearance space.
4) Transient response analysis of the rotor drop at design speed should be used to specify the acceptable level of rotor steady-state vibration amplitude for safe operation considering the rotor drop possibility.
5) Operation at or near the rotor free-free mode should be avoided for AMB rotor designs.
6) Experimental drop results should be compared to the overall trends. The influence of static and dynamic unbalance levels on the rotor drop stability should be confirmed. (Note : This experimental work is in progress and will be published in a future paper.)

ACKNOWLEDGMENTS

This research was sponsored by the Virginia Center for Innovative Technology with additional grants from Magnetic Bearings Inc., Dresser-Rand Turbo Products Division, Pratt and Whitney Aircraft, and the Virginia Tech Rotor Lab Industry Affiliates Group. The authors would also like to acknowledge the support of Rotating Machinery Technology Inc. for supplying the test bushings that are being used for the experimental research to substantiate the results of the analytical predictions.

REFERENCES

Bently, D.E., 1995, "Statement on Magnetic Bearings", ORBIT, Vol. 16, No. 1, March, p. 5.

Engelmann, B.E., 1988, "Dynamics of Structures : Solution Techniques", Lectures notes in Engineering - Finite Element Analysis for Engineering Design, Edited by J.N. Reddy, C.S. Krishnamoorthy, K.N. Seetharamu, Springer-Verlag Publications.

Fumagalli, M., Varadi, P., and Schweitzer, G., 1994, "Impact Dynamics of High Speed Rotors in Retainer Bearings and Measurement Concept", Proceedings of Fourth International Symposium on Magnetic Bearings, August 1994, Zurich, pp. 239-244.

Ishii, T., and Kirk, R.G., 1991, "Transient Response Technique Applied to Active Magnetic Bearing Machinery During Rotor Drop", ASME Conference Proceedings, DE-Vol. 35, pp. 191-200.

Kirk, R.G., and Ishii, T., 1993, "Transient Rotor Drop Analysis of Rotors following Magnetic Bearing Power Outage", Proceedings of MAG '93, pp. 53-61.

Kirk, R.G., Swanson, E.E., Kavarana, F.H., Wang, X., 1994, "Rotor Drop Test Stand for AMB Rotating Machinery, Part I : Description of Test Stand and Initial Results", Proceedings of Fourth International Symposium on Magnetic Bearings, August 1994, Zurich, pp. 207-212.

Raju, K.V.S., Ramesh, K., Swanson, E.E. and Kirk, R.G., 1995, "Simulation of AMB Turbomachinery for Transient Loading Conditions", Proceedings of MAG '95, Alexandria, VA, pp. 227-235.

Ramesh, K., and Kirk, R.G., 1992, "Subharmonic Resonance Stability Prediction for Turbomachinery with Active Magnetic Bearings", Proceedings of the Third International Symposium on Magnetic Bearings, Alexandria, VA, pp. 113-122, 1992.

Schmied, J., Pradetto, J.C., 1992, "Behavior of a One Ton Rotor Being Dropped into Auxiliary Bearings", Proceedings of The Third International Symposium on Magnetic Bearings, Alexandria VA, July, pp. 145-156.

Swanson, E.E., Kirk, R.G. and Wang, X., 1995, "AMB Rotor Drop Initial Transients on Ball and Solid Bearings",Proceedings of MAG '95, Alexandria, VA, pp. 207-216.

DEVELOPMENTS IN IMPELLER/SEAL SECONDARY FLOW PATH MODELING FOR DYNAMIC FORCE COEFFICIENTS AND LEAKAGE

Alan Palazzolo and Avijit Bhattacharya
Texas A&M University
College Station, Texas

Balaji Venkataraman
Atlas Copco Cometec, Inc.
Vorheesville, New York

Mahesh Athavale
CFDRC Corporation
Huntsville, Alabama

and

Steve Ryan and Kerry Funston
NASA George C. Marshall Space Flight Center
Marshall Space Flight Center, Alabama

ABSTRACT

This paper highlights bulk flow and CFD-based models prepared to calculate force and leakage properties for seals and shrouded impeller leakage paths. The bulk flow approach uses a Hir's based friction model and the CFD approach solves the Navier Stoke's (NS) equation with a finite whirl orbit or via analytical perturbation. The results show good agreement in most instances with available benchmarks.

INTRODUCTION

Many analyses of seals, via bulk flow modeling assumptions, have appeared in the literature. Variations on this approach included incompressible/compressible, thermohydrodynamic/constant properties, concentric/eccentric, aligned/misaligned, uniform/tapered/arbitrary clearance profile. Researchers in this area include Black, Childs, Itwatsubo, Frene, Kim, Palazzolo, San Andres, Nelson, Nordmann, Kwanka, and a host of others. Seal flows have also been analyzed with CFD by Noordmann, et. al, Atavale[2], Baskharone[3] and Rhode. Childs[1] developed a shrouded impeller leakage path analysis assuming incompressible flow by employing the bulk flow approach. This work was later followed by the M.S. Thesis work of his student, Nhai the Cao, using a compressible flow model. Baskharone and Nordmann have subsequently modeled impeller leakage paths with CFD methods. The current paper describes a multi-segment approach to seal and impeller leakage path modeling which employs a Hir's bulk flow assumption. This work is currently being validated with the 3D, CFD finite volume code SCISEAL developed by CFDRC under sponsorship of NASA. This objective of this effort is to develop reliable modeling software for the seals and impeller leakage paths in the space shuttle main engine turbopumps.

THEORY

The governing PDE's for the leakage path are obtained by kinematically constraining the N.S. eqs. according to bulk flow assumptions, i.e. no cross film flow or recirculation, rectangular profiles, etc. The results are:

Bulk Flow Continuity Eq.

$$\frac{\partial}{\partial t}(\rho H) + \frac{\partial}{\partial S}(\rho H U_s) + \frac{1}{R}\frac{\partial}{\partial \theta}(\rho H U_\theta) + \rho U_s \frac{H}{R}\frac{\partial R}{\partial S} = 0 \tag{1}$$

Bulk Flow Path Momentum Eq.

$$-H\frac{\partial P}{\partial S} = \tau_{ss} + \tau_{sr} + \rho \frac{H}{R}\frac{\partial R}{\partial S}\left(U_s^2 - U_\theta^2\right) + \frac{\partial}{\partial t}(\rho H U_s) + \frac{\partial}{\partial S}(\rho H U_s^2) + \frac{1}{R}\frac{\partial}{\partial \theta}(\rho H U_\theta U_s) \tag{2}$$

Bulk Flow Circumferential Momentum Eq.

$$-\frac{H}{R}\frac{\partial P}{\partial \theta} = \tau_{\theta s} + \tau_{\theta r} + \frac{\partial}{\partial t}(\rho H U_\theta) + \frac{\partial}{\partial S}(\rho h U_s U_\theta) + \frac{1}{R}\frac{\partial}{\partial \theta}(\rho H U_\theta^2) + 2\rho \frac{H}{R} U_s U_\theta \frac{\partial R}{\partial S} \tag{3}$$

Where

s: leakage path coordinate
R(s): leakage path radius
H(s, θ, t): leakage path film thickness
U_s, U_θ: leakage path flow velocities

and the Hir's bulk flow shear stresses are given by:

Stator Shear Stress - Path Direction

$$\tau_{ss} = \frac{n_s}{2}\rho U_s^2 R_\alpha^{M_s}\left[1 + \left(\frac{U_\theta}{U_s}\right)^2\right]^{\frac{(M_s+1)}{2}} \tag{4}$$

Rotor Shear Stress - Path Direction

$$\tau_{sr} = \frac{n_r}{2}\rho U_s^2 R_\alpha^{M_r}\left[1 + \left(\frac{U_\theta - R\omega}{U_s}\right)^2\right]^{\frac{(M_r+1)}{2}} \tag{5}$$

Stator Shear Stress - Circumferential Direction

$$\tau_{\theta s} = \frac{n_s}{2}\rho U_\theta U_s R_\alpha^{M_s}\left[1 + \left(\frac{U_\theta}{U_s}\right)^2\right]^{\frac{(M_s+1)}{2}} \tag{6}$$

Rotor Shear Stress - Circumferential Direction

$$\tau_{\theta r} = \frac{n_r}{2}\rho U_s\left(U_\theta - R\omega\right)R_\alpha^{M_r}\left[1 + \left(\frac{(U_\theta - R\omega)}{U_s}\right)^2\right]^{\frac{(M_r+1)}{2}} \tag{7}$$

Where the path Reynold's number is defined by:

$$R_\alpha = \frac{2HU_s}{\nu} \quad , \quad \nu = \frac{\mu}{\rho} \tag{8}$$

and

ω : rotor spin velocity
n_r, n_s, m_r, m_s : experimentally derived Hir's coefficients
μ: absolute viscosity

The film thickness expression for the impeller's infinitesimal displacements (x, y, α_x, α_y) shown in figure 1 is given by:

$$H(s,\theta,t) = H_o(s) - \left\{\left(x + \alpha_y\left[z - z_o\right]\right)\frac{dz}{dS} + R\alpha_y\frac{dR}{dS}\right\} - \left\{\left(y - \alpha_x\left[z - z_o\right]\right)\frac{dz}{dS} - R\alpha_x\frac{dR}{dS}\right\} \tag{9}$$

where $H_o(s)$ is the aligned, concentric clearance function and z_o is the z coordinate of the centers of rotation for α_x and α_y.

These equations are non-dimensionalized before being perturbed to form a set of steady-state (zeroeth order) eqs. and a set of linearized (first order) eqs. The former equations are solved with appropriate pressure boundary conditions using a shooting algorithm and Runge-Kutta 4th order

integration. The latter eqs. are solved in a similar manner. Viscosities and densities are obtained from MIPROPS (thermophysical property data base) for liquid hydrogen and LOX.

Leakage paths in turbomachines may be very complex, consequently, a generalized path description was developed. This path model is composed of a series of segments, each segment possessing linearly varying clearance and radius profiles, Hir's coefficients and inlet and exit pressure loss factors as depicted in figure 2. Flow continuity and pressure compatibility conditions are enforced at each interface between neighboring elements, as shown in figure 2. The zeroeth order solution procedure iterates to find the pressure, after the entrance loss, which yields the prescribed exit pressure. The zeroeth order pressure velocities, densities and viscosities are then employed in the first order solution and for leakage and HP loss calculations. The first order pressures are obtained employing a Runge-Kutta Transfer Matrix approach for solving the two point boundary value problem of 12 coupled ODE's. Radial and tangential impedances are derived by integrating the first order pressure, and curved fitted to second order polynomials in the whirl frequency Ω. This yields the principal and cross coupled inertias, stiffnesses and dampings, via the coefficients of the curve fit.

$$\begin{Bmatrix} K + c\Omega - M\Omega^2 \\ -k + C\Omega + m\Omega^2 \end{Bmatrix} = \frac{-1}{C^*} \begin{Bmatrix} F_x(\Omega) \\ F_y(\Omega) \end{Bmatrix} \qquad \textbf{(10)}$$

A second approach to the impeller secondary flow path leakage and dynamic coefficient determination is also being pursued. This approach utilized the code SCISEAL[4] developed by CDFRC under grant from NASA. The code obtains solution for the dynamic pressures of a whirling rotor and for its leakage flow via a finite volume based solution of the full Navier Stoke's equation. The NS equation for concentric whirl are formed in the whirling frame requiring that the film thickness (clearance) be meshed only for a single phase in the whirl orbit. A steady state solution is generated in the whirling reference frame. Concentrated losses, user specified velocity profiles at the inlet/exit, sand grain roughness, eccentric operation and prewhirl are some of the available user options. Mesh and flow visualization is available for model checking and interpretation of results. Multi-Domain grid generation has been employed with the labyrinth seal model presented. SCISEAL follows the standard bulk flow model approach of determining the radial and tangential impedances at various whirl frequency ratios ($f = \Omega/\omega$). The impedances are curve fit in the same manner as discussed for equation (10). Figure 3 shows some basic functions of the SCISEAL Solution Package.

There are five turbulence models available in the SCISEAL code. These models are:

Eddy Viscosity model,
Baldwin-Lomax model,
Standard k-ε model,
Low Reynolds number model, and
2-Layer k-ε model.

The k-ε model is the default model used in SCISEAL and was employed in the current study. The typical seal clearances are small, and when selecting turbulence models, care must be taken to ensure that the model being used is valid for the geometry and grid selected. The main parameter is the distance of the first cell center away from the wall boundaries in terms of the nondimensional

parameter y^+. Following are recommended limits on this parameter:

a. k-ε model with standard wall functions: This model is applicable for $y^+ > 11.5$. To ensure the accuracy of the wall functions, the first cell center must be sufficiently away from the wall. The wall shear is overpredicted if the first cell is too close.

b. Low Re number k-ε model: To ensure the accuracy of this model, the first cell center sufficiently close to the wall so that it will be inside the laminar sublayer, which corresponds to a y^+ of less than 1.

The wall shear calculations affect the leakage rates, since it affects the pressure drop in the seal. The rotordynamic coefficients are calculated using the circumferential pressure generated by an eccentric rotor. This pressure is also affected by the wall shear calculation. To ensure the correct placement of the cell centers nearest to walls, SCISEAL will print out the y^+ distances at all wall boundaries, and then these values can be checked for consistency with the turbulence model being used.

In several instances, the y^+ values are not known *a priori* and the flow regime may fall outside of the limits specified by the selected turbulence model, and a second run with appropriate grid change or with a different turbulence model may be needed. To avoid this, the 2-layer model is implemented in the code. The model automatically switches from the low Re k-ε type information to a wall function type formulation depending on the near wall y^+ distance.

RESULTS

(A.) Multi-Segment Bulk Flow Modeler

Many cases were run to check the accuracy of this leakage path solver. The first set of cases involved axially subdividing annular seal models into 2 to 10 segments with zero internal loss factors and identical Hir's constants. Typical are the results shown in Table 1 for a tapered, LH_2 seal modeled by Scharrer/Nelson and by Childs/Kim. A closed form, zeroeth order solution for the simple geometry shroud seal combination shown in figure 4, was derived. A comparison between the multi-segment model numerical and exact solutions is shown in Table 2.

A third check case was the Bolleter impeller examined in Childs[1]. The impeller profile and its two segment model are shown in figure 5. The parameters employed in the analysis are shown in Table 3. Figures 6 a, b, and c show the zeroeth order path velocity, circumferential velocity and pressure vs. path position. Table 4 compares zeroeth order solution results between the multi-segment code and Childs'[5]. Table 5 shows a similar comparison for rotordynamic coefficients. These coefficients were obtained by curve fitting the impedance curves of figure 7 at frequency ratios of 0.5, 1.25 and 2.0. These figures are taken from Childs'[1] and compared to the current results.

Figure 8 shows a shrouded impeller modeled for compressible (LH_2) leakage by Nhao The Cao and Childs[5]. Figure 9 shows good agreement for the static pressure distribution between Cao and the multi-segment approach. The exit labyseal was treated as a concentrated pressure loss (discharge coefficient) in the models. Figures (10 a, b) show the radial and tangential impedance functions obtained from the two segment model using compressible and incompressible assumptions. The resonant-like nature of these curves are similar to those given by Cao and Childs. Table 6 shows dynamic coefficients obtained from curve fitting the impedances at frequency ratios less than 2.

(B.) SCISEAL

The SCISEAL code was first tested against bulk flow seal models. Figures (11 a, b) show typical results for K_{yy} and K_{yx} vs. eccentricity. The agreement is very good in relation to test results and with the bulk flow model. Table 8 shows a comparison of dynamic coefficients for the same check case assuming different inlet swirl profiles with SCISEAL.

The 3 cross film, inlet swirl profiles include constant at 0.3 Rω, linear at zero (stator) to Rω (rotor), and linear at zero (stator) to 0.6 Rω (rotor). Note the significant increase in K_{xy} with the second inlet swirl profile case.

CONCLUSIONS

This paper highlighted several approaches being employed to model flows in labyseals and impeller leakage paths. The bulk flow approach, though efficient, computation-wise does not include effects of recirculation. This type of flow has been noted in labyrinth seal cavities and in impeller shroud leakage paths where the radial flow component is driven by centrifugal and pressure gradient type sources. The commercially available code SCISEAL is currently being employed to model labyseals for dynamic coefficients. This effort will be extended to shrouded impeller leakage paths in the near future. Plans for comparing the approaches described here to test results from a NASA sponsored magnetic bearing/shroud leakage flow test rig are now being made.

REFERENCES

(1) Childs, D. W., 1989, "Fluid Structure Interactions Forces at Pump Impeller-Shroud Surfaces for Rotordynamic Calculations," ASME Journal of Vibrations, III, pp. 216-225.

(2) Athavale, M. M., Przekwas, A. J., and Hendricks, R., "A 3D CFD Code for Accurate Prediction of Fluid Flows and Fluid Forces in Seals," Rotordynamic Instability Pbs. in Turbomachinery, NASA CP 3239, May, 1993.

(3) Baskharone, E., "Theory vs. Experiment Rotordynamic Coefficients of Incompressible Flow Laby Seals," AIAA Journal of Propulsion and Power, Sept., 1994.

(4) Athavale, M. M., Przekwas, A. J., "SCISEAL: A Computer Program For Study of Fluid Dynamic Forces in Seals," CFDRC Corporation, Huntsville, Al., 35805, May, 1995.

(5) Nhai the Cao, and Childs, D., "Compressibility Effects on Rotor Forces in the Leakage Path Between a Shrouded Pump Impeller and Its Housing," MSME Thesis, TAMU, 1993.

Particulars	Scharrer/Nelson	Childs/Kim	Current
Leakage, Q(kg/s)	---	8.35	8.41
Direct stiffness, Kxx (N/m)	$222.*10^6$	$194.6*10^6$	$197.5*10^6$
Cross coupled stiffness, Kxy (N/m)	$61.*10^6$	$57.9*10^6$	$58.53*10^6$
Direct damping, Cxx (N-s/m)	$25.80*10^3$	$24.36*10^3$	$24.51*10^3$
Cross coupled damping Cxy(N-s/m)	---	$2.72*10^3$	$2.834*10^3$
Direct inertia, Mxx (kg)	0.66	0.66	0.6248
Cross coupled inertia, Mxy (kg)	---	-0.0042	-0.061 (2 segment model)

Table 1 Comparison of Two Segment Bulk Flow Model Results with Scharrer/Nelson Annular Seal.

Closed form solution for frictionless flow through Shroud and Exit Wear-ring Seal

Input Data :

$\Delta P = 0.466 MPa$	*Working Fluid: Water*	$\rho = 1000 kg/m^3$	$\mu = 1.3E\text{-}03\ Pa\text{-}s$
Inlet Loss, $\xi = 0.1$	*Shroud*: $C_i = C_0 = 5.8mm$ *Seal*: $C_i = C_0 = 0.36\ mm$	*Speed*, $N = 2000 rpm$	*Shrd. Length* $L_s = 64mm$ $dr/ds = -0.89$ *Seal Length* $l_{si} = 33mm$
Inlet Dia, $D = 175\ mm$	*Preswirl*, $\gamma = 0.5$	*Shroud*: $n_s, m_s = 0$ *Seal*: $n_s, m_s = 0$	*Shroud*: $n_r, m_r = 0$ *Seal*: $n_r, m_r = 0$

Results :

Particulars	*Closed Form Solution*	*Current Analysis*
Shroud Inlet Path Velocity, Ws(0) (m/s)	0.918	0.9193
Shroud Exit Path Velocity, Ws(L) (m/s)	1.361	1.3626
Shroud Inlet Pressure, P(0) (N/m2)	465,536.5	465,640.6
Shroud Exit Pressure, P (N/m2)	26,363.2	26,420.56
Shroud Exit Swirl Velocity, U(L) (m/s)	27.16	27.163
Leakage, Q (kg/s)	5.85	5.859

Table 2 Comparison of Two Segment, Bulk Flow Model Results with Exact Solution for Shroud/Seal Path.

$\Delta P = 0.466 MPa$	*Working Fluid: Water*	$\rho = 1000 kg/m^3$	$\mu = 1.3E\text{-}03\ Pa\text{-}s$
Shrd. InletLoss, $\xi = 0.1$ *SealInletLoss,* $\xi = 0.1$	*Shroud:* $C_i = C_0 = 5.8mm$ *Seal:* $C_i = C_0 = 0.36\ mm$	*Speed,* $N = 2000 rpm$	*Shrd. Length,* $L_s = 64mm$ *dr/ds* = -0.89 *SealLength,* $l_{si} = 33mm$
Shrd. Inl. Dia $= 175mm$ *SealInl. Dia* $= 118mm$	*Preswirl,* $\gamma = 0.5$	*Shroud* $n_s, m_s = 0.079, -0.25$ *Seal* $n_s, m_s = 0.079, -0.25$	*Shroud* $n_s, m_s = 0.079, -0.25$ *Seal* $n_s, m_s = 0.079, -0.25$
Input Data :			

Table 3 Bolleter Impeller Leakage Path Parameters.

Comparison of ***Leakage (kg/s)*** *with Childs (1989) for Wear-ring seal clearance of 0.36 mm*

Swirl Ratio @ Shroud Inlet	*Childs*	*Current Analysis*
0.5	4.03	3.891
0.6	3.75	3.693
0.7	3.44	3.495

Comparison of ***Swirl Ratios at Seal Inlet*** *with Childs (1989) for Wear-ring seal clearance of 0.36 mm*

Swirl Ratio @ Shroud Inlet	*Childs*	*Current Analysis*
0.5	0.884	0.802
0.6	0.947	0.860
0.7	0.99	0.912

Table 4 Comparison of Two Segment Model with Childs'[1] Bolleter Results. Zeroeth Order Solution.

Particulars	Childs	Current/Shroud
Leakage, Q (kg/s)	4.03	3.88
Direct stiffness, Kxx (N/m)	60050	64231.0
Cross coupled stiffness, Kxy (N/m)	$199.7*10^3$	$196.72*10^3$
Direct damping, Cxx (N-s/m)	1211.0	951.4
Cross coupled damping Cxy(N-s/m)	682.1	105.5884
Direct inertia, Mxx (kg)	2.513	1.095
Cross coupled inertia, Mxy (kg)	2.288	-0.7172

Table 5 Comparison of Two Segment Model with Childs'[1] Bolleter Results. Dynamic Coefficients.

Particulars	Current-Incomp	Current-Comp	Childs/Cao
Leakage, Q (kg/s)	1.575	1.55	1.63
Direct stiffness, Kxx (N/m)	$2.236*10^6$	$1.908*10^6$	---
Cross coupled stiffness, Kxy(N/m)	$3.761*10^6$	$3.828*10^6$	---
Direct damping, Cxx (N-s/m)	1236.	1257.	---
Crs. coupled damping Cxy(N-s/m)	-309.4	-216.4	---
Direct inertia, Mxx (kg)	0.0052	0.0116	---
Cross coupled inertia, Mxy (kg)	-0.097	-0.0994	---

Table 6 Comparison of Incompressible and Compressible Two Segment Model Results for SSME HPFTP Impeller.

eccentricity = 0.

ROTORDYNAMIC Coefficients	* Padavala,Palazzolo Bulk Flow	Constant 0.3*Wvel	Linear Wvel	Linear 0.6*Wvel
			SCISEAL	
Direct Stiffness, K_{xx}	0.423684e+07	0.4315685e+07	0.4282584e+07	0.4314116e+07
Direct Stiffness, K_{yy}	0.423684e+07	0.4315685e+07	0.4282584e+07	0.4314116e+07
Direct Damping, C_{xx}	0.114410e+05	0.1034902e+05	0.1023518e+05	0.1028350e+05
Direct Damping, C_{yy}	0.114410e+05	0.1034902e+05	0.1023518e+05	0.1028350e+05
Direct Inertia, M_{xx}	0.397077e+01	0.4120364e+01	0.4096263e+01	0.4129847e+01
Direct Inertia, M_{yy}	0.397077e+01	0.4120364e+01	0.4096263e+01	0.4129847e+01
Cross Coupled Stiffness, k_{xy}	0.133781e+07	0.1220396e+07	0.2152693e+07	0.1202863e+07
Cross Coupled Stiffness, k_{yx}	0.133781e+07	0.1220396e+07	0.2152693e+07	0.1202863e+07
Cross Coupled Damping, c_{xy}	0.144508e+04	0.1444480e+04	0.1671701e+04	0.1446619e+04
Cross Coupled Damping, c_{yx}	0.144508e+04	0.1444480e+04	0.1671701e+04	0.1446619e+04
Cross Coupled Inertia, m_{xy}	-0.173805e+00	0.9807794e-01	0.1808641e+00	0.1010620e+00
Cross Coupled Inertia, m_{yx}	-0.173805e+00	0.9807794e-01	0.1808641e+00	0.1010620e+00

Table 7 Comparison of Dynamic Coefficients For Different Cross Film, Inlet Swirl Profiles. Falco Check Case.

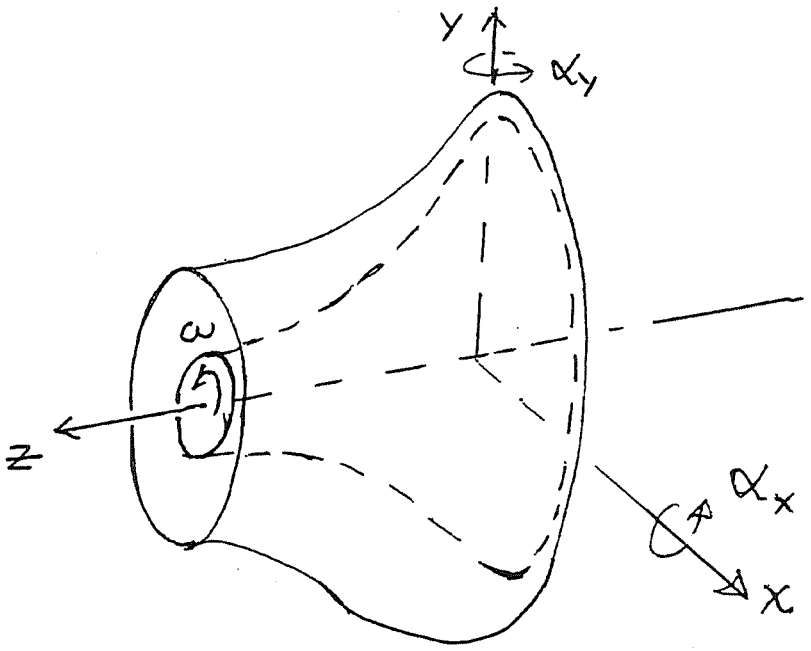

Figure 1 **Generalized Leakage Path Geometry and Impeller Motion Coordinates.**

Linear C
Linear R
within Segment K

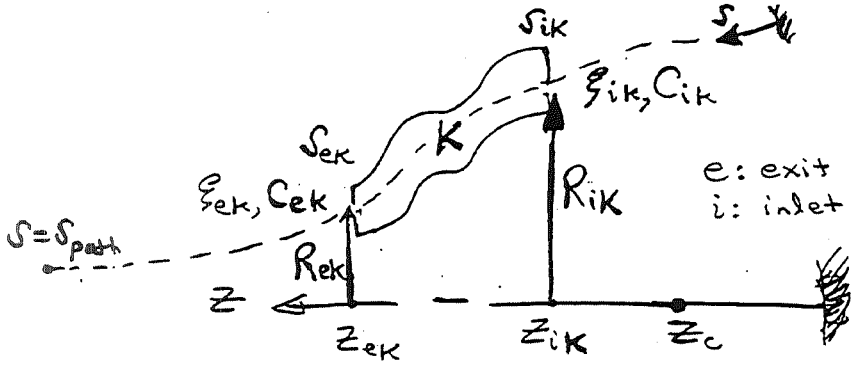

Axial Velocity;
$$W_{sk}^{(s_i^k)} = W_{s,k-1}^{(s_e^{k-1})} \left\{ \frac{R_{e,k-1}}{R_{ik}} \frac{C_{e,k-1}}{C_{ik}} \frac{\rho_{k-1}^{(s_e^{k-1})}}{\rho_k^{(s_i^k)}} \right\}$$

Swirl Velocity;
$$U_{i,k} = U_{e,k-1} \frac{R_{e,k-1}}{R_{i,k}}$$

Inlet Pressure;
$$P_{ik} = P_{e,k-1} + (1-\xi_{e,k-1}) \frac{\rho_{e,k-1}}{2} W_{se,k-1}^2 - (1+\xi_{ik}) \frac{\rho_{ik}}{2} W_{sik}^2$$

Exit Pressure @ End of Path;
$$P_{e,N} = P_e + (\xi_{e,N}-1) \frac{\rho_{eN}}{2} W_{se,N}^2$$

Figure 2 **Segment K of Leakage Path in Bulk Flow Model.**

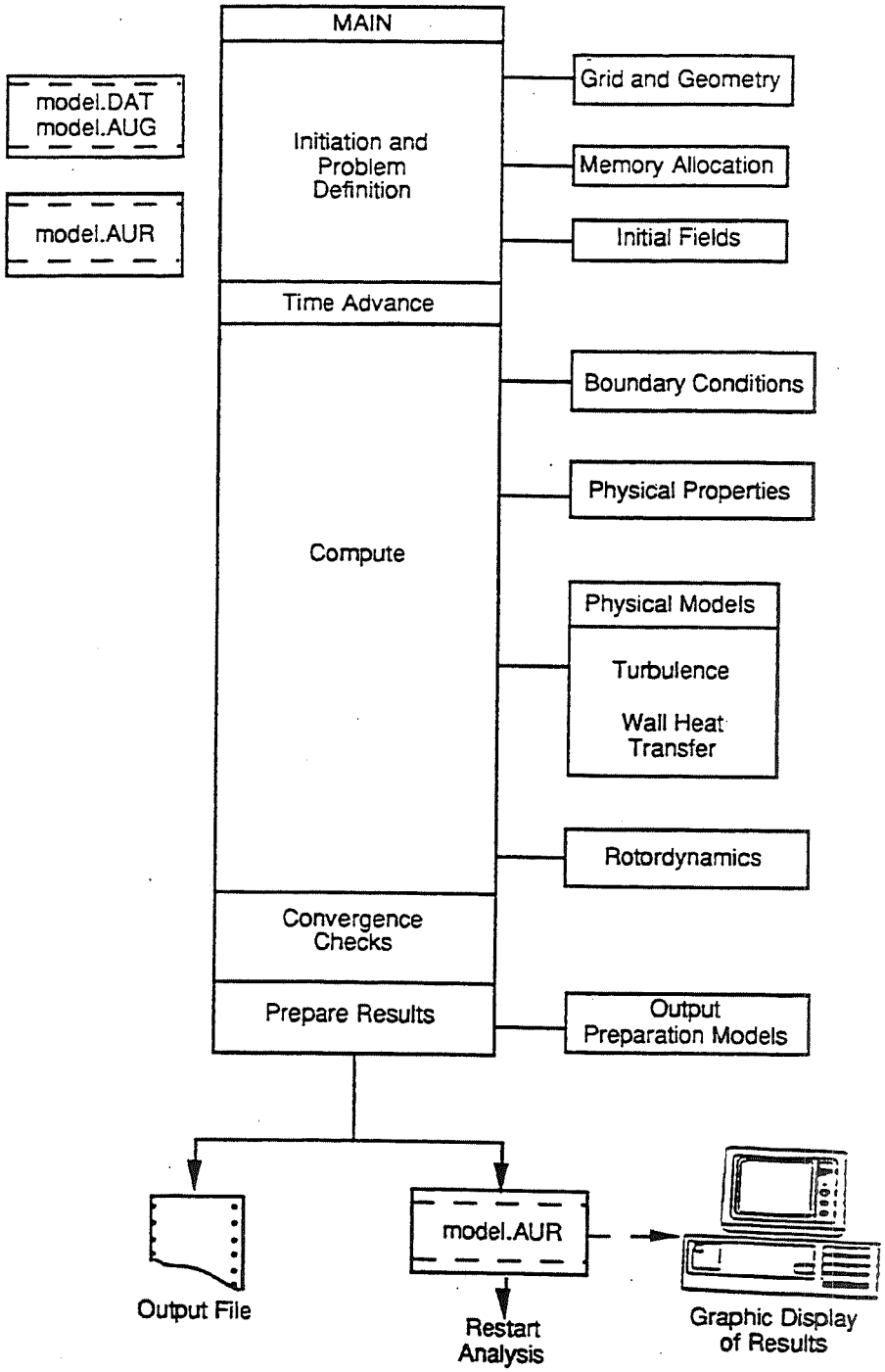

Figure 3 SCISEAL Code Structure.

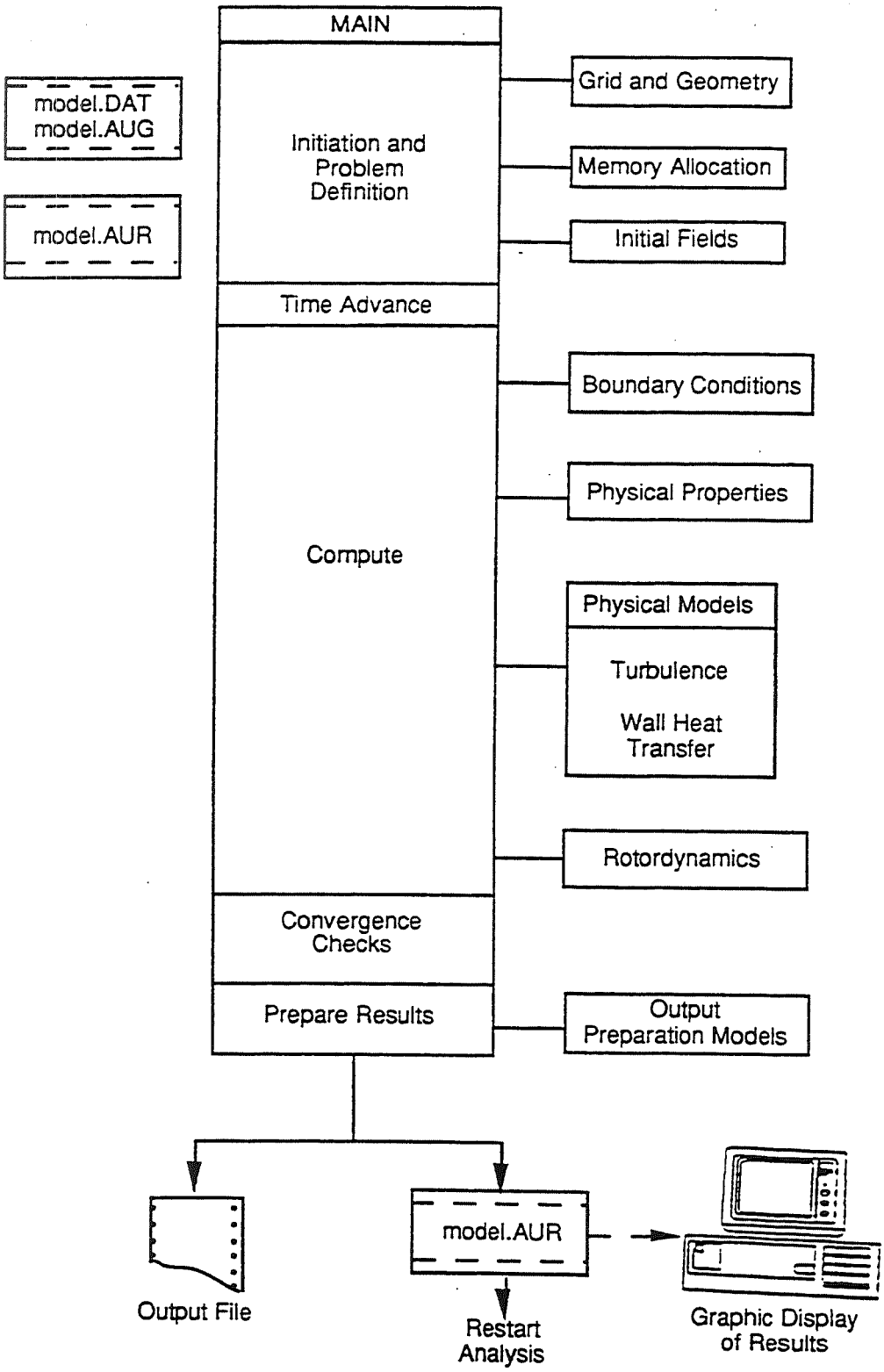

Figure 3 SCISEAL Code Structure.

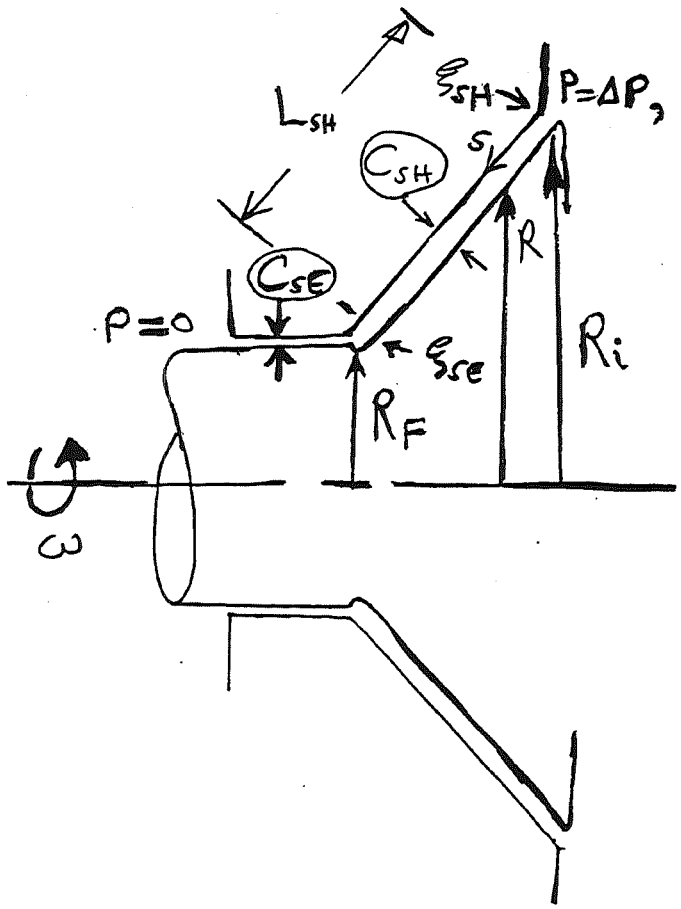

$\eta = \frac{U_o}{R_i \omega}$ = inlet preswirl ratio

$\bar{r} = R_i / R_F$

$\bar{c} = C_{SH} / C_{SE}$

NO FRICTION

$$R = R_i \left(\gamma \frac{s}{L_{SH}} + 1 \right)$$

$$\gamma = \left(R_F / R_i \right) - 1$$

Figure 4 **Parameters for Closed Form Solution of Shroud Leakage.**

$$W_{SHO} = \sqrt{\frac{\frac{2}{\rho}\Delta P - [\eta R_i \omega]^2 (\bar{r}^2 - 1)}{\xi_{SH} + [1 + \xi_{SE}](\bar{c}\bar{r})^2}}$$

$$P_{SHO} = \Delta P - \frac{\rho}{2}(1 + \xi_{SH}) W_{SHO}^2$$

$$W_{SHL} = \bar{r} \; W_{SHO}$$

$$U_{SHL} = \bar{r} \; U_o = \bar{r} \; \eta \; R_i \; \omega$$

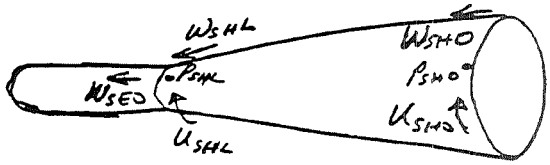

$$P_{SHL} = \left\{ \frac{\frac{2}{\rho}\Delta P - [\eta R_i \omega]^2 (\bar{r}^2 - 1)}{\xi_{SH} + [1 + \xi_{SE}](\bar{c}\bar{r})^2} \right\} \frac{\rho}{2} \bar{r}^2 \left[\bar{c}^2 (1 + \xi_{SE}) - 1 \right]$$

$$W_{SHL} = \bar{r} \; W_{SHO} \;, \quad W_{SEO} = \bar{c} \; W_{SHL} = \bar{c} \, \bar{r} \, W_{SHO}$$

$$\Delta P_{SH} = P_{SHO} - P_{SHL} = \Delta P - \frac{\rho}{2} W_{SHO}^2 \left\{ 1 + \xi_{SH} + \bar{c}^2 \bar{r}^2 (1 + \xi_{SE}) - \bar{r}^2 \right\}$$

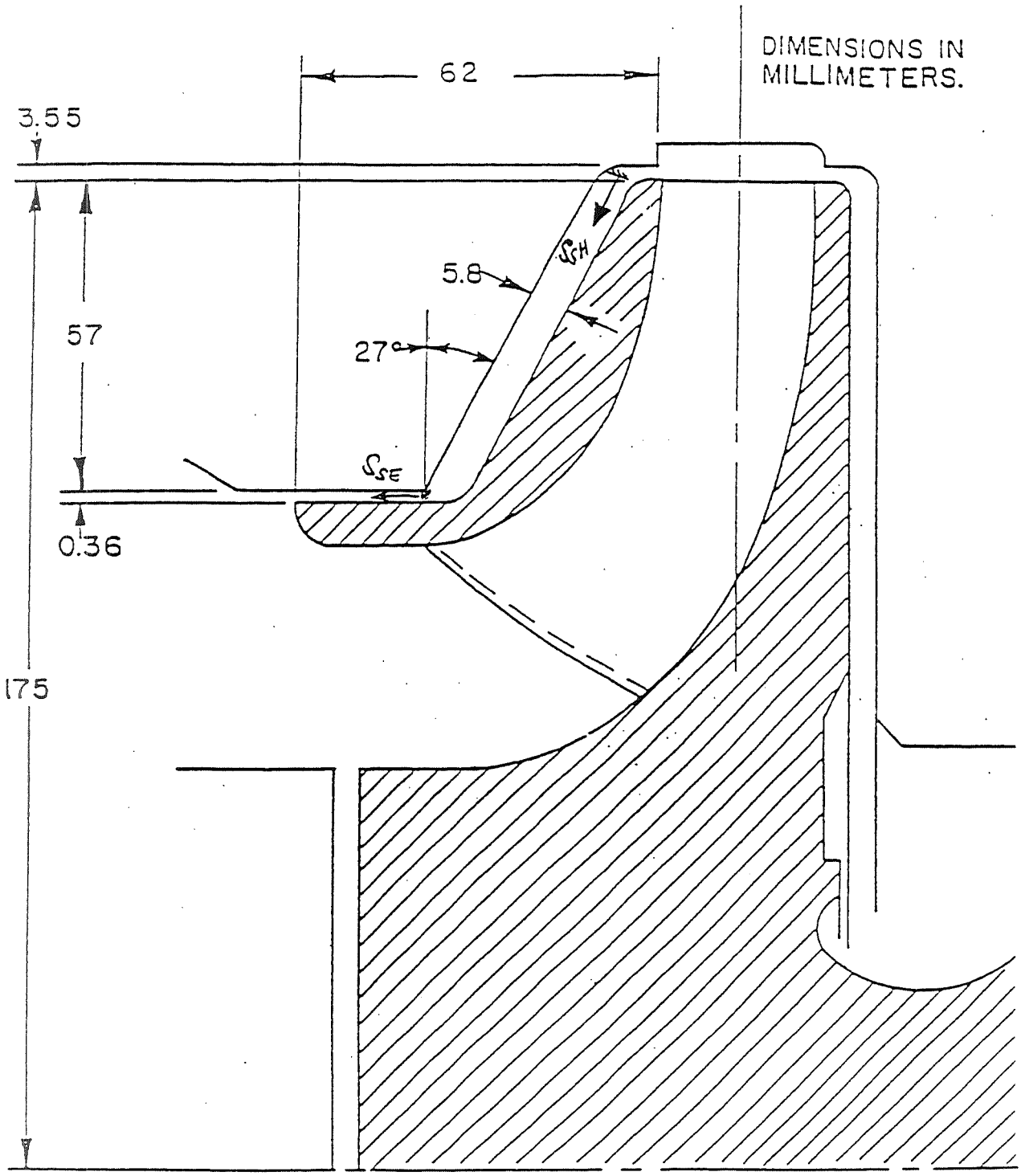

Figure 5 Bolleter Example Impeller Geometry.

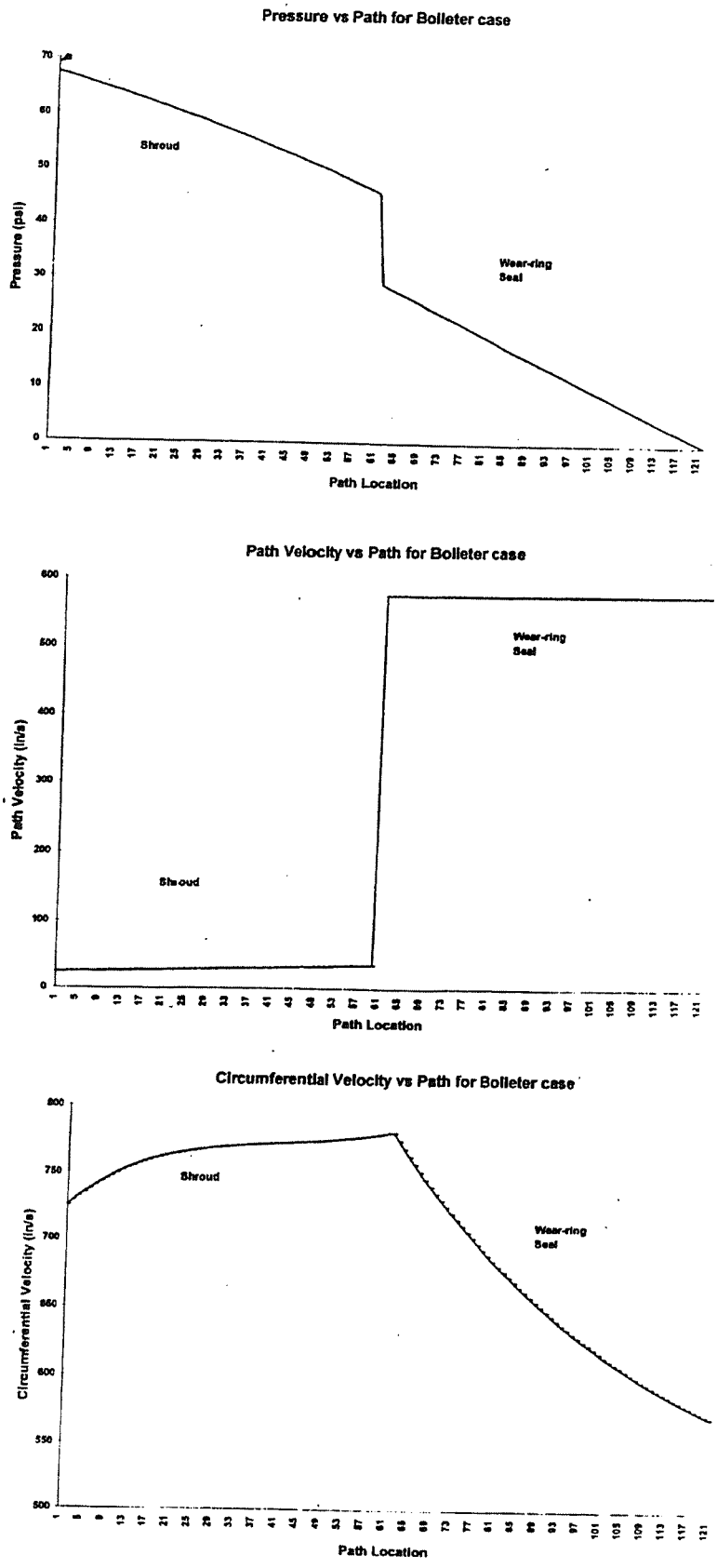

Figure 6 **Steady State Pressure and Velocities for Bolleter Impeller Test Case.**

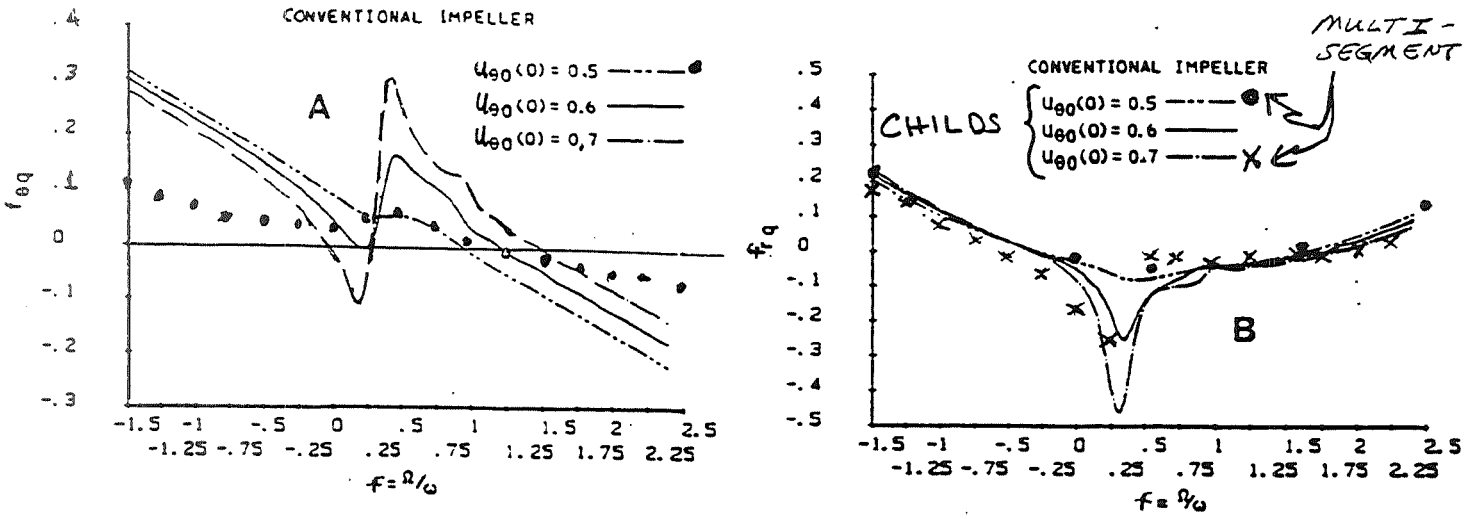

Figure 7 **Circumferential (A) and Radial (B) Impedances - Comparison Between Multi-Segment and Childs [1].**

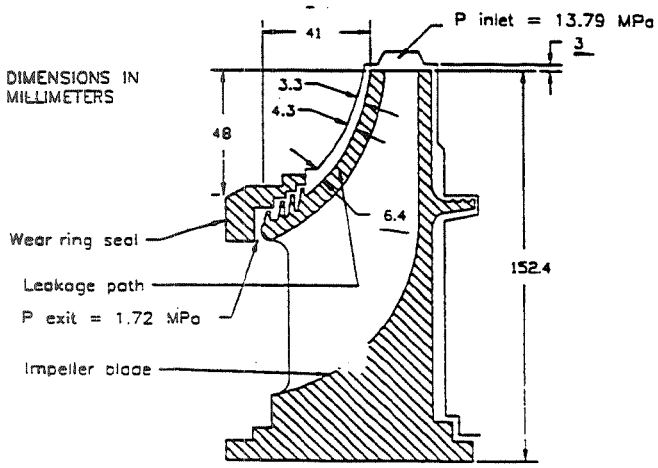

Figure 8

LH_2 SSME HPFTP First Stage Impeller Profile [5]. Model Speed 34,000 rpm.

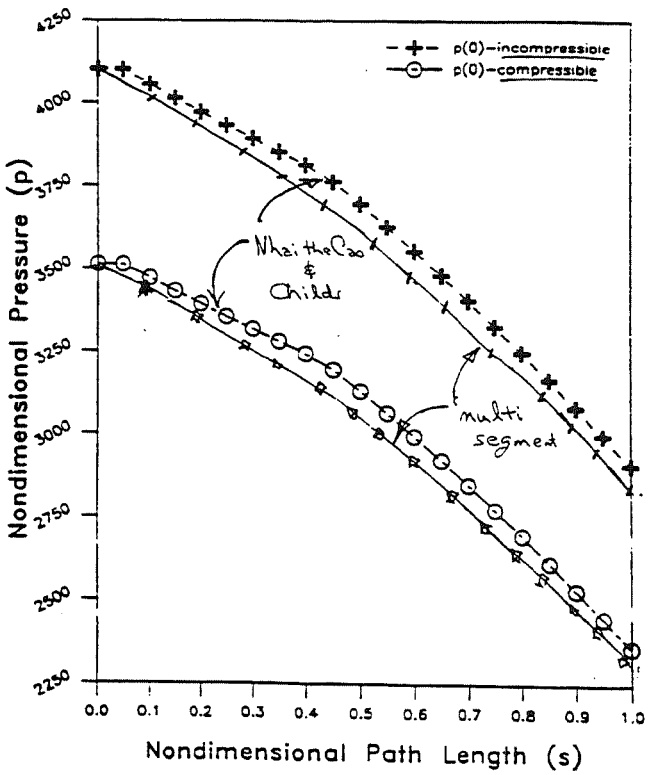

Figure 9

Comparison of Steady State Pressures Nhai the Cao and Childs vs. Two Segment Model ($U_{\theta_0} = 0.7$).

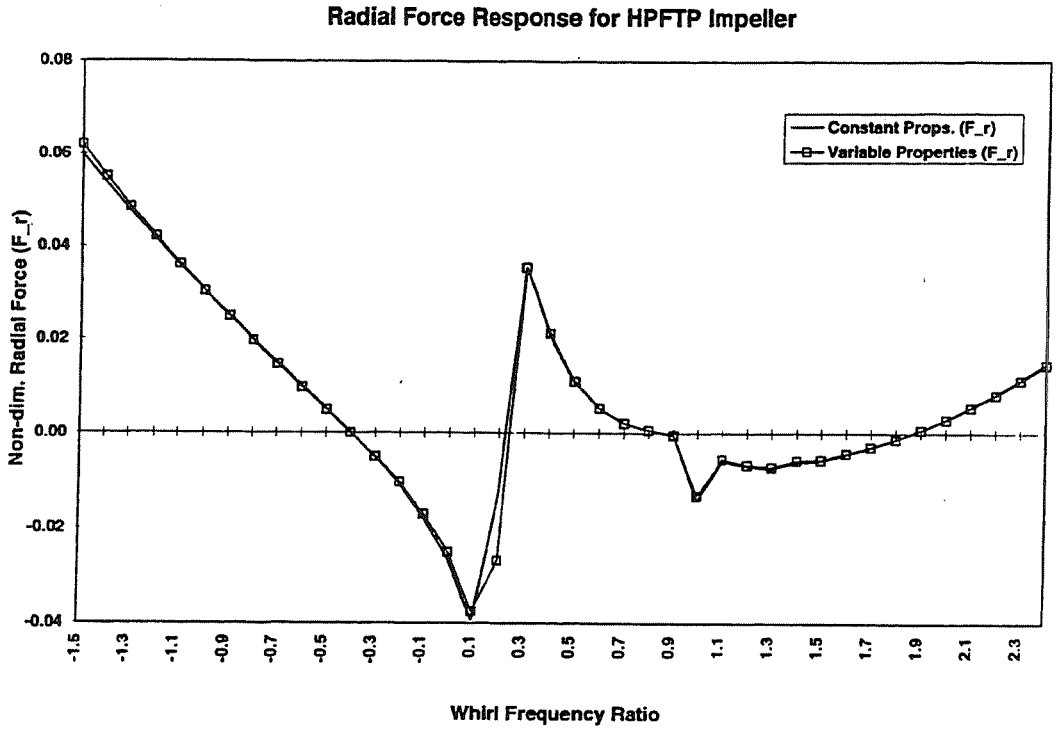

(a)

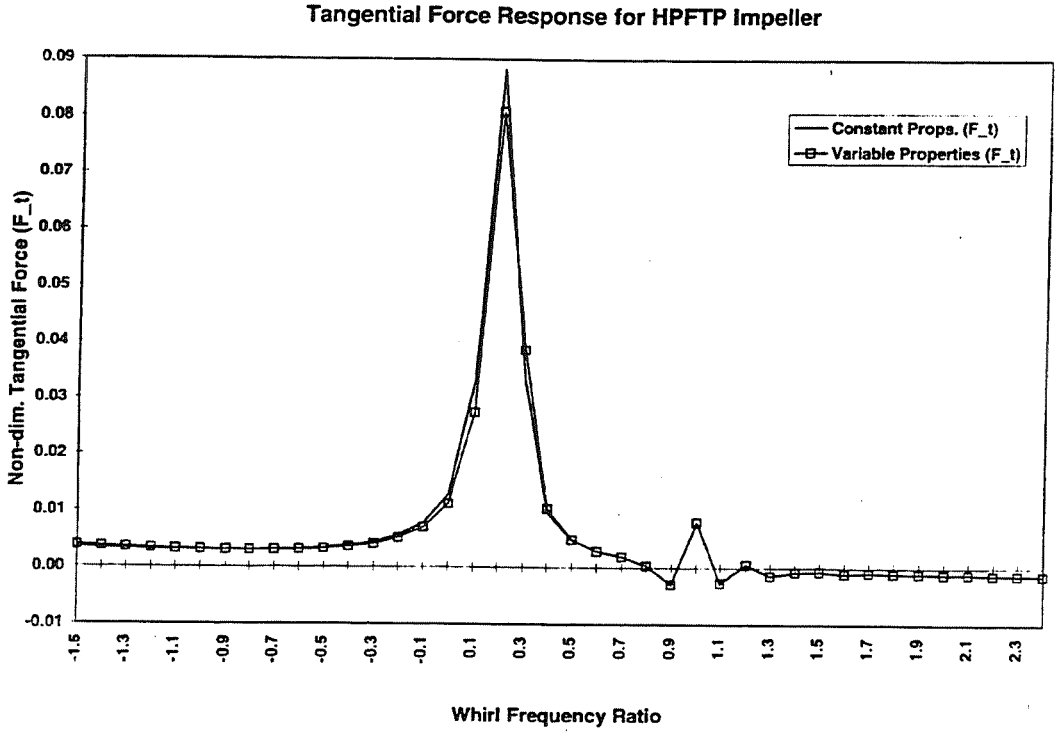

(b)

Figure 10 **Radial (a) and Circumferential (b) Impedance Plots for 1st Stage LH_2 Impeller with 2 Segments Plus Lumped Seal-Discharge Coefficient.**

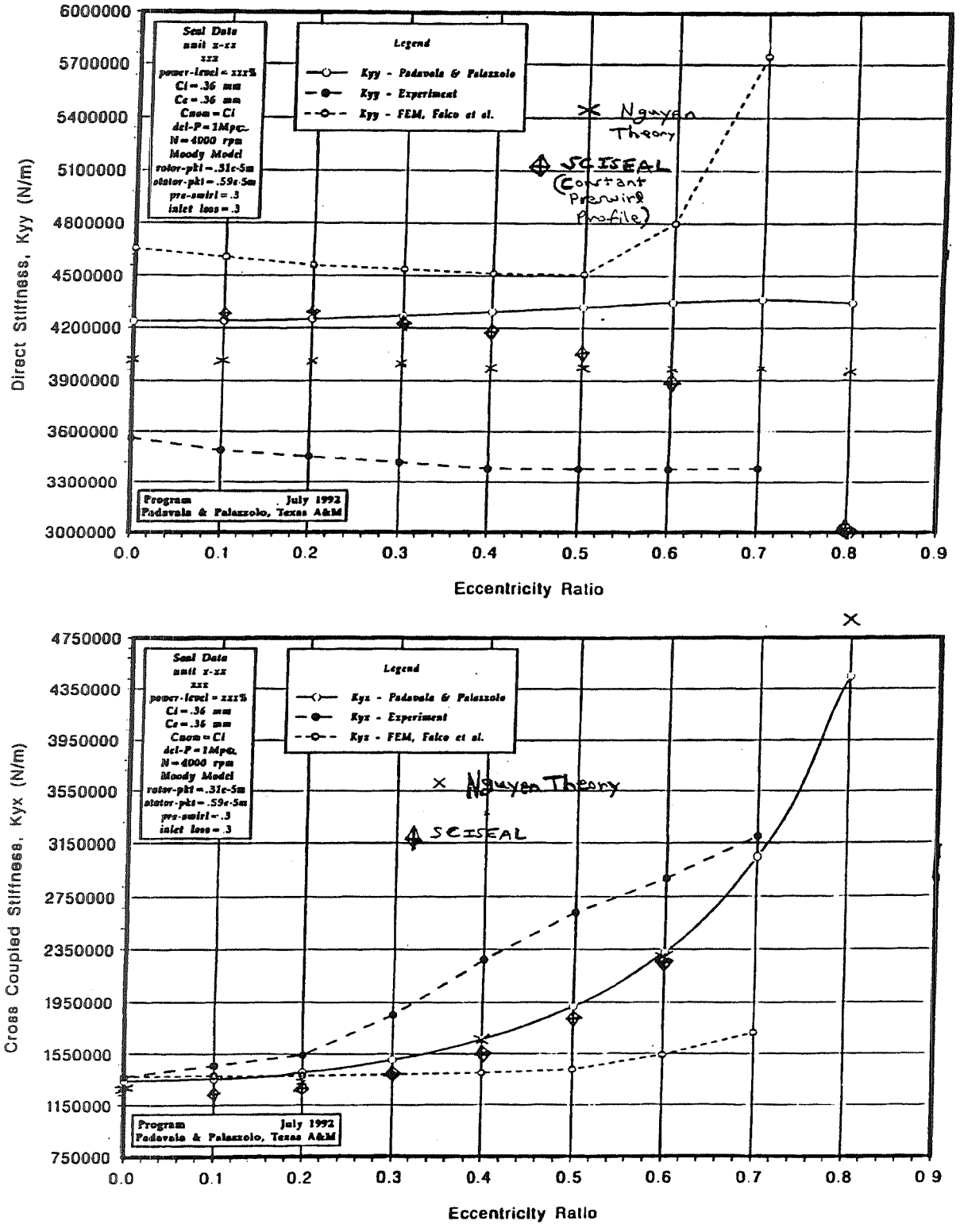

Figure 11 **Comparison of K_{yy} and K_{yx} Coefficients Between SCISEAL, Bulk Flow and Test, for Plain Annular Seal.**

DON'T THIS PAGE

SESSION IV

GENERAL

ROTORDYNAMIC INSTABILITY FROM AN ANTI-SWIRL DEVICE

John Vance and Steven B. Handy
Texas A&M University
College Station, Texas

Abstract

A swirl damper intended for high temperature turbomachinery applications was experimentally investigated for its damping characteristics. The results were disappointing in that only a small amount of damping was obtained. Instead, an instability was produced at a speed which exhibited backward whirl.

The rotor rig that was used exhibited backward whirl over a speed range between two critical speeds. This backward whirl could be prematurely induced by the use of the swirl gas damper. At high damper pressures, the rotor system exhibited an instability. The exact nature of this instability is not known, however, possible causes are presented.

The observations discussed in this paper are also important to those who design swirl brakes or anti-swirl guide vanes for labyrinth seals. The principles involved are similar in that the flow into a labyrinth seal is turned to swirl anti-rotationally as it enters the seal, same as the swirl gas damper.

INTRODUCTION

Current damper design practice for military and commercial gas turbine (jet) engines is the squeeze film damper. This damper uses the lubricating oil as the working fluid. The damper is quite effective but has some limitations. One limitation is the fact that the maximum operating temperature is dictated by the lubricating oil. To significantly increase the efficiency and power output of jet engines, the operating temperatures may need to be raised beyond the capabilities of current lubricating oils. This would then require an alternative damping method to be used. Another limitation to the squeeze film damper is that the damping is not interactive. The squeeze film damper is always "on" when lubrication is required, regardless of the damping requirement. It would be much more favorable to have an interactive system to provide the needed amount of damping on demand. Another limitation of the squeeze film damper is that it must be used in conjunction with the rotor bearings. this limits its possible location to those of the bearing supports. If a node is located at or near the bearing, the squeeze film damper will be ineffective. The ideal damper would be able to be placed anywhere along the rotor. the most desirable location would be the point of maximum vibrational or orbital displacement.

An alternative damping system that could potentially overcome all of the above mentioned limitations is the "Swirl Gas Damper" first described by Brown and Hart at the 1986 Workshop [1]. This damper is independent of the lubricating system and could therefore be used interactively [1,2]. Such a damper would not be limited to the same location as the bearings, but could be placed nearly anywhere along the rotor. The working fluid of the swirl gas damper is compressed air which is readily available from the compressor portion of the gas turbine. The air is injected anti-rotationally to the rotor into an annular gap. This injected air interacts with the vibrating rotor and provides a cross-coupled stiffness rather than a direct damping. The force that results from this cross-coupled stiffness (which acts in the same direction as direct damping) could substantially reduce the synchronous and sub-synchronous response due to unbalance, instabilities, or operating through critical speeds [3].

This paper will discuss test results of a swirl gas damper, designed, built, and tested at Texas A&M University. Although the damping results are disappointing, rotordynamic instabilities occurred during the testing which should be of interest to those employing anti-swirl devices to stabilize labyrinth seals.

THEORETICAL BACKGROUND

The swirl gas damper uses high velocity air injected opposite to the direction of rotation.

Theoretically this velocity U will change as the air travels around the annular gap with the rotor offset to the stator (Figure 1). The velocity will increase as the gap closes and decrease as the gap opens. The offset is due to the vibration or orbit resulting from rotor imbalance or instabilities. The fluid friction force of the air on the rotor is proportional to the square of the velocity and tangential to the surface of the rotor. If the friction force is summed over the surface of the rotor, the total force is perpendicular to the offset displacement. This cross-coupled force acts in the same direction as a direct damping force and will provide damping [3]. This damping would be most effective for forward whirl (direction of rotation) and less effective or even deleterious for backward whirl because the direction of the swirling air is backward driving.

Brown and Hart of Heriot-Watt University developed a simple mathematical derivation to determine the direct stiffness (K_{xx} and K_{yy}) and cross-coupled stiffness (K_{xy} and K_{yx}) associated with a swirl gas damper [1]. Their results were:

Direct stiffness:

$$K_{xx} = K_{yy} = \frac{\pi\rho\bar{u}^2RL}{C} \tag{1}$$

Cross-coupled stiffness:

$$K_{xy} = -K_{yx} = f\frac{\pi\rho\bar{u}^2RL}{C} \tag{2}$$

Where ρ is the density of the gas (air in this case), **R** is the radius of the rotor, **L** is the length of the damper axially, **C** is the radial rotor-stator clearance, f is the friction factor, and $\bar{u}$ is the mean air velocity.

As can be seen from the equation above, three of the variables that determine the cross-coupled stiffness values are the radial rotor-stator clearance, friction factor and the mean air velocity. The mean air velocity will be a function of the air pressure used to inject the swirling air. The friction factor will be a function of the surface finish of the rotor and, to some extent, the air velocity (or Reynolds Number). The principle parameters evaluated in this research were the clearance, damper pressure, and rotor surface finish.

The friction factor and air velocity are difficult to quantify in this case. Therefore, it is desired to simplify the task by developing a relationship of terms that are more easily obtainable. The following derivation will demonstrate one way to accomplish this.

The shear of air (τ) can be written as:

$$\tau = \tfrac{1}{2}\rho\bar{u}^2 f \tag{3}$$

The surface area (A) of rotor is:

$$A = 2\pi RL \tag{4}$$

Total shear force (F) is:

$$F = \tau A \tag{5}$$

By substituting equations 3 & 4 into 5 gives:

$$F = f\pi\rho\bar{u}^2 RL \tag{6}$$

Torque on the rotor (T) can be written as:

$$T = FR \tag{7}$$

Or by substituting equation 6 into 7 gives:

$$T = f\pi\rho\bar{u}^2 R^2 L \tag{8}$$

Solving for friction factor (f) gives:

$$f = \frac{T}{\pi\rho\bar{u}^2 r^2 l} \tag{9}$$

The cross-coupled stiffness equation from Brown & Hart is (equation 2 above):

$$K_{xy} = f\frac{\pi\rho\bar{u}^2 RL}{C} \tag{10}$$

Substituting equation 9 into 10 gives:

$$K_{xy} = \frac{T}{RC} \tag{11}$$

Cross-coupled stiffness is then a function of applied torque (T) by the damper radius (R), and the

clearance (C). There is no need to determine the exact velocity ($\bar{u}$) or friction factor (f).

The cross-coupled stiffness can be expressed as an equivalent damping (C_{eq}) for a particular frequency (ω) by the following relationship:

$$C_{eq} = \frac{K_{xy}}{\omega} \tag{12}$$

ROTOR RIG AND DAMPER

An existing rotor rig (figure 2) was modified by the addition of removable rotor sleeves. These sleeves were changed to alter the surface finish and radial clearance by using rotor sleeves with different diameters. The three radial clearances to be tested were: rotor #1 .020", rotor #2 .040", and rotor #3 .060". The rotor was 26" long and weighed 66 lbs.

It was later discovered that rotor #1 suffered from a static instability. This instability was a vibration induced at very low damper pressures (2-4 psig) without the rotor turning (static). This same phenomena is known as pneumatic hammer in gas bearings [4,5].

This instability necessitated that Rotor #1 be modified so the rotor was tapered from a .020 clearance at the center of the damper to .050 at each end. This resulted in an average clearance of .035". The static stability range was then increased to 22 psig.

Rotor #2 also showed a static instability at 15 psig. This static instability was not affected by the surface finish of the rotor. The knurled rotor #3 showed only a slight static instability at 25 psig. The smooth rotor showed no instability up to the maximum supply pressure of 30 psig.

Once rotors #2 and #3 were tested with a smooth surface they were refinished with a knurled surface and cut down to maintain the original diameter and clearance. These rotors were then tested in the same manner as before.

The damper (stator section) was manufactured from two 1/4" thick steel end plates separated by three rows of 1/2" thick aluminum nozzles (figure 3). Each row was made up of 8 pieces. The nozzles were manufactured to direct flow in a tangential direction. The resulting damper/stator width was 2.0" and the diameter was 6.540". The nozzles were designed to have an .020" opening. Through the manufacturing process the opening ended up being .035". This may be the reason for the static instability of rotor #1 with its .020", rotor/stator clearance. The plenum chamber was enclosed by aluminum walls. The plenum chamber was fed by two 1/2 pipe fittings fitted into the steel end plates. A 0-30 psi Bourdon pressure gage was used to measure the damper plenum pressure.

The damper (stator section) was attached to the rig base plate and could be adjusted vertically and horizontally (both perpendicular to the rotor axis). The axial adjustment was achieved by loosening the rotor and moving it to the proper position before retightening. The lengths of the cantilevered

supports were adjusted to provide high stiffness at the air turbine drive end and low stiffness at the damper end. This was done to ensure rigid mode vibrations and critical speeds at low shaft speeds (approximately 2200 RPM), with the larger amplitudes at the damper.

The rig was fitted with three proximity probes, one to provide for a key phase signal and two for orthogonal displacement measurements.

Computer simulations determined that the rotor would whirl in rigid body modes through the first two critical speeds. The first two split critical speeds were in the test speed range (3000-1500 RPM), and the node points were just beyond the turbine end of the rig. The term "split critical speeds" refers to the fact that the critical speeds are due to the asymmetry of the support stiffness. Figure 4 shows the mode shape and node location. The approximate location of the node point was verified by rap tests.

It should be noted that asymmetrical support stiffnesses will result in two critical speeds in close proximity to each other. The rotor will have the tendency to whirl in the backward direction at speeds between the critical speeds [3]. This was found to be the case with this rotor.

INSTRUMENTATION AND SIGNAL ANALYSIS

The HP signal analyzer was configured to: ***Instrument Mode:*** *2 Channel, Order Analysis;* ***Frequency:*** *Min RPM = 1500, Max RPM = 3000, Track ON;* ***Trace Coordinates:*** *Linear Magnitude, Y-Units Peak;* ***Measurement Data:*** *Order Tracking Channel 1* for channel 1 measurements, *Order Tracking Channel 2* for channel 2, *Math Function* for modulus as defined below. This set-up would then display and record the synchronous response vs RPM. Using the *Function* option, a function was defined which results in the modulus M vs RPM. The modulus is the absolute magnitude of the response as defined below, where CH_1 and CH_2 are the response of channels 1 and 2 respectively.

$$M = \sqrt{CH_1^2 + CH_2^2} \tag{13}$$

Using the Bently-Nevada DVF 2 the run-out was removed (using the NULL) to less than .1 mil_{p-p} for both channels in most cases, and at worst .2 $mils_{p-p}$ in channel 2 while 0 $mils_{p-p}$ in channel 1. This run-out null was consistent from 200 to 500 RPM.

TEST PROCEDURE

The tests consisted of coast-downs from approximately 3000 RPM through both critical speeds to approximately 1500 RPM. During the run, the rate of coast down was maintained at less than 3 RPM per second. It was necessary to use the air turbine to sustain this deceleration rate. If the rotor

decelerated much faster than this, the response amplitude was reduced.

The test was performed at a constant damper pressure, for each rotor with a particular surface finish and clearance. The damper pressure was changed for the next test until runs had been performed from 0 psig to the maximum possible. This maximum was determined by either the maximum air supply available (approximately 10 to 12 psig) or the instability of the rotor (rotor crash). The test pressure was increased by 1 psig to 8 psig and then by increments of 2 psig. It was hoped to test rotors configurations above 13.1 psig to see the effect of sonic air velocities, but this would only have been possible for rotor #3 as all others crashed below this pressure.

A video recording was made of each of the tests which recorded the whirl orbit from the oscilloscope and the RPM reading from the DVF 2 along with the unbalance, damper pressure, and analyzer data file name information. After the test was run, the start and end backward whirl and its associated RPM readings were determined by reviewing the video tape. The *start backward whirl RPM* is defined by the point of planar motion as the whirl went from forward to backward and visa versa for *end backward whirl RPM.*

Once a series of tests were completed on a particular rotor set-up, torque tests were performed. This test began by running the rotor up to 3000 rpm. The time (Δt) required for the rotor to run-down to 1500 rpm at zero damper pressure was recorded. An average frictional torque (T_f) for the run-down range could then be calculated by:

$$T_f = I\frac{\Delta\omega}{\Delta t} \tag{14}$$

Where $\Delta\omega$ is 1500 rpm (3000 - 1500).

This same procedure was used to measure the total torque (T_T) at damper pressures in steps of 2 psi. The applied torque (T) of the damper on the rotor needed to determine the cross-coupled stiffness in equation 11 was found by:

$$T = T_T - T_f \tag{15}$$

The cross-coupled stiffnesses values vs damper pressure for all five rotor configurations were then plotted once all test runs had been completed. Using equation 12 the cross-coupled values were converted to equivalent damping at an assumed frequency equal to 2000 rpm. These results were also plotted. Since modified rotor #1 did not have a constant radius, an average radius value was used to calculate the cross-coupled and equivalent damping values. The plots show cross coupled stiffness and equivalent damping increasing with plenum pressure and with surface roughness. Maximum K_{xy} was 28 lb/in.

DISCUSSION OF RESULTS

The goal of this research was to identify damper configurations that provide significant damping or cross-coupled forces. Only one damper configuration provided an appreciable amount of damping. This was modified rotor #1 which reduced the amplitude to 52% of the zero pressure modulus (figure 5).

It should be noted that even though the modulus response was nearly cut in half, the amount of added damping was not large. From the shape of the response it can be seen that the system has very little inherent damping. Only a small amount of additional damping or cross-coupled force is then required to cut the response in half. Figure 6 shows how the peak response varied with plenum pressure.

As was expected, this rotor did exhibit backward whirl while running between the split critical speeds. At zero or low damper pressures, the rotor would begin to whirl in the backward direction soon after crossing the second critical speed during the coastdown. The whirl would remain backward until just before the first critical speed, where it would switch back to forward whirl. What was not necessarily expected was the fact that the swirl damper induced and magnified the backward whirl effect as defined below.

When reviewing the video tape, it was noticed that at low damper pressures the orbit shape would remain fairly elliptical in shape when running between the critical speeds. As the damper pressure and corresponding damping effect increased, the orbit would become more circular in shape. This is what is meant by "magnifying the backward whirl effect." This does not mean the amplitude of the orbit increased. In fact, most often the amplitude was reduced except when the rotor went unstable.

It should be noted that the backward whirl could be induced as shown in figures 7, 8, and 9, when comparing the start of backward whirl to the second critical speed. Normally, the backward whirl would begin after crossing the critical speed. At higher damper pressures, the backward whirl could be induced before reaching the critical speed. It should also be noted that the backward whirl could be prolonged to a point after the first critical speed at higher pressures as seen in figure 9.

Another peculiar effect was observed just before a rotor crash. Figure 10 shows how the keyphasor voltage pulse affected the orbit trace on the oscilloscope. As viewed on the video, the keyphasor spot would begin to rotate around the orbit trace violently in the CW direction just before the rotor went unstable and crashed. Because the direction is the same as the backward whirl direction, it might be proper to think of this as a backward whirl induced instability. However, the orbit decreased in magnitude as pressure increased before the instability was encountered. If the damper induced the instability by aggravating backward whirl, wouldn't the amplitude increase as the pressure increases? One possible answer to this question is that, perhaps, the instability was not from

inducing backward whirl but was due to the same forces that produced the static instability or pneumatic hammer. If this is true, it does not explain the phenomena of the rotating key phaser signal. For further study of pneumatic hammer references 6, 7, and 8 are given.

In general, damping was increased as the damper plenum pressure increased (only up to the instabilities), as the rotor surface roughness increased, and as the rotor/stator clearance decreased. If the problem of the static instability could be solved, then a significant increased in damping might be realized. In that case, rotor #1 would not need the modifications that were required for stability and could have made use of the smaller clearance and knurling.

As a point of interest, the air flow, exiting the gap at each end of the damper, flowed in nearly opposite directions depending on the position in the gap. As the flow exited close to the rotor, the flow was in the direction of the rotor rotation and slightly axial. When the flow exited the damper gap close to the stator, the flow was in the anti-rotational direction and slightly axial. As the damper pressure was increased and, subsequently the mass flow increased, the direction of the air flow was changed by the increase of the axial component. The axial flow component was reduced when the rotor speed was increased. It was also noted that the high velocity injected air hugged the stator surfaces when the rotor was absent.

The limited success of this damper can be explained partially by the fact that the rotor tended to whirl in the backward direction, which was due to the asymmetric support stiffness. This research was intended for application in gas turbine engines. These bearing support systems are symmetrical on paper, but often turn out to have asymmetric stiffness.

CONCLUSIONS

The following conclusions can be drawn from this research:

1) Only small amounts of damping are obtainable from the tested configurations.
2) Damping increased with an increase of supply pressure up to the point of instability.
3) Damping increased with a decrease in rotor-stator clearance.
4) Damping increased with the knurled rotor surface over that of the smooth rotor surface.
5) Pneumatic hammer is a problem with this swirl gas damper design.
6) Pneumatic hammer is reduced by increase in rotor-stator clearance.
7) Backward whirl is induced and magnified by the swirl gas damper. Two of the three tested configuration crashed while executing backward whirl with the anti-swirl device active.
8) The swirl gas damper increased the critical speeds.
9) Damping performance would be improved for a forward whirling, circular orbiting rotor.

REFERENCES

1. Brown, R.D., Hart, J.A., "A Novel Form of Damper for Turbo-Machinery," *Rotordynamics Instability Problems in High Performance Turbomachinery,* Texas A&M University, NASA Conf. Publ. 2443, 1986, pp. 325-347.

2. Muszynska, A., Franklin, W.D., Bently, D.E., "Rotor Active 'Anti-Swirl' Control," *Transactions of the ASME Journal of Vibrations and Acoustics,* April 1988, pp. 215-222.

3. Vance, J.M., *Rotordynamics of Turbomachinery,* John Wiley & Sons, New York, 1988, pp. 130-132.

4. Vohr, J.H., "The Design of Hydrostatic Bearings," *Fundamentals of the Design of Fluid Film Bearings,* ASME, 1979, pp. 1-13.

5. Grassam, N.S., Powell, J.W., *Gas Lubricated Bearings,* Butterworths, Washington, D. C., 1964.

6. Licht, L., Elrod, H., "A Study of the Stability of Externally Pressured Gas Bearings," *ASME Journal of Applied Mechanics,* June, 1960, pp. 250-258.

7. Mori, H., Mori, A., "On the Stabilizing Methods of Externally Pressurized Thrust Gas Bearings,"*ASME Journal of Lub. Tech.,* July, 1969, pp. 283-290.

8. Blndeel, E., Snoeys, R., Devrieze, L., "Dynamic Stability of Externally Pressurized Gas Bearings,"
ASME Journal of Lub. Tech., October, 1980, pp. 511-519.

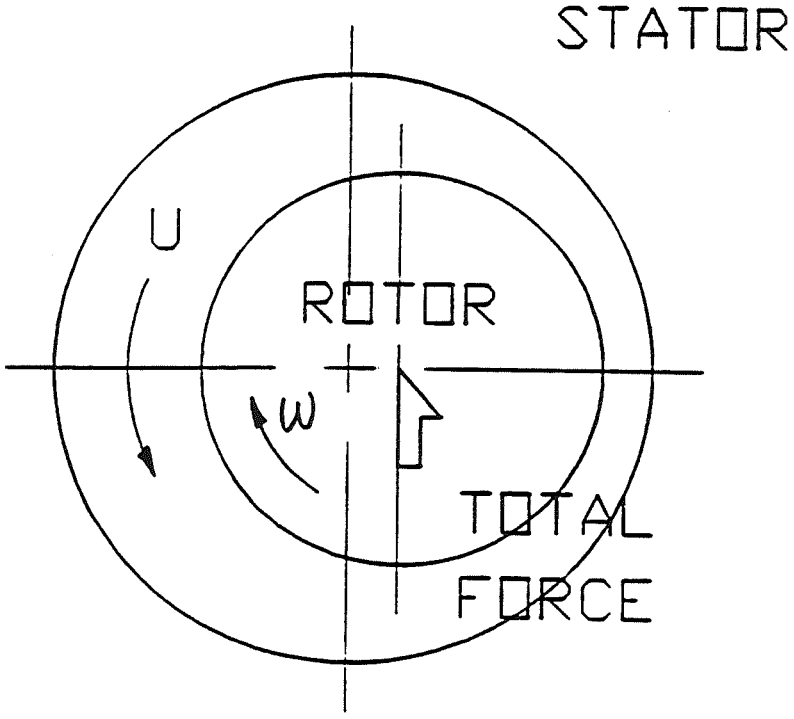

Figure 1: Annular gap geometry between rotor and stator

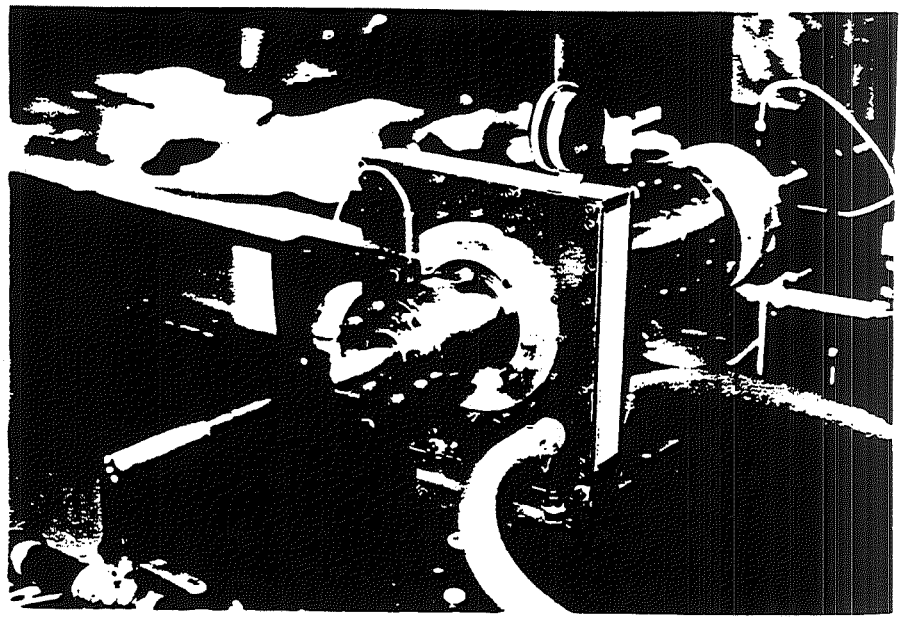

Figure 2: Photograph of the test rig

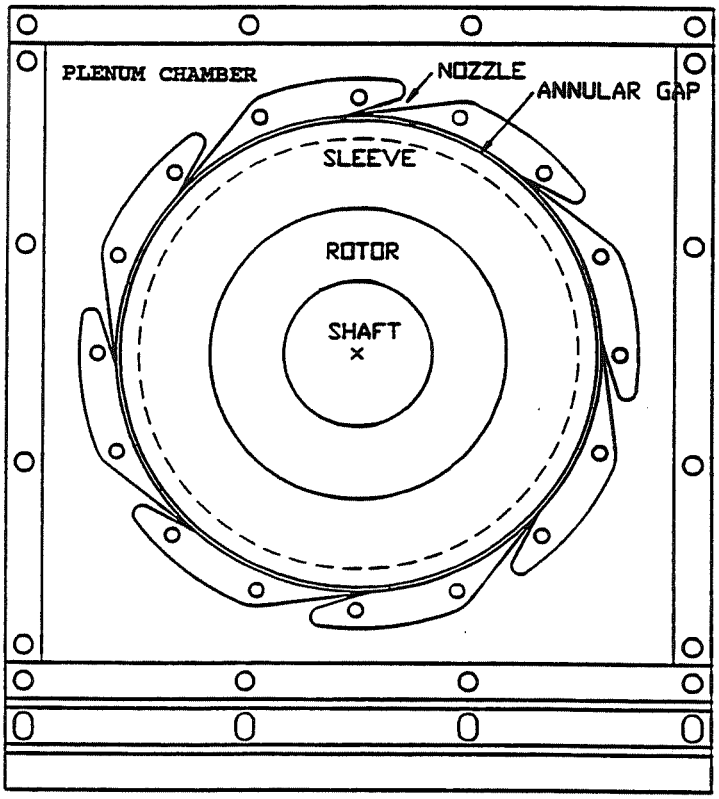

Figure 3: Cross section of the damper

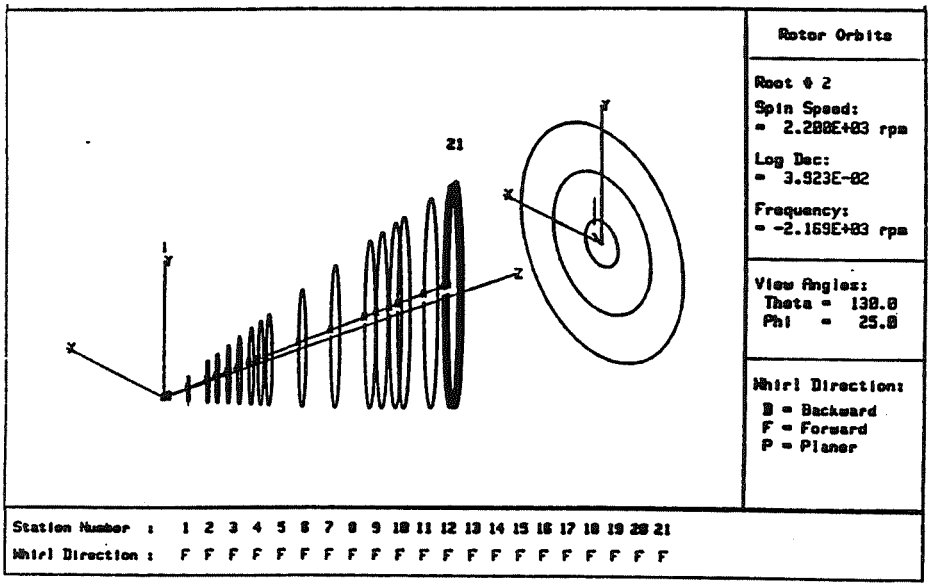

Figure 4: Mode shape of the first critical speed

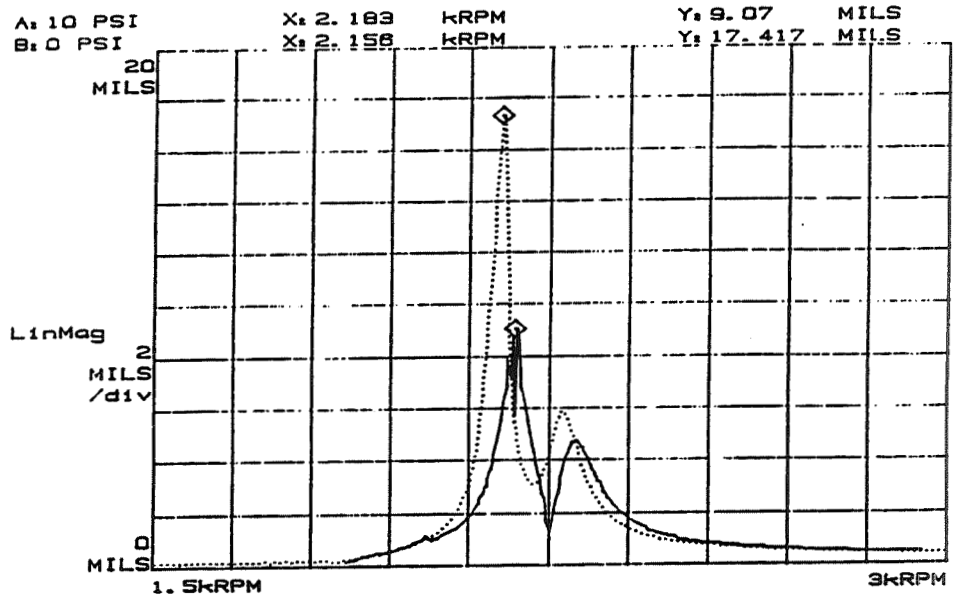

Figure 5: Rotor #1, coastdown amplitude at 10 psi

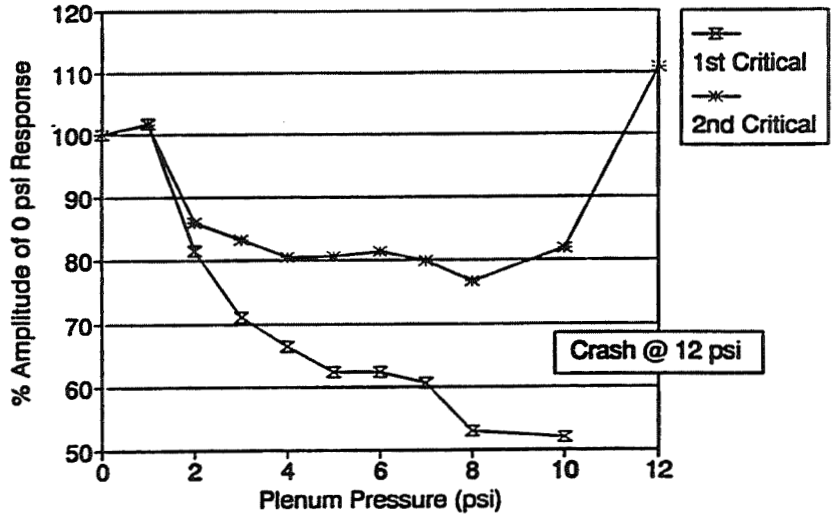

Figure 6: Rotor #1, coastdown amplitude vs, plenum pressure

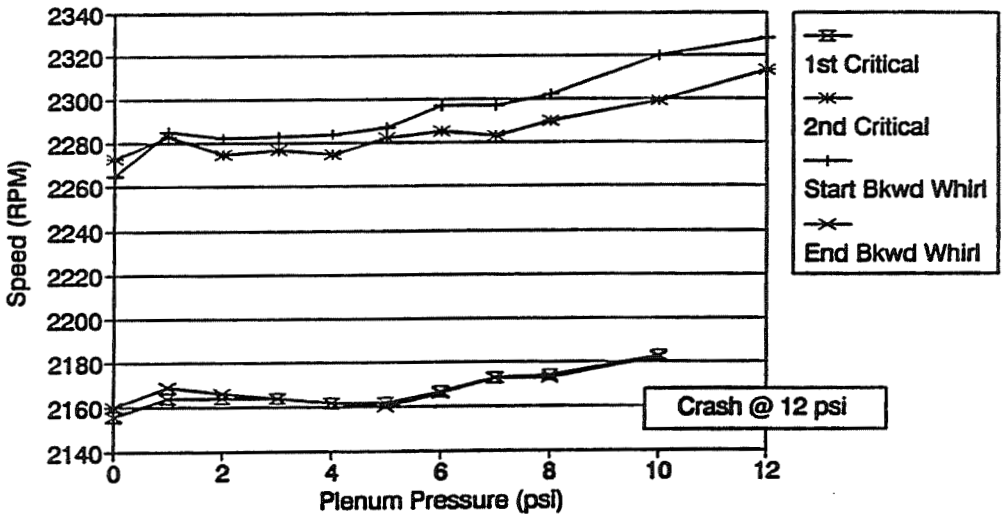

Figure 7: Rotor #1, backward whirl and critical speed RPM vs. pressure

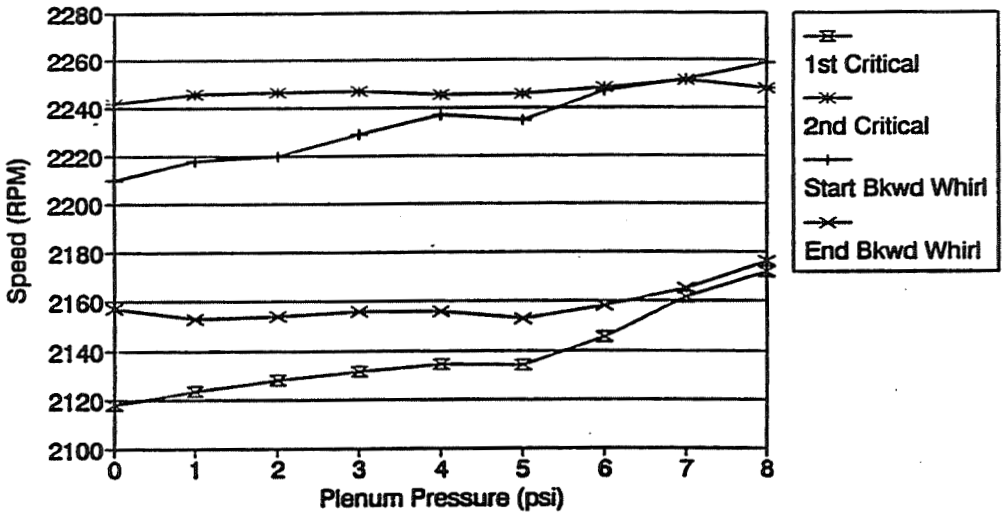

Figure 8: Smooth rotor #2, backward whirl and critical speed rpm vs. pressure

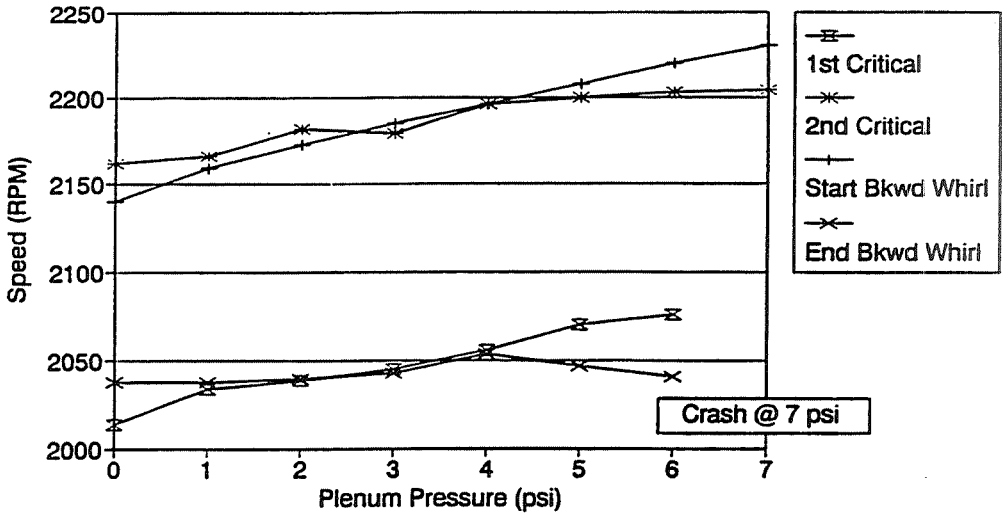

Figure 9: Knurled rotor #2, backward whirl and critical speed RPM vs. pressure

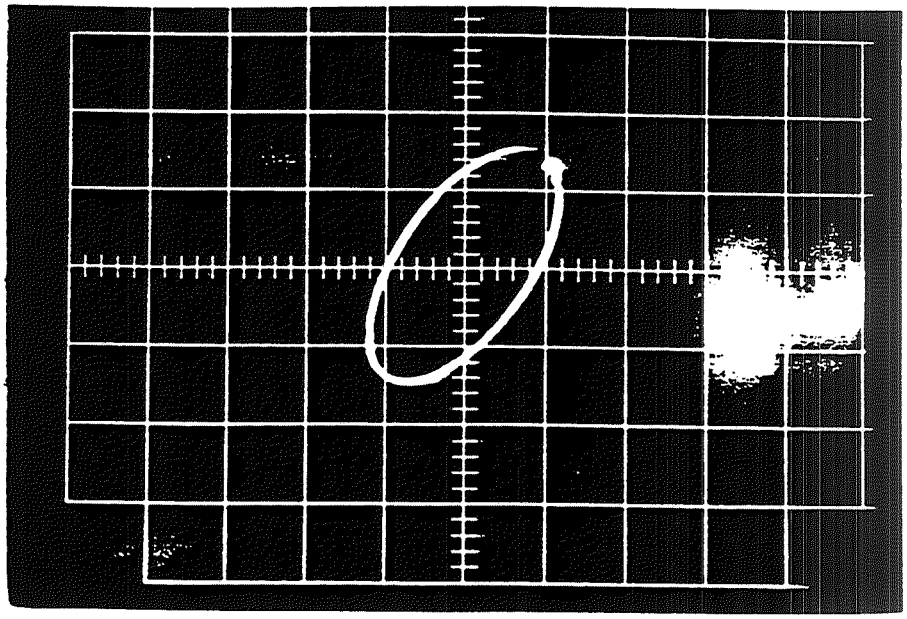

Figure 10: Orbit trace with keyphasor spot

TURBOCHARGER ROTORDYNAMIC INSTABILITY AND CONTROL

Sunil N. Sahay and Gerry LaRue
AlliedSignal Turbocharging Systems
Torrance, California

ABSTRACT

Turbochargers operate over a wide range of speed and lubricating oil inlet conditions. The speed varies between zero to as high as 230,000 rpm, and the oil inlet pressure and temperatures range from 15 to 75 psi, and 0 to 250 degrees F. Due to aerodynamic and heat transfer considerations, a great majority of turbochargers for automotive application use a "double overhung" rotor-bearing configuration with radial flow wheels. Typically, these turbochargers use "fully floating" (free to rotate), plain cylindrical bore bearings, which are subject to various subsynchronous instabilities, such as oil whirl and resonant whip. Experience shows that turbochargers can run satisfactorily with a limited amount of bearing instability, provided the whirl orbit does not exceed a certain percentage of the bearing clearance space. Accurate analytical prediction of bearing instability onset and whirl orbit magnitude is very difficult at the present time due to the nonlinearity and complexity involved.

The well-known solutions for controlling oil film instability such as non cylindrical bore, tilting pad, and ball bearings are NOT very attractive due to high manufacturing cost. However, the use of a "semi floating" bearing (free to nutate but constrained from rotation) with a plain cylindrical bore, can offer a cost effective solution. Compared to fully floating bearings, the unstable whirl orbit can be reduced by more than 35%. The future work at the authors' company involves the use of a Bearing Test Rig to better understand the nature of these instabilities, and to experimentally obtain the bearing characteristics for use in a Rotordynamics computer program.

INTRODUCTION

Many technical papers have been published discussing the nonlinear behavior of rotors supported in hydrodynamic bearings (see, for example, reference 1). In small turbochargers, rotor behavior is particularly complex because they typically use either fully floating or semi floating bearings that have two hydrodynamic oil films in series at each support location. The fully floating bearing, in particular, is generally unstable in the sense of exhibiting subsynchronous whirl for most operating conditions, yet this design may be perfectly acceptable from a durability standpoint. The real issues are: is a stable limit cycle achieved, and is it of an acceptable magnitude? This continues to be a difficult question to answer by purely analytical means and so an empirical approach is necessary. Work is now underway at AlliedSignal to develop a test rig to better understand the instabilities and to generate data for an improved analytic model.

Numbers in bracket designate References at the end of the paper.

NOMENCLATURE:

c	=	diametral clearance	N_r	=	floating ring speed
D	=	journal diameter	N_s	=	shaft speed
L	=	journal length	W	=	bearing load
$N_{inner,\ eff}$	=	inner film effective speed	ε	=	eccentricity ratio
N_j	=	journal speed	Λ	=	load capacity number
N_{load}	=	load speed	μ	=	oil viscosity
$N_{outer,\ eff}$	=	outer film effective speed			

TURBOCHARGER SIZE RANGE

One of the challenges in controlling instabilities is the wide size range of turbochargers currently being produced. Figure 1 illustrates the physical size of our smallest GT12 turbo, and largest TV92. Compressor rotor sizes in these units range from 38mm to 141mm, and journal diameters from 6mm to 22mm. Maximum speeds range from 230,000 rpm, for the smallest, to over 70,000 rpm for the largest. In terms of manufacturing tolerances, however, this size range is quite small, with the result that the smallest, most high speed turbochargers must be made with essentially the same tolerances as the largest units. This means that the bearing clearance tolerances of the small turbochargers are relatively large. This presents a difficult task to find a range of inner and outer clearances that will have adequate stability in the "four corners" shaft motion tests which all turbochargers must pass. This test is described in detail in the "shaft motion" section.

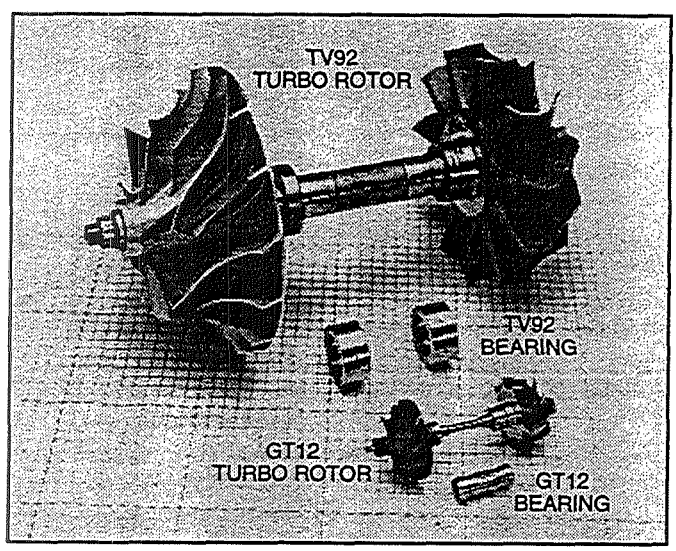

Figure 1. Smallest (GT12) and largest (TV92) AlliedSignal production turbochargers

ROTORDYNAMICS ANALYSIS

As with any high speed rotating machinery, the design of the rotor bearing system of a turbocharger starts with critical speed analysis. Undamped critical speeds are calculated parametrically for a range of expected support stiffness using a Finite Element based rotordynamics program (2). Automotive turbochargers are variable speed machinery and at their maximum operating speed, they run between the second and the third critical speeds (see figure 2). The mode shape associated with the first critical speed is a rigid body "double conical" mode. The mode shape for the second critical speed is a 'bent cantilever' mode with major bending taking place at the compressor end of the rotor. The third critical speed has the classical first bending mode like a 'bow'. These mode shapes are shown at figure 3. **The design goal is to have the maximum operating speed sufficiently below the third critical speed.** After the critical speed calculations, an unbalance response calculation is performed. The rotor and bearing parameters are varied until the unbalance response is reduced to an acceptable level based on previous successful designs. Figure 4 is a typical unbalance response curve.

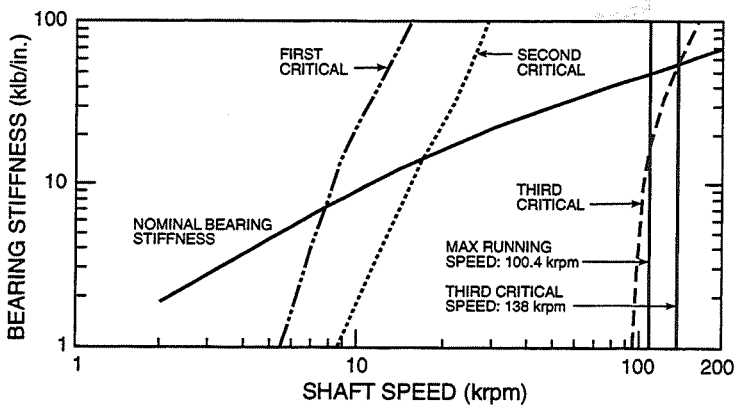

Figure 2. Undamped critical speed map

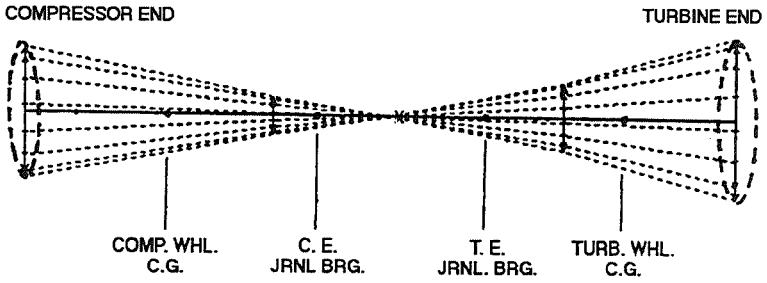

Figure 3a. Rotor mode shape at first critical speed

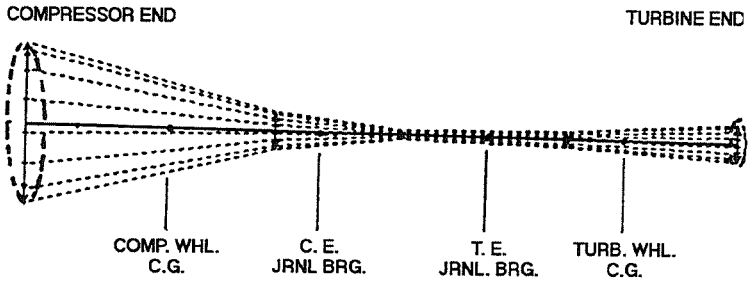

Figure 3b. Rotor mode shape at second critical speed

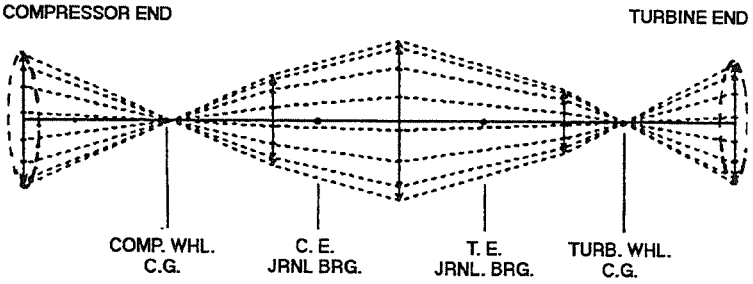

Figure 3c. Rotor mode shape at third critical speed

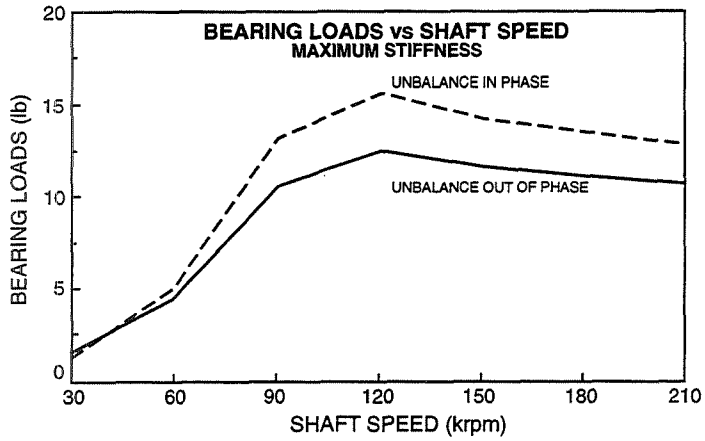

Figure 4. Unbalance response at the bearings

BEARING DESCRIPTION

Turbochargers use three types of bearings: "fully floating" plain bore journal bearings, "semi floating" plain bore journal bearings and ball bearings. These are shown in figure 5. The fully floating bearings are the most common due to simplicity of design and low cost. These are bearings with two hydrodynamically generated oil films in series, i.e., an inner oil film and an outer.

The semi floating bearings have an inner hydrodynamic oil film backed by an outer squeeze film damper. The ball bearings also have an outer squeeze film damper. In both types, the damper is not sealed. The semi floating bearings are the next most widely used bearings, especially when the bearing orbit limits are not met by using the fully floating bearings. The ball bearings are the least used bearings due to their cost but they have the best stability and the lowest bearing power loss.

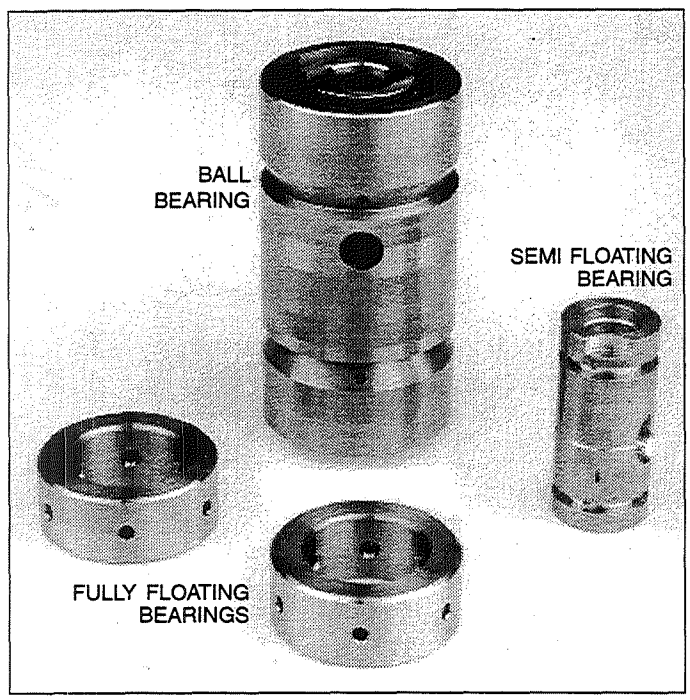

Figure 5. Types of bearings used in AlliedSignal turbochargers

SHAFT MOTION

Shaft motion tests are conducted to qualify a new rotor bearing system for production. Most turbochargers use the double overhung rotor bearing design with the compressor and turbine wheels overhung on either side of the inboard bearings (see figure 6). The overhang on each side is as large as the bearing span. Since the turbochargers rotors are supercritical and run on cylindrical bore sleeve bearings, they are prone to oil whip. Normally, this oil whip results in a "limit cycle" subsynchronous rotor orbit (3), superimposed on a synchronous orbit. During shaft motion testing, the turbocharger is run on a gas stand to simulate operating conditions. The total amount of shaft orbit in the bearing clearance is measured with two displacement probes located at 90 degrees to each other at the compressor end of the rotor (see figure 7) for the entire speed range of the turbocharger. The ratio of the total orbit to the total bearing clearance (known as static clearance), is then plotted as a function of speed to verify if the total shaft motion is within the allowable limits (see figure 8). A plot of speed versus synchronous shaft motion (obtained through a FFT analyzer) is also obtained to verify that the synchronous motion is within the prescribed limits. As shown figure 8, the subsynchronous shaft motion is larger than the synchronous motion.

Typically, the subsynchronous motion is 2 to 3 times larger than the synchronous motion. This test is repeated for all four corners of bearing outside and inside diametrical clearance tolerance. An example of a bearing clearance tolerance box is shown in figure 9 which also lists the operational constraints surrounding the four corners. Experience shows that meeting the shaft motion acceptance criteria is a formidable challenge because a given design must have acceptable shaft motion at all four corners. The rotor-bearing design is iterated until acceptable shaft motion is obtained. Presently, this iteration is performed experimentally because attempts to analytically predict shaft motion have been unsuccessful.

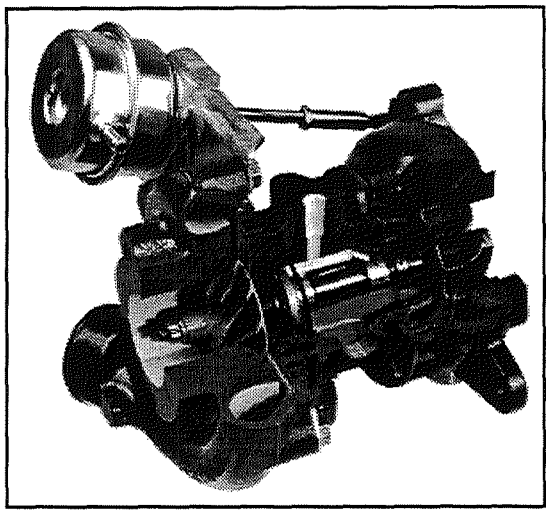

Figure 6. Cut away view of an AlliedSignal turbocharger

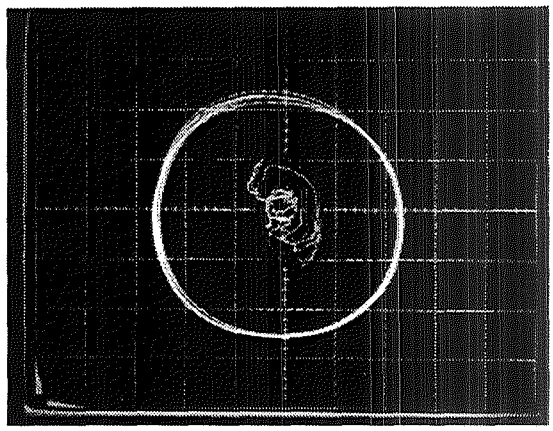

Figure 7. Lissajous pattern of shaft motion

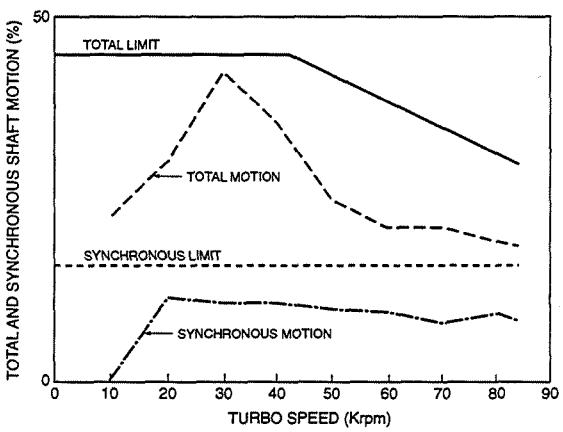

Figure 8. Percent shaft motion versus turbo speed

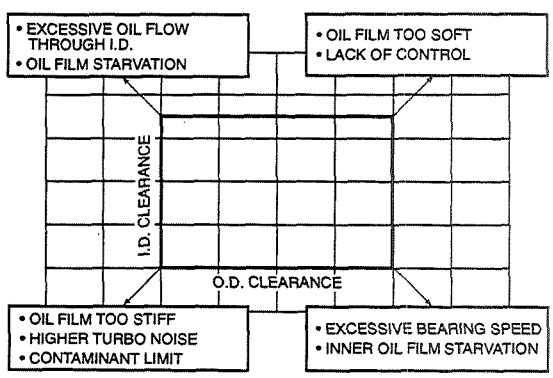

Figure 9. "Four corners" bearing clearance box

SHAFT MOTION COMPARISON

Ball bearings backed by squeeze film damper have the least amount of shaft motion due to almost total absence of subsynchronous motion (see figure 10). However, at the present time their use is limited due to their high cost compared to the semi floating and the fully floating journal bearings. The semi floating bearing backed by a squeeze film damper has the next best shaft motion. The fully floating bearings have the largest shaft motion among the three types currently in production at the authors' company. Figure 10 shows the comparison between the fully floating and the semi floating bearings for an AlliedSignal T15 turbocharger used on passenger cars. The superior stability of the semi floating bearing is due to the fact that it is prevented from rotation and this eliminates the instability in the outer film. Bearing speed is a major contributing factor in the instability of the fully floating bearings. From the results shown at figure 10, we can conclude that a 35% improvement can be obtained by adopting the semi floating bearings.

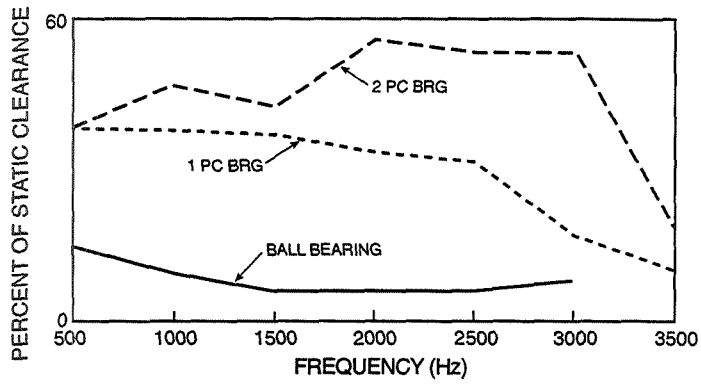

Figure 10. Shaft motion comparison of ball bearing, semi floating bearing and fully floating bearing.

ENGINE SHAFT MOTION

The shaft motion test is performed on a gas stand where the operating parameters, including oil supply temperature and pressure can be precisely controlled. However, it is of interest to find out the difference between gas stand and engine shaft motion. Figure 11 shows this comparison for the T15 turbocharger. Unlike a gas stand, the gas supply to the turbine and the bearing oil supply cannot be controlled precisely. Typically, the engine shaft motion is 20–30% percentage points higher than the gas stand. The increase is mainly due to the engine vibration being transmitted to the turbocharger rotor at the engine firing frequency and its harmonics, and the aerodynamic pulsation's load on the turbine blade from the engine exhaust. Shaft motion testing for a new design is performed on a gas stand for the reasons already explained. Also, since the same model turbocharger can be applied on different engines made by different manufacturers with different engine vibration and pulsation characteristics, a standardized test with standardized operating conditions is required to qualify a generic design.

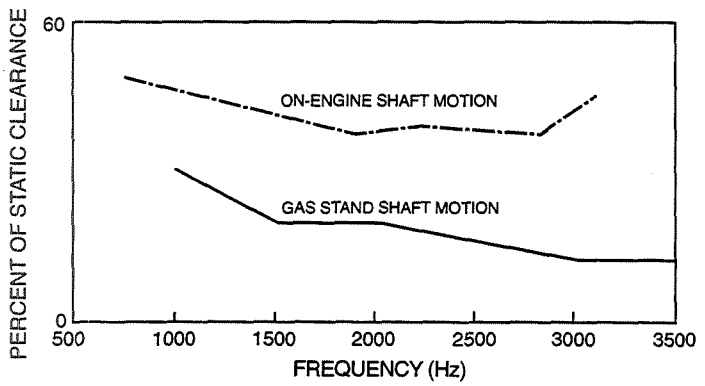

Figure 11. Comparison of gas stand and on-engine shaft motion

POWER LOSS

Figure 12 illustrates the test setup which we have used to measure bearing power loss. Power loss is calculated by measuring the mass flow and temperature drop across the turbine. A turbocharger rotor is used which is assembled without a compressor wheel. Therefore all the work done by the turbine is used in overcoming the power loss in the bearings (thrust and journal) and the windage and seal drag. Although journal bearing friction is not measured directly, by interchanging only the journal bearings, at least a relative power loss comparison can be made.

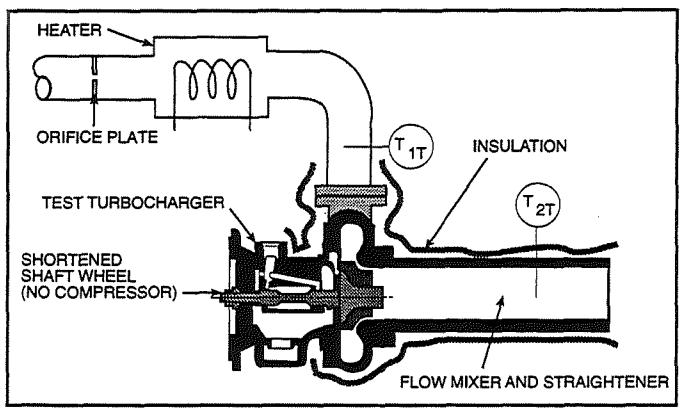

Figure 12. Turbocharger bearing friction test rig schematic

This method of measuring power loss is dependent on carefully insulating the flow path between the upstream and downstream thermocouples. It is also difficult to control swirl and flow stratification in the turbine exhaust. For this reason, a new rig is being designed which will determine bearing losses directly by measuring the drag reaction on a torque arm.

BEARING SPEED

One of the key parameters for floating ring bearings is the ring speed. Both bearing stiffness and damping are dependent on the ring speed. Stone and Underwood (4) developed the concept of "effective speed" that allows comparing the load carrying capacity as well as the stiffness and damping characteristics of different types of bearings. They concluded that the effective speed of a bearing was the absolute value of twice the load speed minus the journal speed. For the inner film of a floating ring bearing loaded by synchronous unbalance, the effective speed is:

$$N_{inner,\ eff} = N_S - N_r$$

For the outer film, the effective speed is:

$$N_{outer,\ eff} = 2N_S - N_r$$

The outer film effective speed is obviously quite large compared with the inner film which allows the outer film to carry the same load as the inner film even though its "journal" is rotating at a relatively low speed, and may have over twice the radial clearance of the inner film.

For the semi floating bearing, both the inner load and journal speeds are N_S so the inner film effective speed is:

$$N_{inner,\ eff} = 2N_S - N_S = N_S$$

For the outer film, the load speed is still N_S but the journal speed is zero so that the effective speed is:

$$N_{outer,\ eff} = 2N_S$$

Aside from its importance in determining stiffness and damping, ring speed can also act as an instability driving mechanism. Certainly any eccentricity or unbalance of the ring will produce a load synchronous with the ring spin speed. In addition, the average fluid velocity of the outer film will be roughly half the ring speed, and the average of the ring speed and shaft speeds for the inner film. For the typical turbocharger, the rigid body critical speeds tend to be in the same frequency range as the ring speed and/or the outer film whirl speed. Load and journal speed combinations can occur which drive the effective speed of a film to zero and thus produce large subsynchronous motions.

It is difficult to choose bearing dimensions which for all four combinations of bearing clearance simultaneously have the desired stiffness and damping properties as well as a ring speed characteristic which avoids coupling with the rigid body natural frequencies. This is particularly difficult in small turbochargers with a relatively large clearance tolerance.

By stopping the rotation of the ring as in the semi floating bearing, the ring speed and outer film oil whirl frequency are eliminated as sources of driven resonance and is one reason why we believe this bearing system has very good shaft motion stability.

Many millions of turbochargers have, of course, been successfully manufactured with fully floating bearings, and continue to be the most popular type of bearing for turbochargers. Obviously it is important to know what the ring speed is in order to avoid resonances in the bearing system and the attendant high shaft motion.

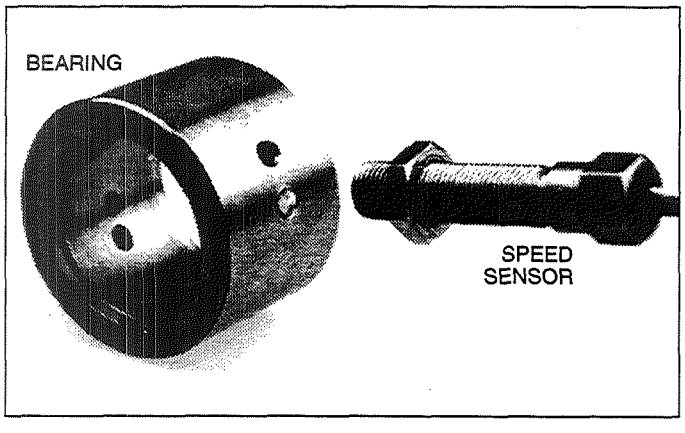

Figure 13. Bearing speed measurement instrumentation

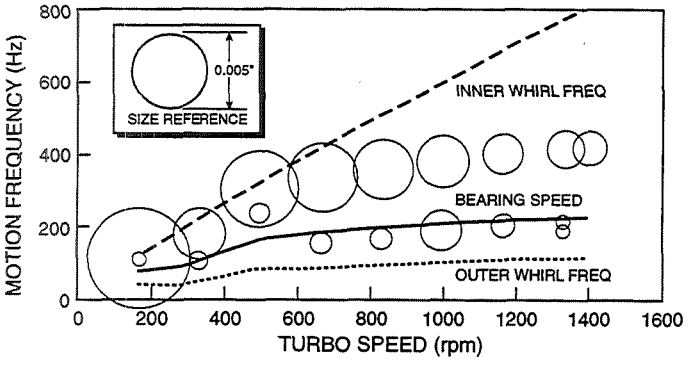

Figure 14. Campbell plot of shaft motion and bearing speed

Ring speed may be measured by implanting two steel set screws 180 degrees opposite of each other in the bronze bearing ring (see Figure 13). The rotation of the ring is then measured using a variable reluctance type sensor screwed into the side of the bearing housing casting. This method of speed measurement has proven to be more robust and reliable than earlier measurements made using eddy current type probes to count the bearing hole passing frequency. Two screws are used to avoid changing the balance of the ring. With this system, ring speed can be recorded during a shaft motion test to help determine the sources of any instabilities.

Figure 14 shows a Campbell plot of shaft motion frequencies and bearing speed versus shaft spin speed measured on a typical turbocharger. This turbocharger, tested without the bearing speed measurement probes, had the same shaft motion characteristics, thus verifying that the screws and probe did not influence the results.

ANALYTICAL DETERMINATION OF BEARING CHARACTERISTICS

Ring speed can also be predicted with some success using the computer program developed in-house to compute bearing stiffness and damping characteristics for input into our rotordynamics programs. This program models the inner and outer oil films using the short bearing theory. For a given inner eccentricity ratio, bearing dimensions, and oil inlet pressure and temperature, the load carried by the inner film can be computed from the following equation:

$$\Lambda = \frac{\mu D L^3 N_{eff}}{60 W c^2} = \frac{\left(1-\varepsilon^2\right)^2}{\pi\varepsilon\left[\pi^2\left(1-\varepsilon^2\right)+16\varepsilon^2\right]^{1/2}}$$

The load carried by both oil films is assumed to be equal. Therefore, the above equation can be solved again for the outer eccentricity ratio. Iteration continues until the assumed bearing speed and oil film temperatures converge. Adiabatic conditions are assumed for the complete bearing. That is, all the heat generated by oil shearing in the two films is carried away by the oil flow but heat transfer is allowed through the bearing from the inner to the outer film. This approach is similar to that described in reference 5.

Although this program has not yet been calibrated with the bearing test rig, it is believed to give reasonable estimates of power loss and stiffness and damping characteristics for design comparison purposes.

BEARING TEST RIG

As mentioned earlier, the correlation between analytical and experimental results for bearing stability is unsatisfactory. The lack of correlation may be attributed to the difficulty in mathematically modelling the non linearities involved in the fully floating and semi floating bearing system. An alternative approach is to experimentally determine the bearing coefficients for different bearing sizes and store this information in a non dimensionalized 'look up' table. This table can then be accessed by the main rotor dynamics program to predict rotor bearing system behavior. In order to meet this objective, a bearing test rig is being built at the authors' company (figure 15). This rig is similar in concept to the test rig in the Turbomachinery Laboratory at Texas A&M University (6). Rotor and bearing displacements, bearing housing vibration, bearing oil film temperature and pressure, and rotor speed will be measured. These inputs will then be processed through a computer program to extract the bearing coefficients. Figure 16 shows an example of rotor and bearing displacement spectrums measured during check-out.

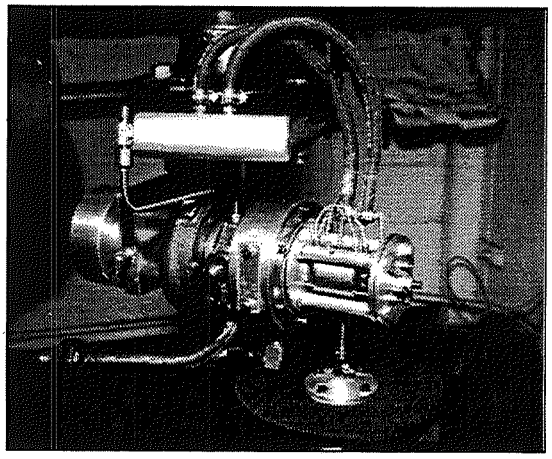

Figure 15. Bearing dynamics test rig

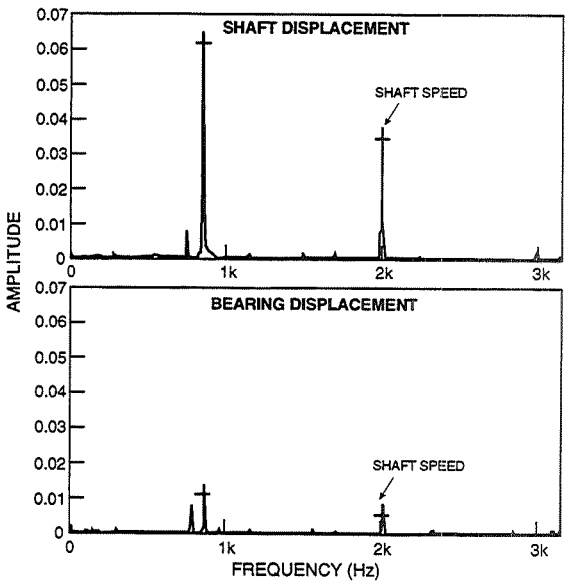

Figure 16. Example shaft and bearing displacements measured on bearing test rig

TRADE OFF BETWEEN BEARING STABILITY AND NOISE REDUCTION

Noise, Vibration and Harshness (NVH) control is a major issue with vehicle manufacturers, who are the main customers for the authors' company. Two types of vehicle noise are generated by a turbocharger rotor bearing system (7). The most common source of noise in a turbocharger is due to mechanical unbalance which results in once per revolution whirl of the rotor. This is transmitted across the oil films to the bearing housing and then to the turbine and compressor housings. From the housing the vibration is further transmitted to the vehicle components that are rigidly connected to the turbocharger, such as the exhaust system, resulting in structure borne noise. The second source of turbocharger noise is from bearing instability. The subsynchronous shaft whirl induces subsynchronous vibration to the bearing housing and then to the vehicle components, similar to the transmission of vibration due to unbalance. Experience shows that a compromise is needed to obtain an optimum balance between reducing shaft motion and reducing transmission of noise. This is because, stiffening the oil film to control shaft motion increases transmission of residual shaft motion to the housings due to a stiffer oil film. A Taguchi test to determine the influence of bearing parameters showed that the most influential parameter is the inside diametral clearance, followed by bearing inner diameter (ID) length and outer diameter (OD) length. Tighter clearance and shorter ID and OD lengths, reduce subsynchronous noise. However, while tighter ID clearance improves shaft motion up to a certain extent, the shorter bearing length increases shaft motion. Therefore, an optimization between the bearing stability and noise is needed when developing a new rotor-bearing system or when applying an existing turbocharger to a new application because of the influence of the vehicle components on the turbocharger related noise.

CONCLUSIONS

The highly nonlinear nature of fully floating bearings, commonly used in small turbochargers, result in shaft motion instabilities under many operating conditions. Because of the lack of a reliable method of analytically predicting these instabilities, a significant experimental effort is still required to achieve satisfactory bearing performance. To improve this situation, a bearing test rig is being developed to better understand the nature of the instabilities, and obtain bearing parameters which will improve our analytic model.

Although a number of technical papers have now been written on floating ring bearings, there is still, in the authors' opinion, room for a better understanding of all the complex motions typically seen in turbochargers equipped with this type bearing.

Another approach in reducing instabilites is to switch to semi floating or ball bearings. These bearing types have been shown to be inherently more stable but their use raises other issues. In the case of ball bearings, higher cost remains an obstacle. For the semi floating bearing, a perception of higher power loss is a concern. Further testing with an improved bearing rig is planned to resolve this issue.

ACKNOWLEDGMENTS

The authors' would first like to thank AlliedSignal for the opportunity to write this paper. We would like to acknowledge and thank several AlliedSignal engineers for their assistance in preparing this paper. In particular, Steve Arnold and Mitou Parios for reviewing and suggesting improvements in the draft, and Jean-Luc Fleury for providing the bearing speed measurement data.

References:

1. "Proceedings of The Fourth International Conference on Rotor Dynamics", edited by R.L. Eshleman and N.F. Rieger, The Vibration Institute, 1994.

2. "The Dynamics of Rotor-Bearing System using Finite Elements", H.D. Nelson and J.M. McVaugh, ASME, 75-WA/DE-19, August, 1976.

3. "Rotordynamics of Turbomachinery", John M. Vance, John Wiley & Sons, 1st edition, Chapter 7.

4. "Load Carrying Capacity of Journal Bearings," J.M. Stone and A.F. Underwood, SAE Quarterly Transactions, Vol 1, No. 1, January, 1947.

5. "High-speed Floating-ring Bearing Test and Analysis," R.J. Trippett and D.F. Li, ASLE 83-AM-3E-2, April, 1983.

6. "A Test Apparatus and Facility to identify the Rotordynamic Coefficients of High-Speed Hydrostatic Bearings," Dara Childs and Keith Hale, Journal of Tribology, Vol 116, pp 337 - 344. April, 1994.

7. " Turbocharger Noise, Generating Mechanisms and Control", Sunil Sahay and Denis Thouvenin, Proceedings, Noise-93, May 31-June 3, 1993, Vol. 5, pp 269 - 277.

STATE SPACE ADAPTIVE CONTROL FOR A LUMPED MASS ROTOR EXCITED BY NONCONSERVATIVE CROSS-COUPLING FORCES

P. Wurmsdobler, H.P. Jorgl, and H. Springer
Technical University of Vienna
Vienna, Austria

Abstract

An adaptive pole-assignment controller is presented in conjunction with a state space model identification for an active magnetic bearing system, consisting of a single mass suspended in an active magnetic bearing excited by nonconservative cross-coupling forces. Simulation results show the success of this algorithm for parameter changes in closed loop operation with system noise but without set point changes.

1 Introduction

In conventional rotor-bearing systems with journal bearings and seals, nonconservative cross-coupling forces may lead to instability. A possible way to cope with this problem is to reduce the influence of the cross-coupling mechanism by applying higher damping to the system, which means dissipation of energy.

If a rotor is levitated by magnetic bearings, one can make use of the controllability of the entire system by active magnetic bearings. Thus it is possible to control nonconservative cross-coupling forces by means of on-line identification and adaptive control techniques. It has turned out, that a state space model identification is appropriate to estimate both system parameters and all states. Additionally, a state space model is a good basis for the calculation of a controller for an unstable system. In this case pole-assignment is the best way for an adaptive controller concerning the future implementation in a real-time application.

Finally, using this algorithm, nonconservative forces can be compensated by control forces without loss of stability and without applying more damping to the rotor-bearing system.

2 State space rotor model

The continuous time state space model of a single mass suspended by an active magnetic bearing (see Figure 1) is given by

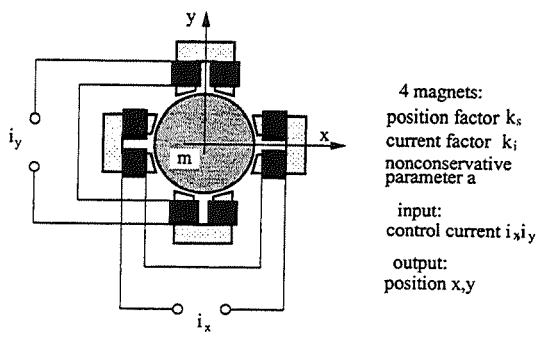

Figure 1: Single mass suspended by active magnetic bearings

$$\dot{\mathbf{z}} = \mathcal{A} \cdot \mathbf{z} + \mathcal{B} \cdot \mathbf{u} \tag{1}$$

$$\mathbf{y} = \mathcal{C} \cdot \mathbf{z} \tag{2}$$

with the system matrix

$$\mathcal{A} = \begin{pmatrix} 0 & 0 & 1 & 0 \\ 0 & 0 & 0 & 1 \\ \frac{k_s}{m} & \frac{a}{m} & 0 & 0 \\ -\frac{a}{m} & \frac{k_s}{m} & 0 & 0 \end{pmatrix},$$

the control matrix

$$\mathcal{B} = \begin{pmatrix} 0 & 0 \\ 0 & 0 \\ \frac{k_i}{m} & 0 \\ 0 & \frac{k_i}{m} \end{pmatrix},$$

the measurement matrix

$$\mathcal{C} = \begin{pmatrix} 1 & 0 & 0 & 0 \\ 0 & 1 & 0 & 0 \end{pmatrix},$$

and the state vector $\mathbf{z} = [x, y, \dot{x}, \dot{y}]^T$, respectively. The lumped mass of the rotor is m. An active magnetic bearing is modelled by the position factor k_s and the current factor k_i. The variable a represents the nonconservative cross-coupling parameter. A transformation to a discrete time system with sampling time T_s yields a model with no particular structure:

$$\mathbf{A} = e^{\mathcal{A} \cdot T_s} \tag{3}$$

$$\mathbf{B} = (e^{\mathcal{A} \cdot T_s} - \mathbf{I}) \cdot \mathcal{A}^{-1} \cdot \mathcal{B} \tag{4}$$

The entire model with system noise $\boldsymbol{\xi}(k)$ and measurement noise $\boldsymbol{\eta}(k)$ can then be written in the form:

$$\mathbf{x}(k+1) = \mathbf{A}\,\mathbf{x}(k) + \mathbf{B}\,\mathbf{u}(k) + \boldsymbol{\xi}(k) \tag{5}$$

$$\mathbf{y}(k) = \mathbf{C}\,\mathbf{x}(k) + \boldsymbol{\eta}(k) \tag{6}$$

Since the discrete state space model should have a minimum number of parameters to be identified, it is transformed into a canonical form. With respect to the calculation of an adaptive controller, a controller canonical form is chosen. The structural indices are for reasons of symmetry $n_1 = 2$ and $n_2 = 2$. The transformation

$$\mathbf{x}_C = \mathbf{\Gamma}_C \, \mathbf{x} \quad \text{and} \quad \mathbf{x} = \mathbf{\Gamma}_C^{-1} \, \mathbf{x}_C \tag{7}$$

can be performed using the transformation matrix

$$\mathbf{\Gamma}_C = \left(\gamma_1, \mathbf{A}^T \gamma_1, \gamma_2, \mathbf{A}^T \gamma_2 \right)^T \tag{8}$$

with its vectors

$$\gamma_i = \left(\mathbf{T}_C^T \right)^{-1} \mathbf{B}_C(:, i), \tag{9}$$

the controller matrix

$$\mathbf{T}_C = [\mathbf{B}(:,1), \mathbf{A}\,\mathbf{B}(:,1), \mathbf{B}(:,2), \mathbf{A}\,\mathbf{B}(:,2)], \tag{10}$$

and the desired control matrix

$$\mathbf{B}_C = \mathbf{\Gamma}_C \, \mathbf{B} = \begin{pmatrix} 0 & 0 \\ 1 & 0 \\ 0 & 0 \\ 0 & 1 \end{pmatrix}$$

with the expression in parenthesis $(:, i)$ denoting the i^{th} column with $i = 1, 2$. This will result in the new system matrix,

$$\mathbf{A}_C = \mathbf{\Gamma}_C \, \mathbf{A} \, \mathbf{\Gamma}_C^{-1} = \begin{pmatrix} 0 & 1 & 0 & 0 \\ -a_2^{(11)} & -a_1^{(11)} & -a_2^{(12)} & -a_1^{(12)} \\ 0 & 0 & 0 & 1 \\ -a_2^{(21)} & -a_1^{(21)} & -a_2^{(22)} & -a_1^{(22)} \end{pmatrix},$$

and a new measurement matrix,

$$\mathbf{C}_R = \mathbf{C} \, \mathbf{\Gamma}_C^{-1} = \begin{pmatrix} c_2^{(11)} & c_1^{(11)} & c_2^{(12)} & c_1^{(12)} \\ c_2^{(21)} & c_1^{(21)} & c_2^{(22)} & c_1^{(22)} \end{pmatrix}.$$

3 Identification algorithm

The identification algorithm is based on the innovations model ([3]):

$$\hat{\mathbf{x}}(k+1, \mathbf{p}) = \mathbf{A}(\mathbf{p}) \, \hat{\mathbf{x}}(k, \mathbf{p}) + \mathbf{B}(\mathbf{p}) \, \mathbf{u}(k) + \mathbf{K}(\mathbf{p}) \, [\mathbf{y} - \mathbf{C}(\mathbf{p}) \, \hat{\mathbf{x}}(k, \mathbf{p})], \tag{11}$$

$$\hat{\mathbf{y}}(k, \mathbf{p}) = \mathbf{C}(\mathbf{p}) \, \hat{\mathbf{x}}(k, \mathbf{p}) \tag{12}$$

using a Kalman filter matrix

$$\mathbf{K} = \begin{pmatrix} k_2^{(11)} & k_2^{(12)} \\ k_1^{(11)} & k_1^{(12)} \\ k_2^{(21)} & k_2^{(22)} \\ k_1^{(21)} & k_1^{(22)} \end{pmatrix} \tag{13}$$

All parameters of this innovations model are gathered within the parameter vector $\mathbf{p}$. The identification algorithm ([1, 2, 3]) can be summarised as:

Prediction error

$$\varepsilon = \mathbf{y} - \hat{\mathbf{y}}(k, \mathbf{p}). \tag{14}$$

Adaptation of error matrix

$$\mathbf{L}(k) = \mathbf{P}(k-1)\,\Psi(k)\,\left[\mathbf{I} + \Psi^T(k)\,\mathbf{P}(k-1)\,\Psi(k)\right]^{-1}. \tag{15}$$

Parameter update

$$\hat{\mathbf{p}}(k) = \hat{\mathbf{p}}(k-1) + \mathbf{L}(k)\,\varepsilon. \tag{16}$$

Update of covariance matrix

$$\mathbf{P}(k) = \frac{1}{\rho(k)}\,\left[\mathbf{P}(k-1) - \mathbf{L}(k)\,\Psi^T(k)\mathbf{P}(k-1)\right]. \tag{17}$$

Based on the new model, a prediction for the next time step can be made in the form

$$\hat{\mathbf{x}}(k+1) = \mathbf{A}(\mathbf{p}(k))\,\hat{\mathbf{x}}(k) + \mathbf{B}(\mathbf{p}(k))\,\mathbf{u}(k) + \mathbf{K}(\mathbf{p}(k))\,\varepsilon, \tag{18}$$

$$\hat{\mathbf{y}}(k+1) = \mathbf{C}(\mathbf{p}(\mathbf{k}))\,\hat{\mathbf{x}}(k+1). \tag{19}$$

The gradient matrix Ψ is derived from the partial derivative of the estimation error as

$$\Psi(k) = -\left(\frac{\partial}{\partial \mathbf{p}}\,\varepsilon(k)\right)^T = \left(\frac{\partial \hat{\mathbf{y}}(k, \mathbf{p})}{\partial \mathbf{p}}\right)^T, \tag{20}$$

and is calculated recursively by

$$\begin{aligned} \mathbf{W}(k+1, \hat{\mathbf{p}}) &= [\mathbf{A}(\hat{\mathbf{p}}(k)) - \mathbf{K}(\hat{\mathbf{p}}(k))\,\mathbf{C}(\hat{\mathbf{p}}(k))]\,\mathbf{W}(k, \hat{\mathbf{p}}) \\ &\quad + \mathbf{M}_k - \mathbf{K}(\hat{\mathbf{p}}(k))\,\mathbf{V}_k, \end{aligned} \tag{21}$$

$$\Psi(k+1) = \mathbf{W}^T(k+1, \hat{\mathbf{p}})\,\mathbf{C}(\hat{\mathbf{p}}(k)) + \mathbf{V}_k^T. \tag{22}$$

The matrices $\mathbf{M}_k$ and $\mathbf{V}_k$ are model specific and result from the partial derivative of the innovations model as

$$\mathbf{M}_k = \frac{\partial}{\partial \mathbf{p}}\,[\mathbf{A}(\mathbf{p})\,\hat{\mathbf{x}}(k) + \mathbf{B}(\mathbf{p})\,\mathbf{u}(k) + \mathbf{K}(\mathbf{p})\,\varepsilon], \tag{23}$$

$$\mathbf{V}_k = \frac{\partial}{\partial \mathbf{p}}\,[\mathbf{C}(\mathbf{p})\,\hat{\mathbf{x}}(k)]. \tag{24}$$

Special attention has to be paid to the forgetting factor $\rho(k)$ in equation 17. If this factor is too small, the covariance matrix will increase too fast, if it is too large (close to 1), the

algorithm will react too slowly to parameter changes. Therefore, the forgetting factor needs to be controlled separately by a statistical value, which gives the change of the variance of the estimation error

$$\delta(k) = \frac{\hat{\sigma}_\varepsilon^2(N_1,k) - \hat{\sigma}_\varepsilon^2(N_2,k)}{\hat{\sigma}_\varepsilon^2(N_2,k)}, \tag{25}$$

with $N_1 \leq N_2$ and $\hat{\sigma}_\varepsilon^2(N,k)$ as estimate for the error variance with a variable memory N. The idea behind this algorithm is, that under the assumption of a stationary process, the variance of the estimation error in a steady state should be stationary as well. The increasing variance of the estimation error indicates a change in parameters of the plant under investigation. If $\delta(k)$ triggers a certain threshold, e.g. 20% of the mean variance, then the forgetting factor $\rho(k)$ is reset to ρ_0 and follows the law such that

$$\rho(k) = k_\rho\, \rho(k-1) + (1-k_\rho)\, \rho_\infty \tag{26}$$

with ρ_∞ the final value and k_ρ determining the rate of change.

4 Adaptive control by pole placement

The control law is defined as

$$\mathbf{u} = -\mathbf{K}_x\, \mathbf{x} \tag{27}$$

with

$$\mathbf{K}_x = \begin{pmatrix} k_2^{(11)} & k_1^{(11)} & k_2^{(12)} & k_1^{(12)} \\ k_2^{(21)} & k_1^{(21)} & k_2^{(22)} & k_1^{(22)} \end{pmatrix}$$

The poles of the closed loop system $\mathbf{A}_{cl} = \mathbf{A}_C - \mathbf{B}\mathbf{K}_x$ result from

$$P(z) = \begin{vmatrix} z & -1 & 0 & 0 \\ k_2^{(11)} - a_2^{(11)} & z + k_1^{(11)} - a_1^{(11)} & k_2^{(12)} - a_2^{(12)} & k_1^{(12)} - a_1^{(12)} \\ 0 & 0 & z & -1 \\ k_2^{(21)} - a_2^{(21)} & k_1^{(21)} - a_1^{(21)} & k_2^{(22)} - a_2^{(22)} & z + k_1^{(22)} - a_1^{(22)} \end{vmatrix}.$$

Here, the advantage of a model description in controller canonical form becomes obvious. If the cross coupling terms are zero by selecting the cross coupling parameters of the control matrix properly, the characteristic polynomial can be reduced to

$$\begin{aligned} P(z) &= \left(z^2 + (k_1^{(11)} - a_1^{(11)})z + k_2^{(11)} - a_2^{(11)}\right) \\ &\quad \left(z^2 + (k_1^{(22)} - a_1^{(22)})z + (k_2^{(22)} - a_2^{(22)})\right). \end{aligned}$$

If this polynomial is compared with the desired one as

$$P_s(z) = \left(z^2 + p_1 z + p_2\right)^2,$$

then all coefficients of the control matrix can be easily calculated in the form

$$k_m^{(ij)} = a_m^{(ij)}, \tag{28}$$

$$k_m^{(ii)} = a_m^{(ii)} + p_m. \tag{29}$$

with $m = 1,2$ and $i,j = 1,2$.

5 Simulation results

The parameters of the system depicted in Figure 1 are given by the following

Parameter	Value	Unit
Rotor mass	28.77	kg
Position factor	$2.39 \cdot 10^6$	N/m
Current factor	299.57	N/A
Nonconservative factor	a	N/m
Sampling time	10^{-4}	s

Further investigations have shown, that the nonconservative stiffness parameter a exclusively affects one parameter of the system matrix, namely $a_1^{(12)}$, which in the following is referred to as p. Additionally, one can make use of the symmetry in this system, and reduce the number of parameters of the Kalman matrix to 4. Thus, only 5 entries remain in the parameter vector $\mathbf{p}$.

The resulting state space model is then

$$\begin{aligned}
\mathbf{x}(k+1) &= \begin{pmatrix} 0 & 1 & 0 & 0 \\ -1 & 2.01 & 0 & p \\ 0 & 0 & 0 & 1 \\ 0 & -p & -1 & 2.01 \end{pmatrix} \mathbf{x}(k) + \begin{pmatrix} 0 & 0 \\ 1 & 0 \\ 0 & 0 \\ 0 & 1 \end{pmatrix} \mathbf{u}(k) + \boldsymbol{\xi}(k) \\
\mathbf{y}(k) &= \begin{pmatrix} 0.52 \cdot 10^{-7} & 0.52 \cdot 10^{-7} & 0 & 0 \\ 0 & 0 & 0.52 \cdot 10^{-7} & 0.52 \cdot 10^{-7} \end{pmatrix} \mathbf{x}(k) + \boldsymbol{\eta}(k).
\end{aligned}$$

After the model has been defined with all parameters to be identified, the matrices $\mathbf{M}_k$ and $\mathbf{V}_k$ have to be calculated once according to equation 23 and 24. With these matrices the identification algorithm structure can be established (see equation 14 to 22). Since the system is open loop unstable, a controller and an observer have to be designed in advance. This has been done according to the nominal system without cross-coupling influence. The poles of the closed loop system have been placed at $z_{1,2,3,4} = 0.97$, or in the continuous complex plane to $s_{1,2,3,4} = -288\mathrm{s}^{-1}$, which would meet the eigenvalue for a mass-spring-system with a negative stiffness factor of the magnetic bearing. The resulting control law is

$$\mathbf{u} = \begin{pmatrix} -0.0591 & 0.0608 & 0 & 0 \\ 0 & 0 & -0.0591 & 0.0608 \end{pmatrix} \mathbf{x}.$$

Similar to the controller, the observer poles have been chosen to $z_{1,2,3,4} = 0.7$, to ensure, that the observer is fast enough to follow the system behaviour. The Kalman matrix in equation 13 is assigned to

$$\mathbf{K} = \begin{pmatrix} 5.3322 \cdot 10^6 & 6.2067 \cdot 10^6 & 0 & 0 \\ 0 & 0 & 5.3322 \cdot 10^6 & 6.2067 \cdot 10^6 \end{pmatrix}^T.$$

The initial parameter vector is set to the a priori values

$$\mathbf{p} = \begin{pmatrix} 0 & 5.3322 \cdot 10^6 & 6.2067 \cdot 10^6 & 0 & 0 \end{pmatrix}^T,$$

with the initial covariance matrix $\mathbf{P}$ as identity matrix. All other recursively calculated matrices have been set to zero. White noise with a maximum deflection value of $1\mu m$ for η was added to the measurement signal to ensure excitation. With the initial conditions $\mathbf{x} = \mathbf{0}$ and all precalculated values for the controller and observer the simulation was started. The resulting displacement of the rotor mass can be seen in Figures 2, 3, 4.

After 0.01s the parameter a changes from 0 to $1 \cdot 10^7$N/m, which corresponds to a value for $p = 3.4766 \cdot 10^{-3}$. This is assumed to be the worst case in a turbomachinery application, e.g. a sudden pressure loss or leakage in sealings will lead to a parameter change in a linear model. Actually, the mechanism of the cross-coupling forces develops slowly, but an abrupt change in the nonconservative stiffness parameter should cover most cases. Immediately after the parameter change the system is unstable in terms of its structure, but the displacements will increase slowly. When a certain signal to noise ratio is achieved, the parameter change is recognised by the algorithm. This means, that the input and output signals have to contain a minimum of information to make the algorithm converge to the new system parameters.

Parallel to the identification, the controller parameters are calculated according to equation 28 and 29. It can be observed, that the feedback gain matrix of the state space controller becomes non-symmetric to the same extent as the parameter of the nonconservative stiffness does. This effect can easily be seen in equation 28. These non-symmetric entries in the controller matrix will cause a force, which directly compensates the nonconservative forces of the system. Due to the adaptation of the controller the rotor bearing system can recover from a parameter change. Simulations have shown, that this positive effect is true for a certain amount of the non conservative forces. If the parameter change is too large (10^8N/m), the control current becomes to large as well and runs into saturation. Then, instability can't be prevented.

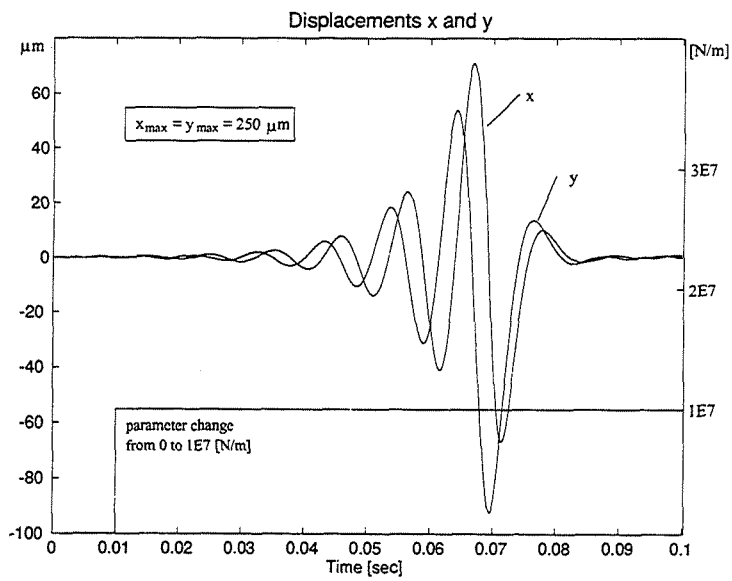

Figure 2: Time history of vertical (x) and horizontal (y) rotor displacements after an abrupt cross-coupling excitation of $a = 10^7$N/m.

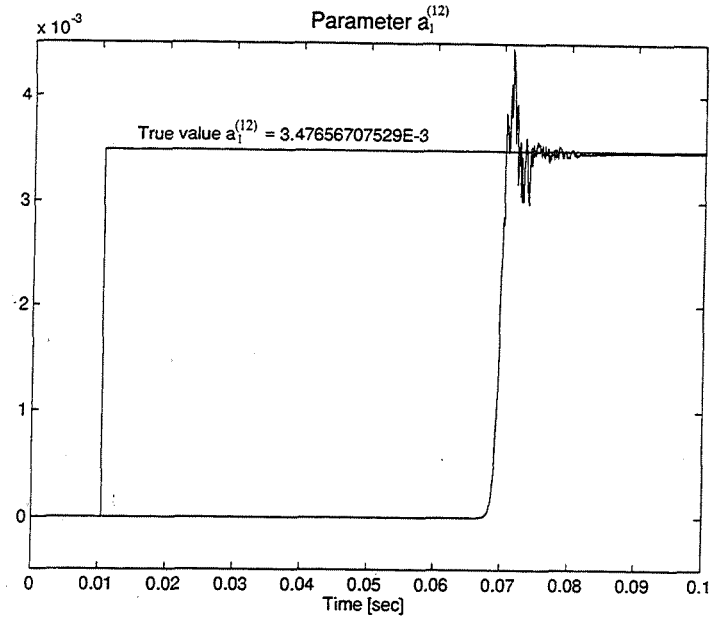

Figure 3: Time history of $\mathbf{p}(1)$. The parameters of the Kalman matrix $\mathbf{K}$ did not change significantly.

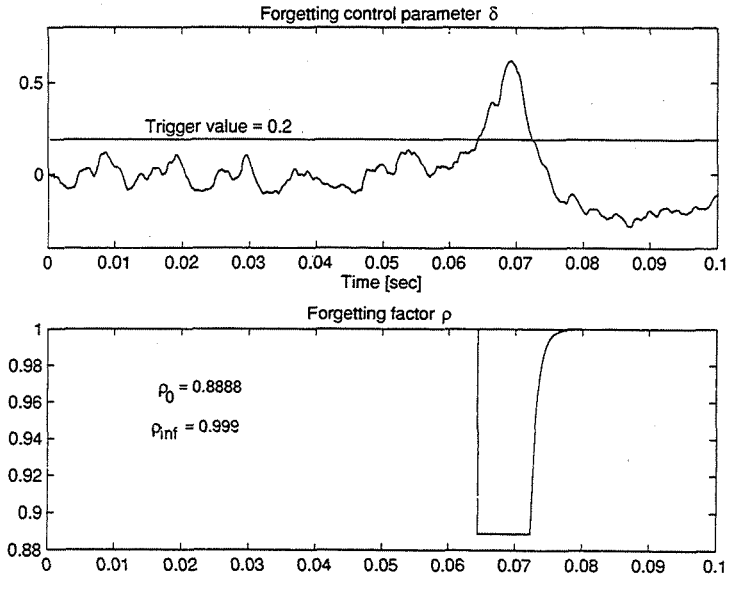

Figure 4: Time history of the forgetting control value δ and the forgetting factor ρ. Approximately after 0.054s the parameter change of the cross-coupling excitation is recognised.

6 Conclusion

It has been shown, that nonconservative cross-coupling forces can be controlled by means of on-line identification and adaptive control techniques. The system under investigation was a lumped mass model of a rigid rotor suspended by an active magnetic bearing controlled by a state space controller. Within a simulation a nonconservative cross coupling force was applied to the system in conjunction with the proposed on-line identification and adaptive control. It has turned out, that a state space model identification is appropriate to estimate both the system parameters and the state vector. In this case, the nonconservative cross-coupling forces were compensated by additional forces generated by a non-symmetric gain in the state space controller matrix. This matrix is calculated by pole assignment from the identified state space model.

Future objectives of investigation will be the extension of this concept for a full identification and central control for a rigid rotor suspended in two magnetic bearings.

7 Acknowledgements

The authors express their honest thanks to the Austrian Science Foundation (FWF) for supporting this project.

References

[1] Nazaruddin, Y.Y.: *Adaptive Zustandsregler für Mehrgrößensysteme und ihre praktische Anwendung*, Ruhr Universität Bochum, Automatisierungstechnik 43, S. 236-241, Oldenburg Verlag 1995.

[2] Nazaruddin, Y.Y.: *Adaptive Regelung von Ein- und Mehrgrößensystemen auf der Basis der Zustandsraumdarstellung*, Dissertation, Ruhr Universität Bochum, Bochum 1994.

[3] Ljung, L. and T. Søderstrøm: *Theory and Practice of Recursive Identification*, MIT Press, Cambridge Massachusetts, 1983.

[4] Bierman, J.G.: *Factorization Methods for Discrete Sequential Estimation*, Academic Press, New York, 1977.

[5] Goodwin, G.C. and K.S. Sin: *Adaptive Filtering, Prediction and Control*, Prentice Hall, Englewood Cliffs, New Jersey, 1984.

NONLINEAR RESPONSE OF ROTOR TO STATOR RUBS

Yang Wei, Xikuan Tang, and Stanley Hogat
Far East Levingston Shipbuilding Ltd.
Singapore

1. Introduction

Rub interaction that happens between rotor and stator of rotating machinery induces complex nonlinear vibration phenomena[1][2]. In general, the transient contact and rub between rotor and stator influence on the operating conditions of rotating machinery in following aspects[3][4]:

A. The contact forces induced by rotor/stator rubs increased the system stiffness. In other words, it is equivalent to introducing an support to the machine system .

B. The advent of contact presents impact to the system and brings about severe transient and nonlinear characteristics.

C. The tangent friction force due to the relative motion between the rotor and stator in contact may cause the reverse whirl motion of the rotor and severe friction which affects the normal stress conditions and causes local thermal distortion of the rotor.

D. The contact introduces the coupling effect which feeds impact force back to the system and complicates the operating conditions of rotating machinery further.

The vibration induced by rotor/stator rubs has been studied by many scholars[5]. Some results are obtained by experiments, engineering experiences and theoretical analysis[10][11][12]. Recent study related the complex vibration regimes to the chaotic behaviors of nonlinear system. It is stated that, in case of partial lateral rubs, for instance, the 1/2x sub-harmonic component relative to the rotating frequency of the rotor is observed in the vibration spectra of rotor . And , with the increasing of the rotating frequency of the rotor , the denominator of the fractional sub-harmonic spectral components is changing depending on the ratio of rotating frequency versus the first natural frequency of the rotor[6] . The spectra of the rub vibration are also affected by the severity of rubs . Especially in full annular rub case[7] , the 2x of rotating frequency super-harmonic component is observed.

A theoretical dynamic parametric excitation vibration model[8] and some other models [9] are proposed which facilitated the research on the rub interactions. In most of these researches the impact and friction forces induced by the contact are represented by additional stiffness and damping coefficient variations in different rub cases which reflected the characteristics of the rub forces. But the impact force feedback mechanism has not been presented sufficiently.

In this paper , the author proposed a new model of the rotor stator rubs derived from classical mechanical theory which takes the feedback of the impact forces in to consideration. The response characteristics of rubs in different rub severity at different speed are presented based on a simple rotor/stator system. Some experiment results are presented also in comparison with the numerical simulation ones.

Nomenclature

x_1, y_1	Horizontal and vertical displacements of rotor
x_2, y_2	Horizontal and vertical displacements of stator
L	System Lagrangian

q_i	System coordinates.
Δ	Radial clearance between rotor and stator

2. An approach of system model of Rotor /stator rubs

First of all, Consider the collision problem of the autonomous system consists of n rigid bodies . According to the Hamilton's principle, the system satisfies following equation :

$$\delta J = \int dt \sum (\frac{\partial L}{\partial q_i} - \frac{d}{dt}(\frac{\partial L}{\partial \dot{q}_i}))\delta q_i = 0 \qquad (1)$$

When collision happens the motion of the system will satisfy following equations:

$$\mu_j = 0 \,(j=1, 2, \ldots \ldots) \qquad (2)$$

Where μ_j is the distance between the j'th pairs of contacting rigid bodies. These equations mean that no penetration is allowed between the rigid bodies and the contact are equivalent to sudden constraints imposed on the system . Then we have

$$\sum_j \lambda_j \mu_j = 0 \;\; (j=1, 2, \ldots \ldots) \qquad (3)$$

That is

$$\sum_i (\sum_j \lambda_j \frac{\partial \mu_j}{\partial q_i})\delta q_i = 0 \qquad (4)$$

Combine equation (1) and (4) We have the equations of the system with collision:

$$\begin{cases} \dfrac{d}{dt}(\dfrac{\partial L}{\partial \dot{q}_i}) - \dfrac{\partial L}{\partial q_i} = \sum_j \lambda_j \dfrac{\partial \mu_j}{\partial q_i} & (j = 1, 2, \ldots \ldots) \\ \mu_j = 0 \end{cases} \qquad (5)$$

For a non-autonomous system the equations are as follows:

$$\begin{cases} \dfrac{d}{dt}(\dfrac{\partial L}{\partial \dot{q}_i}) - \dfrac{\partial L}{\partial q_i} = \sum_j \lambda_j \dfrac{\partial \mu_j}{\partial q_i} + Q_i & (j=1, 2, \ldots \ldots) \\ \mu_j = 0 \end{cases} \qquad (6)$$

where λ_j is collision forces between the jth pairs of collision rigid bodies and Q_i is the sum of other forces applied to the system.

Equation (6) expressed the system property when collision happened inside the system . It showed that when collision happened the displacements of the system were not independent of each other any more while the velocities were independent instead . Only in case of complete non-elastic collision we have an additional equation as follow[13]:

$$\dot{\mu}_j = 0 \qquad (7)$$

It means the velocities were not independent of each other also.

For rotor to stator rub interaction the equation (6) takes form as follows:

$$\begin{cases} [M]\ddot{\bar{x}} + [C]\dot{\bar{x}} + [K]\bar{x} = \bar{f}(t) + [f_\varphi(\bar{x})]\{\Lambda\} \\ \mu_j(\bar{x}, t, \{\Lambda\}) = 0 \end{cases} \qquad (8)$$

where $\bar{f}(t)$ is system excitation vector and $[f_\varphi(\bar{x})]\{\Lambda\}$ is the collision force term. That is

$$[f_\varphi(\bar{x})]\{\Lambda\} = \sum_j \lambda_j \frac{\partial \mu_j}{\partial q_i} \tag{9}$$

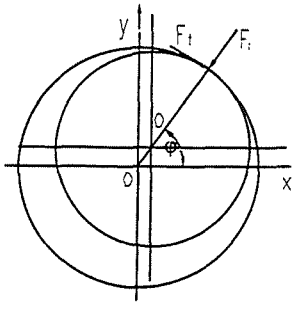

Figure 1. Rub forces

If the dry friction is considered only, as being shown in figure 1, the impact force F_r and friction force F_t at contact point can be expressed as:

$$F_r = (\frac{\mu - |\mu|}{2\mu})\lambda = \begin{cases} 0 & \mu \in (0^+, \infty) \\ \lambda & \mu \in (-\infty, 0] \end{cases} \tag{10}$$

$$F_t = uF_r = u(\frac{\mu - |\mu|}{2\mu})\lambda \tag{11}$$

where u is coefficient of Coulomb friction and λ is the amplitude of the impact force. by equations (12) we can translate the two forces to x ,y direction .

$$\begin{Bmatrix} F_x \\ F_y \end{Bmatrix} = \begin{bmatrix} -\cos\varphi & u\sin\varphi \\ -\sin\varphi & -u\cos\varphi \end{bmatrix} \begin{Bmatrix} \lambda \\ \lambda \end{Bmatrix} \tag{12}$$

Where F_x and F_y are the contact force components in x ,y direction respectively. That is the reason that the rotor/stator rub equations have the form of equation (8).

One of the advantages of equation (8) is that the contribution of system parameters is emphasized rather than that of the local parameters of the contact points. By μ_j=0, the subsystem of rotor and that of stator are combined together and the coupling of contact forces are considered. Therefore, The system parameters may be elaborated to eliminated the rub effect for some question under scrutiny with that equation.

It is shown that , except system stiffness and damping parameters , equation (8) does not contain any local contact parameters at all . But that does not mean that this equation has omitted the contact property. Actually for engineering application one can construct suitable model for ones application by applying FEM. method or other to the local contact point. That is, to regard the local contact point as a component of mass, damping and stiffness parameters and to combine the local parameters into the system matrices.

Another characteristics of the equation (8) is that it intrinsically neglects the difference between the different rub phenomena. That means the partial lateral rub and full annular rub can be studied with the same equation. Hence the rub evidence signature in different operation conditions and of different rub severity can be obtained and compared.

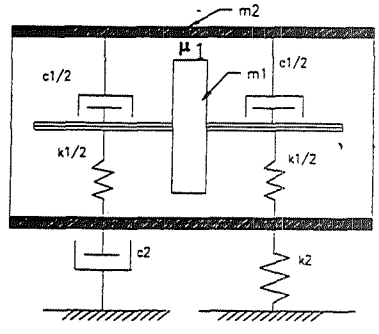

Figure 2. Rotor/Stator model

3. Nonlinear Response of Rotor to Stator Rubs

A Simple Rotor/stator system ,as shown in figure 2., was studied with the method expressed above by numerical simulation[13]. The rotor and stator were considered to be flexibly supported. Given the system displacement vector was $\bar{x} = \{x_1 \quad y_1 \quad x_2 \quad y_2\}$. Then the system equation was as follows:

$$[M]\ddot{\bar{x}} + [C]\dot{\bar{x}} + [K]\bar{x} = \{f(t)\} + [f_\varphi]\{\Lambda\} \qquad (13)$$

where [M] ,[C] and [K] were system matrices of mass , damping and stiffness respectively. The {f(t)} was unbalance force vector and $[f_\varphi]\{\Lambda\}$ was the rub force term which had the form as follow:

$$[f_\varphi]\{\Lambda\} = \begin{bmatrix} -\cos\varphi & u\sin\varphi & 0 & 0 \\ -\sin\varphi & -u\cos\varphi & 0 & 0 \\ 0 & 0 & \cos\varphi & -u\sin\varphi \\ 0 & 0 & \sin\varphi & u\cos\varphi \end{bmatrix} \begin{Bmatrix} \lambda \\ \lambda \\ \lambda \\ \lambda \end{Bmatrix} \qquad (14)$$

The clearance between rotor and stator was expressed as follow;

$$\mu = \Delta - \sqrt{(\delta + x_1 - x_2)^2 + (y_1 - y_2)^2} \qquad (15)$$

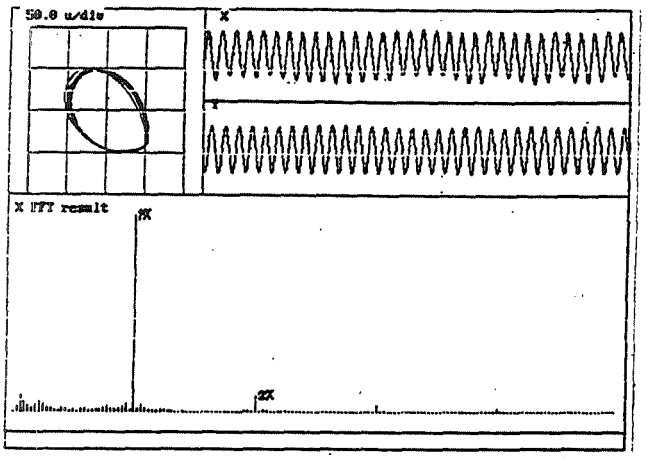

Figure.3 Response between 0.15 to 2 times of natural frequency

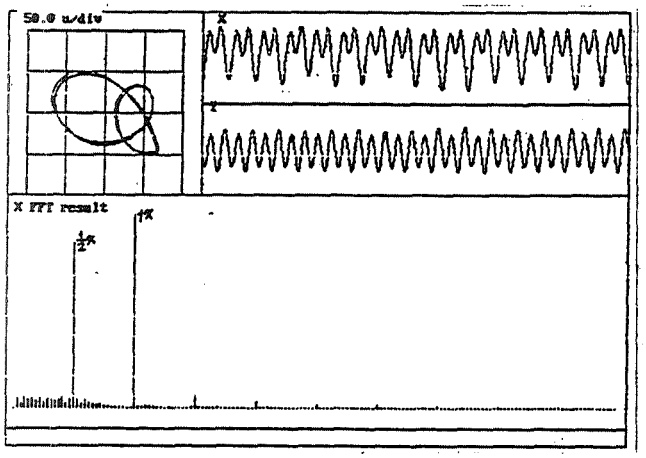

Figure.4 Response between 2 to 4 times of natural frequency

and the angle of contact position was

$$\varphi = \tan^{-1}\frac{y_1 - y_2}{\delta + x_1 - x_2} \qquad (16)$$

The procedure of the numerical simulation is that, at every integral step the value of μ is calculated according to the system displacement obtained . If the value is positive, the simulation will go on as contact free system case . If the value is negative that means the contact happens at the exact time. In the later case equation (14) is added into the system equation and an iterative procedure is invoked to find out the value of λ that forces the dynamic clearance between rotor and stator, μ, be zero[13]. On the other hand , if a negative value of λ is obtained , or the $\mu > 0$, in other words , the clearance between rotor and stator will increase , that means the rotor and stator will not contact to each other at next integral step . Hence these two conditions switch the calculation procedure from rub case to rub free case.

The integration method used to solve the equation is no other but Runge-Kutta method. It is consider to be symplectic to conserve the energy and momentum of the nonlinear system[15] which may help in verifying the simulation results to be induced by system characteristics rather than by calculation error .

The integral step is selected 2048.points per rotating period because of the transient impact characteristics of the contact force and the calculation results are recorded after 200 rotating cycles to eliminate initial value transient effect. In calculation an eccentricity value of rotor against stator, δ , is given and adjusted to obtain steady state contact output. The mass and stiffness parameters of the system are selected such that the ones of rotor are much smaller than the ones of stator as to conform to practical system. The simulations were carried out at different rotating frequency from 0.15 to 7 times of the rotor system natural frequency with rotating frequency increment of 0.5Hz and ,under each rotating velocity, using the result of the last integral step of the simulation at last rotating velocity as initial condition. The results are as follows:

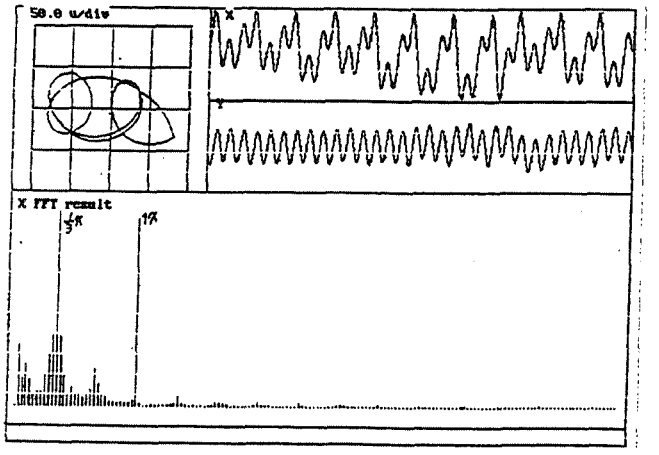

Figure.5 Response between 4 to 6 times of natural frequency

Figure.3 presented the obits , wave forms and spectrum of the rotor displacement . Figure.3 was obtained in the condition that the rotating speed was below 2 times of the first order natural frequency of the system .The spectral characteristics of the response induced by rotor to stator rubs in that rotating frequency range are identical. It is shown that the supper-harmonic components of the rotating frequency are induced by rubs. They are exactly 2x ,3x of the rotating frequency . Some irregular sub-harmonic components also appear below the rotating frequency but not significant.

Figure.4 was obtained at the rotating frequency between two to four times of the first order nature frequency of the system. The vibration regime observed in figure.4 is distinctly different in contrast to figure.3. It is seen that 1/2x sub-harmonic component was excited significantly with 1-1/2x, 2x ,... components also appear as super-harmonic components though not significant. In this case, the denominator of the fractional spectral components is 2.

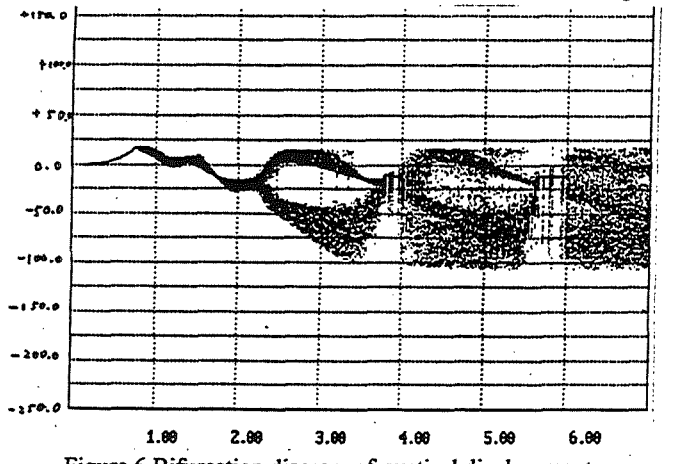

Figure.6 Bifurcation diagram of vertical displacement

When system was simulated at the rotating frequency above four times of the natural frequency of the system. another new vibration regime is observed as shown in Figure.5. The fractional sub-harmonic spectral components shown in it are 1/3x, 2/3x , ... etc. A intricate obit pattern was also observed.

Some conclusions can be derived from these simulation results . Figure.6 summarized simulation results by the bifurcation diagram of the vertical displacement of the rotor obtained through the simulation results . The horizontal axis represents the ratio of rotative

frequency and the vertical axis represents the 100 vibration amplitude values which are sampled once per revolution under every rotative speed. The rotating frequency is varied from 0.15 to 7 times of the first order system natural frequency with increment step of 0.5 Hz in order to eliminate the transient influence of the speed variation . Being sampled after 200 revolutions, the data were obtained at the times when the direction of unbalance force coincided with the vertical axis. These 100 amplitude values sampled represents the Poincare points[14] in 100 rotative revolutions. Hence, If contact occurs under a certain rotating speed , the 100 amplitude values sampled will vary due to the nonlinear chaotic regime introduced by rubs or else they will degenerate to one point in the diagram for periodic response.

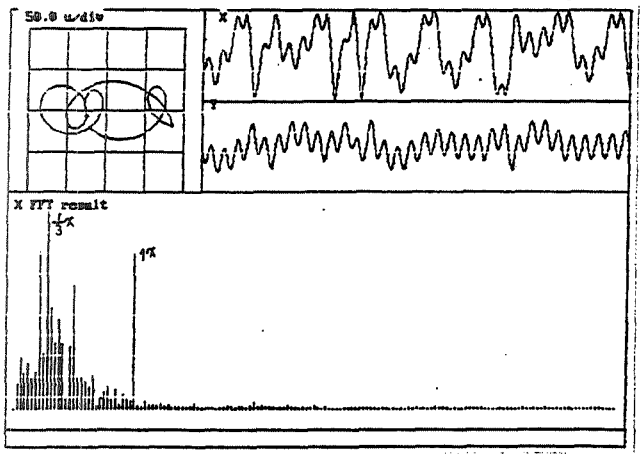

Figure 7. Moderate heavy rub response

As shown in Figure.6, it is seen that when rotative speed varies the system behaves differently. For the system operates at the rotative frequency of below two times of the system natural frequency , the spectrum shows 2x 3x, superharmonic components . While the speed is between 2.0 to 4.0 times of the natural frequency , the fractional sub-harmonic components of denominator 2 appear. The bifurcation diagram, Figure 6, shows two branch bifurcation occurs in this range of rotative frequency, which means the points obtained under a rotative frequency at that range distinctly divided into two groups. When the rotating frequency is between 4.0 to 6.0 times of the natural frequency the 1/3x fractional components present significantly in the spectrum of the system displacement with three branch bifurcation is identified in figure 6. Extensively, when the rotative frequency is above 6.0 times of natural frequency , 1/4x components will appear in the spectra[13] though the spectrum is not shown in this paper.

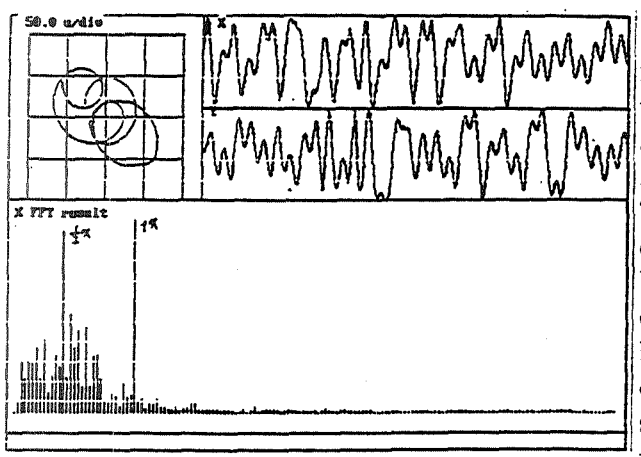

Figure.8 Heavy rub response

These results show that the bifurcation diagram illustrated the relationship between the fractional subharmonic components in the spectra and the branch numbers in the diagram . On the other hands, it seems some critical states exist between those rotative frequency ranges expounded above which may be of some interest . Some parametric sensitive characteristics can be observed near the rotative frequency of 6 times of the natural frequency also.

Above all , It should be mentioned that these result are obtained under a certain parameter δ, the eccentricity between the rotor and stator. The vibration characteristics of the rotor/stator rubs also vary with different rub severity. Figure 7. to Figure 9. depicted the results obtained with different rub severity at a rotative speed above 6 times of the system natural frequency.

In case of the light rub severity, the rub response regime of the system operates in above mentioned rotative frequency range is dominated by 1/4x fractional components(Not show in this paper). With increase of the rub severity, the fractional components varies from 1/3x (Figure.7).to 1/2x(figure.8) and finally, 2x ,i.e. the full annular rub (Figure.9). In other rotative frequency ranges, spectral components follows the same varying tendencies.

4. Experiment of Rotor/stator Rub Response

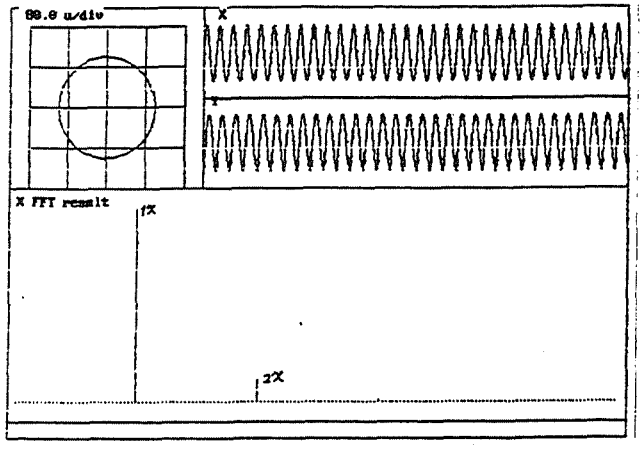

Figure 9. Full annular rub response

Figure.10 showed an experiment rig which was used in a research on the rub event at the compressor of a helicopter turboshaft engine. One aim of the research was to identify the characteristics of the aircraft engine vibration signals when rubs presented between the rotor and stator for an database application in turbo-engine monitoring and diagnosis system. The rotor of the system consist of two mass m_1 and m_2 as shown in Figure 10.. The rotor assembly is supported by ball bearing and mounted on a flexible platform m_3 which is to simulate the elasticity of inlet duct of the engine. The disk m_1 was assembled at the cantilever end of the shaft. An annular rub ring m_4 was assembled on the platform m_3. There is a air gap between m_4 and m_1 which can be adjusted to get the stable rubs between m_4 and m_1 or, to vary the rub severity . The platform was bolted on two supports which are flexible also. Hence , this rig had both flexible rotor and stator.

The rotor was well balance to eliminate the initial unbalance influence on the experiment result before any rub experiments. The First order natural frequency of the system was carefully determined by experiments also.

The experiments was carried out in the condition that the rotor is operated at the rotative speed of below the second order natural frequency of the system. Vibration displacement of disk m_1 was recorded by displacement transducers under different rub severity.

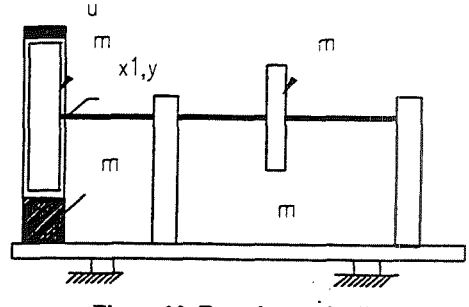

Figure 10. Experiment rig diagram

Figure.11 is the cascade of the vibration signal spectra in vertical direction recorded in different rotating velocity at certain rub severity . It shows that the rub interaction induces the 2x super-harmonic vibration in the whole experimental rotating frequency range.

On the other hand, the system dynamic equation was obtained by FEM. method according to the rub model discussed above. The Bearings are considered to have linear damping and stiffness parameters. The experiments carried out with that experiments rig were numerically simulated based on that equation. The author omitted the detail of the experiment rig

dynamic parameters Because it is of less significance for discussion the results of the experiments.

It is also seen that a significant sub-harmonic components also appear in the spectra. This component is at around 1/2x of the rotative frequency but not exactly. Actually it is not contradict to the results discussed above . Figure.12 and Figure.13 showed the typical results from experiment and numerical simulation . The resemblance between the results is obvious. Both of them shows the components below the rotative frequency and similar 2x and 3x super-harmonic components .Some other phenomena can also be obtained . The amplitude modulating property of the system is observed with the two spectral components symmetric to that at rotative frequency. These result only illustrated that the response induced by rotor/stator rub interaction is system structure reliant.

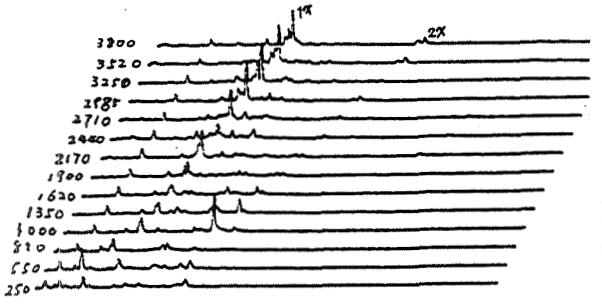

Figure.11. Cascade of spectra at different speeds

Different system will have different vibration regime result from nonlinearity and feedback loop introduced by contact and impact. The experimental and simulation results also showed this component around 1/2x rotative frequency which will shift left when the rub severity increased. It suggested that the sub-harmonic low frequency components are associated with the rub severity. In fact, the rub response under different severity are studied with both experiments and numerical simulations. Both the experimental and simulating results show that the energy of the low frequency component will increase to a limit with the increase of the rub severity. When the rub severity increases further , the low frequency components will be suppressed. If other energy dissipation factors can be ignored , The author believes that the dry friction at the contact point may be concerned in this phenomena. With the increase of the rub severity, The friction at the contact point will increase and deplete the self-excited vibration energy in low frequency range.

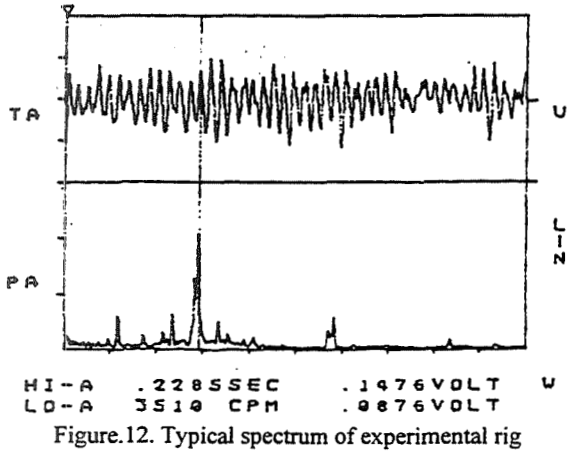

Figure.12. Typical spectrum of experimental rig

Figure.14 showed a turboshaft engine compressor rub vibration signal spectrum obtain from laboratory test. The engine was operated at 879Hz. This frequency is right above the first order natural frequency of the lateral vibration of the compressor rotor. It can be seen that the rub induced 2x (1759Hz) and 3x(2637Hz) super-harmonic spectral components. The result is in line with the experimental and numerical analysis ones discussed above.

5.Conclusion

Rotor to stator rubs is a typical nonlinear dynamic problem. The vibration regimes induce by it are complex not only because of the rub interaction itself but also, as stated[3] , because of

the fact that the rub interaction can be induced by other failures in machines. Hence the response of the rotor/stator rubs varies with the operating conditions of rotating machinery.

This paper presented a theoretical analysis method of the rotor/stator rubs which derived from classical dynamic theory in which the influences of the impact feedback on the rotor/stator system is considered prior to the local contact force properties. This model can be used to analysis different forms of rub and contact cases happened in the rotating machines and may also be able to be used to study other questions involving transient contacts. The application of the method to certain questions showed that the feedback of the impact forces may have more significant effect on the response of system subjected to rubs than that of the local impact force characteristics.

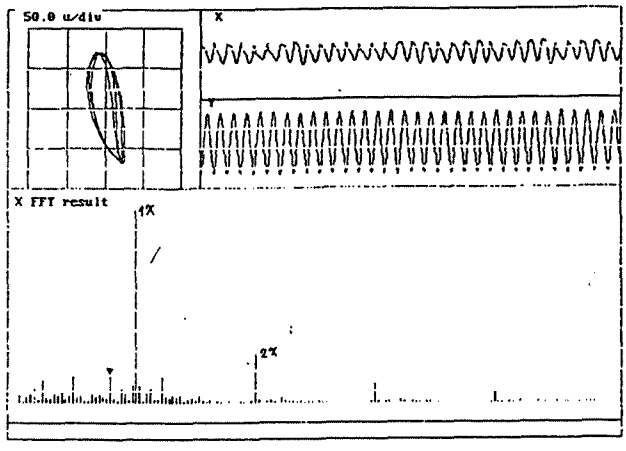

Figure.13 Typical results of numerical analysis

The nonlinear responses of the rubs under different rotative frequencies and different rub severity were discussed in this paper based on a simple rotor/stator system . The results was presented by the bifurcation diagram of the vibration displacement of the system. The conclusion are as follows: With the variation of the rotating velocity the response will changed to different regimes , When the rotative velocity is in the range below 2 times of the system nature frequency the response will contain 2x ,3x super-harmonic component, In other ranges the responses of the rubs will be consisted of 1/(i+1)x fractional sub-harmonic components where i is the mode 2 of the ratio of rotative frequency to the system nature frequency. The regimes are different under different rub severity also. The low frequency components below the rotating frequency are affect by the tangent friction force at contact point in such a way that , with the rub severity increases , low frequency components are suppressed after passing through a maximum energy limitation.

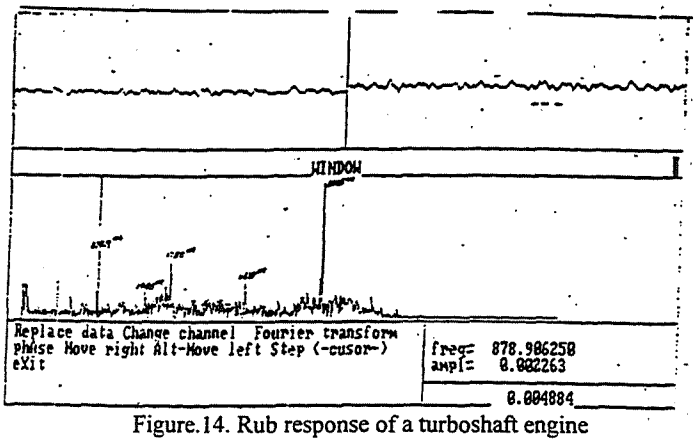

Figure.14. Rub response of a turboshaft engine

Finally, the experimental and numerical simulating results of an experiment rig which was used to study the rub event in a turboshaft engine were presented and compared with turboshaft engine signal. These results showed resemblance to each other. The amplitude modulating properties of the system is also observed both in experimental and numerical results Which may depend on the specific system structure. This results are useful for fault diagnosis of the rotor machinery.

Acknowledgment

The authors gratefully acknowledge Dr. A. Muszynska of BENTLY ROTOR DYNAMICS RESEARCH CORPORATION for her valuable help. she offered her experiment results and new research to the authors and advised numerical simulation works on bifurcation diagrams.

References

[1] Bently, Donald et al, "A Butterfly Rub Response", Bently Rotor Dynamics Research Corporation., BRDRC. Report 3. 1992.

[2] Muszynska, A. , "Rotor-to-Stationary Element Rub-Related Vibration Phenomena in Rotating Machinery", The Shock and Vibration Digest, Vol.21, No.3 pp3-11.

[3] Muszynska, A. "Rub-an Important Malfunction in Rotating Machinery", Proc. Senior Mechanical Engineering Seminar , Bently Nevada Corporation , Carson City Nevada., June , 1983.

[4] Kascak, A. F. "Effects of Different Rub Models on Simulated Rotor Dynamics", NASA Technical paper 2220, 1984.

[5] Choy, F.K.,et al "Rub Interaction of Flexible Casing Rotor System", ASME, Journal of Engineering for Turbines and Power , Vol.111, Oct. 1989.

[6] Bently, D. E. " Forced subrotative Speed Dynamic Action of Rotating Machinery", ASME Publication 74-Det-16.

[7] Muszynska , A., " Synchronous and self-excited Rotor Vibrations Caused by a Full Annular Rub", 8th machinery Dynamics Seminar , Halifax , N.S. Canada , 1994.

[8] Childs, D.W. "Rub Induced Parametric Excitation in Rotors", ASME Journal of Mechanical Design Vol.101 No.4, pp640-644.

[9] Padovan, J., et al "Nonlinear Dynamics of Rotor /Blade/Casing Rub Interaction", ASME Paper No.86-DE-6.

[10] Ehrich , F. F., "Observations of Subcritical superharmonic and Chaotic response in Rotordynamics", DE-35, Rotating Machinery and Vehicle Dynamics. ASME , 1991 , pp1-9.

[11] Curam A. , et al "On The Rubbing Phenomena in turbomachinery", Proc. of Int. Conf. on Rotor Dynamics, 1986, Tokyo.

[12] Choy, F. K., et al "Nonlinear Transient analysis of Rotor-casing Rub Events", Journal of Sound Vibration, Vol.113, No.2.

[13] Yang, W. , Tang, X. K., "Research on the Chaotic Response of Rotor to Stator Rub", A-PVC'93,Japan, Nov, 1993.

[14] Fischer, P. et al "Chaos , Fractals, and Dynamics", Newyork, Marcel Dekker , 1985.

[15] Simo, J. C., et al "Exact Energy -Momentum Conserving Algorithms and symplectic Scheme for Nonlinear Dynamics", Comp. Method in Appl. Mech. Eng., Vol.100,1992.

ROTORDYNAMIC ANALYSIS APPROACH TO AUXILIARY BEARING DESIGN TO AVOID DELEVITATION INDUCED WHIRL INSTABILITY OF AN AMB ROTOR, A CASE STUDY

L. Tessier
Revolve Technologies Inc.
300, 707-10th Avenue S.W.
Calgary, Alberta TZROB3
CANADA
Phone: (403) 781-3300
Fax: (403) 232-4255

Paper was not available at the time of printing. Contact the author for further information.

SEAL LEAKAGES FOR HONEYCOMB OR SMOOTH CONFIGURATIONS

Mahesh M. Athavale
CFD Research Corp.
Huntsville AL 35805

R.C. Hendricks
NASA Lewis Research Center
Cleveland, OH 44135

OVERVIEW

3D-CFD simulations were attempted to analyze the flow field in a honeycomb flat plate tester. This discussion reviews some of the numerical difficulties and relations, including those relating the honeycombs to labyrinth throttles and the consistency of selected seal and tester data sets.

CFD RESULTS

The unfunded project attempted to use a steady state approach to defining the fiction factor within the flat plate tester, ref 1, and illustrated as figure 1 in three views. Fig 1(a) represents a broken top view with pressure tap locations; fig. 1(b) a cross-sectional view of the axial flow path illustrating honeycombs on top and bottom of the flow passage; fig 1(c) a section of the honeycomb top and side views.

Compressible-turbulent flow simulations of the flat plate tester were undertaken using the seals code SCISEAL. The geometries considered were for the 0.79 mm honeycomb width with a clearance of 0.38 mm and two cell depths of 3.05mm for the cases where the friction factor jumped and 3.8 mm when the flow was normal. The flow was modeled assuming steady state flow with central differencing using a two-layer k-ε turbulence model. The standard k-ε turbulence model was considered invalid as cavity flows are too slow. The compressible flow precludes the use of periodicity in the flow-wise direction and requires modeling of the entire domain. In the present case, there were about 60 honeycomb cells in the flow direction of which only 6 could be modeled within a reasonable computational cost.

The geometry was gridded with approximately 90,000 cells, figure 2. While not an unreasonable assumption, flow symmetry was assumed to apply to half of the honeycomb tester and to the top and bottom. The latter is perhaps too ideal as there is no data record of how the upper and lower honeycombs were placed relative to one another. Thus these calculations would represent an ideal situation and others would require an additional 90,000 cells. The computations were restricted to the 6-inlet cells with 3-downstream cells simulated as uniform flow, see figure 2, was a compromise to maintain a reasonable computational time and effort. Each honeycomb cell had an approximate grid of 14x14x45 points. While expedient, this grid is still too coarse for good resolution within the cavities. The pressure was specified at the exit and stagnation conditions were specified at the inlet. The inlet represents two-webs of a honeycomb, the most likely configuration based on figure 1, and the mass flow was input at the these two angles. The calculated friction factors represented an average across the tester.

The issues of coarse grid and limitation on simulation of 6 of 9 cells has already been cited, yet a further limitation is the assumption of steady state, which occurred on the average in the experiment, represents a time dependent process. Nevertheless the simulation represents a first step.

For an inlet pressure of 6.9 bar, the velocity vectors at the center plane within the cells is complex, figure 3. Several vortices are formed and move toward and away from the line of symmetry and up and down within the cavity effecting a deep vortex in the first cavity that tends to dissipate over the next cavity into a carryover jet at the outlet.

The static pressures along the center plane for this coarse grid, figure 4, illustrate variations that could excite tones as in closed pipes; however no unusual variations were found.

The calculated friction factors remained invariant with cell depth change from 3.05mm to 3.8 mm at 0.043. There seems to be little relation to data where the friction factor varied 0.027-0.037 for the 3.8mm depth cell and 0.06 to 0.149 for the 3.05 mm depth cell.

We know from other analyses that modeling portions of the flow field are insufficient to model the flows; thus a time accurate solution over the entire upper and lower offset plates with boundary conditions set at the inlet and exit would be required. Of course such a computation would be expensive and the simplified approach that was taken in the calculations was unable to predict the experimental results.

A new analysis of the flows in honeycomb seals that predict the proper behavior of the honeycomb data is given by Kleynhans and Childs (ref 9). The time dependent clearance continuity equation is modified to permit a flow into the cell and a corresponding time continuity equation is written for the cell control volume. An acoustic model developed for the system shows the effect of cell depth to clearance ratio that tends to function like a compressibility effect related to and controlling the wave speed. This analysis represents a major step in the right directions albeit some discrepancies at higher exit Mach numbers and validated over a narrow range of excitation frequencies.

SIMPLIFIED ANALYSIS

Suppose there is no friction, or it falls into a flow coefficient, then the Bernouli relation holds and the flow rate can be expressed as:

$$\dot{W} = C_d A\sqrt{2\rho\Delta P} \tag{1}$$

In terms of the pressure ratio as expressed by Childs et al. Ref 1, which varies from 0.4 to 0.67

$$\text{Pra} = \text{Pback/Preservior} = \text{Pb/Pr} \tag{2}$$

and assuming perfect gas relations hold (note if pv^{γ}=const were used the ratio would be less)

$$\langle\rho\rangle = \frac{(P_r + P_b)}{2RT}$$

$$2\langle\rho\rangle\Delta P = \frac{\left(P_r^2 - P_b^2\right)}{RT} = \frac{P_r^2}{RT}\left(1 - \left(\frac{P_b}{P_r}\right)^2\right) \tag{3}$$

$$\dot{W} = \left(CdA/\sqrt{RT}\right)P_r\left(\sqrt{1 - P_{r_a}^2}\right)$$

Therefore for a fixed Pra and nearly isothermal flows, and for a given geometry, the ratio of flow rates and Reynolds numbers becomes,

$$\left(\frac{\dot{W}}{\dot{W}_{ref}}\right)\left(\frac{Pr_{ref}}{Pr}\right)=\frac{C_d}{C_{d_{ref}}}$$

or

$$\left(\frac{Re}{Re_{ref}}\right)\left(\frac{Pr_{ref}}{Pr}\right)= \tag{4}$$

The computed flow rates used later to determine flow coefficients become:

At an absolute pressure of Pr = 5 bars and pressure ratio of Pra = 0.4

$$\langle\rho\rangle=\frac{0.001138(5+2)}{2}=3.98\ \text{kg/m}^3$$

$\Delta P = 0.3\text{MPa}$

$$\sqrt{2\langle\rho\rangle\Delta P}=1.54\times10^3\ \text{kg/m}^2-\text{s}$$

$\dot{W}/C_d = 1.54\times10^3(0.23\times151.97\times\pi)\times^{-6} = 54\pi\times10^{-3}\text{kg/s}$
and from data, the flow rate is W=0.065, so $\pi C_d = 1.2$

At an absolute pressure of Pr =20bars and pressure ratio of Pra=0.4
$\langle\rho\rangle = 0.00138(20+8)/2 = 15.9$ kg/m3
$\Delta P = 1.2\text{MPa}$

$\sqrt{2\langle\rho\rangle\Delta P} = 6.2\times10^3\text{kg/m}^2-\text{s}$

$\dot{W}/C_d = 0.216\pi$ kg/s

The experimental value of $\dot{W} = 0.28$, so $\pi C_d = 1.25$.

SMOOTH SEAL RELATIONS

For the **smooth** seal described in ref 2, and **no swirl,** the clearance is 0.23 mm and the shaft diameter is 151.97mm with an L/D = 50.8/.23 = 221. L/D = 1/3 and Cr/R = 0.003 . The results of Table 1 are based on the data of ref (TL-SEAL-16-92 Griffin, Kleynhans, Alexander, Pierce and Childs), Figure 13. $\dot{W}$ ref is the result of a linear extrapolation of data to the 0.05 kg/s mass which is approximately 5 bars (=Pr,ref) absolute pressure. The flow rate $\dot{W}$ is taken at 20 bars (= Pr) in the same manner at a fixed pressure ratio. The $\dot{W}/\dot{W}$ ref ratios vary between 4 and 5.4, and had the analogy followed the ratio would have been Pr/Pr,ref = 4. If the housing deformed under pressure by a little as 0.03mm, these values would be quite close; or possibly some leakage at the stator holder and possibly the simplicity of the analysis is at fault.

Flat Plate Honeycomb Tester

For the stated stagnation absolute pressures of Pr = 0.69 to 1.79MPa, or Pr/Pr,ref= 2.6 Importing the analogy cited prior for the flat plate tester smooth wall or honeycomb results, ref. 1, the Reynolds number ranges are large compared to the established pressure ratios, Table 2. Thus it is unclear how the Reynolds number range is large when the Pr range is low.

HONEYCOMB HOUSING/SMOOTH ROTOR

The consistent data sets of refs. 3, 4 are now investigated using the $\dot{W}/\dot{W}$ ref analogy. The no-swirl data sets were used to provide the following insights: (see figure 5 for the seal configuration of refs. 3 and 4). The use of πCd has no special significance, with the exception of appearing in the area; a constant x πCd can be used to group the data in terms of cell parameters for the data set of refs 3, 4.

Perhaps these results and those of other data sets can be represented by some rather simple relations. For the no-swirl data sets illustrated at 5000 rpm in Table 3, and data for various rpms in Table 4, a simple relation was found, equation 5, where for the smooth case Cw -> ∞ (large) and the units are for cell width Cw (mm), absolute stagnation pressure Pr (bars) and the rotor speed in thousands of rpm's,

$$4\ \pi Cd/5 = (1.3 - 0.26/Cw)(1 - 0.006\ Pr)(1.1 - 0.02\ krpm)(0.7 + 0.3\,Pr\,a) \qquad (5)$$

And for this consistent data set, the ratios of $\dot{W}/\dot{W}$ ref are nearly the same as P/Pref. , i.e., about 4 and 4.15 respectively, as they should be if they follow equation 3.

A new set of test data which provides a comparison of honeycomb and hole-pattern seals has been provided by Yu and Childs (ref. 10), Table 8, while leaking less at larger clearances and twice the cell size, are nevertheless consistent with changes in absolute stagnation pressure.

Relations of the Honeycomb Seal data to Labyrinths

Throttles as per Labyrinth seal approximations of Egli ref. (5) are investigated. Note that the honeycomb seal configurations and the flat plate (ref. 1) were run nearly the same type of apparatus.

The term cell as used in this section is the honeycomb cell + adjacent web. In terms of cell width,

$\sqrt{3}\ W_h$; the adjacent web in the axial direction. $W_h/\sqrt{3}$ and the honeycomb point to point is $2W_h/\sqrt{3}$. The geometry is defined in figure 6.

The honeycomb seals are 50.8 mm in length so in terms of throttles or cells (N),

W_h mm	$\frac{50.8}{W_h\sqrt{3}}$		N
0.79	37.1 cells	Actual, maybe	36
0.4	73.3 cells	Actual, maybe	72

Based on the honeycomb seal data TL-SEAL-14-92, and TL-SEAL-13-92, and the calculations illustrated in Table 6, the flow coefficient in terms of throttles can be represented in terms of the φ factor of Martin, ref. 6, or in terms of throttles,

$$\varphi^2 = \frac{\left(1 - Pr_a^2\right)}{N - \ln(Pr_a)}$$

$$C_d = \frac{5\sqrt{2}\varphi}{4} \qquad (6)$$

$$C_d = \left(\frac{N}{2}\right)^{-0.45}$$

There is a strong argument that N = 2 x N-cells because each cell has sequential walls equivalent to two throttles. In this case the φ term becomes about $10\varphi/4$ instead of $7.07\varphi/4$, ie.,

$$C_d = \frac{10\varphi}{4}$$

$$C_d = N^{-0.45}$$

and perhaps this should be used and eliminate the controversy?

Flat Plate Honeycomb Tester

Looking at the test apparatus of ref 1, and using equation 6 for Cd, the Reynolds number range is significantly smaller than that cited in ref. 1. The assumptions and sample calculations are given in Table 7. At Pr = 17.9 and Pra =0.67, the estimated Reynolds number is 47,300 and for Pra =0.4 58,400. The data are in good agreement with these values at Re = 55,000. However for Pr=6.9, Pra=0.67, Pb = 4.62, the estimated Reynolds number is 18,320 and nearly double the data Reynolds number of 9900. The actual backpressure is not known, yet Pra = 0.9 would be required to give the data result. This issue remains unresolved.

SUMMARY

The CFD analysis suffers from the lack of being able to complete a full simulation of the total number of honeycomb cells in the tester within a reasonable computational cost. Also the problems of unsymmetrical upper and lower boundaries and use of the steady state assumptions add to the cost. The lack of friction factor and jump predictions will require significant computations to show the competency of bulk flow models and resolve flat plate tester data relative to the full seal results which have not shown the friction factor jump.

The honeycomb seal flow rate data can be related to a simple flow coefficient relation, but this only provides some rule of thumb estimate as to the leakage.

The same set of data can be qualitatively related to labyrinth throttles where either the cell length or the number of honeycomb vertical walls (2 x cells) can be used.

Using the consistent set of honeycomb seal data, the Reynold number ranges could not be predicted for the flat plate tester.

The data sets for reference 1 are necessary for further calculations and maybe they are available from Prof. Childs?

References:

1. Ha, T.W., Morrison, G.L., Childs, D.W.: Friction-Factor Characteristics for Narrow Channels with Honeycomb Surfaces, Trans. ASME Jourl. Tribology, Vol 114, Oct 1992, p714-721.

2. Griffin, M., Kleynhans, G., Alexander, C., Pierce, T., and Childs D.W. Experimental Rotordynamic Coefficient and Static Characteristic Results for A Smooth Seal with L/D =1/3, Cr/R= 0.003., TL-SEAL-16-92 #362, May 1992.

3. Griffin, M., Kleynhans, G., Alexander, C., Pierce, T., and Childs D.W. Experimental Rotordynamic Coefficient and Static Characteristic Results for a Honeycomb Seal with L/D = 1/3, Cr/R = 0.003, Ch = 2.29 mm, and Cw = 0.40 mm. TL-SEAL-14-92, #360, May 1992.

4. Griffin, M., Kleynhans, G., Alexander, C., Pierce, T., and Childs D.W. Experimental Rotordynamic Coefficient and Static Characteristic Results for a Honeycomb Seal with L/D = 1/3, Cr/R = 0.003, Ch = 2.29 mm, and Cw = 0.79 mm. TL-SEAL-13-92, #359, May 1992.

5. Egli, A. The Leakage of Steam Through Labyrinth Seals ASME Trans. p 115-122, 1958. Paper FSP-57-G.

6. Martin, H.M.: Steam Leakage in Dummies of Ljungstrom Type, Engineering, Jan. 1919, pp 1-3.

8. Hendricks, R.C. and Stetz, T.T: Plow Through Aligned Sequential Orifice-Type Inlets, NASA TP 1967, March 1982.

9. Kleynhans, G. and Childs, D. (1996) The Acoustic Influence of Cell Depth on the Rotordynamic Characteristics of Smooth-Rotor/Honeycomb-Stator Annular Gas Seals. Eighth Workshop on Rotordynamic Instability Problems in High-Performance Turbomachinery. Texas A&M University, May 6-8.

10. Yu, Z. and Childs, D.(1996) A Comparison of Experimental Rotordynamic Coefficients and Leakage Characteristics for Hole-Pattern Gas Damper Seals and a Honeycomb Seal. Eighth Workshop on Rotordynamic Instability Problems in High-Performance Turbomachinery. Texas A&M University, May 6-8.

Table 1. Based on smooth seal data of TL-SEAL-16-92 Griffin, Kleynhans, Alexander, Pierce and Childs, Figure 13. Extrapolated data to the 0.05 kg/s mass flow rate = $\dot{W}$,ref for an absolute pressure of 5 bars. $\dot{W}$ is taken at 20 bars. Flow rates are linear with absolute pressure at fixed pressure ratios.

Pra	$\dot{W}/\dot{W}$ ref	rpm	Pr = 5 to Pr= 20
.67	.25/.05 = 5	5000	
	.23/.05 = 4.6	12000	
	.2/.05= 4	16000	
.4	.27/.05= 5.4	5000	
	.25/.05= 5	12000	
	.225/.05 = 4.5	16000	
			-> Pr/Pr,ref= 4

Table 2. Flat plate tester data comparisons for absolute pressure range Pr,ref= 0.69MPa to Pr = 1.79 Mpa. Data from Ha, Morrison, Childs. ASME trans.

At C=0.38mm	7<Re<96	Smooth surfaces run 2 Table 1, ref.	Re/Re, ref = 13.7
		Friction factor ratio	f/f,ref = 2
	6 < Re < 60	Honeycomb run 20 Table 1, ref.	Re/Re,ref= 10
		Friction factor ratio	f/f,ref = 1.4

Pr= 0.69 to 1.79MPa or Pr/Pr,ref= 2.6

Table 3. Flow coefficient based on calculations, equation 3, and data from Figures 13, TL-SEAL-16-92, TL-SEAL-14-92, and TL-SEAL-13-92, No Swirl case at 5000 rpm at pressure ratios of 0.4 and 0.67 for cell widths of 0.4mm and 0.79 mm where L/D = 1/3, Cr/R=0.003, Ch=2.29mm.

		0.4 mm cell width			0.79mm cell width		Smooth	
Pra	Pr	$\dot{W}$,ref kg/s	$\dot{W}$ kg/s	πCd	$\dot{W}$ kg/s	πCd	$\dot{W}$ kg/s	πCd
.4	20	.216 pi	.143	.66	.219	1.03	.283	1.3
	5	.054 pi	.032	.59	.05	.93	.065	1.2
.67	20	.175 pi	.129	.74	.185	1.06	.25	1.43
	5	.044 pi	.026	.62	.044	1.	.05	1.14

Table 4. Data used to determine equation 5, based on data from Figures 13, TL-SEAL-14-92, and TL-SEAL-13-92, No Swirl case at pressure ratio Pra = 0.4 and absolute stagnation pressure Pr=20.

	0.79 mm cell width	0.40 mm cell width
krpm	$\dot{W}$	$\dot{W}$
5	.219 kg/s	.143 kg/s
12	.192	.129
16	.165	.117

Perhaps these results can be represented by some rather simple relations for the no-swirl (maybe the others as well?) set of data illustrated above (smooth Cw -> ∞) (large): Cw (mm) Pr (bars)

$$4\ \pi Cd/5 = (1.3 - 0.26/Cw)(1 - 0.006\ Pr)(1.1 - 0.02\ krpm)(0.7 + 0.3\,Pr\,a) \qquad (5)$$

Table 5. Three checks on equation 5, using equations 1 and 5.

1. Smooth, Pr = 10, Pra = .56, 12krpm, $1.25\ \pi\ Cd = 1.3 \times .94 \times .86 \times .87 = 1.14$
   data flow rate = 0.11 kg/s
   calc: $\rho = ((5.6 + 10)/2)\ 0.001138 = 8.9$ kg/m3

   $$\frac{<\rho>}{\sqrt{2x8.9x0.44x10^6}}\ (.23 \times 152\ pi) = 0.098\ kg/s$$

   0.098x 1.14=0.11 kg/s
   Error = -close enough %

2. Cw=.79
   πCd=0.85
   flow rate = 0.083 kg/s
   data flow rate = 0.085 kg/s

3. Cw=.4
   πCd=0.58
   flow rate = 0.056 kg/s
   data flow rate = 0.054 kg/s

Table 6. Calculations of flow rate reduction parameter based on Martin and Egli, and the experimental data of TL-SEAL-14-92, and TL-SEAL-13-92.

1. flow rate = $C_d A\sqrt{2<\rho>\Delta p}$

$A = 0.23^* 152\ pi = 110\times10^{-6}\ m^2$
Pr= 20 bars, Pra = 0.4 Pb = 8bars
ΔP = 1.2 Mpa
ρ = ((20+8)/2) 0.001138 = 19.3 kg/m3

Flow rate = Cd (ll0×10^{-6}) sqrt(2 *1.2*19.3×10^{6}) = 0.749 Cd kg/s

2. w = 0.4 mm honeycomb

Flow rate data = 0.143 kg/s at 5000 rpm
Cd = .143/.749 = .19

(Does not follow 1/Cd=5.237; $N=(1/C_d)^2$=27.4)

3. Throttle tlow reduction of Martin, ref 6.

$$\varphi^2 = \frac{\left(1-Pr_a^2\right)}{N-\ln(Pra)} \qquad (6)$$

$$= (1-(.4)^2)/(72-\ln(0.4)) = 0.01118$$

$$\varphi = 0.109$$

The sequential choked orifice work of Hendricks and Stetz shows the flow as a function of N**(-.4). Applying this exponent, φ=0.181 is low.

4. For the w= 0.79 mm cell, flow rate data = 0.219 kg/s for same pressure conditions at 5000rpm,

Cd = .219/.749=0.292 and there are 50.8/$\sqrt{3}$ W_h = 37.1 cells, and assuming cut ends, used 36 cells.

φ**2 = (1-.4**2)/(36 -ln(.4)) =0.024
φ = 0.155

These relations can be represented by $C_d = \frac{5\sqrt{2}\varphi}{4}$ and reasonably well by $C_d = \left(\frac{N}{2}\right)^{-0.45}$ and are summarized as follows,

w_h mm	Pr	Cells	Cd,exp	$C_d = \frac{5\sqrt{2}\varphi}{4}$ $10\ \varphi^1/4$	(N/2)**(-.45)	Error %
.4	.4	72	.19	.192	.206	3
.79	.4	36	.29	.274	.272	-6

φ_1 uses N=2xN-cells

Table 7. Estimation of Reynolds Numbers for the flat plate test apparatus of ref 1, using the Cd relation equation 6.

1. Geometry and Cd

w_h= 1.75 mm cell width
H = 0.38 mm clearance
Cell = $\sqrt{3}\ W_h$ = 2.72mm
Seal length = 76 mm
Cell = 76/2.72 = 28 = Nc
N = 2 Nc = 56
$C_{do}^2 = (1 - 0.67^2)/(56 - \ln 0.67) = 0.01$
CdH = 0.25

Pr = 17.9 Pra =0.67

2. Flow

$\rho = ((17.9 + 12)/2)\ 0.001138 = 17\ kg/m^3$
$\Delta P = 0.59 MPa$
$\dot{W} = 0.25\ (.38 * 64\times10^{-6})\ \sqrt{2\ 17.56\ 10^6} = 0.027\ kg/s$
$G = 1120\ kg/m^2\text{-}s$

3. Reynolds number estimates

$Re = 2HG/\mu = 2\ 0.38\ 10^{-2} * 1120/0.18\ 10^{-4} = 47{,}300$ (Re = 58,400 for Pra = 0.4)

If I am reading figure 7 (figure 5 of ref 1) correctly, data Re = 55000

4. Estimations of Reynolds number at elevated pressures

For Pr=6.9 Pra=0.67 Pb = 4.62

$\rho = (6.9+4.6)/2 * 0.001138 = 6.56$ kg/m^3
$\Delta P = 0.23$ MPa
$\dot{W} = .25\ A\ (.23 * 6.56 * 2\ \ 10^6) = .0106$kg/s
$G = 434$ kg/m^2 - s

$Re = 2HG/\mu = 2\ 8.38\ 10^{-2} * 434/.18\ 10^{-4} = 18{,}320$

data Re = 9900

The actual test backpressure is unknown and, a Pra = 0.9 would be required to give the data result.

Table 8. Comparison of Data from Yu and Childs (ref 10) with TL-SEAL-14-92, and TL-SEAL 13-92, and TL-SEAL-10-92.

From the presentation of Yu(ref 10), figure 7a for honeycomb seals, Cw= 1.588mm, Ch = 2.29mm, Cr= 0.3mm, L/D = 1/3, D= 152 mm, L= 50.8mm, Cr/R= 0.004, 4680rpm, Pra= 0.4

Pr= 5 $\dot{W}$= 0.05 kg/s

Pr=20 $\dot{W}$= 0.193 kg/s

These flows are very close to those cited in TL-SEAL-13-92.

From TAM report TL-SEAL-10-92 with Cw = 0.79mm, do not have comparable data for Cw =1.588mm,

Pr =5 $\dot{W}$= 0.075 kg/s

Pr=20 $\dot{W}$= 0.33 kg/s

The point here is for an increase in clearance, one would expect an increase in leakage flow; in some manner the increase in cell size, double, has compensated for the clearance increase.

Cr.004/Cr.003 = .3/.23 = 1.3 Implying W.004/W.003 = 1.3

Pr	$\dot{W}$.003	$\dot{W}$.004	$\dot{W}$.004/$\dot{W}$.003	$\dot{W}$(Yu)	
5	0.05	.075	1.5	0.05	kg/s
20	0.219	.33	1.5	0.193	kg/s

Actually the flows changed more than the clearance would suggest. A rotor diameter change of one-mil or that of the honeycomb effective clearance would bring the ratio to 1.36 vs 1.3 and is very sensitive to thermal conditions and component tolerances. However comparing the change in W with Pr, for a pressure change of 20/5 = 4, the flow ratios remain consistently close to that value, i.e.,

($\dot{W}$.003,Pr-20/ $\dot{W}$.003,Pr=5) = 4.4

($\dot{W}$.004,Pr=20/ $\dot{W}$.004,Pr=5) = 4.4

($\dot{W}$(Yu),Pr-20/ $\dot{W}$(Yu),Pr=5) = 3.9

ATTENDEE LIST

Mahesh M. Athavale
CFD Research Corporation
3325 Trianna Blvd.
Huntsville, AL 35805
Phone: (205) 536-6576
Fax: (205) 536-6590

Florin Dimofte
NASA Lewis Research Center.
M.S. SPTD-3
21000 Brookpark Rd.
Cleveland, OH 44135
Phone: (216) 977-7468
Fax: (216) 977-7545

David Elrod
The University of Alabama in Huntsville
Huntsville, AL 35899
Phone: (205) 890-7208
Fax: (205) 890-7205

Fred Evans
AMOCO Corp.
3700 Bay Area Blvd.
Houston, TX 77058
Phone: (713) 212-7186
Fax: (713) 212-1615

Rene Fongang
Technical University of Darmstadt
MESYM, Petersenstr. 30
Darmstadt 64287
GERMANY
Phone: (0049) 6151-3973
Fax: (0049) 6151-5332

Kostandin Gjika
Allied Signal Automotive
Turbocharging Systems
3210 West Lomita Blvd.
Torrance, CA 90505-5064
Phone: (310) 517-1269
Fax: (310) 517-1490

Eric J. Hahn
The University of New South Wales
Head, Applied Mechanics Dept.
School of Mechanical and Manufacturing Engineering
Sydney 2052
AUSTRALIA
Phone: 61-2-385-4142
Fax: 61-2-663-1222

Hidetsugu Ishimaru
Kobe University-Mechanical Engineering Dept
1-1 Rukkodai
Naba, Kobe 657
JAPAN
Phone: (078) 803-1130
Fax: (078) 803-1131

Takuzo Iwatsubo
Mechanical Engineering Dept.
The Faculty of Engineering
Kobe University
1-1, Rokkodai Nada Kobe 657
JAPAN
Phone: 81-78-803-1100
Fax: 81-78-803-1131

Chang-Ho Kim
Korea Institute of Science and Technology
Hawolgok-dong 39-1
Songbuk-gu, Seoul
KOREA
Phone: 82-2-958-5652
Fax: 82-2-958-5659

George Kleynhans
Turbomachinery Laboratory
Texas A&M University
College Station, TX 77843-3254
Phone: (409) 862-4745
Fax: (409) 845-6382

Dr. Klaus Kwanka
Technische Universität München
Chair of Thermal Power Systems
Lehrstuhl Thermische Kraftanlagen
80290 München
GERMANY
Phone: 49-89-289-16272
Fax: 49-89-289-16271

Gerald Morrison
Turbomachinery Laboratory
Texas A&M University
College Station, TX 77843-3254
Phone: (409) 845-5414
Fax: (409) 845-3081

Michael Matros
Universität Kaiserslautern
Arbeitsgruppe Maschinedynamik
Postfach 3049
D-67653 Kaiserslautern
GERMANY
Phone: 49-631-205-3309
Fax: 49-631-205-4312

Rainer Nordmann
Technical University of Darmstadt
Petersenstr. 30
Darmstadt 64287
GERMANY
Phone: 49-6151-16-2074
Fax: 49-6151-16-5332

Alan Palazzolo
Texas A&M University
Mechanical Engineering
College Station, TX 77843-3123
Phone: 409-845-5280
Fax: 409-845-1835

Krishnaswamy Ramesh
Virginia Polytechnic Institute & State University
Dept. of Mechanical Engineering,
Randolph Hall
Blacksburg, VA 24061
Phone: (540) 231-6745
Fax: (540) 231-9100

Sunil Sahay
AlliedSignal Turbocharging
3201 West Lomita Blvd.
Torrance, CA 90505-5064
Phone: 310-517-1403
Fax: 310-517-1490

Luis San Andres
Texas A&M University
Mechanical Engineering
College Station, TX 77843-3123
Phone: 409-845-0160
Fax: 409-845-1835

Ilmar Ferreira Santos
DPM
UNICAMP
13083-970 - Campinas
SP - BRAZIL
Phone: 55-192-398-384
Fax: 55-192-393-722

Klaus Steff
Demag Delaval Turbomachinery
Mannesmann Demag, AG
Verdichter, Postfach 10 15 07
D-47015 Duisburg
GERMANY
Phone: 49-203-605-3293
Fax: 49-203-605-3525

Lynn Tessier
Revolve Technologies Inc.
300, 707-10th Avenue S.W.
Calgary, Alberta TZROB3
CANADA
Phone: (403) 781-3300
Fax: (403) 232-4255

John Vance
Turbomachinery Laboratory
Texas A&M University
College Station, TX 77843-3254
Phone: (409) 845-1257
Fax: (409) 845-1835

Norbert Wagner
Demag Delaval Turbomachinery
Mannesmann Demag. AG
Verdichter. Postfach 10 15 07
D-47015 Duisburg
GERMANY
Phone: 49-203-605-3293
Fax: 49-203-605-3525

Peter Wurmsdobler
Insitute for Machine and Process
Automation
Technical University Vienna
Gußhausstr. 27-29
A-1040 Vienna
AUSTRIA
Phone: 43-1-58801 3673
Fax: 43-1-504 92 64

Zephing Yu
Turbomachinery Laboratory
Texas A&M University
College Station, TX 77843-3254
Phone: (409) 862-4745
Fax: (409) 845-6382

REPORT DOCUMENTATION PAGE

Form Approved
OMB No. 0704-0188

1. AGENCY USE ONLY (*Leave blank*)	2. REPORT DATE	3. REPORT TYPE AND DATES COVERED
	May 1997	Conference Publication

4. TITLE AND SUBTITLE

Rotordynamic Instability Problems in High-Performance Turbomachinery 1996

5. FUNDING NUMBERS

WU–233–1B–1B

6. AUTHOR(S)

7. PERFORMING ORGANIZATION NAME(S) AND ADDRESS(ES)

National Aeronautics and Space Administration
Lewis Research Center
Cleveland, Ohio 44135–3191

8. PERFORMING ORGANIZATION REPORT NUMBER

E–10502

9. SPONSORING/MONITORING AGENCY NAME(S) AND ADDRESS(ES)

National Aeronautics and Space Administration
Washington, DC 20546–0001

10. SPONSORING/MONITORING AGENCY REPORT NUMBER

NASA CP–3344

11. SUPPLEMENTARY NOTES

Responsible person, R.C. Hendricks, organization code 5300, (216) 977–7507.

12a. DISTRIBUTION/AVAILABILITY STATEMENT

Unclassified - Unlimited
Subject Category 37

This publication is available from the NASA Center for AeroSpace Information, (301) 621–0390.

12b. DISTRIBUTION CODE

13. ABSTRACT ***(Maximum 200 words)***

The first rotordynamics workshop proceedings (NASA CP-2133, 1980) emphasized a feeling of uncertainty in predicting the stability of characteristics of high-performance turbomachinery. In the second workshop proceedings (NASA CP-2250, 1982) these uncertainties were reduced through programs established to systematically resolve problems, with emphasis on experimental validation of the forces that influence rotordynamics. In the third proceedings (NASA CP-2338, 1984) many programs for predicting or measuring forces and force coefficients in high-performance turbomachinery produced results. Data became available for designing new machines with enhanced stability characteristics or for upgrading existing machines. In the fourth proceedings (NASA CP-2443, 1986) there emerged trends towards a more unified view of rotordynamic instability problems and several encouraging new analytical developments. The fifth workshop (NASA CP-3026, 1988) supported the continuing trend toward a unified view with several new developments in the design and manufacture of new turbomachineries with enhanced stability characteristics along with new data and associated numerical/ theoretical results. The sixth workshop report (NASA CP-3122, 1990) provided field experience and experimental results, and expanded the use of computational and control techniques with integration of damper, bearing, and eccentric seal operation results. The seventh workshop report (NASA CP-2329, 1993) provided field experiences, numerical, theoretical, and experimental results and control methods for seals, bearings, and dampers with some attention given to variable thermophysical properties and turbulence measurements, and introduction of two-phase flow results. In the present workshop, active magnetic bearings (AMB's) evolve into a new method of measuring rotordynamic coefficients with discussions on honeycomb seals, drop of magnetically supported rotors, seals, bearings and dampers with new data being reported. The intent of the workshop and this proceedings is to provide a continuing impetus for an understanding and resolution of these problems.

14. SUBJECT TERMS	15. NUMBER OF PAGES
Rotordynamics; Seals; Bearings; Turbomachinery; Instabilities	300
	16. PRICE CODE A13

17. SECURITY CLASSIFICATION OF REPORT	18. SECURITY CLASSIFICATION OF THIS PAGE	19. SECURITY CLASSIFICATION OF ABSTRACT	20. LIMITATION OF ABSTRACT
Unclassified	Unclassified	Unclassified	